Second-generation High-Order Harmonic Sources — From CPA to OPCPA

Rudawski, Piotr

2014

Citation for published version (APA):
Rudawski, P. (2014). *Second-generation High-Order Harmonic Sources — From CPA to OPCPA*. [Doctoral Thesis (monograph), Atomic Physics].

Total number of authors:
1

SECOND-GENERATION HIGH-ORDER HARMONIC SOURCES

FROM CPA TO OPCPA

Piotr Rudawski

Doctoral Thesis
2014

1666

LUND UNIVERSITY

SECOND-GENERATION HIGH-ORDER HARMONIC SOURCES
—
FROM CPA TO OPCPA

Printed in Sweden by Media-Tryck, Lund, 2014

Division of Atomic Physics
Department of Physics
Faculty of Engineering, LTH
Lund University
P.O. Box 118
SE–221 00 Lund
Sweden

http://www.atomic.physics.lu.se

ISSN 0281-2762
Lund Reports on Atomic Physics, LRAP 487 (2014)

ISBN 978-91-7473-939-8
ISBN 978-91-7473-940-4

to Agnieszka

ABSTRACT

This thesis presents two sources of extreme ultraviolet (XUV) radiation based on high-order harmonic generation (HHG) in gases. The sources were developed for experiments requiring high-flux harmonic beams or HHG pulses at high-repetition rate. These were used experimentally to image nano-scale objects. The high-flux HHG source was used for digital in-line holography, and the high-repetition rate source for photoemission electron microscopy. In addition, a conceptual design for a high-flux gas beamline for a large scale facility, Extreme Light Infrastructure - Attosecond Light Pulse Source, is described.

The work focuses on the construction and development of the driving laser systems and the HHG sources, as well as on the optimization of their performance. The thesis describes the two lasers used to drive the HHG sources: a high-power laser system and a newly built optical parametric chirped pulse amplification (OPCPA) system. The two systems are both based on the chirped pulse amplification technique, but the amplification process is carried out in different ways. The high-power laser system is based on linear amplification in Ti:Sapphire while the OPCPA system uses nonlinear amplification via difference frequency generation.

Furthermore, the use of multi-color driving fields to manipulate the generation process, both from the microscopic and the macroscopic points of view, was investigated. The combination of the fundamental field with its second harmonic in a non-collinear geometry allows us to probe and control macroscopic properties. The addition of low-order odd harmonics in a collinear geometry results in an enhancement of the single atom response.

POPULAR SCIENCE SUMMARY

What happens on a time scale unavailable to the human eye? How often have we wondered about this while admiring nature or discussing a sport event in which a referee took a dubious decision? To solve the puzzle we could use a camera to record a movie and simply replay it frame-by-frame.

A similar question bothered painters and horse race fans in the middle of the nineteenth century: whether a galloping horse at any instant has all four feet off the ground? The answer was provided by a British photographer, Eadweard Muybridge, using innovative cameras. He took a series of images to freeze a horse at consecutive instants of time during a gallop. His cameras were able to snap an image in only six milliseconds (6×10^{-3} seconds), fifty times faster than a blink of an eye. During that time a mechanical shutter was opened, allowing the light pass to a photosensitive element. His photographs solved the mystery, and provided inspiration to artists, scientists, and the emerging art of the motion picture.

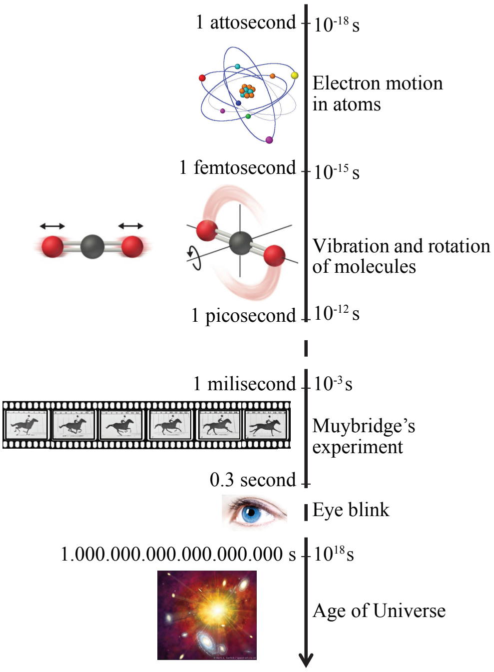

Figure 1: Spans of time.

Today's challenges

Nowadays the Muybridge experiment can be carried out with readily available cameras. The shutters of modern cameras can be open during only 0.1 millisecond (sixty times shorter than in the Muybridge camera). This tool can help every one of us answer questions about motion in nature. However, in laboratories we would like to trace the movements of much faster and incomparably smaller objects, far beyond the capability of the Muybridge camera. This need is driven by

fundamental questions in modern biology, chemistry, and physics, in particular: *How to control the motions of electrons in atoms or molecules?*

To observe the movements of these kinds of objects, we have to use a different strategy than Muybridge, since no mechanical shutter can move sufficiently fast. Instead, we can record an image by illuminating an object with a flash of light which lasts for a shorter time than the observed event – exactly the same way as taking a picture with a flash in commonly used cameras.

Femtosecond flashes of light (1 femtosecond = 10^{-15} second), which are generated using laser pulse technology, allow the study of the motion and disintegration of molecules. However, observation of an electron on its natural time scale requires a pulse with duration of a few tens of attoseconds (1 attosecond = 10^{-18}). This duration is so short that comparing it to a second is like comparing a second to the age of the universe. How do we make such a pulse?

Atto-tools

Over the last three decades scientists have developed a technique called high-order harmonic generation to make these pulses. The generated beam is like a laser beam: well collimated and coherent. The laser pulse driving the generation process is extraordinary itself. It is already a very short pulse, with a duration of femtoseconds, and peak power of the order of terawatts (10^{12} Watts). When such a pulse interacts with an atom it rips the electron away, leaving the atom in an ionic state. Under certain conditions the electron may come back into the parent atom, and by interacting with it, a photon may be emitted. The emitted photons have much shorter wavelengths than to the laser photons, lying in the ultraviolet or soft X-ray spectral ranges. The bunch of emitted photons lasts only a few tens of attoseconds.

Sources based on this technique have an important drawback: poor efficiency in their conversion of energy. A highly energetic laser beam has to be used in order to obtain only a moderate energy of the generated radiation. For 1 Joule of energy in the driving field only 0.00001 Joule is generated, corresponding to a conversion efficiency of 10^{-5}.

The atto-tools presented in the thesis

To construct efficient high-order harmonic sources we looked at the process from the microscopic and macroscopic points of view. We enhanced the response of one atom to an intense laser field and developed a technique to involve as many atoms as possible in the process.

The results of the work are two sources of high-order harmonics, built at the Lund Laser Centre (LLC). Each of the sources is driven by an advanced laser system. One is based on the traditional chirped pulse amplification (CPA) method, and the second on optical parametric chirped pulse amplification (OPCPA). The later technology only recently became available for attosecond science. We have shown how novel, high-repetition rate, high-order harmonic sources can be realized with the new laser amplification technique.

The experience gathered during the construction of the HHG sources in Lund was used to design a beamline under a pan-European project, Extreme Light Infrastructure

(http://www.eli-hu.hu/). The beamline will provide powerful attosecond pulses for the European scientific community.

Future

John Tisch, from Imperial College London, UK, has stated *"At the moment our work is like that of a movie cameraman, recording the movements of the electrons. One day, we would like to become like movie directors, making the electrons move where we want. If we could do this, we could control chemical reactions, design new materials, and create faster, more efficient electronic devices"*.

Nowadays, it is hard to find applications of atto-tools in everyday life. Our work towards the creation of an efficient and simple table-top source of XUV radiation which is readily accessible for scientists might help them to become movie directors in the atto-world. Perhaps our tools will lead to breakthroughs in medicine or chemistry. In the future we might have similar difficulty imagining our lives without atto-tools as is it now difficult to imagine life without cinematography.

POPULÄRVETENSKAPLIG SAMMANFATTNING

Vad händer på en tidskala otillgänglig för ett mänskligt öga? Hur ofta har vi undrat över det, när vi beundrar den omgivande naturen eller när vi diskuterar en sporthändelse, där en domare tog ett tvivelaktigt beslut? För att lösa detta pussel, kan vi använda en kamera för att spela in en film och helt enkelt återspela den händelsen bildruta för bildruta.

Liknande frågor ställde målare och hästkapplöppare i mitten av 1800-talet: Släpper en häst vid något tillfälle alla hovarna från marken när den galopperar? Svaret gavs av en engelsk fotograf, Eadweard Muybridge, med hjälp av innovativa kameror. Han tog serier av bilder för att registrera en galopperande häst. Hans kameror kunde ta en bild på endast 6 millisekunder (6×10^{-3} sekund), 50 gånger snabbare än ett öga kan blinka. Under den tiden öppnades en mekanisk slutare för att låta ljuset passera till ett fotokänsligt element. Hans fotografier löst mysteriet och gav inspiration till konstnärer, forskare och den framväxande konsten av filmen.

Dagens utmaningar

Muybridges experiment kan nu utföras med lättillgängliga kameror. Slutarna i moderna kameror kan öppnas under endast 0,1 millisekund (60 gånger kortare än i Muybridges kamera). Detta verktyg kan hjälpa var och en av oss att svara på frågor som vi har om rörelser i naturen. Men i laboratorier vill vi kunna registrera rörelser av mycket snabbare händelser och ojämförligt mindre objekt, långt bortom kapaciteten av Muybridges kamera. Detta behov är drivkraften i fundamentala frågor i modern biologi, kemi och fysik, särskilt: *Hur kan vi kontrollera rörelse av elektroner i atomer och molekyler?* För att observera riktigt snabba förlopp, måste vi använda en annan strategi än Muybridge, eftersom ingen mekanisk slutare kan röra sig så snabbt. Vi kan ta bild genom att belysa ett föremål med en ljusblixt, kortare än den observerade händelsen - exakt på samma sätt som när man tar en bild med blixt i vanliga kameror, men här med ännu kortare blixtar.

Femtosekundljusblixtar (1 femtosekund = 10^{-15} sekund), som genereras med hjälp av laserpulsteknik låter oss studera atomära rörelser i molekyler. För att observera elektroner på sin naturliga tidskala krävs ljusblixtar (laserpulser) av endast några tiotals attosekunders (1 attosekund = 10^{-18} sekund) varaktighet. Dessa blixtar är så korta så att jämföra dem med en sekund är som att jämföra en sekund med universums ålder. Men hur skapar man sådana pulser?

Atto-verktyg

Under de senaste tre decennierna har forskare utvecklat en teknik som kallas övertonegenerering, för att skapa dessa attosekundspulser. Laserpulsen, som driver genereringsprocessen, är i sig själv extraordinär. Den är redan en mycket kort (femtosekundspulse) och har en toppeffekt av storleksordningen terawatt (10^{12} Watt). När sådan puls växelverkar med en atom, sliter den loss en elektron, driver bort den och lämnar atomen i ett joniserat tillstånd. Under vissa villkor drivs elektronen tillbaka till sin moderatom och vid växelverkan med denna emittera en foton. De genererade fotonerna har mycket kortare våglängd i jämförelse med laserfotonerna, i det ultravioletta eller röntgenområdet. En grupp puls av utsända fotoner varar endast några tiotals attosekunder.

Källor som baseras på denna teknik har en betydande nackdel, nämligen relativt dålig effektivitet för omvandling av energi. För att erhålla en rimlig puls energi av den alstrade strålningen, måste kraftiga laserstrålar användas.

Atto-verktyg presenterade i doktorandarbetet

För att konstruera effektiva harmoniska källor har vi tittat på processen från både mikroskopiska och makroskopiska synvinklar. Vi har optimerat atomära responsen på ett intensivt laserfält och utvecklat en teknik för att få så många atomer som möjligt att samverka i processen.

Två nya övertonskällor har utvecklats vid Lunds Lasercentrum (LLC). Varje källa är driven av ett extraordinärt lasersystem. En baseras på den traditionella metoden som kallas chirped pulse amplification (CPA), och den andra på optical parametric chirped pulse amplification (OPCPA). Den senare tekniken har nyligen blivit tillgänglig för attofysik. Vi visar hur källor med hög repetitions frekvens kan konstrueras utnyttjande ny laserförstärkningsteknik. Erfarenheter från byggandet av övertonskällor i Lund har utnyttjats för att utarbeta designen för strålröret i ett gemensamt europeiskt projekt Extreme Light Infrastructure i Ungen (http://www.eli-hu.hu/). Denna källa kommer att ge mycket kraftfulla attosekundspulser, med tidigare onåbara energier, till det europeiska forskarsamfundet.

Framtiden

John Tisch, från Imperial College London, UK, sade *"Just nu är vårt arbete som hos en filmfotograf, registrering av rörelse av elektroner. En dag, vill vi bli som filmregissörer, som säger till elektronerna att röra sig dit vi vill. Om vi kunde göra det, skulle vi kunna kontrollera kemiska reaktioner, designa nya material och skapa snabbare, mer effektiva elektroniska aparater".*

Numera är det svårt att hitta tillämpningar av atto-verktyg i vardagen. Vårt arbete med att skapa en effektiv, enkel källa för attosekundspulser, och lättillgänglig för forskare, kan hjälpa dem att bli filmregissörer i atto-världen. Kanske våra verktyg även kommer att leda till genombrott inom medicin eller kemi. I framtiden kan man kanske ha problem att föreställa sig sitt liv utan atto-verktyg, på samma sätt som det nu är svårt att föreställa sig sitt liv utan filmkonst.

LIST OF PUBLICATIONS

This thesis is based on the following publications, which will be referred to by their roman numerals in the text.

I **Temporal and spatial effects inside a compact and CEP-stabilized, few cycle dual-stage OPCPA system at high repetition rates**
J. Matyschok, T. Lang, T. Binhammer, O. Prochnow, S. Rausch, M. Schultze, A. Harth, P. Rudawski, C. L. Arnold, A. L'Huillier and U. Morgner.
Opt. Express **21**, 29656–29665 (2013).

II **Compression of TW class laser pulses in a planar hollow waveguide for applications in strong-field physics**
A. Jarnac, F. Brizuela, C. M. Heyl, P. Rudawski, F. Campi, B. Kim, L. Rading, P. Johnsson, A. Mysyrowicz, A. L'Huillier, A. Houard, and C. L. Arnold.
(2014) *Manuscript in preparation.*

III **A high-flux high-order harmonic source**
P. Rudawski, C. M. Heyl, F. Brizuela, J. Schwenke, A. Persson, E. Mansten, R. Rakowski, L. Rading, F. Campi, B. Kim, P. Johnsson, and A. L'Huillier.
Rev. Sci. Instrum. **84**, 073103 (2013).

IV **Carrier-envelope phase dependent high-order harmonic generation with a high-repetition rate OPCPA-system**
P. Rudawski, A. Harth, C. Guo, E. Lorek, M. Miranda, C. M. Heyl, J. Matyschok, T. Binhammer, U. Morgner, J. Mauritsson, A. L'Huillier, and C. Arnold.
(2014) *Manuscript in preparation.*

V **Conceptual Design Report for a gas HHG beamline at ELI-ALPS**
C. M. Heyl, P. Rudawski, F. Brizuela, P. Johnsson, C. L. Arnold, and A. L'Huillier.
(2012) *Report ELI-ALPS.*

VI **Efficient high-order harmonic generation boosted by below-threshold harmonics**
F. Brizuela, C. M. Heyl, P. Rudawski, D. Kroon, L. Rading, J. M. Dahlström, J. Mauritsson, P. Johnsson, C. L. Arnold, A. L'Huillier.
Scientific Reports **3**, 1410 (2013).

VII **Macroscopic Phase Effects in Noncollinear High-order Harmonic Generation**
C. M. Heyl, P. Rudawski, F. Brizuela, J. Mauritsson, A. L'Huillier.
(2014) *Phys. Rev. Lett., in print.*

VIII **Digital in-line holography on amplitude and phase objects prepared with electron beam lithography**
J. Schwenke, E. Lorek, R. Rakowski, X. He, A. Kvennefors, A. Mikkelsen, P. Rudawski, C. M. Heyl, I. Maximov, S. G. Pettersson, A. Persson, and A. L'Huillier.
Journal of Microscopy **247**, 196201 (2012).

IX **Imaging localized surface plasmons by femtosecond to attosecond time-resolved Photoelectron Emission Microscopy - "ATTO-PEEM"**
S.H. Chew, K. Pearce, Ch. Späth, A. Guggenmos, J. Schmidt, F. Süssmann, M. Kling, and U. Kleineberg, E. Mårsell, C.L. Arnold, E. Lorek, P. Rudawski, C. Guo, M. Miranda, F. Ardana, J. Mauritsson, A. L'Huillier, A. Mikkelsen.
(2014) *Manuscript in preparation, chapter of a book "Attosecond Nanophysics", editors Peter Hommelhoff and Matthias Kling, Wiley-VCH Verlag GmbH and Co. KGaA.*

ABBREVIATIONS

CPA	Chirped Pulse Amplification
OPCPA	Optical Parametric Chirped Pulse Amplification
OPA	Optical Parametric Amplification
NOPA	Non-collinear Optical Parametric Amplification
HHG	High-order Harmonic Generation
ELI-ALPS	Extreme Light Infrastructure - Attosecond Light Pulse Source
Ti:Sapphire	Sapphire doped with Titanium
PEEM	PhotoEmission Electron Microscopy
CCD	Charge-Coupled Device
MCP	MicroChannel Plate
LLC	Lund Laser Centre
GV	Group Velocity
GVD	Group Velocity Dispersion
GD	Group Delay
GDD	Group Delay Dispersion
TOD	Third-Order Dispersion
FOD	Fourth-Order Dispersion
CEP	Carrier to Envelope Phase
FWHM	Full-Width at Half-Maximum
SVEA	Slowly Varying Envelope Approximation
CW	Continuous Wave
ML	Mode-Locking
KLM	Kerr-Lens Mode-locking
SI	Spectral Interferometry
DCM	Double Chirped Mirror
SPIDER	Spectral Phase Interferometry for Direct Electric-field Reconstruction
D-scan	Dispersion scan
AC	Autocorrelation

SFG/DFG	Sum/Difference Frequency Generation
SHG	Second Harmonic Generation
KDP	Monopotassium phosphate
BBO	Beta Barium Borate
BiBO	Bismuth triborate
LBO	Lithium-Barium Oxide
FWM	Four Wave Mixing
THG	Third Harmonic Generation
SPM	Self Phase Modulation
GRIN	Gradient-index lens
CVBG	Chirped Volume Bragg Grating
GRISM	Assemble of GRating and prISM
Nd:YAG	Yttrium Aluminium Garnet doped with Neodymium
Nd:YVO$_4$	Yttrium Vanadate doped with Neodymium
ASE	Amplified Spontaneous Emission
DAZZLER	Acousto-optic programmable dispersive filter
OPO	Optical Parametric Oscillator
PVWC	Poynting Vector Walk-off Compensation
TPM	Tangential Phase-Matching
TDSE	Time-Dependent Schrödinger Equation
SAP	Single Attosecond Pulse
DOG	Double Optical Gating

Electromagnetic spectrum

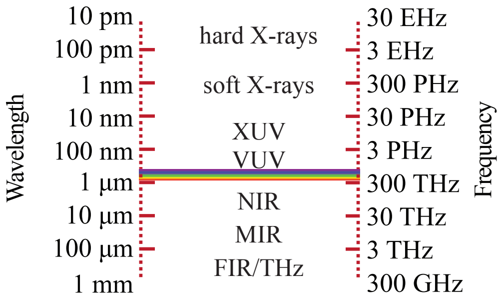

CONTENTS

Papers

Chapter 1

Introduction

Twenty seven years have passed since the discovery of the high-order harmonic generation (HHG) process [1, 2]. Sources based on this phenomenon have led to a number of groundbreaking experiments in the field of attosecond science [3], such as the observation of valence electron motion [4] or the measurement of ionization time delays [5, 6]. In addition, there is a growing interest in the fields of high-resolution imaging [7], free-electron-laser seeding [8], and nonlinear optics in the soft X-ray region [9, 10].

To a large extent, successful applications depend on further progress in HHG technology. HHG sources deliver pulses with interesting, sometimes unique, characteristics such as attosecond pulse duration [11, 12], high spatial coherence [13], excellent beam quality [14], a wide range of photon energies from VUV to X-ray [15–19], and up to μJ pulse energies, even for single attosecond pulses [20].

It is important to generate such harmonics with laser fields of the highest quality, since distortions are transfered to the harmonics (in fact, they are somewhat amplified by the nonlinear process). Laser beam distortions and spatio-temporal effects in general, reduce focusability, which leads to a reduced HHG conversion efficiency. For single attosecond pulse generation, the fundamental pulses must have reproducible electric fields (stable carrier envelope phase and energy) and short pulse durations (often below 5 fs).

In recent years, applications of HHG sources have grown considerably, raising new problems and requiring further development of HHG sources and their driving laser systems (for example, the development of a high repetition rate or tunability of the driving central wavelength). Thus, what at the beginning could be seen as a simple relation High-power lasers → HHG sources → Applications, nowadays is an interaction between these three inseparable components of the attosecond field.

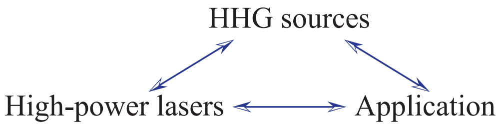

High-flux HHG sources are obviously interesting for attosecond science, opening the possibility to perform attosecond-pump – attosecond-probe experiments. Other types of experiments will strongly benefit from HHG sources operating at high-repetition rates. Examples of such experiments are those requiring coincidence detection of two or more particles per laser shot [21] or time-resolved photoemission electron microscopy (PEEM) [22, 23]. Since the first use of HHG, the driving laser systems have used chirped pulse amplifiers (CPAs) based on amplification in population-inverted media, usually sapphire doped with titanium (Ti:Sapphire). These are limited in repetition rate to a few kHz. Presently, there is a great interest in optical parametric chirped pulse amplifiers (OPCPAs). These systems, which are based on optical parametric amplification (OPA) can amplify few-cycles pulses at a MHz repetition rate, in a very compact table-top design [24–28].

Examples of applications which drive the development of HHG sources are presented in *Papers* **VIII** and **IX**. These applications aim to combine attosecond temporal resolution with observation of nano-scale objects (this has so far been demonstrated on the femtosecond time scale [29]). *Paper* **VIII** presents digital in-line holography experiments on test amplitude and phase objects, whereas *Paper* **IX** shows imaging of localized surface plasmons by photoemission electron microscopy. The two applications use the sources developed in this work and described in this thesis. We will now take a closer look at the two techniques and their requirements.

Imaging with HHG

Imaging of microscopic objects, with dimensions down to a few nanometers, is limited by many factors, such as the properties of imaging systems, beam quality, and fundamentally, by diffraction. The smallest possible focal spot size obtained by an optical element (with numerical aperture NA ≈ 1) is approximately equal to half the light wavelength. Hence, imaging of nano-scale objects requires light with a wavelength of approximately a few nanometers – in the X-ray range – combined with high-quality imaging systems.

HHG provides short wavelength radiation (the shortest wavelength reported is below 1 nm [30]). At the outset of this thesis work, we used an HHG beam to image nanostructures on SiN membranes using a digital in-line holography setup (*Paper* **VIII**). A HHG beam from high-power laser system was tightly refocused by a multilayer coated Schwarzschild objective. The multilayer coating selects a narrow part of the emitted bandwidth, centered around 37 nm (the 21^{st} harmonic of 800 nm). An object was placed a few millimeters behind the focus of the harmonic source and the resulting interference pattern was recorded by a multichannel plate (MCP) detector imaged by a visible-light CCD camera. The object was reconstructed numerically both in amplitude and phase from the reconstructed hologram [31, 32].

Another approach to image nano-scale objects is described in *Paper* **IX**, which is a book chapter presenting a report on electron microscopy using HHG. Instead of recording photons, electrons emitted by the photoelectric effect are detected. The spatial resolution that can be obtained is potentially much better than with optical methods, since the electron de Broglie wavelength is much smaller than the light wavelength. Typical resolution achieved with photoemission electron microscopy is of the order of nanometers. In the experiment, HHG is used as a source to emit electrons from the metallic surfaces (for example, from Ag nanowires on an Au surface). The electrons are then accelerated by external electric fields, which act as an objective lens, projecting an image of the nanostructures onto an MCP detector.

The two applications place contradicting requirements on the HHG pulse energy. Biological or chemical samples imaged using holographic experiments might be easily affected by the light pulse. Nevertheless, a high quality hologram can be recorded in a single-shot experiment using an ultrashort pulse which may subsequently lead to the destruction or modification of the sample. The requirement for single-shot operation is stringent when nano-scale imaging is combined with time-resolved studies. Besides single-shot operation, the interaction efficiency of the light with the sample is usually low in the XUV spectral range, hence the photon number carried by the beam has to be high to be detectable. On the other hand, in PEEM experiments, the interaction between the emitted electrons' space charge imposes a limit on the number of these electrons per shot, and thus on the intensity of the HHG radiation [22, 33]. Nevertheless, to obtain an image of good quality a large total number of electrons has to be recorded, over many shots. The two applications thus require systems with very different pulse energies and repetition-rates. Whereas holography needs a high-pulse energy at a low-repetition rate, PEEM benefits from a high-repetition rate system with moderate pulse energy.

When nano-scale imaging is combined with the attosecond time resolution provided by scanning pump-probe interferometric setups, both experiments require high stability and reproducibility of the generated pulses. Hence compact and long-term stable systems with implemented pointing or energy stabilizations, as well as a vibration damping support, are desired.

Aim and Outline

With these applications in mind, the goal of my Ph.D. project was:

to develop new high-order harmonic sources for high-flux and high-repetition rate experiments. The driving lasers for those sources will be the high-energy TW laser operating at 10 Hz repetition rate at the Lund Laser Center, and a newly developed optical parametric chirp pulse amplification (OPCPA) laser with a repetition rate of 200 kHz.

The work is presented in nine publications referred in the thesis as *Papers* **I** to **IX**. The publications are based on two HHG systems, which were constructed during the Ph.D. project. One is operated at a 10 Hz repetition rate and provides high-energy HHG pulses (described in *Paper* **III**) and the second is operated at a 200 kHz repetition rate and delivers broad low-energy harmonic pulses (presented in *Paper* **IV**). The first system was used for holography experiments (*Paper* **VIII**), the second system for PEEM experiments (*Paper* **IX**).

HHG requires constant development of the driving lasers. In the case of our high-power laser system, the path from the last amplifier to the HHG setup was significantly rebuilt, leading to better beam and pulse quality, and higher output energy. Furthermore, the system output was post-compressed in a planar waveguide setup to a duration of less than 15 fs with high throughput (*Paper* **II**). The second system, a high-repetition rate OPCPA, was built as a collaborative project with a laser company, VENTEON Laser Technologies GmbH (see *Papers* **I** and **IV**).

The experience gathered during the construction of the intense HHG setup in Lund was used to design a beamline for the ELI-ALPS[1] project. The conceptual design is presented in *Paper* **V**. The beamline, based on generation of HHG in gases, will provide single attosecond pulses as well as pulse trains, with high HHG energies.

In general, HHG sources suffer from low-conversion efficiency. Thus, experiments using a driving field mixed with several colors were carried out to overcome this problem. The single atom response was enhanced by shaping the driving field using low-order harmonics (*Paper* **VI**). Moreover, a two-color field interacting with the generation medium in a non-collinear geometry was used to probe and optimize the macroscopic properties of the generation process (discussed in *Paper* **VII**).

The thesis is structured as follows. Chapter 2, *Ultrashort Laser Pulses*, gives the background and mathematical description of ultrashort optical fields generated from laser sources or HHG setups. Chapter 3, *Pulse Amplification*, discusses the linear and nonlinear amplification techniques used in this work, with their advantages and drawbacks. Chapter 4, *High-order Harmonic Generation*, presents the basics of the high-order harmonic generation process (both from the microscopic and macroscopic points of view), as well as the two HHG systems. Chapter 5 summarizes the work and gives a brief outlook.

---

[1] Extreme Light Infrastructure - Attosecond Light Pulse Source.

CHAPTER 2

ULTRASHORT LASER PULSES

An ultrashort laser pulse is an electromagnetic field, generally in the visible to the extreme ultraviolet (XUV) region, in which the width of the envelope is in a range which varies from picoseconds (10^{-12} s) to femtoseconds (10^{-15} s), and currently reaches down to tens of attoseconds (10^{-18} s) [11]. This definition of "ultrashort" or "ultrafast" is not strict. The progress in the field is so significant that what is called ultrafast in 2014 will most likely not be ultrafast in 50 years time. Progress is not only towards generation of shorter and shorter pulses, but also requires new pulse detection and amplification methods.

Development is strongly driven by applications, both in basic and applied science. The availability of femtosecond pulses created a new field of chemistry, called femtochemistry, that led to the award of the Nobel Prize to Ahmed Zewail in 1999 [34, 35]. Moreover, the pulse peak powers allow the study of nonlinear optics in the perturbative (below multi-photon ionization) and the non-perturbative (high-order harmonic generation) regimes. The nonlinear processes induced by the pulses are applied in multiphoton fluorescence microscopes [36] and in THz generation [37].

The aim of this chapter is to give an introduction to the spatial and time/frequency description of ultrashort pulses (Sections 2.1 and 2.2) as well as their propagation in linear optical media (Section 2.3), so as to provide a background for the following chapters. The description can be applied for pulses generated by mode-locked lasers as well as for attosecond radiation obtained from the HHG process. We will describe ultrashort pulses using Gaussian shapes both in space and time/frequency. An exhaustive description, including shapes other than Gaussian, can be found in references [38–40].

The second part of the chapter focus explicitly on the laser pulses, describing their spatial and temporal couplings (Section 2.4), their generation method (Section 2.5), and the pulse duration measurement methods used in the thesis (Section 2.6). The last section (Section 2.7) discusses nonlinear effects, whose use enables the possibility to manipulate the pulse parameters, as was frequently done in this thesis work.

2.1 Spatial characterization

Ultrashort pulses are described in the spatial domain using a Gaussian beam, in which the electric field is equal to

$$E(x,y,z) = \frac{A}{iz_R}\frac{w_0}{w(z)}\exp\left(-\frac{(x^2+y^2)}{w^2(z)}\right)\exp\left(-i\left(kz-\frac{k(x^2+y^2)}{2R(z)}+i\xi(z)\right)\right), \tag{2.1}$$

where w_0 is the beam radius at the waist, A is a constant, $z_R = \pi w_0^2/\lambda$ is the Rayleigh range, and k is the length of the z component of the wave vector. The beam radius, $w(z)$, defined at $1/e^2$ (corresponding to 86 % of the total power), is equal to

$$w(z) = w_0\sqrt{1+\left(\frac{z}{z_R}\right)^2}, \tag{2.2}$$

the wavefront curvature is

$$R(z) = z\left(1+\left(\frac{z_R}{z}\right)^2\right), \tag{2.3}$$

and, $\xi(z)$, the Gouy phase

$$\xi(z) = \arctan\left(\frac{z}{z_R}\right), \tag{2.4}$$

represents a retardation of the beam phase with respect to a plane wave. It is equal to $-\pi/2$ $(+\pi/2)$ at a distance $z=-\infty$ $(z=+\infty)$.

The Rayleigh range, z_R, describes a distance from the beam waist, over which the beam intensity falls to half its value at the waist. At this range the wavefront curvature is at its largest. The Rayleigh range is inversely proportional to the wavelength, thus a beam with a longer wavelength has a shorter Rayleigh range than a beam with a shorter wavelength. For example, if we assume $w_o = 100\ \mu m$, $\lambda = 800\,\mathrm{nm}$, then $z_R = 0.4\,\mathrm{m}$ whereas at $\lambda = 20\,\mathrm{nm}$ $z_R = 1.6\,\mathrm{m}$. The confocal parameter, b, is equal to $2z_R$.

The intensity of a Gaussian beam (see Figure 2.1), is equal to

$$I(x,y,z) = \frac{1}{2}\epsilon_0 c\left|E(x,y,z)\right|^2, \tag{2.5}$$

and is at a maximum at x, y and z equal to 0, decaying as $1/(1+z/z_R)^2$ along z axis. In the equation, c is the speed of light in the vacuum and ϵ_0 is the permittivity of free space.

The far field divergence half angle of the beam can be approximated by

$$\theta \approx \frac{w_0}{z_R}, \tag{2.6}$$

and the product

$$2w_0 2\theta = \frac{4\lambda}{\pi}, \tag{2.7}$$

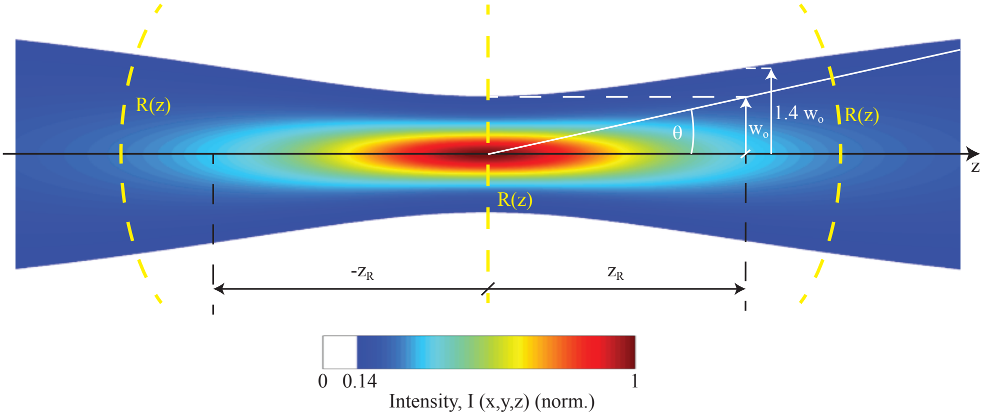

Figure 2.1: A normalized Gaussian beam intensity, with beam parameters labelled.

is invariant for Gaussian beams. Thus a beam with a small beam waist will diverge more than a beam with a large beam waist.

If a Gaussian beam, with parameters w_0 and z_R, is focused by a lens, the beam waist at the focus is equal to

$$w_0' \approx \frac{w_0}{\sqrt{1 + z_R^2/(f^2)}}, \tag{2.8}$$

where f is the focal length of the lens.

2.2 Time-frequency characterization

In the time domain, complex electric field of ultrashort pulses is described as

$$E(t) = \varepsilon(t)\exp(i\omega_0 t)\exp(-i\phi(t)), \tag{2.9}$$

where $\varepsilon(t) = \sqrt{2I(t)/(\epsilon_0 c)}$ is the real field envelope, $I(t)$ is the time dependent intensity, ω_0 is the carrier angular frequency (often identified as the frequency at the pulse peak), and $\phi(t)$ is the phase. The instantaneous angular frequency is defined as

$$\omega_{inst}(t) \equiv \omega_0 - \frac{\partial\phi(t)}{\partial t}. \tag{2.10}$$

The frequency description of the pulse can be obtained via the Fourier transform of the optical field

$$E(\omega) = \mathcal{F}(E(t)) = \int_{-\infty}^{\infty} E(t)\exp(-i\omega t)\mathrm{d}t = \varepsilon(\omega)\exp(-i\Phi(\omega)), \tag{2.11}$$

where $\varepsilon(\omega) = \sqrt{4\pi S(\omega)/(\epsilon_0 c)}$ is the spectral envelope, $S(\omega)$ is the spectral intensity, and $\Phi(\omega)$ is the spectral phase. The spectral phase distortion corresponds to a delay, called the group delay (GD), defined as

$$t_{GD}(\omega) \equiv \frac{\partial\Phi(\omega)}{\partial\omega} + t_0, \tag{2.12}$$

for the pulse centered at t_0.

The spectral and the temporal phase can be analyzed by Taylor expansion in the vicinity of the pulse center or the central frequency. The temporal phase expanded around the pulse center ($t_0 = 0$) is equal to

$$\phi(t) = \phi_0 + \left.\frac{\partial\phi(t)}{\partial t}\right|_{t_0} t + \frac{1}{2}\left.\frac{\partial^2\phi(t)}{\partial t^2}\right|_{t_0} t^2 + \frac{1}{6}\left.\frac{\partial^3\phi(t)}{\partial t^3}\right|_{t_0} t^3 + ..., \tag{2.13}$$

whereas in the spectral domain, the spectral phase expanded around ω_0 is equal to

$$\Phi(\omega) = \Phi_0 + \left.\frac{\partial\Phi(\omega)}{\partial\omega}\right|_{\omega_0} (\omega-\omega_0) + \frac{1}{2}\left.\frac{\partial^2\Phi(\omega)}{\partial\omega^2}\right|_{\omega_0} (\omega-\omega_0)^2 + \frac{1}{6}\left.\frac{\partial^3\Phi(\omega)}{\partial\omega^3}\right|_{\omega_0} (\omega-\omega_0)^3 + ... \tag{2.14}$$

The zero-order phase, ϕ_0 or Φ_0, is the "carrier to envelope phase" (CEP, see Figure 2.2 a-b), which is the same in both domains, since the Fourier transform is linear. The first-order temporal (spectral) phase corresponds to a shift in frequency (time), which is also a simple consequence of the Fourier transform $\mathcal{F}(E(t-\tau)) = E(\omega)\exp(-i\omega\tau)$ and the inverse Fourier transform $\mathcal{F}^{-1}(E(\omega-\omega_0)) = E(t)\exp(i\omega_0 t)$. The first-order temporal phase shifts ω_{inst} (in addition to ω_0) according to Equation 2.10. The second-order temporal (spectral) phase represents a linear ramp of frequency in time, called linear chirp. The second-order phase has opposite sign in the temporal and spectral domains. Positive linear chirp (Figure 2.2 c-d) refers to a linear increase of the instantaneous frequency with time. Higher-order phase components give rise to nonlinear changes in the instantaneous frequency. A pulse with a third-order phase is shown in Figure 2.2 e-f.

The pulses shown in Figure 2.2 have a Gaussian shape, described by

$$E(t) = E_0 \exp\left(-2\ln 2\left(\frac{t}{\Delta\tau}\right)^2\right)\exp(i\omega_0 t)\exp(-i\phi(t)), \tag{2.15}$$

where $\Delta\tau$ is the pulse duration at the full-width at half-maximum (FWHM). The Fourier transform is also a Gaussian function.

The relation between spectral bandwidth and pulse duration depends on the pulse shape. In case of a Gaussian pulse, the product of the two quantities is such that

$$\Delta\omega\Delta\tau \geq 2.76. \tag{2.16}$$

When $\Delta\omega\Delta\tau = 2.76$ the pulse is called Fourier-limited or transform-limited. For example, a 5 fs transform-limited pulse will have a bandwidth, $\Delta\omega$, of 0.55 PHz (10^{15} Hz) that corresponds to a spectral bandwidth of 187 nm for a central wavelength of 800 nm. Such pulses have only a few cycles of the carrier frequency enclosed by the envelope, and in the following we will refer to these as *few-cycle* pulses.

2.3 Pulse propagation

Propagation of an ultrashort pulse in a medium changes its phase and amplitude. While the influence of propagation can often be neglected for pulses with durations longer than 100 fs, for a few-cycle pulse even propagation through air has to be taken

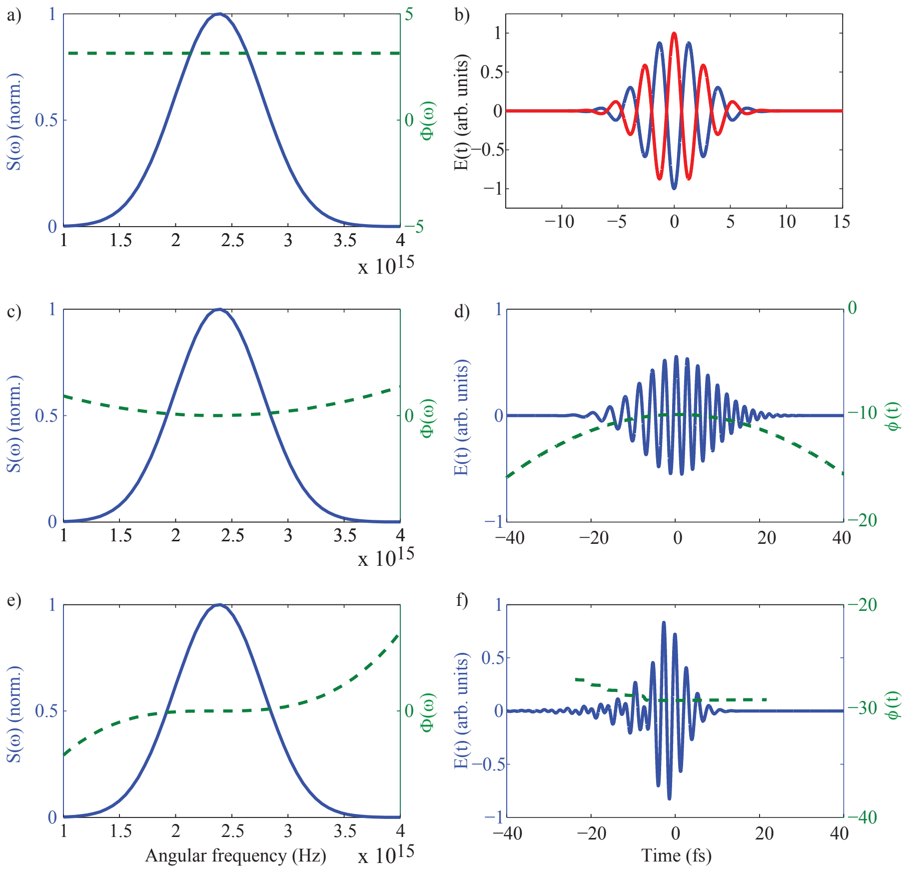

Figure 2.2: Gaussian pulses in the spectral (left) and the temporal (right) domain. a) Normalized spectral intensity (solid blue line) and constant phase $\Phi = \pi$ (green, dashed line), b) Real electric field in time for two values of CEP $\phi_0 = 0$ (red line) and $\phi_0 = \pi$ (blue line), c) Normalized spectral intensity and spectral phase with only a second-order contribution, d) Corresponding real electric field and phase in time, e) Normalized spectral intensity and spectral phase with only a third-order contribution, d) Real electric field and phase.

into account. This is a consequence of the large pulse bandwidth, which can reach hundreds of nanometers (see Section 2.2) as well as the frequency dependent response of linear (and nonlinear) media. The medium may act on the amplitude through absorption or amplification (see Chapter 3), and on the phase through dispersion. A pulse with an initial phase, $\Phi_{ini}(\omega)$, and an amplitude $A_{ini}(\omega)$ at the output of the medium is equal to

$$E_{out}(\omega) = \underbrace{A_{ini}(\omega)\exp(-\Lambda(\omega)L)}_{\text{output amplitude}} \cdot \underbrace{\exp(-i(\Phi_{ini}(\omega) + k(\omega)L))}_{\text{output phase}}, \tag{2.17}$$

where Λ is the absorption coefficient, and L is the medium length. It is customary to Taylor expand $k(\omega)$ around the central frequency

$$k(\omega) = k_0(\omega_0) + \underbrace{\left.\frac{\partial k}{\partial \omega}\right|_{\omega_0}}_{1/\mathrm{GV}}(\omega-\omega_0) + \frac{1}{2}\underbrace{\left.\frac{\partial^2 k}{\partial \omega^2}\right|_{\omega_0}}_{\mathrm{GVD}}(\omega-\omega_0)^2 + \frac{1}{6}\left.\frac{\partial^3 k}{\partial \omega^3}\right|_{\omega_0}(\omega-\omega_0)^3 + \ldots . \quad (2.18)$$

A monochromatic wave, with frequency ω_0, propagates in a medium at a velocity equal to c/n(ω_0), called phase velocity, v_p. Similarly a pulse, propagating in a non-dispersive medium and with a carrier frequency ω_0, propagates with the phase velocity, v_p (see Figure 2.3a). In a dispersive medium higher components of the $k(\omega)$ Taylor expansion are not negligible. If only the first-order term is considered, the pulse propagates at a group velocity (GV), v_g ($v_g = [(\partial k/\partial\omega)|_{\omega_0}]^{-1}$) and the pulse envelope is delayed by $t_d = L/v_g$ with respect to a pulse propagating in a non-dispersive medium (see Figure 2.3b).

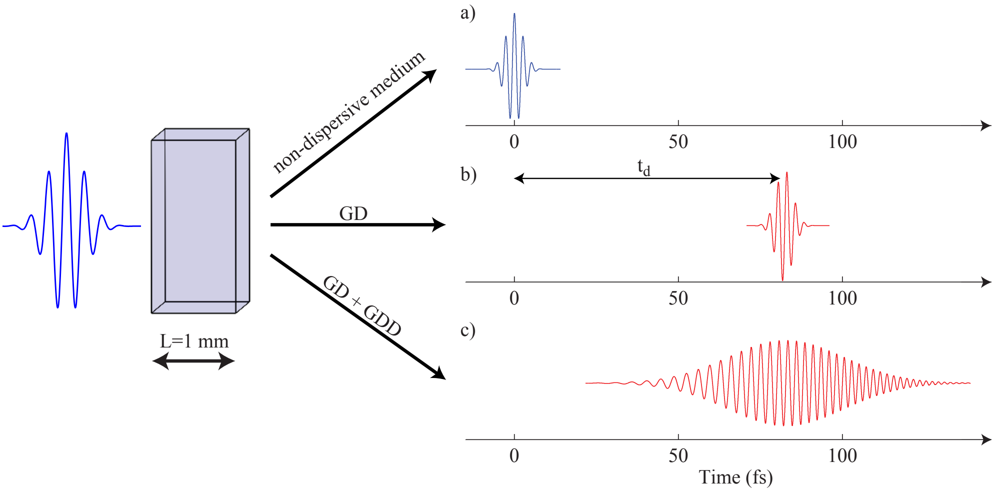

Figure 2.3: Sketch of the propagation of a transform limited pulse, with a 5 fs duration and a spectral bandwidth centered at 800 nm, through 1 mm of BK7 glass, assuming contributions from different dispersion orders: a) pulse propagating through vacuum, b) the wave vector is a linear function of frequency, c) the wave vector is a quadratic function of frequency. Plots a-c are shown in a frame moving at the phase velocity.

The first-order component in Equation 2.18 not only delays the pulse, but also changes its CEP. This effect is due to different group and phase velocities in a medium. The CEP after propagation through the medium is equal to

$$\Phi_0(L) = \Phi_0(0) + \left(\frac{L}{v_p} - \frac{L}{v_g}\right) = \Phi_0(0) + \left.\frac{L\omega_0^2}{c}\frac{dn}{d\omega}\right|_{\omega=\omega_0} . \quad (2.19)$$

The CEP dependence as a function of material insertion was used in *Paper* **IV** to investigate high-order harmonic generation as a function of the driving pulse CEP.

If the quadratic component in Equation 2.18 is not negligible (see Figure 2.3c) then, as is shown in Section 2.2, the group delay changes linearly with frequency, and in the time domain, the pulse acquires a positive linear chirp. The chirp introduced by most materials is positive for wavelengths in the visible and NIR. $\partial^2 k/\partial\omega^2|_{\omega_0}$ is the group velocity dispersion (GVD). Note that $k(\omega)L$ gives the spectral phase (see Equation 2.14) introduced by the propagation through the medium. L/v_g is called the group delay (GD), GVD $\cdot L$ the group delay dispersion (GDD). Higher-orders are called third-order and fourth-order dispersion (TOD, FOD) and so on. The refractive index is often characterized by combinations of phenomenological fit functions, called the Sellmeier equation.

For pulse durations of tens of femtoseconds, it is usually sufficient to describe the medium's influence on the phase by taking into account only the group velocity and the group velocity dispersion. For very short pulses <10 fs, higher order dispersion must be included.

2.4 Space-time coupling

The description of ultrashort pulses independently in the time and the space domains, as was presented in sections 2.1 and 2.2, is only possible in the case of pulses for which the slowly-varying envelope approximation (SVEA) [39] applies (see Section 2.2). However, the spatial properties may affect the temporal ones and vice versa. For pulses with a spectral bandwidth of hundreds of nanometers in the visible part of the spectral range, an interplay between space and time domains simply results from pulse propagation. As an example, consider a Gaussian beam away from the focus. According to Equation 2.6, longer wavelengths diverge more than shorter ones. Consequently, the spectrum shifts from short wavelengths on the optical axis to long ones at distances away from the optical axis [39] (Figure 2.4a). Thus, the pulse duration varies in the transverse plane. This effect, which is very difficult to compensate, is an example of distortion induced by space-time coupling. Other types of spatio-temporal couplings are introduced upon reflection or refraction of ultrashort pulses by optical elements. In this section, these effects are briefly and qualitatively described (see references [38, 41] for a more exhaustive description).

The most common type of spatio-temporal distortion is the spatial chirp, defined as change of central wavelength over the transverse coordinates. A spatial chirp can be introduced by propagating through a tilted dispersive medium (Figure 2.4b). Even when the element is placed perpendicularly to the pulse propagation axis, a spatially-chirped pulse propagating through a dispersive element experiences another well known spatio-temporal distortion called pulse-front tilt (Figure 2.4c). This is due to different spatial portions of the beam having different group velocities.

Both effects, spatial chirp and pulse-front tilt, are consequences of transmission through (or reflection from) angularly-dispersing elements, such as prisms or diffraction gratings. These components change the propagation direction for different frequency components. This property is used in pulse compressors and pulse stretchers to introduce or compensate temporal chirp. In principle, angular dispersion introduced by one component should be exactly compensated in the setup by another angularly dispersing element. Unfortunately, this is only true for perfect alignment. Imperfect alignment results in spatial chirp and/or pulse-front tilt, which severely deteriorates the pulse properties. For example, when a pulse with pulse-front tilt is focused, the pulse becomes longer and its peak intensity is strongly reduced, which is undesirable

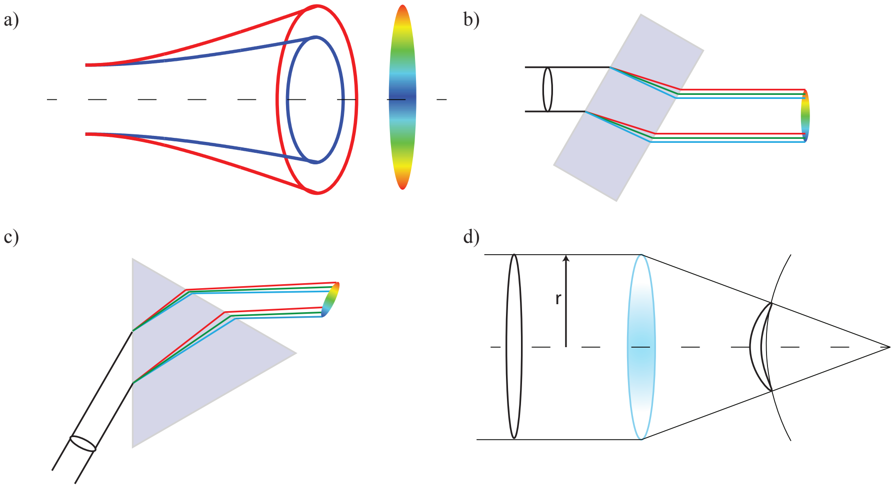

Figure 2.4: Spatio-temporal effects: a) distribution of spectral components due to wavelength-dependent divergence, b) spatial chirp, c) pulse-front tilt, d) pulse-front distortion due to propagation through a single lens.

for most applications. It is therefore important to measure and carefully compensate a pulse-front tilt. One method implemented in the present thesis for the alignment of our high-power CPA system (see Section 3.2.4) uses an inverted field interferometer [42], where the pulse-front tilt is encoded as a fringe contrast. The inverted field interferometer was built to measure the spatio-temporal distortion of the system output beam.

Focusing systems for ultrashort pulses can introduce other, and more complex spatio-temporal distortions. The use of simple lenses leads to strong temporal distortion [43, 44], due to differences in the group and phase velocities (see Section 2.3). Since the lens thickness varies with distance, r, from the element's optical axis, different radial parts of the pulse will exhibit different delays with respect to the wavefront. While the lens may produce a perfect spherically converging wavefront, the pulse front exhibits deformation, and in particular, a delay of the central part of the beam relative to the boundary (Figure 2.4d). Additional distortion may arise due to higher order effects such as GDD, as well as lens aberrations, such as spherical, astigmatic, or chromatic aberrations.

Pulse-front distortion and chromatic aberrations can be avoided if the ultrashort pulse is focused with an achromatic lens or a mirror. From the alignment point of view, focusing with an achromatic lens (such as that used in *Paper* **IV**) is much simpler than with a paraboloidal or toroidal mirror. However, the lens introduces a large GDD because it has large amounts of material, which will stretch the pulse in time, and needs to be precompensated in order to keep the pulse short.

2.5 Pulse generation

Femtosecond laser pulses are generated by phase synchronization of modes created in a laser resonator, using a technique called mode-locking (ML) [45–47]. Usually, the modes, with random phase, compete for gain. Hence the laser output, in the absence of other measures, is narrowed independently of the gain bandwidth. This mode of operation is called CW (or continuous wave).

When the phase relation between the modes is fixed, the modes interfere constructively leading to creation of a short pulse [39], whose intensity is equal to

$$I(t) = I_0 \left(\frac{\sin(N\Delta\phi(t)/2)}{\sin(\Delta\phi(t)/2)} \right)^2 , \tag{2.20}$$

where $\Delta\phi(t)$ is the phase difference between modes, equal to $\Delta\phi(t) = 2\pi\nu_F t$. The modes' frequency separation is equal to $\nu_F = c/2d$, where d is the cavity length. The equation shows that the pulse peak power increases and the time duration decreases with an increasing number of interfering modes. Thus it is desirable to use a gain medium with a broad bandwidth in order to amplify many modes simultaneously.

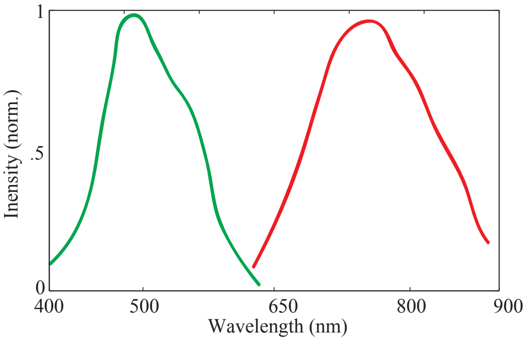

Figure 2.5: Ti:Sapphire absorption (green line) and emission (red line), data from reference [48].

In the earliest femtosecond laser systems dye solutions were widely employed. Dyes could provide a gain bandwidth up to approximately 100 nm (Rhodamine 6G), but due to maintenance problems such as parameter degradation, and the dyes' carcinogenicity, solid state materials were preferable. The most popular solid state gain medium, providing the broadest gain bandwidth (from 600 nm to 1000 nm), is Ti:Sapphire [49] (see Figure 2.5).

In this work, two femtosecond sources have been used as front-end pulse generators for the laser systems, which are described in details in Chapter 3. Both generators are based on passive mode-locking. To synchronize the modes, additional losses are passively introduced for CW operation, whereas for ML operation losses are kept low. This selectivity is obtained by means of a nonlinear effect, called self-focusing (for details see Section 2.7). This effect creates intensity-dependent lensing in the gain medium, changing the size of the ML beam with respect to CW beam. An aperture set in the resonator at the point where the two beams differ the most in diameter can favor ML operation over CW. The pump beam diameter in the gain medium can serve as an aperture, if the beam's size in ML operation is well matched with the size of the pump spot. This is called soft aperturing.

A typical z-shaped cavity used in generators is shown in Figure 2.6. The cavity contains an active medium at the Brewster angle, two curved mirrors to match the spatial modes of the pump and signal beams, and a dispersion control unit. Dispersion compensation is needed to balance the acquired phase of a broadband pulse during one round trip in the resonator. Such a unit can be a prism compressor, as illustrated in Figure 2.6. For oscillators emitting pulses with a duration of a few femtosecond specially tailored chirped mirrors are more common.

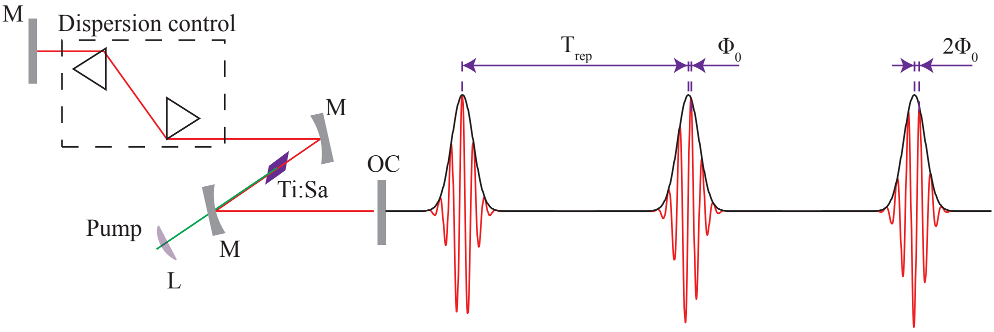

Figure 2.6: Typical geometry of a femtosecond resonator cavity; M - mirror, OC - output coupler, L - pump focusing lens.

In an ultrafast oscillator, the pulse circulates in the cavity and each time it reaches the output coupler (OC in Figure 2.6) it is partly transmitted through it. Thus, a train of femtosecond pulses is observed at the output, with pulses separated in time by

$$T_{rep} = \frac{c}{2d}. \tag{2.21}$$

Due to intracavity dispersion the phase and group velocity are not equal. Hence, the output pulses have different zero-order phases as is illustrated on the right of Figure 2.6. Furthermore, the CEP often experiences random fluctuations as the pulse propagates through an optical setup due to environmental influences on the medium's refractive index, for example, from thermal effects, or because of vibrations.

Experiments performed with ultrashort, few-cycle pulses often require measurement and stabilization of the CEP. High-order harmonic generation depends nonlinearly on the pulse's electric field, and consequently is strongly affected by the pulse CEP, as is presented in *Paper* **IV**. The CEP has to be actively stabilized in order to deliver repeatable pulses to an experiment. In special cases the CEP can be passively stabilized by the help of a parametric process [50, 51]. The measurement of the CEP is discussed in the following section.

2.6 Laser pulse measurement in the spectral and temporal domains

The availability of methods to fully characterize an ultrashort laser pulse is crucial for many applications. Direct measurement using electronic devices is not possible, since the pulse duration is significantly faster than the rise time of any photodetector. Moreover, even if an appropriate detector did exist, it would only provide information about the pulse intensity. It is essential to characterize both the intensity and the phase in either the temporal or the spectral domain, using the concepts outlined in Section 2.2.

Here, the different characterization techniques used to measure the pulse duration of the two laser systems presented in Chapter 3 are described. For a detailed review of ultrashort laser pulse characterization see references [38, 52].

Spectral Interferometry

Many of these methods originate from spectral interferometry (SI), and are based on spectrally interfering the pulse to be measured with a known reference pulse with the same spectral width. Let us denote by $\Phi(\omega)$ and $S(\omega)$ the spectral phase and intensity of the pulse to be determined, and by $\Phi_r(\omega)$ and $S_r(\omega)$, those of the reference pulse. The two pulses, delayed with respect to each other by a small constant value τ, are detected by a spectrometer. They interfere and the interference signal is

$$\mathrm{SI} = S_r(\omega) + S(\omega) + 2\sqrt{S_r(\omega)S(\omega)}\cos\left(\omega\tau + \Phi_r(\omega) - \Phi(\omega)\right). \tag{2.22}$$

If the two pulses are identical (self-referencing interferometry) $\Phi_r(\omega) - \Phi(\omega) = 0$ and the detected spectrum, modulated by a factor $\cos(\omega\tau)$, does not provide any information about the phase. Nevertheless, this technique can be used to measure a phase introduced by an optical component, if such a component is placed in one arm of the interferometer (see Figure 2.7a). For example, we used the technique to characterize double chirped mirrors (DCMs) in our OPCPA system compressor (see *Paper* **I**).

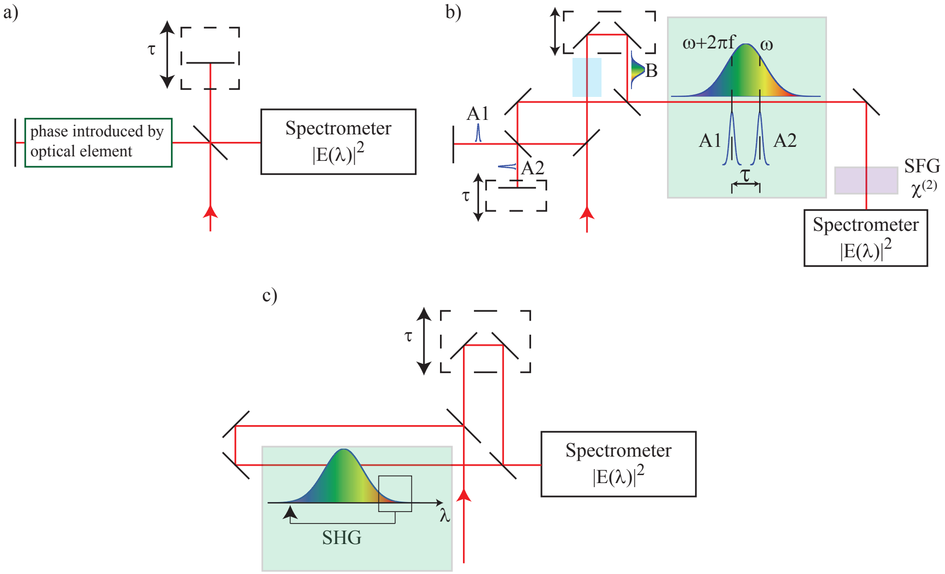

Figure 2.7: Sketch of the detection setups used for: a) spectral interferometry, b) SPIDER, c) CEP measurement, f-to-2f interferometer.

The phase of the pulse can be extracted by spectral interferometry if one of the pulses is frequency shifted by a factor $2\pi f$. The interference signal becomes

$$\mathrm{SI} = S(\omega) + S(\omega) + 2\sqrt{S(\omega)S(\omega)}\cos\left(\omega\tau + \Phi(\omega + 2\pi f) - \Phi(\omega)\right). \tag{2.23}$$

The technique called SPIDER (spectral phase interferometry for direct electric-field reconstruction) is based on this principle [53]. A sketch of the technique is presented in Figure 2.7b. An input pulse is divided into two pulses (A and B). Pulse A is additionally divided in an interferometric setup into two pulses, A1 and A2. A1 is delayed with respect to A2 by a constant τ. The pulse B propagates through a piece of glass, and due to dispersion becomes linearly chirped (see Section 2.3). The three pulses (A1, A2 and B) nonlinearly interact in a sum frequency generation (SFG) crystal. The delay, τ, defines the frequencies of the B pulse, with which the A1 and A2 interact (see Figure 2.7b). If the shift in frequency is small enough, then $\Phi(\omega + 2\pi f) - \Phi(\omega)$ can be related to the group delay as

$$t_{GD}(\omega) = \frac{\Phi(\omega + 2\pi f) - \Phi(\omega)}{2\pi f} \approx \frac{\partial\Phi(\omega)}{\partial\omega}. \tag{2.24}$$

A commercial implementation of the technique[1] was used to characterize our two laser systems (see *Papers* **I**, **II**, and **IV** and Chapter 3).

The SPIDER technique is unable to measure the CEP (see Section 2.2), although another modification of a spectral interferometer can be used. To understand the principle of such a measurement, we examine the frequency comb generated in an oscillator (see Section 2.6). The frequencies of the longitudinal modes are

$$f_n = \omega_n/2\pi = n f_{rep} + f_{CEP}, \tag{2.25}$$

where $f_{rep} = 1/T_{rep}$ is the repetition rate (see Figure 2.6) and f_{CEP} is the frequency offset related to the CEP by

$$f_{CEP} = \Phi_0 f_{rep}/2\pi. \tag{2.26}$$

To determine Φ_0, the pulses which contain more than an octave of frequencies propagates through a nonlinear crystal. The crystal doubles the lower frequency part of the pulse, at ω, to 2ω, which spectrally interferes with the part of the pulse at this frequency [54]. The second harmonic of the nth mode is equal to

$$2f_n = 2\omega_n/2\pi = 2n f_{rep} + 2f_{CEP}. \tag{2.27}$$

The spectral interference fringes created when the two pulses interfere allow us to determine the CEP according to

$$\mathrm{SI} = 2S(\omega) + 2S(\omega)\cos(\omega\tau + \Phi_0 - 2\Phi_0). \tag{2.28}$$

The detection setup presented in Figure 2.7c is called an f-to-2f interferometer. Optionally, instead of detection in the spectral domain, the CEP can be measured in the time domain by analyzing the beat frequency between the two signals [55].

For a pulse which does not have an octave spanning spectrum, and hence does not initially contain the required frequencies, the spectral bandwidth has to be broadened

---

[1] VENTEON | PULSE: FOUR SPIDER

by self phase modulation (see Chapter 2.7) in an optical medium (such as a BaF_2 crystal) [56].

Two f-to-2f interferometers are built into our OPCPA system. The first is based on detection in the time domain and the second uses detection in the spectral domain. CEP measurements for long term CEP stabilization are described in *Paper* **I**.

D-scan

Another technique to characterize ultrashort pulses is called d-scan (the abbreviation stands for "dispersion scan"). The technique, developed in Lund [57, 58], is based on recording spectra from second harmonic generation (SHG) while modifying the pulse spectral phase. The phase is then iteratively reconstructed from the scan. During the measurement, the pulse chirp changes from negative to positive (or vice versa) reaching, at certain point, the shortest duration. The experimental setup, shown in Figure 2.8, is very simple, since negatively chirped pulses are easily produced at the output of the laser chain. The setup contains a medium with a variable amount of dispersion, for example, a pair of wedges, a thin SHG crystal, and a spectrometer. The technique was used to characterize the pulses from our OPCPA system (*Paper* **IV**).

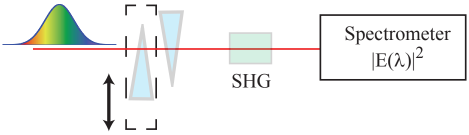

Figure 2.8: Sketch of the d-scan experimental setup.

Autocorrelation

The above presented techniques are based on detection in the spectral domain. In the time domain, the simplest available technique is autocorrelation. Experimentally, it is very similar to SI. The first-order autocorrelator differs from SI only by the detection method. Here, the spectrometer is replaced by a photodiode. A first-order autocorrelation yields only the pulse coherence time, which by Fourier transformation can be related to the pulse spectrum. To gain more information from autocorrelation measurements, a second-order autocorrelation ($\mathrm{AC}^{(2)}$) has to be implemented. In the AC setup, presented in Figure 2.9a, a pulse is first divided into two replicas, and one part is variably delayed. The two pulses are overlapped in a SHG crystal. The signal is detected by a photodetector. The measurement yields three components

$$\mathrm{AC}^{(2)} = \int \left|(E(t) + E(t-\tau))^2\right|^2 \mathrm{d}t = C_0(\tau) + 4Re(C_1 \exp i\omega_0\tau) + 2Re(C_2 \exp i2\omega_0\tau), \tag{2.29}$$

where τ is the delay. The first component, $C_0(\tau)$, is the intensity autocorrelation

$$A_c(\tau) = \int I(t)I(t-\tau)\,\mathrm{d}t, \tag{2.30}$$

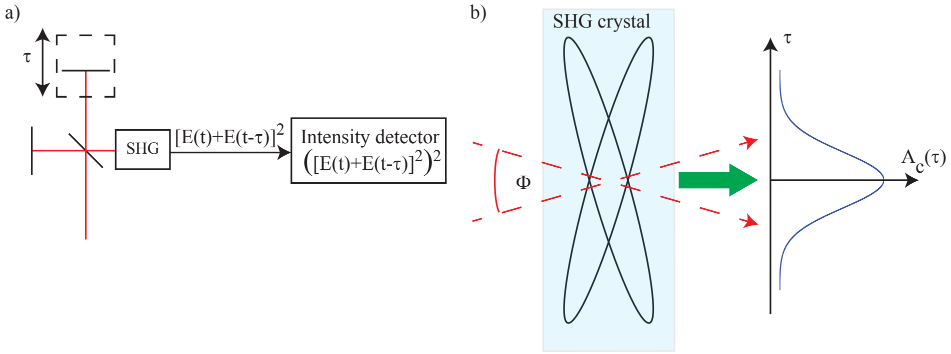

Figure 2.9: Sketch of the detection setups used for: a) multi-pulse, and b) single-shot autocorrelation.

which does not provide information about the phase, but allows the estimation of the pulse duration assuming a certain pulse shape. For a Gaussian shaped pulse the pulse duration is equal to $\Delta\tau = \sqrt{2}\Delta t$, where Δt is the FWHM of the autocorrelation trace[2].

The other two components, C_1 and C_2, which are centered at the carrier frequencies ω_0 and $2\omega_0$ respectively, carry information about the phase. This measurement is called interferometric autocorrelation.

The most common autocorrelators use several pulses for the measurement, since the delay, τ, must be scanned. These autocorrelators are only suited for pulse sources with a high repetition rate, since in order to obtain good statistics many pulses and small time steps are necessary. The measurement is based on an assumption that all pulses have the same amplitude and phase. To characterize low-repetition rate sources a single-shot version of the intensity autocorrelator [59] can be used. In a single shot autocorrelator the two pulses interact non-collinearly in the SHG crystal, leading to geometrical time-to-space mapping (see Figure 2.9b). The introduced delay is distributed along the transverse coordinate (zero delay corresponds to the center of the two beams). A commercial implementation[3] of the single-shot autocorrelation technique has been used for daily characterization of the high-power CPA system.

Autocorrelation based on SHG (or any second order process), always leads to a symmetric function, thus introducing ambiguities. For example, the measurement of an asymmetric pulse such as a pulse with 3^{rd} order phase distortion (see Figure 2.2 in Section 2.2), cannot distinguish between positive and negative phase values. Similarly an additional pulse can be diagnosed, but it is impossible to predict whether it is before or after the main pulse.

In all measurements using a nonlinear frequency conversion, it is assumed that the nonlinear process has a phase-matching bandwidth broader than the pulse being measured. In general, the optical components which are used should not affect the measurement, although it is possible to measure their influence carefully and subtract it from the final results.

---

[2] For another frequently used pulse shape, $sech^2$, the relation is $\Delta\tau = 1.543\Delta t$, which gives more optimistic values of pulse durations.

[3] Amplitude Technology Bonsai.

2.7 Ultrashort, perturbative nonlinear optics

When a light wave passes through a medium, it interacts with the electrons of the constituents of the medium. In case of a weak field the medium response is linear and electrons oscillate with the driving field frequency. On the other hand, for a strong field (of the order of $\sim 10^8$ V/m) the response of the medium becomes nonlinear and the electron starts to oscillate at new frequencies. This new source radiates a new wave, which co-propagates and, in general, interacts with the incident light. In this section further interactions of the generated waves will be neglected. This assumption, called the first Born approximation [39], is accurate when the amplitude of the new wave is small. Note that this approximation breaks down when the efficiency of the nonlinear process is high, for example in optical parametric amplification (see *Paper* **I**).

The response of the medium is described by the induced polarization, which can be expanded as

$$P(E) = P^L + P^{NL} = \epsilon_0(\chi^{(1)}E + \chi^{(2)}E^2 + \chi^{(3)}E^3 + ...), \tag{2.31}$$

where $\chi^{(1)}$ is the linear susceptibility, $\epsilon_0 = 1/(\mu_0 c^2)$ is the electric permittivity of free space, μ_0 is the vacuum permeability, and c is the speed of light in vacuum.

Generally, all materials exhibit nonlinear optical phenomena, but the required peak power necessary to observe these effects depends strongly on the microscopic structure of the medium. The induced nonlinear polarizations, for media where $P^{NL} \propto \chi^{(2)}E^2$ and $P^{NL} \propto \chi^{(3)}E^3$, are shown in Figure 2.10 (a) and (b), respectively. In the first case, the induced polarization is an asymmetric function. A positive field induces a higher material response than the negative one. Thus, since the input wave is symmetric, the asymmetric response has to be a consequence of the medium's microscopic structure. A centrosymmetric medium (such as a noble gas) is not able to create a second-order material response. This feature is valid for all even-order effects, and plays an important role in the generation of low-order perturbative harmonics as well as high-order nonperturbative harmonics (discussed in Chapter 4).

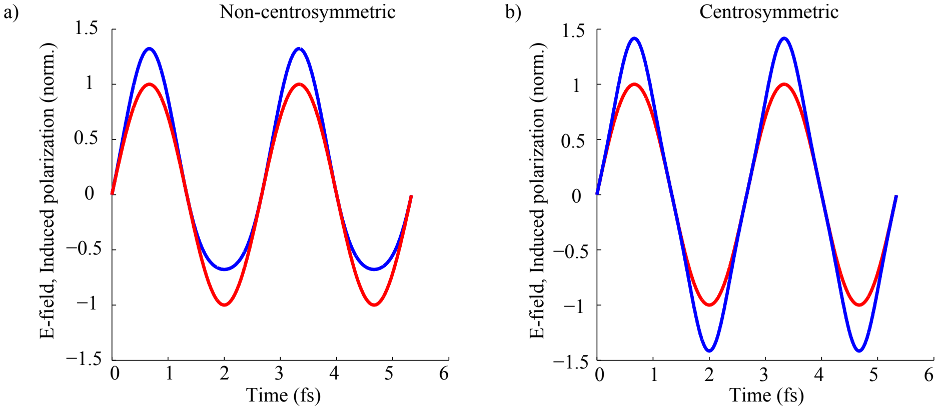

Figure 2.10: E-field (red line) and induced polarization (blue line) for: a) $P^{NL} \propto \chi^{(2)}E^2$ and b) $P^{NL} \propto \chi^{(3)}E^3$.

The interaction of intense waves with a non-centrosymmetric medium can lead to a number of nonlinear effects (see Figure 2.11a). Two waves, with angular frequencies ω_1 and ω_2, propagating through the medium can generate a third wave with a frequency that is the sum (sum frequency generation, SFG) or the difference (difference frequency generation, DFG) of the individual frequencies. DFG is the fundamental process in optical parametric amplification (OPA) as will be discussed in Chapter 3. When the two incoming waves have the same frequency the third wave is generated with the double frequency (second harmonic generation, SHG). Direct SHG in a KDP[4] crystal was used in *Paper* **I** to convert the output from an IR fiber amplifier to visible radiation, and in *Paper* **V** (also see Section 4.4.1) where the SHG wave was non-collinearly mixed with the fundamental wave for HHG. A combination of SHG and consecutive SFG mixing with the fundamental light was used in *Paper* **VI** to generate a third harmonic wave.

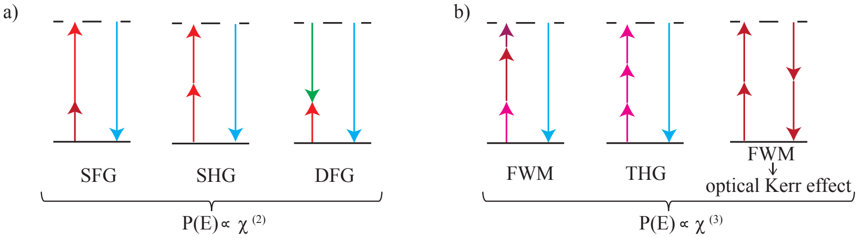

Figure 2.11: Nonlinear effects schematically: a) $P(E) \propto \chi^{(2)}$ and b) $P(E) \propto \chi^{(3)}$. The dashed lines for the upper levels indicates virtual states.

Four wave mixing (FWM) induced by $\chi^{(3)}$, includes processes where three input waves (with angular frequencies ω_1, ω_2, and ω_3) generate the fourth wave $\omega_4 = \omega_1 \pm \omega_2 \pm \omega_3$. If the three frequencies are equal, $\omega_1 = \omega_2 = \omega_3$, the process is called third harmonic generation (THG). Another important third-order phenomenon is the optical Kerr effect, in which the medium's refractive index changes proportionally to the incident field intensity

$$n = n_0 + n_2 I, \tag{2.32}$$

where n_0 is the intensity independent refractive index, and n_2 is the nonlinear refractive index. n_0 is dimensionless, while n_2 is given in cm^2/W and is of the order of $10^{-16}\,\mathrm{cm}^2/\mathrm{W}$ (Sapphire). For example, the beam from the high-power laser system presented in Section 3.2.4, propagating through a Sapphire window at full power (25 TW) in a beam of 4 cm diameter, changes its refractive index by a value of 1×10^{-8}. Even such a small modification of the refractive index has many consequences, such as self-focusing and self phase modulation (SPM).

Self-focusing is a consequence of the beam's spatial intensity distribution and its rotational symmetry. The refractive index is modified to a greater extent on-axis than off-axis, so that the medium behaves as a focusing lens, in a way similar to a gradient-index (GRIN) lens.

---

[4] Monopotassium phosphate

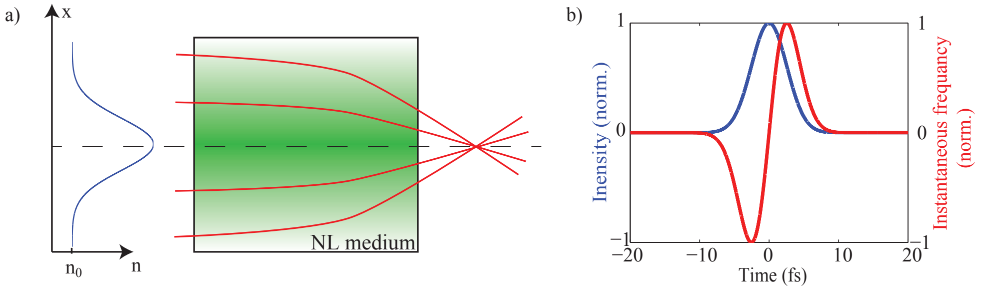

Figure 2.12: Nonlinear effects induced by the third-order susceptibility: a) self-focusing, also called Kerr-lensing, with a Gaussian beam; b) SPM, where the blue line is a normalized field intensity and the red line shows the variation of the instantaneous frequency proportional to $\partial I(t)/\partial t$.

SPM is a consequence of the optical Kerr effect with a time-dependent intensity, and is especially important for ultrashort pulses with high peak powers. The time-dependent phase due to SPM can be written as

$$\phi_{SPM}(t) = n_2 I(t) \omega_0 L/c. \tag{2.33}$$

Thus, the instantaneous frequency, defined by Equation 2.10, is modified, and new frequencies appear in the spectrum. As is shown in Figure 2.12b, the instantaneous frequency is shifted to low frequencies at the leading edge of the pulse, and towards high frequencies at the trailing edge.

SPM is frequently used to spectrally broaden fundamental pulses in post-compression setups. We used the process to post-compress the output of the high-power laser system in a planar waveguide, as is presented in *Paper* **II** (see also Section 3.2).

The expansion of the induced polarization does not stop after the third-order. Higher-order susceptibilities lead to a broad range of effects, among which, generation of higher-order harmonics is the most common. The influence of low-order odd harmonics (3^{rd} to 7^{rd}) generated in a centrosymmetric medium on the non-perturbative HHG process is discussed in *Paper* **VI**.

Macroscopic effects

To be efficient, nonlinear frequency conversion phenomena require to add coherently the emission from many microscopic sources. The generated waves have to be in phase to add constructively (i.e. they must be phase-matched). This requirement is a manifestation of the momentum conservation law, which for mixing of three waves is

$$\mathbf{\Delta k} = \mathbf{k} - \mathbf{k}_{\omega_1} - \mathbf{k}_{\omega_2} = 0, \tag{2.34}$$

where $\mathbf{k}_{\omega_i}$, with $|k_{\omega_i}| = n_i(\omega_i)\omega_i/c$ are the wave vectors, and $\mathbf{\Delta k}$ is the wave vector mismatch. For $\mathbf{\Delta k} \neq 0$ the conversion is limited. Let us consider for example SHG. The second harmonic intensity in presence of a mismatch, $\mathbf{\Delta k}$, is equal to

$$I_{2\omega} \propto d_{\text{eff}}^2 I_\omega^2 L^2 \text{sinc}^2\left(\frac{\Delta k L}{2}\right), \tag{2.35}$$

where L is the medium length, and d_{eff} is the effective nonlinear susceptibility[5]. The normalized second harmonic intensity, shown in Figure 2.13, quickly decreases from the maximum at $\Delta k = 0$, to zero at $\pm 2\pi/L$ and efficient generation is obtained over the coherence length

$$L_{coh} = \frac{\pi}{|\Delta k|}, \tag{2.36}$$

which is typically of the order of a few micrometers.

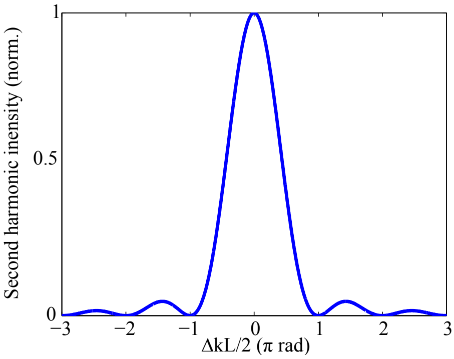

Figure 2.13: Normalized intensity of a second harmonic field.

In the case of second harmonic generation, phase-matching requires that the fundamental and second harmonic waves have to propagate at the same speed. In general, this requirement is difficult to achieve due to dispersion. A solution to this problem is to use anisotropic media. In an anisotropic medium the refractive indexes n_x, n_y, and n_z are generally not equal and the wave velocity depends on the propagation direction $v = c/n(\theta)$. For uniaxial crystals[6] (see Figure 2.14) the refractive indexes $n_x = n_y = n_0$ are called ordinary and $n_z = n_e$ extraordinary. The refractive index of the extraordinary wave propagating at an angle θ with respect to the z-axis (also called the optical axis, OA) can be found using a formalism of the refractive index ellipsoid. An ellipsoid of a negative uniaxial crystal is shown in Figure 2.14 (the inset shows an ellipsoid for positive uniaxial crystal). The nonlinear crystal is called negative or positive depending on whether n_e is smaller or larger than n_0.

The refractive index of a wave propagating at an angle θ with respect to the optical axis, can be found by taking a cross-section through the center of the ellipsoid perpendicular to the propagation vector $\mathbf{k}$ of the wave. In general, the cut has the shape of an ellipse, whose axes correspond to the refractive indexes.

Depending on the propagation direction, three cases can be distinguished (see Figure 2.14): a) a beam propagating parallel to the optical axis always propagates as an ordinary wave with index n_o; b) if the propagation direction is perpendicular to the optical axis the wave is either extraordinary with index n_e (for polarization along the OA), or ordinary (for polarization perpendicular to the OA); c) if the wave propagates at an angle θ to the OA, and the polarization is not perpendicular to the OA, its index of refraction is angle dependent

---

[5] These expressions assume non-depleted and slowly-varying fundamental field.

[6] For the experiments presented in this work only uniaxial crystals were used, such as KDP or BBO, for which $n_x = n_y \neq n_z$. Further discussion will be based on this type of crystals.

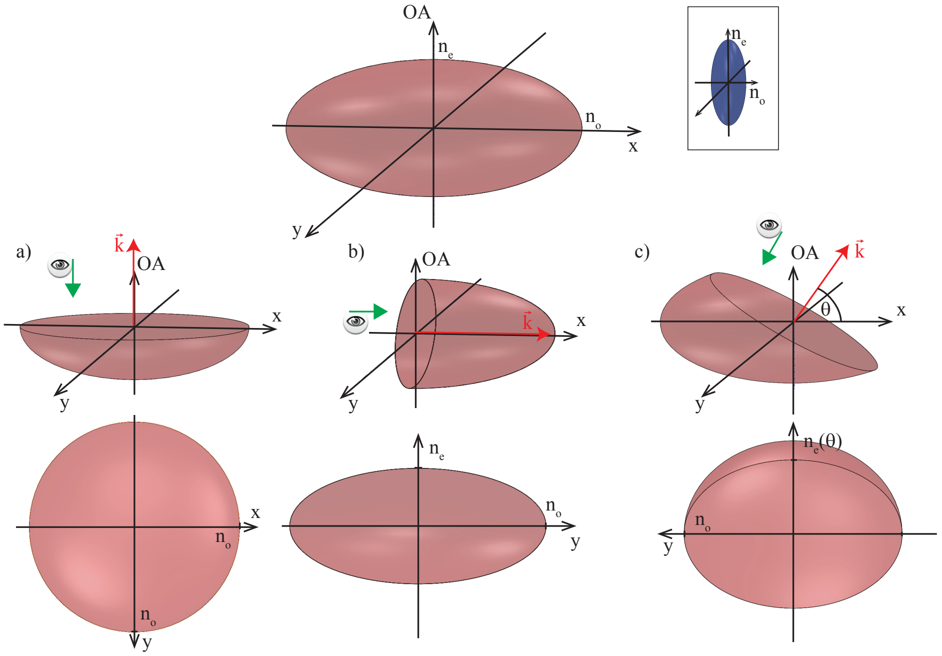

Figure 2.14: Refractive index ellipsoid, for negative uniaxial crystals, $n_e < n_0$ (the inset shows an ellipsoid for positive uniaxial crystals, $n_e > n_0$). The three cases (a), (b) and (c) correspond to an optical wave propagating parallel, perpendicular and at an angle to the optical axis (OA). The propagation of the waves in these three cases is discussed in text. The bottom row shows a cross section of the ellipsoid cut perpendicular to the wave vector, the projection direction is indicated by the green arrows.

$$n_e(\theta) = \frac{n_0 n_e}{(n_0^2 sin^2\theta + n_e^2 cos^2\theta)^{1/2}}. \tag{2.37}$$

Therefore, the phase-matching condition can be fulfilled by adjusting the refractive index (i.e velocity) of waves taking part in the process. For example, a fundamental ordinary wave with a central wavelength of 800 nm can be efficiently converted to the second harmonic in a KDP crystal, if it propagates at an angle of 44.9 ° to the optical axis. In this case, the second harmonic propagates as the extraordinary wave. This choice of wave polarization is called Type I phase-matching ($o + o \rightarrow e$), which is one of many possible phase-matching types. In addition to Type I, a Type II phase-matching is often used, in which the second harmonic is ordinary polarized in the medium ($o + e \rightarrow o$), while the two fundamental waves have ordinary and extraordinary polarization [60].

The extraordinary wave propagating in an anisotropic crystal experiences a spatial walk-off effect. This effect, which is very important for conversion efficiency in any frequency generation process, has a particular influence on optical parametric amplification, as will be discussed in the following chapter. It arises from the fact that the direction of power flow of the wave, described by the Poynting vector, $\mathbf{S} = \mathbf{E} \times \mathbf{H}$, is different from the propagation direction defined by the wave vector $\mathbf{k} = \mathbf{D} \times \mathbf{H}$. This is due to non-parallel $\mathbf{D}$ and $\mathbf{E}$ vectors in anisotropic media (in contrast, $\mathbf{D}||\mathbf{E}$

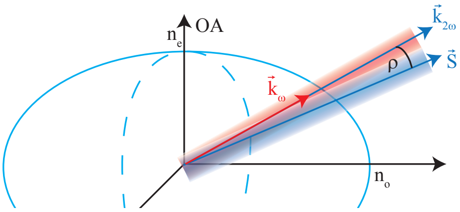

Figure 2.15: Power flow and beam propagation in an anisotropic medium, the red represents the driving field propagation direction (ordinary wave in the medium), and the blue the second harmonic propagating as an extraordinary wave and experiencing a walk-off in the **S** direction.

in an isotropic medium). The Poynting angle (see Figure 2.15), ρ, between these two directions typically takes values in the range $1 - 3\,^\circ$.

Chapter 3

Pulse Amplification

Femtosecond pulses have found applications in the physical, chemical, and biological sciences, as well as in industry [61]. The high degree of interest has stimulated the development of femtosecond sources. Nowadays, commercially available Kerr-lens mode-locked (KLM) oscillators [62] provide pulses with central frequencies from the visible to the FIR and transform-limited duration owing to excellent intracavity dispersion management [63–66]. Commonly, the sources provide excellent quality beams ($M^2 < 1.2$), with high repetition rates (tens of megahertz), and stable electric fields (reproducible CEP and energy).

The majority of applications require pulse energies higher than those achieved after initial generation (which are of the order of nJ). Therefore, ultrashort pulses need to be amplified. Generally, two amplification methods exist, based on linear or nonlinear processes. Linear amplifiers are based on stimulated emission from a population-inverted medium, while nonlinear types use a nonlinear interaction with another beam in a crystal. The description given here aims to answer the question: *how are the properties of the generated ultrashort pulses preserved by the two amplification methods?*

The content of the chapter is articulated around two laser systems installed at the Lund Laser Centre: a high-power, low-repetition rate Ti:Sapphire chirped pulse amplifier, and a high-repetition rate Optical Parametric Chirped Pulse Amplifier. Both systems were used and partly developed by the author for HHG experiments: the Ti:Sapphire CPA for the work presented in *Papers* **III**, **VI** – **VIII**, and the OPCPA for *Papers* **I**, **IV**, and **IX**. In this chapter, after a general introduction to chirped pulse amplification (Section 3.1), two techniques will be presented: i) CPA in population-inverted gain media, with a focus on Ti:Sapphire (Section 3.2) and ii) OPCPA (Section 3.3).

3.1 Chirped Pulse Amplification

Regardless of the chosen method, the amplification process has a fundamental limit imposed by the pulse peak power. The increasing power in each amplification step may easily reach the damage threshold of the amplifier's optical components. Even before any damage occurs, nonlinear effects perturb the amplification process and affect the pulse characteristics. To cope with these problems a technique called chirped pulse amplification (CPA) [67, 68] is used. The pulse is stretched in time, to reduce the peak power, is amplified, and is then compressed back to its original duration (see Figure 3.1).

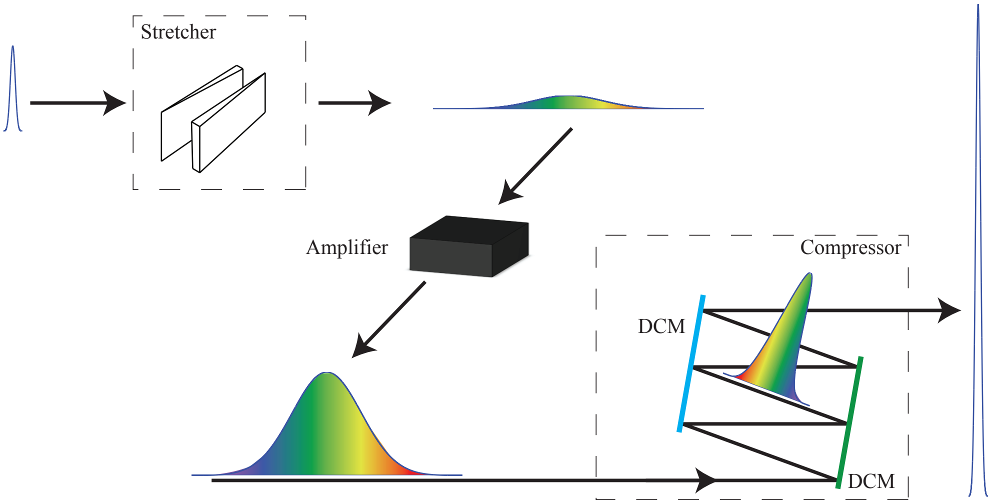

Figure 3.1: The CPA method. The stretcher and compressor are those used in our OPCPA system (see Section 3.3.3). DCM - double chirp mirror.

The two systems presented in the thesis are CPA based. The systems use different combinations of stretcher-compressor, what illustrates possible solutions. Detailed discussions of possible stretcher and compressor arrangements can be found in reference [38]. Pulse stretching may be implemented either by introducing a negative or positive linear chirp (see Section 2.2). In the normal dispersion regime, negatively chirped pulses shorten during propagation through materials, thus positively-chirping stretchers are usually chosen. The key feature of the setups is a frequency dependent optical path length, which, in order to achieve a positive (negative) chirp, is longer (shorter) for longer wavelengths. Positive chirp can be simply introduced by pulse propagation through an optical medium. This effect is used in our OPCPA system (see Section 3.3.3). The pulses are stretched by propagation though a wedge pair and compressed by double chirped mirrors (DCMs) [69, 70] (see Figure 3.1).

However, these type of stretchers may not be sufficient due to their low stretching factor. Hence, for systems with a stretching factor >100 000, such as our 10 Hz high-power laser (see Section 3.2.4), a combination of an Öffner triplet stretcher [71] and reflection grating compressor [72, 73] can be used. The combination has a few drawbacks, mainly that it has a long optical-path-length (which affects the stability of the pulse CEP), relatively small bandwidth, and a low transmission (approximately 60%). Thus, its applicability in broadband table-top systems is limited.

Another combination of stretcher-compressor is built into the fiber amplifier part of the OPCPA system. This requires a compact setup as well as high throughput. It was achieved by using a chirped volume Bragg grating (CVBG) [74, 75] for the stretcher. The compressor is another CVBG, with the same dispersion characteristic but with opposite sign, in the first amplifier and a GRISM (an assembly combining a prism and transmission grating) [76] in the second.

3.2 Chirped pulse amplification in population-inverted media

Stimulated emission in a population-inverted medium, employed in laser oscillators, can also be used in amplifiers to further increase the energy. To preserve the pulse bandwidth, the gain media must have properties matched to the pulse's spectral characteristics (the gain bandwidth should be at least as large as the pulse bandwidth).

3.2.1 Principle

Population inversion in Ti:Sapphire is obtained by pumping the medium, usually longitudinally, with a green laser (for example, with Nd:YAG or Nd:YVO$_4$ frequency-doubled radiation). The pump pulse energy, which arrives prior to a signal pulse, is stored in the medium for a duration of approximately $3\,\mu$s. If the input pulse to be amplified has a time duration much shorter than any excited state lifetime involved in the amplification process, it can fully extract that energy [77, 78]. The gain of a lossless amplifier of length l, calculated for a pulse with a fluence J_s^{in} is equal to

$$G = \frac{J_{sat}}{J_s^{in}} \ln\left(G_0\left(\exp\left(\frac{J_s^{in}}{J_{sat}}\right) - 1\right) + 1\right), \tag{3.1}$$

where J_{sat} is the saturation fluence ($J_{sat} \sim 1\,\mathrm{J/cm^2}$ for Ti:Sapphire), and $G_0 = \exp(g_0 l)$ is the small signal gain, where g_0 is the gain coefficient. The gain depends on the pump properties, absorption by the medium, spectral content, time duration, energy, pump geometry, and also on the doping concentration [77]. g_0 takes values between 0.05 and $0.2\,\mathrm{cm^{-1}}$.

For a weak input pulse ($J_s^{in} << J_{sat}$), which does not affect the population inversion, $G \approx G_0$ and the pulse energy grows linearly. For a higher input pulse fluence ($J_s^{in} >> J_{sat}$) the gain is approximated by

$$G \approx 1 + \frac{J_{sat}}{J_s^{in}} g_0 l. \tag{3.2}$$

In these conditions, called saturated amplification, the signal pulse extracts the total stored energy in the medium. Saturated amplification ensures the maximum conversion efficiency. Furthermore, the signal pulse output energy is much less dependent on pump and signal power fluctuations than in amplifiers working below saturation. The majority of long pulse amplifiers (with pulse duration $>10^{-9}\,$s) are therefore operated in the saturation regime. Saturated amplification in femtosecond CPA systems is not desirable, since the gain saturation influences the temporal pulse profile. In an amplifier a pulse is amplified more at the front than at the back, since the pulse front reduces the gain. Thus a chirped pulse with wavelengths distributed under the envelope experiences a wavelength selective amplification (i.e. gain narrowing). Nevertheless, the saturation regime has very clear advantages, and is often chosen as the last amplification step in CPA amplifiers.

The main drawback of the amplifiers based on stimulated emission is the amplification of the optical radiation background, and especially spontaneously emitted photons. The process of amplified spontaneous emission (ASE), schematically presented in Figure 3.2, lasts from the arrival of the first pump photons to the time when all of the energy is extracted. ASE significantly reduces the gain [38], often long before the arrival of the pulse to be amplified. Moreover, it creates a nanosecond duration background, which co-propagates with the main pulse, and is further amplified in succeeding amplification stages.

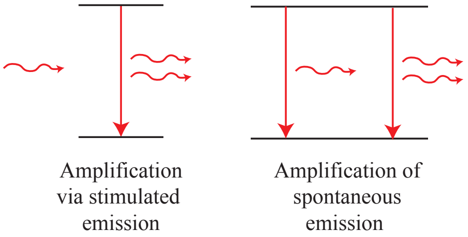

Figure 3.2: Schematic representation of amplification via stimulated emission and amplification of spontaneous emission.

ASE can be partly eliminated by using various types of filters in the spatial or temporal domain. One of the solutions, employed in high-field plasma physics, is to use a plasma mirror [79], or to control the main pulse polarization state with respect to the background (for example, by a Pockels cell and polarizers).

3.2.2 Multipass geometry

In general, the small signal gain in stimulated emission CPA is a factor of between two and five. Thus, single pass amplification is not very efficient. To increase the pulse energy by several orders of magnitude, many passes through the amplifier are necessary. This can be realized in a multipass configuration or in a cavity.

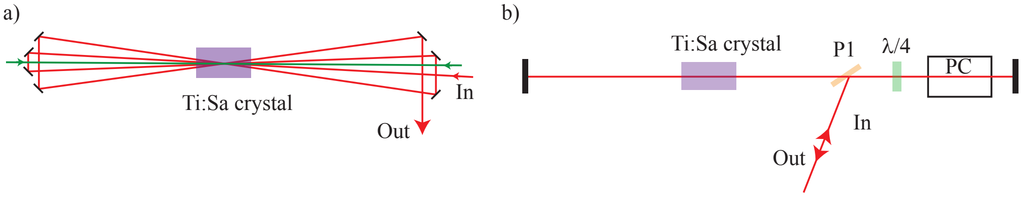

Figure 3.3: a) Multi-pass and b) regenerative amplifiers.

In the former case (Figure 3.3a) the pulsed beam angle with respect to the active medium axis, changes for each pass. The amplifier is called multi-pass amplifier (also bow-tie or butterfly). The drawback of the design is a limited number of passes (all the passes have to overlap with the pumped volume in the crystal) and difficulty of alignment, whose complexity increases as the number of passes increases.

In the second design, called a regenerative amplifier, which is presented schematically in Figure 3.3b, a Pockels cell (PC) is used to control the pulse polarization state. The gain medium is placed between two mirrors, creating a resonator. A vertically polarized pulse enters the regenerative amplifier by reflection off a polarizer (P1) and propagates towards a quarter-wave plate ($\lambda/4$), a Pockels cell (PC), and a mirror. In the first pass, the PC and the waveplate rotate the pulse polarization to keep the pulse in the amplifier (the pulse is transmitted through the polarizer, P1). The voltage of the Pockels cell is changed before the pulse's second pass through the cavity (for a 2 m long amplifier, approximately 10 ns). This voltage is maintained for the time necessary to obtain good amplification (typically 10 - 20 passes). The voltage is then changed again, so that the pulse polarization becomes vertical and the pulse is reflected out from the regenerative amplifier.

Both types of amplifiers were used in the high-power laser system used in the present work (*Papers* **II**, **III**, **VI**, **VII**, **VIII**).

3.2.3 Temporal and spatial effects

Typical amplification factors in high-power laser systems reach 10^6 and even as high as 10^9. In this section we will discuss to what extent the pulse properties are preserved during amplification.

In order to keep the input pulse duration, the amplifier, i.e. the gain medium and optical components, must act over a flat bandwidth, which must, as a minimum, be equal to the pulse bandwidth. In general, this requirement is fulfilled for optical elements but not for the gain medium (see Figure 2.5).

In the present work, the oscillator which is the front-end of the high-power system has a bandwidth of 50 nm. Even though the bandwidth is significantly smaller than the Ti:Sapphire bandwidth a gain narrowing is observed, even with external compensation (for details see Section 3.2.4). This is a consequence of higher amplification of the wavelengths at the center of the gain bandwidth than those at the edges. This effect, shown in Figure 3.4, is boosted n-times, for n-pass amplifiers, thereby significantly narrowing the pulse bandwidth. A pulse with 5 fs initial duration is more than 20 fs-long at the amplifier output.

Gain narrowing can be reduced by using a spectral filter, which suppresses wavelengths at the peak of the amplification bandwidth. Such a filter can be a multi-layer mirror [80, 81], an assembly of a birefringent crystal and polarizers (Lyot filter [82]), or an acousto-optic programmable dispersive filter (DAZZLER) [83].

Other effects limiting amplifier performance, are due to inhomogeneities in the deposited heat. The heat, from the pump beam, modifies the medium mainly due to three mechanisms: i) a change of the medium's refractive index via the thermooptic effect, ii) a thermally-induced mechanical stress (photoelastic effect), and iii) the bulging of the gain medium faces. The three effects lead to distortions of the output beam wavefront. In the case of longitudinal pumping, the heat distribution creates a lensing effect, similar to the Kerr lensing presented in Section 2.7. The deposited heat

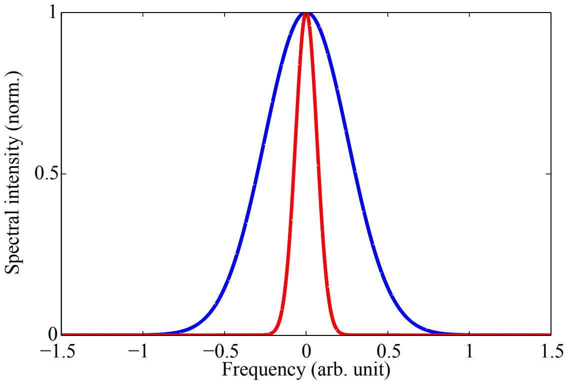

Figure 3.4: Gain narrowing after 15 passes through a gain medium with a bandwidth equal to the input pulse bandwidth. The normalized spectra: input (blue line), and output (red line).

limits the duty cycle during which the amplifiers can operate, and therefore has to be removed. Often cryogenic cooling is a solution to the problem, since the thermal conductivity of Ti:Sapphire is greatly increased at low temperatures. At around 35 K it is as good a conductor as copper or silver are at room temperature, and the thermal gradient is significantly reduced. A drawback of cryo-coolers are vibrations, which are an additional source of CEP noise [84].

Heat management, as well as the lack of appropriate pump sources limit the repetition rate of Ti:Sapphire CPA systems to tens of kHz. Continuously-pumped systems demonstrate complex dynamics [85]. Nevertheless, Ti:Sapphire systems operating at MHz repetition rates with energies up to 12 μJ (at 200 kHz) and durations of < 60 fs have been demonstrated [86, 87].

3.2.4 High-power, low-repetition rate system at LLC

The high-power Ti:Sapphire CPA system has been the main workhorse at the Lund Laser Centre (LLC), since 1992. The system has been constantly developed during the author's Ph.D. project. It generates and amplifies near-IR pulses to energies as high as 1 J, with a duration 40 fs. The peak power thus reaches 25 TW. It is used for generation of high-intensity high-order harmonics (as described in the following chapter and *Paper* **III**), and also for high-intensity experiments, such as acceleration of electrons and protons. These experiments are not discussed in this thesis. The arm used for HHG experiments has been rebuilt by the author. A spatial filter and active beam pointing stabilization were added. Furthermore, this arm of the system was mounted on rigidly connected optical tables. The upgrade led to higher output energy, better beam quality and better pointing stability, which was essential for post-compression and efficient HHG.

The system front-end (Figure 3.5) is a passively mode-locked oscillator based on Kerr-lens mode locking (see Section 2.5). The oscillator produces pulses at an 80 MHz repetition rate, with a spectral bandwidth of 50 nm centered at 800 nm. Directly after the oscillator the repetition rate is reduced to 10 Hz by means of a Pockels cell and a Glan polarizer (PP in Figure 3.5). After the pulse picker, pulses are preamplified in a multipass setup with six passes through a gain medium. The preamplification is carried out in order to reduce ASE and thereby increase the pulse temporal contrast. Subsequently, the pulses are transmitted through a DAZZLER, which controls the amplitude and phase of the pulse spectral components. The DAZZLER is used to partially pre-compensate for the gain-narrowing in the system. The pulses are then directed to the Öffner triplet-type stretcher [71]. Elongated to approximately 300 ps, they are than amplified in a regenerative amplifier (through ten passes) to an energy of ∼ 6 mJ. Different polarizers (P1 and P2) are used for injection and extraction. In both steps a $\lambda/2$ voltage (∼ 7 kV) is applied to the Pockels cell. The pulses are temporally cleaned by two Pockels cells and Glan polarizers before being guided to a multipass amplifier. Passing through the medium five times leads to a pulse energy of ∼ 350 mJ.

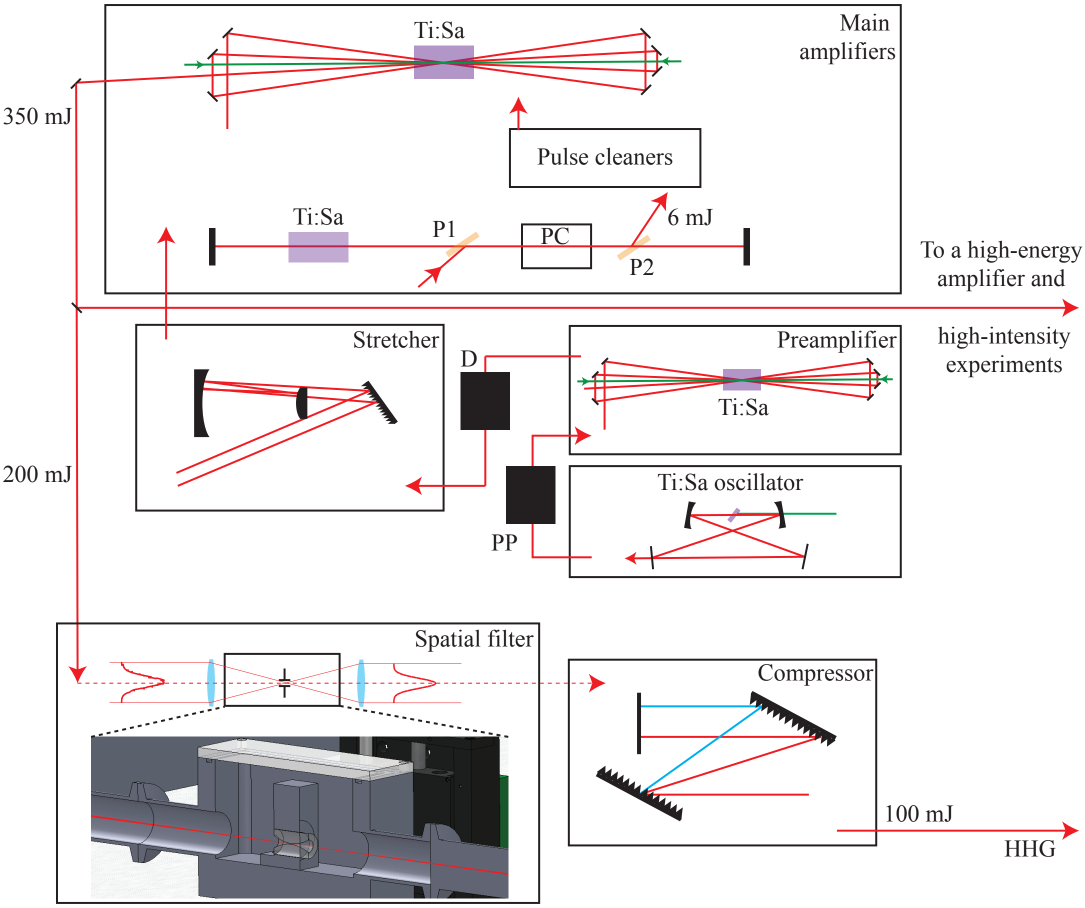

Figure 3.5: Schematic of the high power, low-repetition rate system. PP - pulse picker, D - DAZZLER, PC - Pockels cell, P1, P2 - polarizers.

The 350 mJ pulse is divided into two independent arms. The part driving the HHG setup, ∼ 200 mJ, passes a spatial filter with a conical pinhole mounted in a vacuum chamber (see Figure 3.5). The radiation is focused by a 1.7 m focal length lens at the pinhole waist (500 μm). To avoid damaging the pinhole, the beam position fluctuations are actively compensated. The pulsed beam with 30 mm diameter directed to the grating compressor has an energy of 190 mJ and a 30 nm FWHM bandwidth. The pulse re-compression leads to 45 fs duration and 100 mJ energy.

Post-compression in a planar hollow waveguide

To counteract the relatively long pulse duration of the Ti:Sapphire amplifier, a number of post-compression schemes have been proposed. Post-compression of energetic pulses relies on nonlinear spectral broadening, mostly due to self phase modulation (for details see Section 2.7) and plasma blue-shift, usually followed by compression with chirped mirrors. Efficient spectral broadening is achieved in waveguides, such as hollow capillaries [88], planar hollow waveguides [89], or in self-guiding filamentation [90].

In our setup, the broadening takes place in a gas-filled planar hollow waveguide [89, 91] (see Figure 3.6a) instead of ordinary hollow capillary [88]. This guiding geometry is chosen because of the high transmission of the setup, reaching 80%, and because a high input energy could be used.

Guiding takes place in one dimension, whereas in the the other the pulse propagates freely. The pulse is coupled into the waveguide by a metallic cylindrical mirror with a focal length of 2 m, and after the waveguide, recollimated with a similar mirror. The pulse is compressed by a set of double chirp mirrors (8 bounces from Layertec commercial mirrors and 4 from custom-made VENTEON DCMs). The pulse spectrum and duration measurement before and after post-compression (using Ar gas at 400 mbar) are shown in Figure 3.6 (a) and (b), respectively. The setup together with the post-compression results are described in detail in *Paper* **II**.

3.3 Optical parametric chirped pulse amplifiers

The first demonstration of parametric amplification in a nonlinear medium [92], was carried out shortly after the invention of the laser [93]. At that time, nonlinear optics was mostly limited by phase-matching and birefringent crystal technology. Until the introduction of the CPA technique in 1985 [67], and the first OPCPA [94], the parametric amplification method was slowly developed by only a few laboratories. Since then, it has been introduced and applied in a growing number of laboratories worldwide [95, 96].

The technique has many advantages. Problems described in the previous section, which are encountered when using amplification in population inverted media, including ASE, gain narrowing, and thermal beam deterioration, thermal lensing, either fade away, or are strongly reduced. Moreover, the range of possible central wavelengths is only limited by crystal transmission [95], and extends from the UV to the FIR. Very often at values, for which amplification in the population inverted media is not possible [97]. OPCPA can amplify an ultrashort pulse (as short as 3.9 fs [98]) at a large range of repetition rates from a few Hz [99] to hundreds of kHz [24, 27].

This section deals exclusively with a femtosecond OPCPA amplifying radiation centered around 800 nm, the maximum of the Ti:Sapphire gain curve (see Figure 2.5). Such a system is described in *Papers* **I** and **IV** and was installed in Lund in the summer of 2012. The fundamentals of OPA are described, indicating similarities and

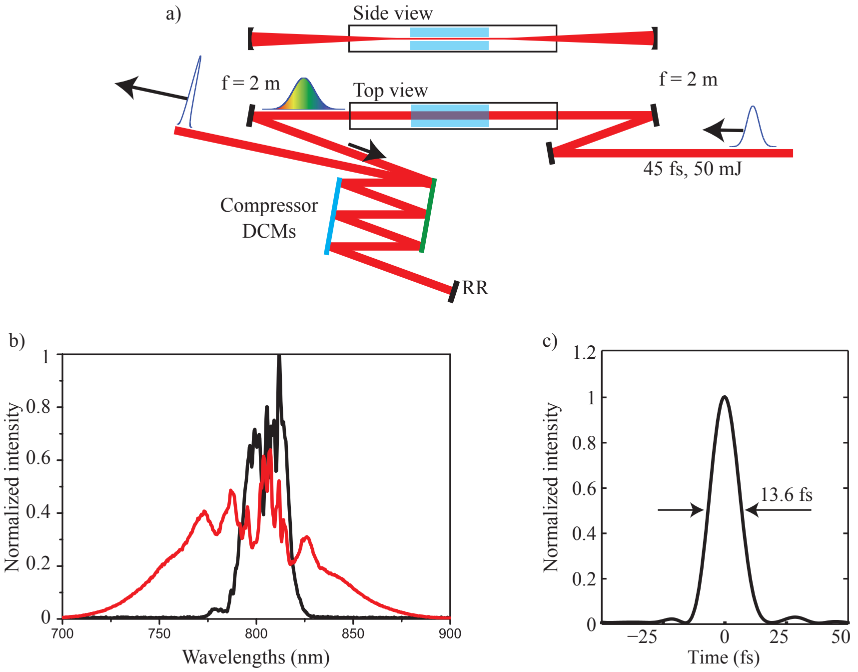

Figure 3.6: a) Post-compression setup, RR - retro reflector, DCM - double chirped mirrors; b) Pulse spectrum before (black line) and after (red line) post-compression; c) Pulse duration after post-compression.

differences between the parametric and population inverted amplifiers, and the spatial and temporal effects associated with this type of amplification.

3.3.1 Principle

An optical parametric amplification is a difference frequency generation process, as was described in Section 2.7. In the process, the energy of an intense pump wave, with a frequency ω_p, is transfered to a weak signal wave (also called the seed), with a frequency ω_s (see Figure 3.7). Due to energy conservation, a third wave is generated, called the idler, with a frequency ω_i

$$\omega_i = \omega_p - \omega_s. \tag{3.3}$$

In a special case, called degeneracy, the idler and the seed have the same frequency. One pump photon is split into two equal photons (this is the opposite of SHG). The idler wave generation can be considered as an intrinsic parasitic process, since part of the pump energy is transfered to the idler. The idler can also be considered as another amplifier output, which may be used in applications. The number of photons in the idler beam is comparable with the number in the amplified signal, and the frequency bandwidth is as broad as that of the signal, although it is usually centered in the near-IR [96]. Moreover, if the signal wave is generated directly from the pump wave (for example through white-light generation), the idler is free of CEP variation[1] [50, 51].

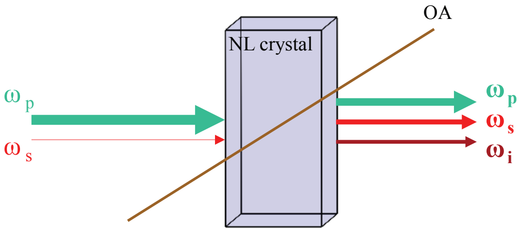

Figure 3.7: Optical Parametric Amplification.

OPA is characterized by a very high pump-to-signal optical conversion efficiency, reaching ∼ 30% (see reference [100] and *Paper* **I**). Moreover, the parametric gain[2] after a crystal with length L, defined as

$$G = \frac{1}{4}\exp(2\Gamma L), \tag{3.4}$$

can reach 10^6. In Equation 3.4, Γ is the gain coefficient dependent on the pump intensity, the effective nonlinear coefficient, the refractive index, and the wavelengths of the interacting waves.

Amplification in the parametric process takes place only for a phase-matched bandwidth, when both pump and signal waves temporally and spatially overlap. This can be seen both as an advantage and a drawback of the process. An advantage, because in the case of perfect pump-signal overlap the pump energy is only transferred to the signal and corresponding idler waves. A drawback, since the perfect overlap conditions have to be preserved over a long time and with a high accuracy (spatially a few μm and temporally a few fs) to obtain a stable ultrashort pulse source. Hence all possible mechanical vibrations, and temperature and humidity variations, should be eliminated.

If the overlap conditions are not fulfilled, not only is the gain reduced, but in addition, photons created by spontaneous down conversion of the pump (called superfluorescence), will also be amplified [101]. Superfluorescence amplification is a problem in high-gain high-energy OPA systems. Fortunately, it can be avoided in ultra-broadband OPCPA, if the following conditions are fulfilled [102]: i) the gain is of the order of 10^3; ii) an appropriate pump-seed delay is chosen; iii) spatial filtering is used in the case of multi stage OPCPA; and iv) the seed energy exceeds 1 nJ.

To reduce superfluorescence, the first stage of the Lund OPCPA system is seeded by 2.5 nJ (and the second by ∼ 3 μJ), the signal is spatially cleaned between the

---

[1] The nonlinear conversion preserves the CEP up to a constant. Signal resulting from the pump (broadened by the SPM process) has a phase equal to $\Phi_{pump} + \pi/2$. The OPA phase relation is $\Phi_{idler} = -\pi/2 + \Phi_{pump} - \Phi_{signal} = -\pi$.

[2] The gain calculation is based on a collinear geometry, neglecting pump depletion, and assuming perfect phase matching [96].

stages, and to preserve the time overlap between pump and signal waves over a long period, automatic pump-signal delay stabilization is implemented (see *Paper* **I**).

Superfluorescence can also be used similarly to spontaneous emission in the case of a laser oscillator. If a nonlinear crystal is enclosed in an optical resonator the superfluorescence will be further amplified. These types of nonlinear oscillators are called optical parametric oscillators (OPO) [103].

3.3.2 Collinear and non-collinear geometries

Optical parametric amplifiers allow for an increase of signal energy from the nJ level obtained from an oscillator, to μJ or mJ level after a single pass through a nonlinear medium. To reach a high gain the crystal's nonlinear effective coefficient has to be high. Thus, borate group crystals are often used, such as BBO[3], BiBO[4] or LBO[5]. BBO has a high effective nonlinear coefficient of 2.2 pm/V, a low hygroscopicity, a transparency range from 190 nm to 3500 nm, and a high damage threshold $> 7\,\mathrm{GW/cm^2}$. The following discussion is based exclusively on this crystal, which is used in the Lund OPCPA system.

Most often, Type I phase-matching is used (see Section 2.7). The extraordinarily polarized pump beam propagates at an angle θ to the crystal optical axis, whereas the signal and idler are ordinarily polarized. This phase-matching gives the largest bandwidth with respect to other phase-matching configurations [96].

The simplest OPA geometry is the collinear one, presented schematically in Figure 3.8a. The phase-matching bandwidth is proportional to

$$\Delta\nu \propto \left(\frac{1}{L}\right)^{1/2} \left|\frac{1}{v_{gs}} - \frac{1}{v_{gi}}\right|^{-1}, \tag{3.5}$$

where

$$\left|\frac{1}{v_{gs}} - \frac{1}{v_{gi}}\right|^{-1}, \tag{3.6}$$

is the group velocity mismatch between the signal and the idler waves. Thus, the largest bandwidth is expected at degeneracy. In general, the phase-matching bandwidth in the collinear geometry is rather small, approximately a few tens of THz. Hence the shortest pulse duration, assuming perfect compressibility, is in the range of 30 fs.

A method to extend the phase-matching bandwidth, i.e. to minimize the difference between the idler and signal group velocity, is to use a non-collinear geometry, as is shown in Figure 3.8b. The signal and pump beams propagate at an angle, α (called the non-collinear angle), which gives an additional degree of freedom for optimizing the amplification.

The phase-matching condition can be obtained from the vector equation $\mathbf{\Delta k} = \mathbf{k_p} - \mathbf{k_s} - \mathbf{k_i}$. Projecting this equation onto the signal wave vector and perpendicular to it, we obtain

---

[3] Beta barium borate.

[4] Bismuth triborate.

[5] Lithium-barium oxide.

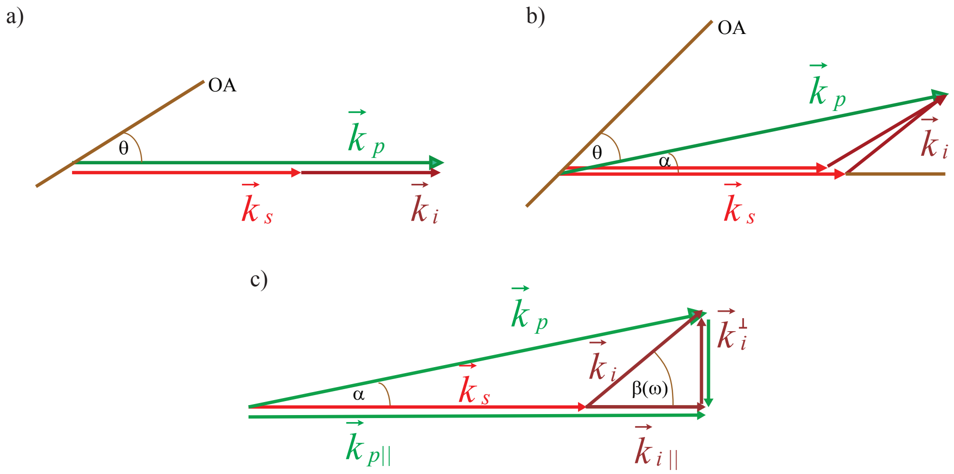

Figure 3.8: OPA geometries: a) collinear and b) non-collinear; c) geometry of the wave vectors.

$$\Delta k_{||} = k_p \cos\alpha - k_s - k_i \cos\beta, \text{ and } \Delta k_{\perp} = k_p \sin\alpha - k_i \sin\beta, \tag{3.7}$$

where β is the angle between the idler and the signal (see Figure 3.8c). Both quantities should vanish for the process to be phase-matched. A mathematical transformation of these two equations, which can be found in references [96, 104], leads to a simple equation connecting the idler and signal group velocities

$$v_{gs} = v_{gi} \cos\beta. \tag{3.8}$$

Thus the process can be phase-matched if the signal group velocity and the idler group velocity projection onto the signal are equal.

The phase-matching bandwidth in this geometry reaches more than 400 nm, around a non-collinear angle of $\pm 2.4^0$, as is shown in Figure 3.9. In this range, the amplification is constant over the bandwidth, and so gain narrowing is negligible. The shortest pulse obtained using this geometry reaches a duration of 4 fs [98, 105]. A non-collinear geometry was implemented in the Lund OPCPA system for both stages. The phase-matching presented in the figure corresponds to the first stage configuration (for details see Section 3.3.3).

As is shown in Figure 3.8, the idler wave is strongly angularly dispersed. Therefore, to use the idler for an applications is difficult, although several setups have been proposed for compensation of the spatio-temporal distortion [106, 107].

Due to the symmetry of the generation process, the signal wave can propagate either at an angle $\theta+\alpha$ or $\theta-\alpha$ to the optical axis. The two geometries, called Poynting vector walk-off compensation (PVWC) and tangential phase-matching (TPM) are presented in Figure 3.10 (a) and (b) respectively.

The PVWC geometry is often more advantageous than TPM. The extraordinarily polarized pump wave spatially walks-off towards the signal (see Section 2.7). Thus this geometry ensures better spatial overlap between the two waves. The Poynting angle in a BBO OPA pumped at 515 nm with a seed at 800 nm is $\rho = 3.1^{\circ}$ while $\alpha = 2.4^{\circ}$. However, the PVWC geometry has a drawback in systems based on BBO. The signal

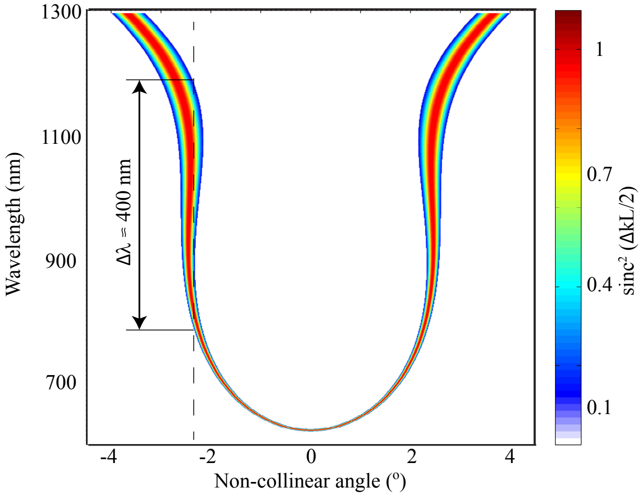

Figure 3.9: Phase-matching bandwidth for a 515 nm pump beam propagating at an angle $\theta =$ 24.35 ° through a BBO crystal with length 0.3 mm.

propagates at an angle equal to $\theta + \alpha \approx 26$ °, which is the phase-matching angle for Type I collinear SHG at $\lambda \approx 890$ nm. This is why TPM is often chosen in parametric amplifiers, especially in case of loosely focused beams. In this geometry, the spatial overlap is preserved over the crystal length [108] in spite of the spatial walk-off (the pump energy propagates at an angle $\alpha + \rho$ away from the signal). In our system, due to tightly focused interacting beams and long BBO crystals, PVWG is used for both stages.

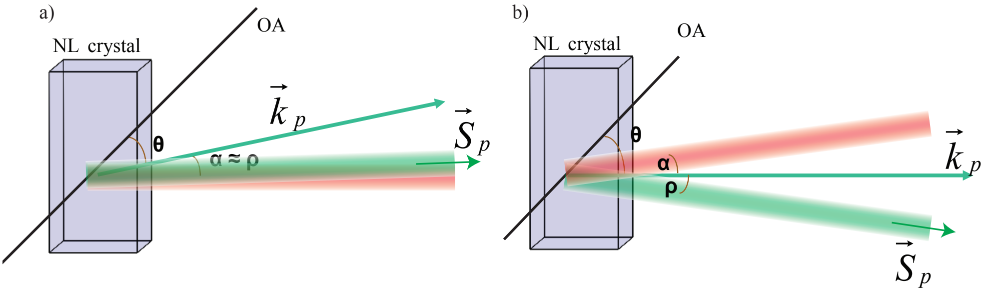

Figure 3.10: Non-collinear geometries: a) PVWC and b) TPM.

Further increases in the phase-matching bandwidth can be accomplished by multi-stage setups with a phase-matching angle detuned for each stage, or with different central frequency waves for the pump [28].

3.3.3 High-repetition rate system at LLC

This section presents the Lund OPCPA system, which is an example of amplification in the non-collinear geometry at high-repetition rate. The system was developed in cooperation with VENTEON, first in Hanover, where the company is situated, and later in Lund, where the system was moved in the summer of 2012. I have participated in the development since March 2012 (including a three months secondment to VENTEON).

The system, schematically shown in Figure 3.11, is composed of three parts: a Ti:Sapphire oscillator, a two stage non-collinear optical parametric amplifier (NOPA), and a fiber amplifier. The oscillator produces a spectrum spanning more than an octave at 80 MHz repetition rate, which supports the generation of CEP stable pulses with duration below 5 fs. The pulse CEP is measured by an f-to-2f interferometer and a correction signal is sent to CEP stabilization electronics. The signal modulates the oscillator pump power as well as the position of a pair of intracavity wedges. The main part of the oscillator spectrum serves as seed for both the OPCPA and the fiber amplifier, which assures low time jitter between pulses interacting in the NOPA stages.

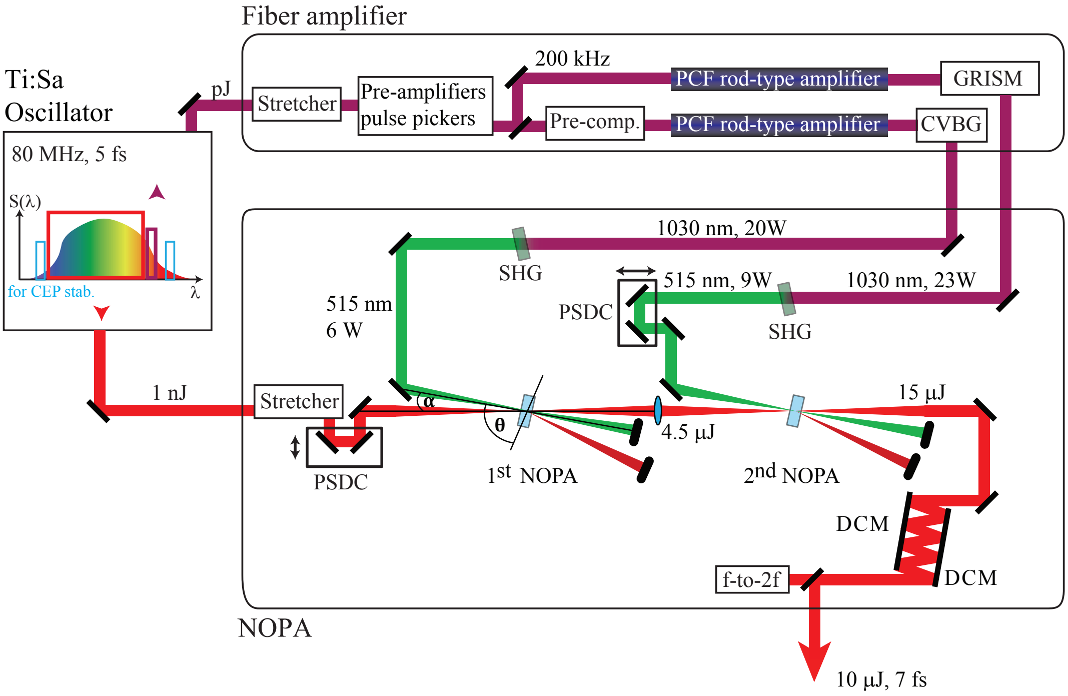

Figure 3.11: The OPCPA system; PCF - photonic crystal fiber, CVBG - chirped volume Bragg grating, SHG - second harmonic generation in BBO crystals, PSDC - pump-signal delay control, NOPA - non-collinear optical parametric amplification in BBO crystals, α - non-collinear angle, θ - phase-matching angle, DCM - double chirped mirror.

The ytterbium doped fiber amplifier, a CPA system itself, is seeded by the oscillator spectral content centered at 1030 nm with a 10 nm bandwidth, at an energy of 40 pJ.

The fiber seed is stretched in a chirped volume Bragg grating (CVBG, 27 ps/nm) to $\sim$ 250 ps. The stretched pulse is pre-amplified in a three stage fiber preamplifier. The preamplifier also includes two fiber-based pulse pickers, one electro-optical and one acousto-optical, which are used to control the repetition rate from 80 MHz to 200 kHz. After pre-amplification, the pulses are divided into two independent main amplifier arms. Each arm is composed of a photonic crystal rod-type fiber (NKT, DC 285/100, PM-Yb-ROD) and an independent compressor. In the first amplifier arm, the pulse is pre-compressed, prior to amplification, since the final compressor (a CVBG) can only remove the dispersion introduced by the stretcher. In the second amplification stage the compressor is an assembly of a prism and transmission grating (GRISM). The two amplification stages, after compression, provide 20 and 23 W average power, respectively. The outputs are frequency doubled in BBO crystals with 6.5 and 8.9 W second harmonic power corresponding to 27 and 44 μJ energy per pulse (at 200 kHz).

The two 515 nm beams pump the two NOPA stages. The seed wavelength spans a range from 650 to 1020 nm with an energy of 2.5 nJ. In each NOPA stage, the delay between the seed and the pump is controlled by a manual translation stage (PSDC in the Figure). Additionally, the first NOPA stage consists of a motorized delay stage used for an automatic delay stabilization. A large amplification bandwidth is obtained for a non-collinear angle of $\alpha = 2.43\,^\circ$ and a phase-matching angle of $\theta = 24.35\,^\circ$ in a 5 mm BBO crystal aligned for Type I phase-matching. The second stage also employs Type I phase-matching in a 5 mm BBO crystal. However, the angles are slightly detuned with $\alpha = 2.36\,^\circ$ and $\theta = 24.2\,^\circ$. Both stages work in the PVWC geometry, and their seed pulse durations are matched to the duration of the pump by propagation of the seed through a pair of wedges. The signal wave is amplified at a repetition rate of 200 kHz to 4.5 μJ in the first stage and to 15 μJ in the second. The final compressor uses a pair of DCMs (-120 fs^2). After 16 bounces from the mirrors the pulses reach a duration below 7 fs. The compressor was optimized by appropriately chosen DCM mirrors, from a set of commercial and custom-made mirrors, whose dispersion properties were measured by spectral interferometry. A small part of the compressed beam, less than 60 mW, is sent to the second f-to-2f interferometer. A slow interferometric measurement is fed back to the fast oscillator CEP stabilization loop for correction of slow CEP changes. The compressed pulses have an energy of 10 μJ which at a 200 kHz repetition rate corresponds to 2 W average power.

3.3.4 Temporal and spatial effects in OPCPA

As was shown in the previous sections, parametric amplification can preserve the input spectrum. Moreover, if the pump intensity is much higher than the seed intensity, the phase-matched frequency components preserve the initial phase [104]. Unfortunately, retaining the spatial properties is more difficult, mostly due to spatial walk-off effects and parasitic nonlinear effects, such as second harmonic generation from the part of the signal radiation in the PVWC geometry. Additionally, if the beam is tightly focused in a nonlinear medium, the phase-matching properties might change along the propagation direction due to the large variation in the wave-vector directions.

All these effects were experimentally and theoretically investigated for the Lund OPCPA. The results are discussed in *Paper* **I**. The main conclusions of the simulation are summarized here.

The theoretical investigation was carried out with help of a simulation code developed by Lang *et al.* [108]. The simulation considers ordinary and extraordinary beams inside a nonlinear crystal, as a function of time and two spatial dimensions (in the plane which contains the beams). It includes linear and nonlinear propagation effects such as: diffraction, focusing, phase-matching, and walk-off effects. Various cascade nonlinear effects observed experimentally in the parametric amplification can be identified (see Figure 3.12).

The geometry of the wave vectors in the main OPA process is shown schematically in Figure 3.12b. The 515 nm pump (feature A) interacts nonlinearly with the broadband seed (between 0.27 - 0.46 PHz, feature B), which propagates at $\alpha = 2.43°$. Due to energy conservation an angularly-dispersed idler wave is generated in the NIR part of the spectrum (D). Since the geometry is PVWC, the signal is phase-matched for the parasitic SHG conversion at 0.7 PHz (C). Moreover, part of the idler wave is frequency doubled to the visible region (E). In addition to the main DFG process and parasitic SHG, further cascade effects can be recognized. The idler (D) interacts with the doubled signal (C) via a DFG process resulting in a new wave (F) (C is a pump and D is a signal, see Figure 3.12c). Also visible in Figure 3.12a are wave (G) (the SFG between F and the IR part of the signal, the wave vector geometry for this is shown in Figure 3.12d), and the superfluorescence amplification (H) with its corresponding idler (I) (see Figure 3.12e). No clear explanation had been found for (J).

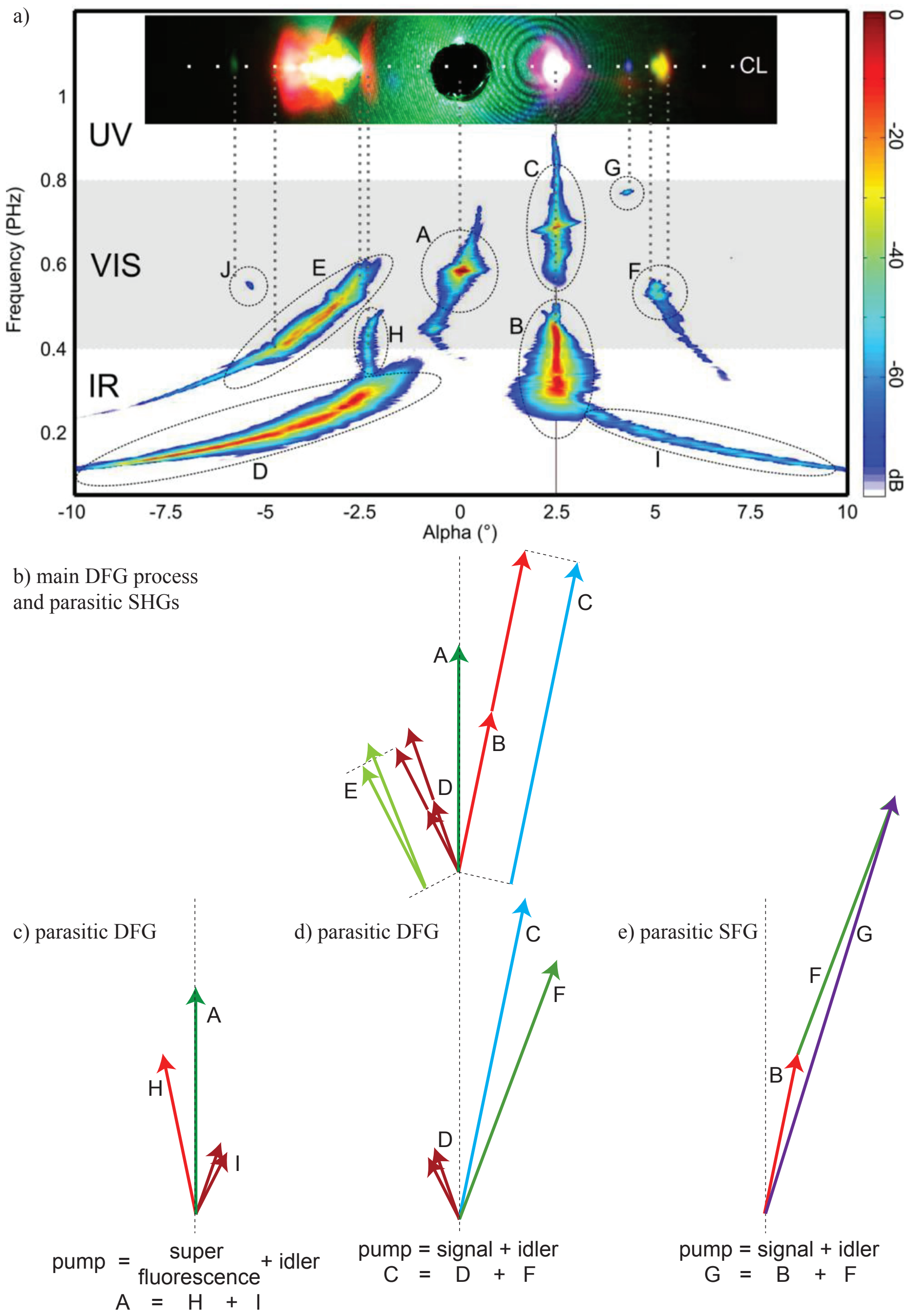

Figure 3.12: a) Numerical simulation compared with experimental results for the OPCPA system at the first parametric stage. The shaded area indicates the visible part of electromagnetic spectrum. The inset shows a photograph taken from a screen behind the first BBO crystal with a hole for the pump light, where CL indicates the plane of the simulation; b) wave vector geometry of the main DFG process (A-pump = B-signal + D-idler) and second harmonic conversion of signal (C) and idler (E); c) parasitic DFG and SFG processes, superfluorescence amplification (A-pump = H-signal + I-idler), DFG (C-pump = D-signal + F-idler) and SFG (G = B + F).

CHAPTER 4

HIGH-ORDER HARMONIC GENERATION

High-order harmonic generation is a process which creates coherent extreme ultraviolet (XUV) radiation by nonlinear interactions between an intense laser field and atoms. The process, discovered by two groups in France [2] and the United States [1] in the late 1980s, led to the construction of small-scale laboratory sources of XUV radiation. The sources have evolved significantly over the years and their applications resulted in many groundbreaking experiments, mostly due to the generation and measurement of attosecond light pulses [109]. Examples of applications are the observation of valence electron motion [4], the measurement of ionization time delays [5, 6], or nonlinear optics in the soft X-ray spectral range [9, 10].

HHG was achieved under various conditions, such as in high-pressure gas jets [110], gas cells [111], semi-infinite media, and gas-filled capillaries [112]. Conversion efficiencies of 10^{-7} in neon [111], 10^{-5} in argon [113], and slightly below 10^{-4} in xenon, were obtained. The low conversion efficiency leads to moderate XUV pulse energy, with the highest reported to date being $10\,\mu$J [114]. The low energy output significantly limits the range of applications.

The aim of this thesis was to construct efficient HHG sources with two different characteristics: one with high peak power (*Paper* **III**) and one with a high repetition rate (*Paper* **IV**). The first source provides intense high-order harmonics generated by loosely focusing high-energy Ti:Sapphire laser radiation into a gas filled cell. The second source is driven by a novel OPCPA laser and delivers attosecond pulses at a rate of 200 kHz rate. A conceptual design of an HHG gas beamline for the large scale facility ELI-ALPS[1] is presented in *Paper* **V**.

This chapter presents a basic description of HHG from the microscopic (Section 4.1) and macroscopic (Section 4.2) points of view. The sources are described in Section 4.3. The last section (Section 4.4) presents HHG from multi-color fields (*Papers* **VII** and **VI**).

---

[1] Extreme Light Infrastructure - Attosecond Light Pulse Source.

4.1 Single-atom response

4.1.1 Three-step model

High-order harmonic emission from a single atom is described by the semi-classical three-step model [115, 116], as is shown in Figure 4.1. In each half-cycle, an electron first tunnels through the atomic potential barrier distorted by an intense laser field. In the second step, the freed electron is accelerated away from the parent ion and then at later stage, when the electric field reverses sign, towards it again. For a linearly polarized laser field, the electron may return to the vicinity of the parent ion, and there is a finite probability that it will recombine, leading to emission of an XUV photon.

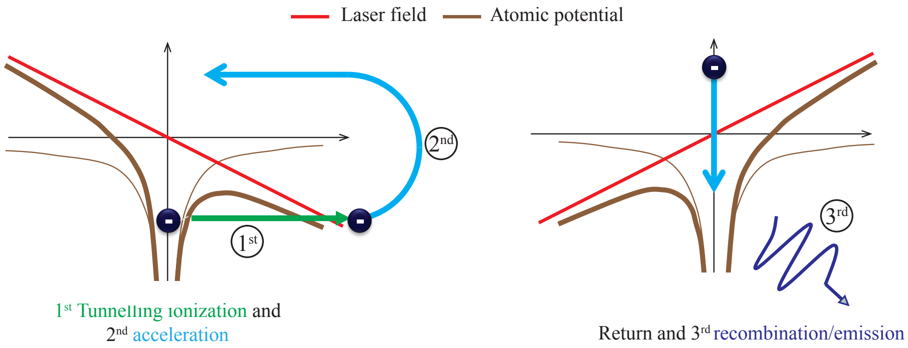

Figure 4.1: The three-step model.

The electron's trajectory depends on the time of its emission into the continuum. An electron tunneling out in the first quarter of the field's cycle never comes back to the parent ion, as is marked in black in Figure 4.2a. A photon can be emitted when the electron leaves the atom in the second quarter of the field's cycle as is indicated by the colored lines in Figure 4.2. This is repeated every half-cycle of the laser field. A given photon energy, (see Figure 4.2b), can be generated in two main trajectories, which differ by the time spent in the continuum. These trajectories are called short and long to express the electron excursion time. The maximum photon energy is defined by the cut-off law [117]

$$E = 3.17U_p + I_p, \tag{4.1}$$

where U_p is the ponderomotive energy and I_p is the atomic ionization potential. The ponderomotive energy is the average electron kinetic energy, equal to

$$U_p = \frac{e^2 E_0^2}{4m_e\omega} = \frac{e^2\lambda^2 I}{8\pi^2 m_e \epsilon_0 c^3}, \tag{4.2}$$

where e is the electron charge, ω and λ are the central angular frequency and wavelength[2], and m_e is the electron mass. The equation shows that the maximum photon

---

[2] In the previous chapters, ω_0 and λ_0 were used as central frequency and central wavelength of a broadband pulse and ω and λ were variables. Here, it is more convenient to denote by ω and λ the central frequency and central wavelength of the fundamental field.

energy increases with increasing driving wavelength and laser intensity. The HHG sources driven by MIR OPCPA systems allow the generation of HHG in the keV X-ray region [30, 118, 119].

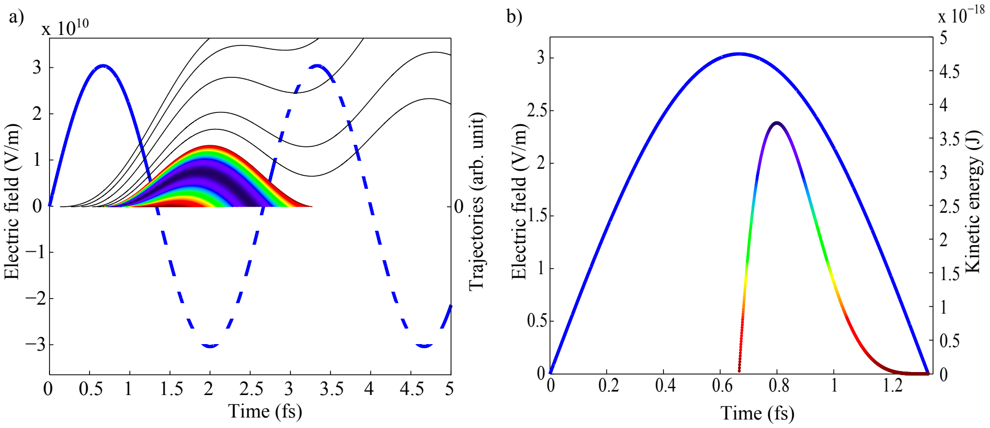

Figure 4.2: a) Electron trajectories (rainbow colors) for the first plotted half-cycle of the 800 nm field (blue solid line). The trajectories which never cross zero are in black. The colors indicate the return energy of the electron following the corresponding trajectory. b) A half-cycle of the 800 nm field and the return energy of electrons as a function of ionization time. The color scale is unified for both plots.

The short and long trajectories contribute to HHG radiation with different phase properties [120], and they therefore feature different spatial and spectral characteristics, as well as different phase-matching, as will be discussed in Section 4.2. The divergence is smaller and the harmonic bandwidth narrower for the short trajectory contribution than for the long one [121].

Although the three-step model gives insights into HHG emission, a quantitative description requires more advanced quantum mechanical calculations [122], including a more realistic treatment of the atomic system.

The emission from one half-cycle has a continuous spectrum, whose highest photon energy, expressed by Equation 4.1, depends on the generation medium. Experimentally observed HHG spectra generated in gaseous media are schematically presented in Figure 4.3. The spectral amplitude for the low-order harmonics below the ionization threshold decreases rapidly with increasing photon energy. In the region called the plateau, the harmonic intensity remains approximately constant before dropping at the cut-off.

The large emitted bandwidth from each half-cycle supports the production of an attosecond pulse [123–125]. Techniques based on interferometry [109] or streaking [126] allow pulse duration to be measured down to a few tens of attoseconds [11].

4.1.2 Multi-cycle HHG

The previous section describes emission only from one half-cycle. In case of the HHG setups presented in this work, the driving wave contains several half-cycles, and most

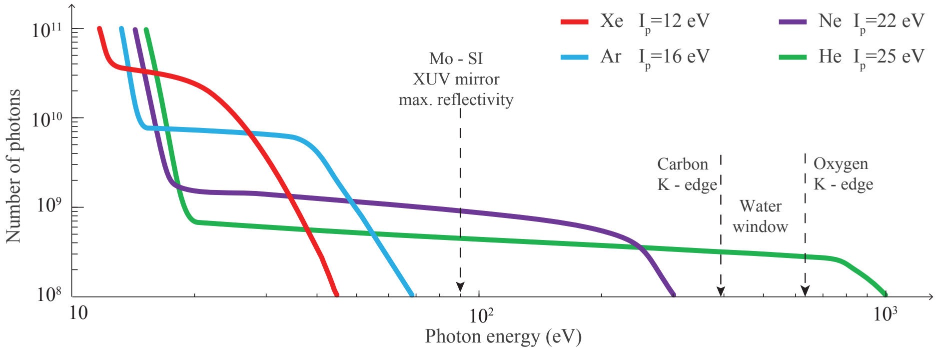

Figure 4.3: HHG spectra for different gases. Characteristic wavelengths in the XUV range are marked.

of them contribute to the generation of an XUV burst of light. Multi-cycle generation leads to a HHG spectrum, due to spectral interferences.

Let us consider for example the case of a square pulse with N identical generating sub-cycles. The emitted attosecond pulses contain the same spectral components i.e. with amplitude $S_s(\Omega)$ and constant phase difference, $\Delta\Phi$, except for a π-shift between consecutive pulses[3].

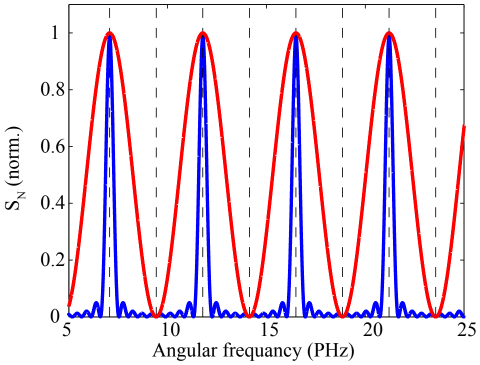

Figure 4.4: Multiple wave interference for $N = 2$ (red solid line) and $N = 10$ (blue solid line). The dashed line indicates the position of the harmonics of 800 nm radiation (both even and odd).

The spectrum resulting from the interference of these N pulses can be written as [39]

$$S_N(\Omega) = S_s^2(\Omega)\left(\frac{\sin(N\Delta\Phi/2)}{\sin(\Delta\Phi/2)}\right)^2. \tag{4.3}$$

The phase difference, $\Delta\Phi$, of waves generated in consecutive IR half-cycles is equal to $\Omega T/2 + \pi$, where $T/2 = \pi/\omega$. In the case of a large number of waves the maximum is

---

[3] This neglects phase-matching effects, and especially time-dependent ionization.

obtained when the denominator is zero

$$\sin(\Delta\Phi/2) = 0 \Rightarrow \Delta\Phi/2 = n\pi, \tag{4.4}$$

and the maxima are obtained at frequencies $\Omega = (2n-1)\omega$, where $(2n-1)$ is an odd number. In other words, constructive interference occurs at the odd harmonics of the fundamental frequency[4].

In Figure 4.4 the spectrum corresponding to two (red) and ten (blue) pulses is presented. The spectral bandwidth of each harmonic is inversely proportional to the number of the interfering pulses. For a low number of pulses, secondary maxima can be observed between the main peaks. The number of maxima, N_m, is related to the number of the pulses, N_w, [127] by

$$N_m = N_w - 2. \tag{4.5}$$

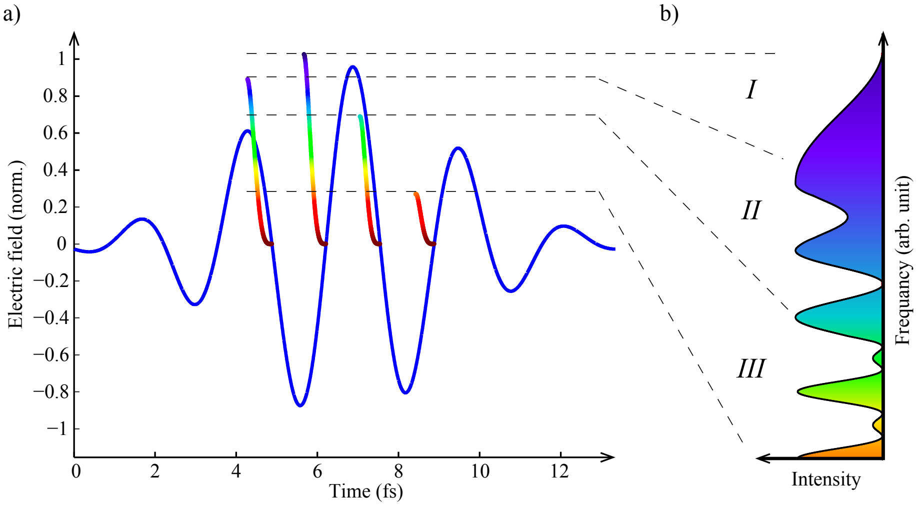

Figure 4.5: a) Return energy of the short trajectory electrons (solid line with rainbow colors) as a function of the ionization time. The fundamental is a 5 fs pulse with carrier wavelength of 800 nm and CEP ≈ 4 rad (blue solid line); b) Corresponding HHG spectrum. The color scale is the same in both graphs. The origin of different spectral components is indicated by the numbers I, II, III.

In a more realistic situation, for a few-cycle pulse, the emission differs from one half-cycle to the next. As is shown in Figure 4.5, the spectral content of the emission corresponding to the short trajectories (shown in rainbow colors in the figure) varies. The highest photon energy is obtained for the half-cycle with the highest amplitude. This gives the possibility to restrict the emission to only this half-cycle by spectral filtering of the continuous spectral region indicated as part *I* in the figure. This method to produce single attosecond pulses is called amplitude gating [12]. Another technique

---

[4] In case of two interfering pulses, $N = 2$, the equation 4.3 simplifies to $S_N(\Omega) = S_s^2(\Omega) 4\cos^2(\Phi/2)$.

used to gate the emission to only one half-cycle is polarization gating [128]. The technique takes advantage of the dependence of the HHG emission on the driving light's ellipticity (the probability of an electron recombination decreases with increasing ellipticity). A single attosecond pulse can be generated by using a driving pulse with a linear polarization lasting for one half-cycle.

In region *II*, where two pulses contribute, the interference depends on the CEP of the fundamental pulse. The spectral amplitude and phase of the attosecond pulses depend on the intensity, and changes with the CEP. When the CEP, varies the position of the spectral peaks changes. The harmonic peaks return to their position, $\Omega = (2n-1)\omega$, after a CEP variation equal to a multiple of π. Phase distortions of the fundamental wave or emitted radiation lead to more complicated interference patterns, as discussed in reference [129].

Paper **IV** discusses HHG driven by the short pulses of our OPCPA system. The generated high-order harmonic spectrum as a function of CEP is shown in Figure 4.6. The CEP was changed by translating a pair of wedges. The harmonics are spectrally broad and overlap with each other. The intensity of the harmonics depends on the CEP in a complex manner. The interpretation of the interference pattern is presented in *Paper* **IV**.

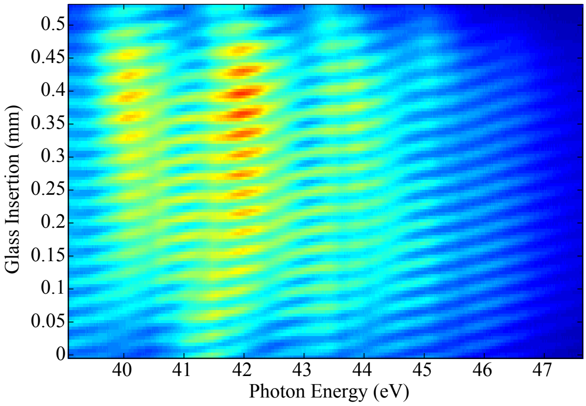

Figure 4.6: HHG spectrum as a function of glass insertion generated by the interaction of a 8 fs pulse from the OPCPA laser system (see Section 3.3.3) with argon gas.

4.2 Macroscopic effects

4.2.1 Phase-matching

Efficient HHG requires constructive addition of all sources in the generation volume [130, 131] (see Figure 4.7). This can be described by introducing the coherence length $L_{coh} = \pi/\Delta k$, similarly to perturbative nonlinear optics (see Section 2.7). To maximize the emission, the wave vector mismatch, Δk, must be minimized. For a given harmonic order q, Δk is equal to

$$\Delta k = qk_{\omega} - k_{q\omega}, \tag{4.6}$$

where k_ω and $k_{q\omega}$ are the wave vectors of the induced polarization, at frequency $q\omega$, and harmonic field, respectively[5]. In a non-guiding geometry, Δk is a function of time and space with four contributing terms

$$\Delta k = \Delta k_g + \Delta k_n + \Delta k_p + \Delta k_d, \tag{4.7}$$

where Δk_g is the Gaussian beam phase gradient, Δk_n and Δk_p are due to the neutral and plasma dispersion, respectively, and Δk_d is the wave vector mismatch resulting from the dipole phase. In general, phase-matching is obtained if the four components compensate each other for all radial and longitudinal positions during the pulse [132].

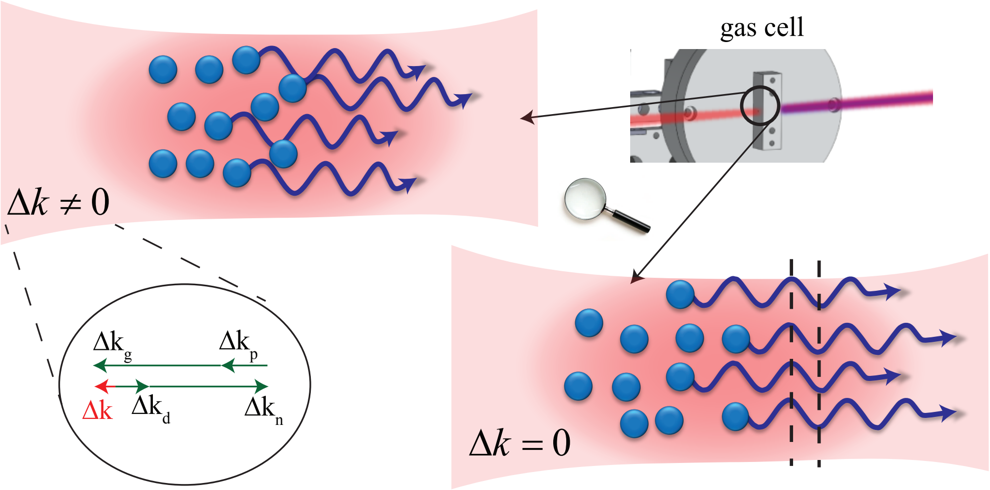

Figure 4.7: Schematic representation of phase-matching in two cases: non-phase-matched ($\Delta k \neq 0$) and phase-matched ($\Delta k = 0$) generation.

The Gaussian beam phase gradient is the derivative of the Gouy phase (see Equation 2.4 in Chapter 2). This gradient depends on the spatial coordinates and always takes negative values, with a minimum at the beam focus, where it is equal to $-q/z_R$. Since the Rayleigh range increases with focal length, this contribution is small for a loosely focused beam.

The wave vector mismatch resulting from neutral dispersion is positive. A neutral medium has a higher refractive index for an IR driving field than for XUV harmonic radiation. The medium is always partially ionized. Thus, the refractive index has an additional contribution equal to

$$n_{el} = \sqrt{1 - \left(\frac{\omega_p}{\Omega}\right)^2} \text{ where } \omega_p = \sqrt{\frac{e^2 N_{el}}{\epsilon_0 m_e}}, \tag{4.8}$$

where $\Omega = \omega$ for the fundamental and $\Omega = q\omega$ for the q^{th}-harmonic. n_{el} is smaller for the IR field than for the high-order harmonic field. The wave vector mismatch gained

---

[5] In the literature, phase-mismatch is sometimes defined as $\Delta k = k_{q\omega} - qk_\omega$. This definition leads to opposite signs of the wave vector mismatch components.

during propagation through such a medium is always negative. In the equation N_{el} is the electron density, while e and m_e are the electron charge and mass, respectively. Both Δk_n and Δk_p depend linearly on gas pressure.

The dipole phase gradient is the partial derivative of the phase gained by the electron in the continuum [120]. The phase varies approximately linearly with the laser intensity and can be expressed as

$$\phi(\Omega, I) \approx -\alpha(q\omega)I. \tag{4.9}$$

The proportionality constant, α, depends on the harmonic order, q, and the electron trajectory. α can be determined by solving the time-dependent Schrödinger equation (TDSE) [133] or by using the strong field approximation [134]. Δk_d is negative before the focus and positive after the focus.

Δk_d is significantly different for the long and short trajectories. For the 27^{th} harmonic, in argon $\alpha = 5.1 \times 10^{-14}$ cm^2/W for the short trajectory and 19.2×10^{-14} cm^2/W for the long [135]. Thus, phase-matching is achieved in different conditions for the two trajectories. Figure 4.8 shows the total wave vector mismatch Δk is calculated on-axis as function of the z coordinate. For short trajectories (Figure 4.8a), the phase-matching condition ($\Delta k \approx 0$) is achieved behind the laser focus, where Δk_g compensates Δk_d.

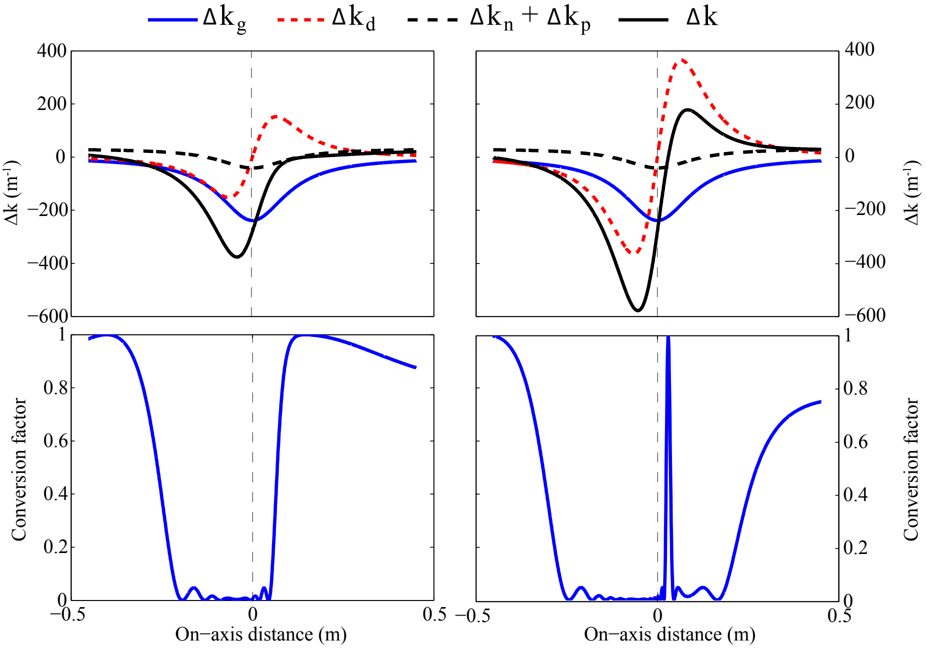

Figure 4.8: Phase-matching for short (left column) and long trajectories (right column). The upper row shows the wave vector mismatch contributions and their sum. The bottom row presents the conversion factor $\text{sinc}^2(\Delta kL/2)$. Calculation in argon for the 27^{th} harmonic and an ionization degree of 2%.

In the same conditions the long trajectories (Figure (4.8b) are not phase-matched on-axis. Partial phase-matching for long trajectories can be obtained off-axis, and as a consequence the long trajectory beam is ring-shaped. Different spatial shapes of the two contributions as well as a larger divergence angle for the long trajectories [135], allow the spatial selection of only the short trajectory beam for further applications [136].

As indicated at the beginning, phase-matching is a time-dependent process, due to time-dependent ionization and dipole phase. Δk_p increases during the laser pulse. Driving HHG with intensities above 10^{15} W/cm^2 leads to phase-matched generation at the pulse front and to depletion of the complete medium at the pulse tail. Hence, a careful choice of the generation conditions, allows for gating of HHG to only half an optical cycle, and thus to generate a single attosecond pulse (SAP) [137]. This method was proposed as a gating technique for SAP production in the conceptual design of the gas HHG beamline at ELI-ALPS (see *Paper* **V**).

The phase-matching terms are dependent on the setup parameters, the geometry, and the generation medium. The Gaussian beam phase gradient varies with the gas cell position relative to the laser focus and the Rayleigh range. The neutral and plasma dispersion can be controlled by the gas pressure and the degree of ionization, which depends on the intensity. The dipole phase gradient changes with the driving pulse energy as well as the position with respect to the laser focus. Control of these parameters allows for the optimization of the harmonic radiation. Moreover, a change of one parameter often influences many phase-matching terms. Therefore, the optimization requires an iterative procedure, where all setup parameters are readjusted accordingly. This procedure was automatized for the high-intensity HHG source, and is presented in the following section.

Phase-matching in tight focusing

In the tight focusing geometry, for which z_R is of the order of tens of micrometers, phase-matching is dominated by Δk_g. In addition, the volume in which an intensity of the order of 10^{14} W/cm^2 (required for HHG) is obtained, is very small. Hence, the pressure required for efficient HHG has to be high, of the order of a few bars [138]. In practice, it is complicated to operate a gas jet with a pressure of several bars in a vacuum. The maximum pressure is limited by pumping capacity and optimum phase-matching is difficult to achieve (see *Paper* **IV**).

Phase-matching in loose focusing

The phase-matching conditions in the loose focusing geometry are discussed in *Paper* **III**. The loose focusing geometry can be defined as a geometry where the Rayleigh range is longer than a few tens of millimeters. We can neglect the dipole phase contribution, which is small for a loose geometry. We assume that we are close to the focus. The HHG amplitude is maximized when the plasma dispersion and Gouy phase gradient are compensated by the neutral dispersion, which can be written as

$$|\Delta k_n(p_{match})| - |\Delta k_g| - |\Delta k_p(p_{match}, r_{ion})| = 0, \tag{4.10}$$

where r_{ion} is the ionization degree. For certain r_{ion} phase-matching is achieved at a given p_{match}. Figure 4.9 shows the variation of p_{match} in argon as a function of the degree of ionization for three harmonic orders and two different focusing geometries ($f_\# = f/D = 100$ and 400 where D is the beam diameter). Phase-matching can only be achieved at a low degree of ionization, of the order of a few percent.

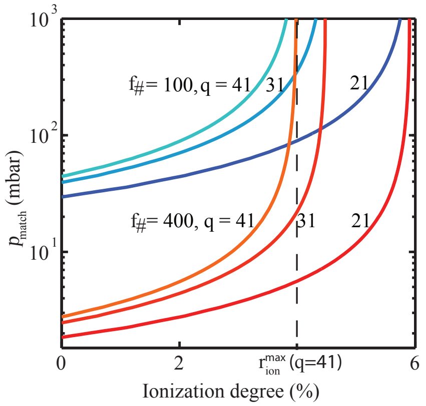

Figure 4.9: Phase-matching pressure as a function of ionization degree. The pressure is plotted for two focusing geometries and three harmonics. The calculations were carried out for generation in argon with a driving pulse with 800 nm central wavelength and 45 fs duration.

For attosecond pulse generation the phase-matching pressure should be approximately constant for a broad range of high-order harmonics, therefore an even lower ionization degree is required than for the optimization of a single harmonic. As a rule of thumb, the optimum value is approximately $r_{ion}^{max}/2$ (see Figure 4.9) for the highest harmonic in the considered attosecond bandwidth ($\sim 2\%$ in the figure).

Using a loose focusing geometry is a way to increase HHG in setups driven by high-energy femtosecond systems. There is a significant increase in the interaction volume over which the intensity required for the HHG process is reached. The transverse dimension increases as a linear function of the focal length, whereas the longitudinal dimension scales with the square of the focal length [138]. Scaling of HHG is further discussed in part 4.2.3.

4.2.2 Absorption-limited generation

Once phase-matching is achieved the photon number increases as the square of the medium length, leading to a high conversion efficiency. However, harmonics are generated in the spectral region which spans from the VUV to the soft X-rays. Radiation emitted in this region is strongly absorbed by most media including the generation gas.

Following the work of Constant *et al.* [140], the number of photons emitted on axis[6] is equal to

---

[6] Assuming a constant atomic response over the generation volume for a certain harmonic q.

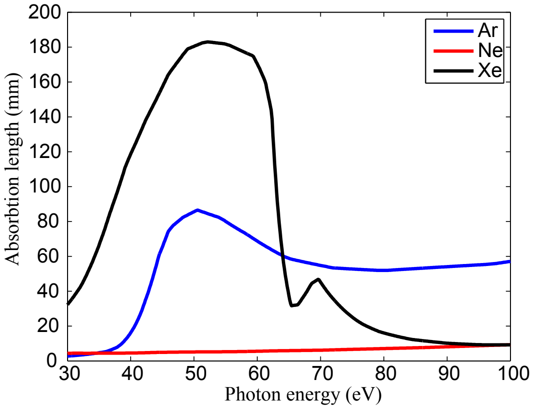

Figure 4.10: Absorption lengths in Ar, Ne and Xe at 5 mbar. Based on [139].

$$N_{out}(q) \propto \frac{4L_{abs}^2}{1+4\pi^2(L_{abs}^2/L_{coh}^2)}\left[1+\exp\left(\frac{-L_{med}}{L_{abs}}\right)-2\cos\left(\frac{\pi L_{med}}{L_{coh}}\right)\exp\left(\frac{-L_{med}}{2L_{abs}}\right)\right], \tag{4.11}$$

where $L_{abs}(\omega)$ is the frequency dependent absorption length, over which the number of photons drops to $1/e$ (36%) of the initial value [140]. Absorption lengths for the gas media used for HHG are shown in Figure 4.10.

"Absorption-limited HHG" corresponds to phase-matched generation limited by absorption. It can be defined by the relation

$$L_{med} > 3L_{abs} \text{ and } L_{coh} > 5L_{abs}, \tag{4.12}$$

presented as black line in Figure 4.11 [140].

If the coherence length is comparable with the absorption length, the number of photons oscillates with the length of the medium, and a maximum is obtained over a length of medium approximately equal to L_{coh} (e.g. $L_{coh}/L_{abs} = 2$, blue line in Figure 4.11).

More than 95% of the maximum number of photons can be obtained when $L_{med}/L_{abs} > 10$ and $L_{coh}/L_{abs} > 100$ (see black line in Figure 4.11).

4.2.3 Scaling HHG

Once absorption-limited and phase-matched emission is established, a further increase of the signal can be achieved by scaling up the generation process. This requires an appropriate change of the setup parameters in order to preserve the phase-matching conditions and the intensity required for HHG. The scaling laws were developed for loose focusing in *Paper* **III** (see also similar consideration for tight focusing in [138]) and were used in *Paper* **V** to predict optimal generation conditions for the gas beamline to be constructed at the ELI-ALPS facility.

We consider the focal region ($\Delta k_d = 0$) and assume Gaussian shaped fundamental and HHG beams. To indicate the linear dependence of Δk_n and Δk_p on gas pressure, these two terms can be written as $p\partial(\Delta k_{n,p})/\partial p$, where $\partial(\Delta k_{n,p})/\partial p$ is pressure independent. Equation 4.7 can be written as

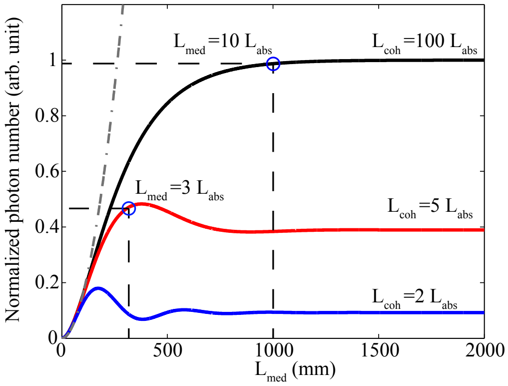

Figure 4.11: Number of photons as a function of medium length for $L_{abs} = 100\,\mathrm{mm}$ and three values of L_{coh}. The double dashed line indicates the photon number increase in the absence of absorption.

$$\frac{\Delta k_g f^2}{f^2} + p_{match}\left(\frac{\partial(\Delta k_n)}{\partial p} + \frac{\partial(\Delta k_p)}{\partial p}\right) = 0, \tag{4.13}$$

where $\Delta k_g f^2$ is independent of the focal length. Simple mathematical transformations lead to

$$p_{match} f^2 = -\frac{(\Delta k_g f^2)}{\left(\frac{\partial(\Delta k_n)}{\partial p} + \frac{\partial(\Delta k_p)}{\partial p}\right)}. \tag{4.14}$$

Thus phase-matching conditions are focal-length invariant if the product $p_{match} f^2$ is constant, or in other words, if p_{match} scales as $1/f^2$. The change of focal length requires also a change of the fundamental pulse energy to maintain the required intensity. Using Gaussian optics, the intensity at the focus is

$$I_0 = \frac{E_f}{\tau \pi w_0^2} = \frac{E_f \pi}{4\tau \lambda_0^2 f_\#^2}, \tag{4.15}$$

where E_f is the fundamental pulse energy, and D is the beam diameter before focus. The pulse energy has to change proportionally to f^2 in order to keep the intensity constant. Scaling of phase-matching pressure and the required fundamental pulse energy with focal length is presented in Figure 4.12 for the 21^{st} harmonic.

Since the scaling preserves the conversion efficiency (η), the HHG energy

$$E_{\mathrm{h}} = \eta \cdot E_f, \tag{4.16}$$

also scales as f^2. Here, E_f is the driving pulse energy. A conversion efficiency as high as 10^{-5} has been reported [114, 141], which led to an energy of $1\,\mu$J. Using the scaling method, a change of focal length by a factor of 4 leads to a 16 times higher HHG energy $16\,\mu$J.

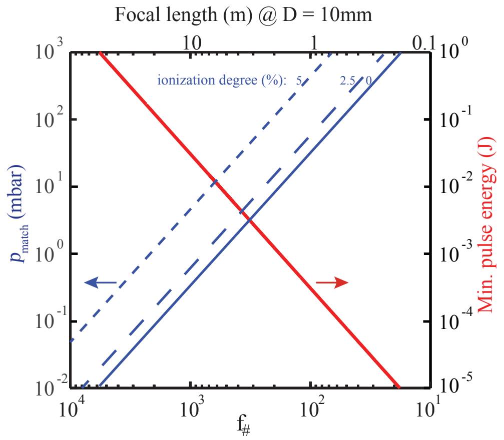

Figure 4.12: Phase-matching pressure and fundamental pulse energy as a function of $f_\#$. The dependence is calculated for the 21^{st} harmonic, assuming an intensity of 1.5×10^{14} W/cm^2.

4.3 Experimental realization of HHG

In this section two HHG systems are presented. The systems were constructed and developed during the thesis. The first system is the high-intensity HHG source, described in *Paper* **III**. The system is driven by the high-power low-repetition rate laser system presented in Section 3.2. The second HHG source, driven by the OPCPA laser, works at a high-repetition rate (described in Section 3.3) and is presented in *Paper* **IV**.

The two sources are constantly under development. Thus the following description corresponds to their status when the experiments presented in the thesis were carried out. Detailed descriptions of the HHG sources can be found in the articles.

4.3.1 High-intensity HHG source

The high-intensity HHG source consists of three sections: generation, diagnostic, and application (see Figure 4.13). All sections are mounted on a vibration damping support, which provides high stability for pump-probe experiments.

High-order harmonics are generated by loosely focusing a high-energy laser beam into a noble gas. The beam can be focused either by a lens or a mirror (with focal lengths up to 10 m). Figure 4.13a shows the setup configured for 4 m focusing with a lens, and Figure 4.13b presents a possible configuration with a 6 m focal length. The spatio-temporal distortions introduced by long focal length lenses (see Section 2.4), are negligible due to the large radius of curvature of lenses with such focal lengths. Immediately after the focusing optics the fundamental beam enters vacuum. The focused beam interacts with a noble gas confined in a cell. The gas is released at the repetition rate synchronized with the laser system (10 Hz) by a piezo-electrical valve [142, 143]. The position of the generation medium with respect to the laser focus can be adjusted by means of a translation stage.

The generation chamber is designed to work simultaneously with up to two gas cells. Cells mounted in series were used for the enhancement of the HHG process (see

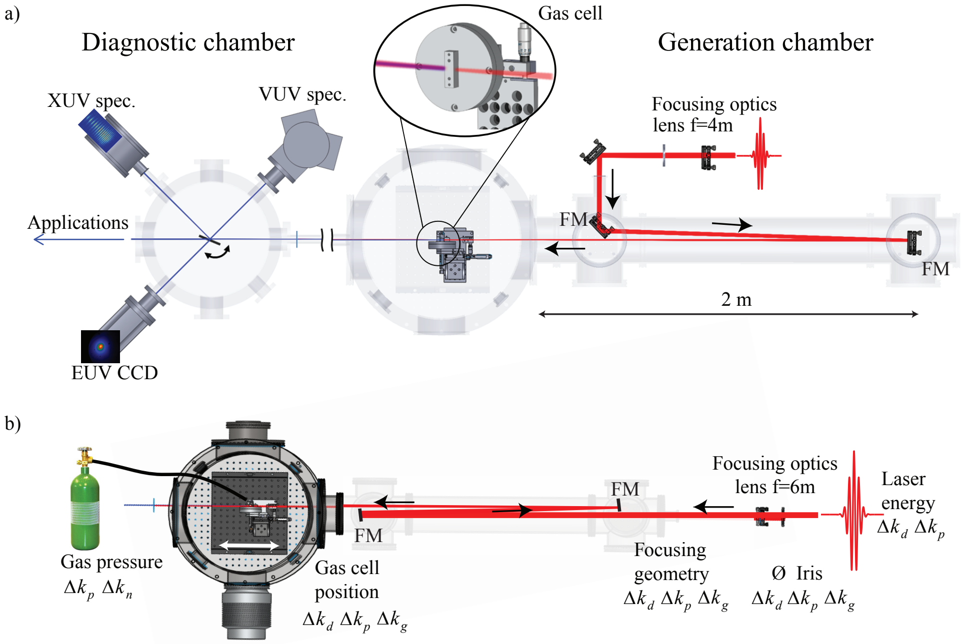

Figure 4.13: a) HHG setup configured for 4 m focusing with a lens; b) Setup parameters controlled for phase-matching optimization. The setup is that corresponding to a 6 m focus. FM - folding mirror.

Paper **VI** and Section 4.4.2).

The generated harmonic beam propagates collinearly with the fundamental radiation to the diagnostic chamber. The two beams can be separated by using aluminum filters. The filters are mounted on a manual translation stage placed at the entrance of the diagnostic chamber, and controlled from the outside of the vacuum chamber.

Spectral characterization is carried out by a flat-field XUV spectrometer (Jobin-Yvon PGM-PGS 200) or, for the low-order harmonics, by a vacuum ultraviolet monochromator (McPherson 234/302). Additionally, spatial profiles and energy measurements are carried out by using a back-illuminated XUV-CCD camera (Andor iKon-L). The XUV beam is sent to the different instruments by using a metallic flat mirror mounted on a rotation stage.

An iterative optimization procedure has been implemented, which allows us to find a set of parameters for phase-matched generation. The optimization is based on the analysis of the spectra with simultaneous automatic control of the parameters indicated in Figure 4.13b. The procedure allows for an optimization of either a single harmonic or a broad range of harmonics.

4.3.2 High-repetition rate HHG source

The high-repetition rate HHG source, shown in Figure 4.14, uses a tight focusing geometry. The setup consists of two parts: generation and characterization, which are separated by a small conically expanding hole for differential pumping. A negatively chirped fundamental pulse enters the vacuum through an anti-reflection coated window

(Wi, see Figure 4.14). The pulse phase is tuned by a pair of AR coated wedges (W). The beam diameter is expanded by an all-reflective telescope (T). The fundamental beam in the generation chamber is focused with an achromatic lens (L) into argon gas provided through a jet (J).

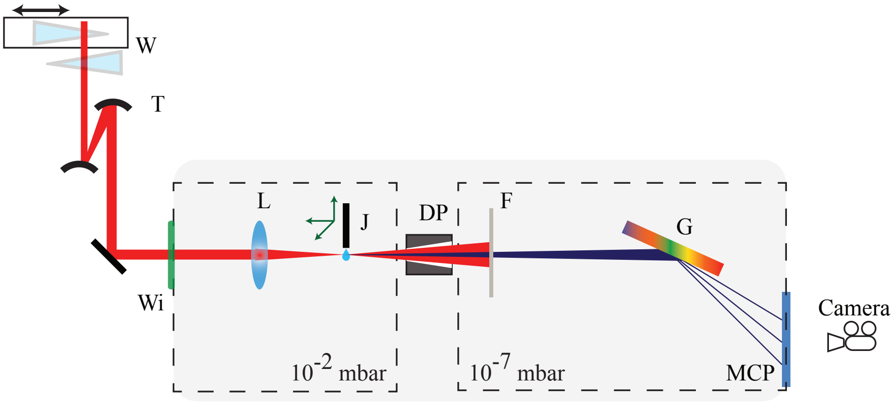

Figure 4.14: The HHG setup; W - wedge, T - reflective telescope, Wi - vacuum entrance window, L - achromatic lens, J - argon gas jet, DP - differential pumping hole, F - motorized filter mount, G - diffraction grating, MCP - microchannel plate with phosphor screen.

The fundamental field and high-order harmonic radiation co-propagate through the differential pumping hole (DP) to the characterization chamber, where a home-built XUV spectrometer is placed. The XUV can be separated from the fundamental by metallic filters, such as 200 nm thick aluminum and titanium filters installed in a motorized filter mount (F). The XUV spectrometer provides spatially resolved harmonic spectra by dispersing the beam with a diffraction grating onto a microchannel plate (MCP) detector. The MCP, coated with a CsI layer, can detect radiation up to 250 nm. The MCP phosphor screen is imaged with a CCD camera. The spectrometer is calibrated based on the transmission curves of the metallic filters [139].

4.4 HHG driven by multi-color field

The generation process presented in the previous section is based on the assumption that HHG is driven by a single-color field, usually with carrier frequency of 800 nm. In the two following sections, experiments are presented, where the driving field is modified either by addition of its second harmonic or of low-order odd harmonics [144]. The resulting sub-cycle control allows us to enhance the single atom response (*Paper* **VI**) or to optimize phase-matching (*Paper* **VII**). In the case of $\omega/2\omega$ experiments even harmonics are generated. Experimentally, HHG using several colors can be controlled by variation of the relative intensity and phase between the fields.

4.4.1 Two-color, $\omega/2\omega$ driven HHG

A two-color field composed of waves with carrier frequency ω and its second harmonic, 2ω, is described as

$$E = E_0 \sin(\omega t + \phi(\omega)) + rE_0 \sin(2\omega t + \phi(2\omega)), \tag{4.17}$$

where $\phi(\omega)$ and $\phi(2\omega)$ are the phase of the fundamental and second harmonic fields, and r is the amplitude ratio. HHG by a two-color field is illustrated in Figure 4.15.

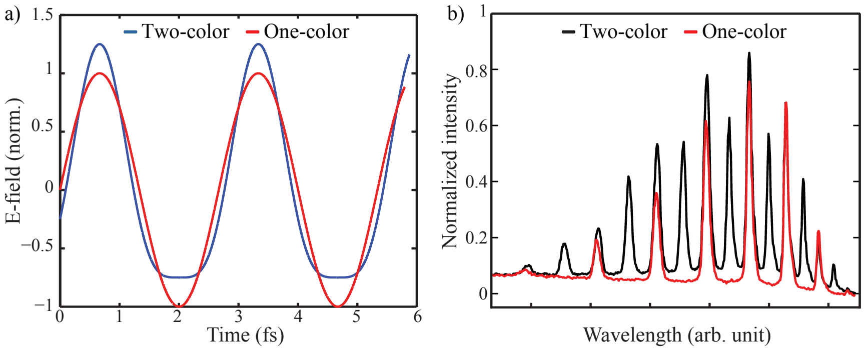

Figure 4.15: One and two-color HHG: a) driving field and b) HHG spectra.

The advantages of two-color driven HHG have been pointed out by many groups [145]. One of the very important applications of $\omega/2\omega$ driven HHG is the possibility to reduce the number of "recollision" events to once per fundamental pulse cycle, due to the broken symmetry of the process. This relaxes slightly the conditions for isolating a single attosecond pulse and is often added to gating techniques. A combination of $\omega/2\omega$ and polarization gating (see section 4.1.2), called double optical gating (DOG) [146], has been proposed in *Paper* **V**.

We have also investigated (*Paper* **VII**) the possibility of controlling phase-matching of the HHG process using two colors and a non-collinear geometry. The odd and even harmonics are generated by different combinations of photons absorbed from the two driving fields. Each combination leads to an emission at a different angle. Denoting m_1 and m_2 the number of photons absorbed from the fundamental and second harmonic fields, the q^{th}-harmonic frequency is equal to

$$q\omega = m_1\omega + m_2 2\omega, \tag{4.18}$$

where m_1 and m_2 can be chosen positive and negative corresponding to a sum or difference frequency generation. $m_1 + m_2$, which reflects the number of absorbed photons, has to be odd in order to satisfy parity conservation. This photon picture [147], shown in Figure 4.16a, has a corresponding wave picture, where the two waves interfere at the focus creating an intensity pattern to which the medium responds nonlinearly. The intensity pattern at the focus and a far-field HHG spatial profile are shown in Figure 4.16b.

To investigate two-color non-collinear HHG generation, we used a Michelson interferometer (Figure 4.16c). The fundamental field is frequency-doubled and the ω and 2ω fields are separated by a dichroic mirror. The mirror has high reflectivity at 400 nm and high transmission at 800 nm. The two fields are recombined by the same type of mirror. The delay is roughly adjusted by a manual translation stage, while a sub-cycle delay is introduced by rotation of a thin glass plate. The two beams are

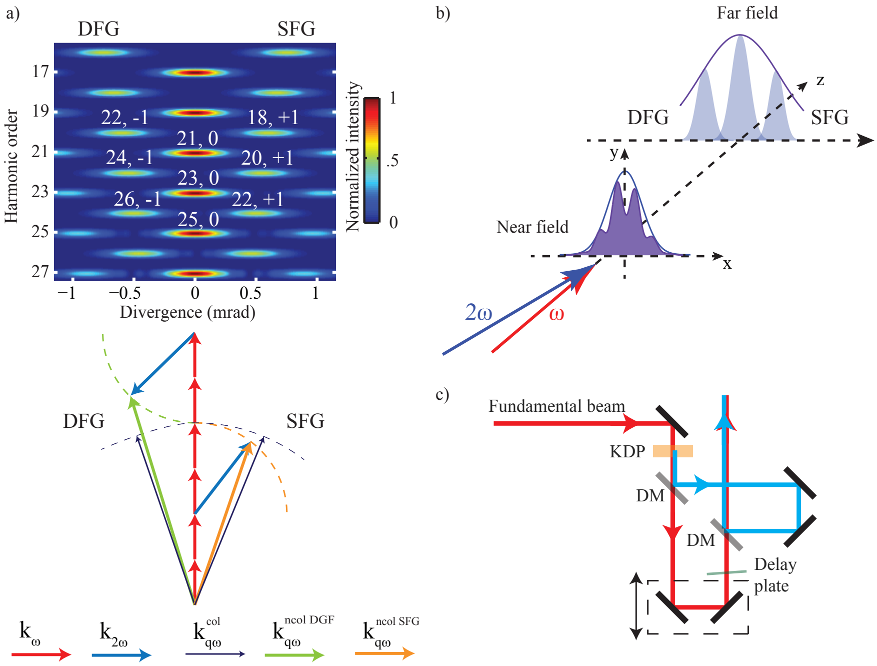

Figure 4.16: a) Harmonic spectrum as a function of divergence angle. The number above each harmonic emission corresponds to the number of absorbed photons (m_1, m_2). b) Wave picture, nonlinear response of the generation medium to the interference pattern created by the non-collinear two-color field. c) Two-color interferometer, DM - dichroic mirror (high reflectivity at 400 nm and high transmission at 800 nm).

shifted in the transverse direction and focused by a 2 m focal length mirror. They cross at the focus at a small angle.

The non-collinear generation leads to an additional phase-matching factor which can be used to optimize the collective HHG emission, as is described in *Paper* **VII**. This factor can be either positive, for sum frequency generated harmonics, or negative for difference frequency generation (Figure 4.16). The q-harmonic wave vector generated by the DFG process is longer than that generated by SFG (orange and green wave vectors in the figure). Thus, depending on the sign and magnitude of the collinear wave vector mismatch (see Section 4.2), HHG can be phase-matched on the SFG or DFG side. Moreover, the non-collinear part of the wave vector mismatch can be used to probe the value of the wave vector mismatch in the collinear geometry for each harmonic (see Equation 4.6).

Interference effects arising at small non-collinear angle are also presented in *Paper* **VII**.

4.4.2 Multi-color driven HHG

The additional degree of freedom given by a combination of ω and 2ω fields allows the control of the single atom response [148] as well as the phase-matching of the generation process. In a similar manner, HHG can be controlled by other harmonic fields. The fundamental field entering a HHG medium generates all harmonics up to the cut-off, including rather intense below-threshold low-order frequencies (see Section 4.1.1). These harmonics can be used to modify the sub-cycle fundamental field, thus influencing the HHG process.

We consider the two-color field ($\omega/3\omega$), since the 3ω field should have the largest impact on the generation, because it has the highest field amplitude among all the generated harmonics. The total field can be written as

$$E = E_0 \sin(\omega t) + rE_0 \sin(3\omega t + \Delta\phi), \tag{4.19}$$

where $\Delta\phi$ is the relative phase between the fundamental and third harmonic fields, and r is the amplitude ratio.

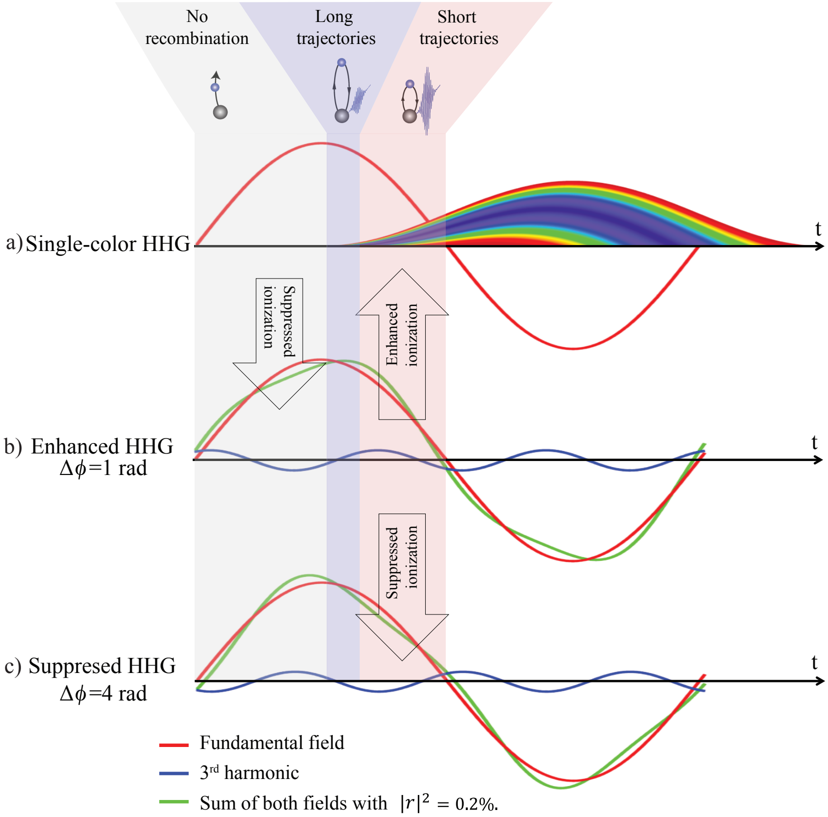

Figure 4.17: HHG with: a) a single-color field, and a two-color field ($\omega/3\omega$) with relative phase equal to b) 1 rad and c) 4 rad. The first half-cycle of the field is divided into three parts indicating times of tunneling for electrons that do not lead to HHG (no recombination) and electrons with long and short trajectories.

The addition of the third harmonic field changes the driving field strength. When the relative phase between the ω and 3ω fields is equal to 1 rad, the total field has a higher amplitude when the electrons corresponding to the short trajectories are born. The field increase at the instant of ionization leads to an enhanced tunneling probability. Moreover, ionization of electrons that do not lead to HHG (no recombination), and of electrons traveling on long trajectories, are suppressed. At a the relative phase between the ω and 3ω fields equal to 4 rad, the effect is reversed leading to suppression of the short trajectory contribution.

Proof of principle

As a proof of principle, we have performed experiments using ω and 3ω fields [144] (see Figure 4.17). The 3ω field is generated using nonlinear crystals and the ω and 3ω are combined using an interferometer.

The setup presented schematically in Figure 4.18 is a Michelson-type interferometer, where the first part of the interferometer is a two-color $\omega/2\omega$ interferometer (see Figure 4.16). In this part, half of the fundamental field is doubled and the relative delay between ω and 2ω is compensated by a manual delay stage. Furthermore the IR field polarization is rotated. The two colors overlap in a Type I KDP crystal for sum frequency generation. An addition of ω and 2ω leads to generation of a third harmonic wave with an efficiency of $\sim 1\%$. The generated wave is recombined with the second part of the fundamental field by a dichroic mirror. The mirror has high reflectivity at 267 nm and high transmission at 800 nm. The sub-cycle delay is introduced by rotation of a thin glass plate placed in the IR beam. The two beams are sent to the high-intensity HHG setup described in Section 4.3.1. The beams enter vacuum via an uncoated UV-enhanced fused silica window. The window introduces a difference in a group delay for the two colors. The delay is compensated in the interferometer. The beams are focused in a pulsed gas cell by a metallic mirror. The enhancement results are presented in Figure 4.20c (see also *Paper* **VI**).

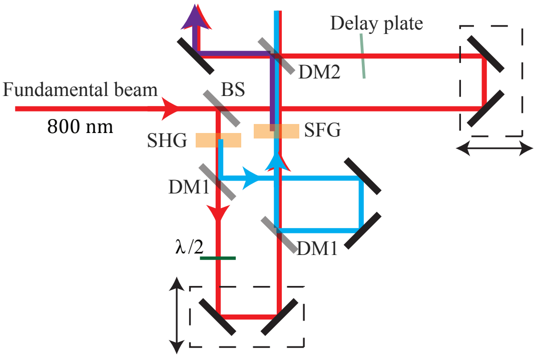

Figure 4.18: Two-color $\omega/3\omega$ interferometer; BS - 50:50 beam splitter for 800 nm, DM1 - dichroic mirror with HR@ 400 nm and HT@ 800 nm, DM2 - dichroic mirror with HR@ 267 nm and HT@ 800 nm, SHG - KDP crystal for Type I second harmonic generation, SFG - KDP crystal for Type I sum frequency generation, $\lambda/2$ - half wave plate for 800 nm.

Dual cell

A similar effect can be obtained in a much simpler setup. Low-order harmonics can be generated using a gaseous medium instead of a crystal. The medium is placed few centimeters before the HHG cell situated at the laser focus (see Figure 4.19). The relative phase between the fundamental and low-order harmonic fields is adjusted by controlling the pressure of the gas in the first cell.

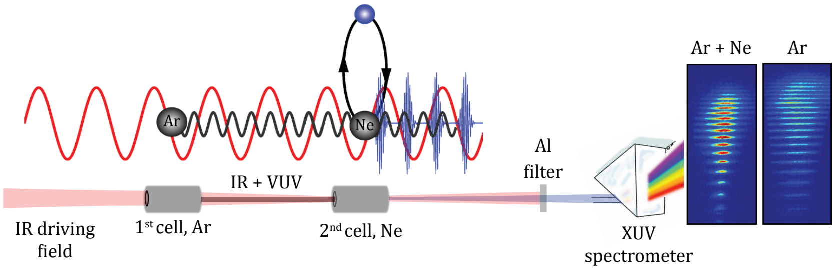

Figure 4.19: The two-cell setup.

The setup has important advantages with respect to the interferometric setup. First the full energy of the fundamental beam can be used (not half as in the case of the interferometric setup). Second, the time and space overlap between the fundamental and the low-order harmonic fields is inherently preserved. In the interferometric setup the overlap is easily affected by the environment (vibration, mechanical drift, temperature changes). Note that it has to be stable at the sub-cycle level, since very small changes in relative phase difference can lead to suppression instead of enhancement of the HHG field.

Experiments using argon gas in the first cell and neon in the second cell are presented in Figure 4.20a. The experimental results are well reproduced by a calculation using the strong field approximation for the single atom response to the two-color field combined with a simulation of the generation of low-order harmonics in the 1st cell. For comparison, results obtained with the interferometric setup are also shown.

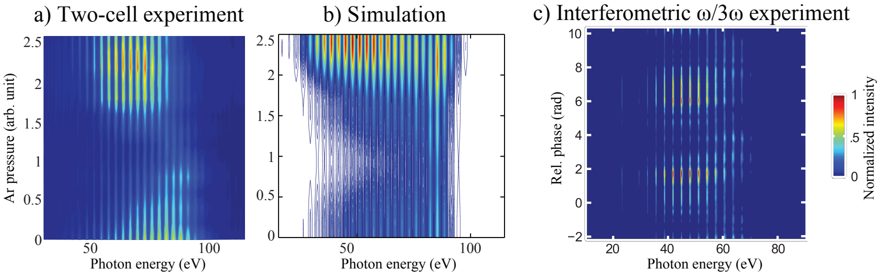

Figure 4.20: a) Enhancement results using argon gas in the first cell and neon in the second cell; b) SFA simulation; c) enhancement using an interferometric $\omega/3\omega$ setup.

The lack of high-order harmonics generated from the argon cell when neon harmonics are enhanced allows us to exclude the interpretation that the enhancement is an effect of single-photon ionization [149–152]. Also, other possible effects leading to enhancement (e.g. field reshaping) were ruled out by an experimental investigation of the fundamental field passing the first cell. Spectral measurements for varying gas pressure allow us to eliminate the field reshaping due to SPM as well as plasma de-focusing.

Chapter 5

Summary and Outlook

The thesis presents two sources of XUV radiation based on high-order harmonic generation installed at the Lund Laser Centre. The sources were constructed for experiments requiring high-flux harmonic beams (source presented in *Paper* **III**) and HHG pulses at high-repetition rate (see *Paper* **IV**). The work focuses on the construction and development of the sources and the driving laser systems as well as on the optimization of their performances (see *Papers* **I** and **II**). Moreover, a conceptual design of a high-flux gas beamline for a large scale facility, ELI-ALPS, is presented in *Paper* **V**.

The two HHG systems were applied to experiments which imaged nano-scale objects. The high-flux HHG source was used for digital in-line holography (*Paper* **VIII**), and the high-repetition rate source for photoemission electron microscopy (*Paper* **IX**). In addition, the use of multi-color driving fields to manipulate the generation process, both from the microscopic and macroscopic points of view, was investigated. The combination of the fundamental field with its second harmonic in a non-collinear geometry allowed us to probe and control macroscopic properties of HHG (see *Paper* **VII**). The addition of low-order odd harmonics in a collinear geometry resulted in an enhancement of the single atom response (*Paper* **VI**).

The thesis describes the driving lasers of the two HHG sources: the high-power 10 Hz laser system and a newly built OPCPA system. The amplification techniques used in the two lasers are described. OPCPA systems have the potential to replace Ti:Sapphire lasers as drivers for HHG sources. This is especially true at high-repetition rate, where traditional amplifiers are limited.

The two sources are constantly developed and their performances improved. The high-repetition rate system profits from the feedback of the application in electron microscopy. To optimize the source for the application, we extensively investigated the dependence of the generated XUV spectrum on CEP of the fundamental pulses. Also to assure long therm stability of the system, we built a soft-shell clean-room.

The mutual interaction between the OPCPA laser system, HHG source, and PEEM led to the first improvement of the spatial resolution of recorded images with respect to previous experiments using a 1 kHz repetition-rate HHG setup at LLC (see *Paper* **IX**).

PEEM carried out with this source (providing a relatively high number of photons) was limited in resolution due to strong space-charge effects, when a sample was placed at the focus of the XUV. Thus, the photon number per shot had to be artificially reduced by approximately a factor of 300. The large attenuation combined with the 1 kHz repetition rate resulted in a low average number of photo-emitted electrons available for detection, and hence, in a long acquisition time for a PEEM images. Therefore, the obtained resolution was at the level of 200 nm [22] (the fundamental limit of our PEEM is 20-50 nm). A PEEM image of 200 nm thick Ag nanowires taken by using this source is shown in Figure 5.1a.

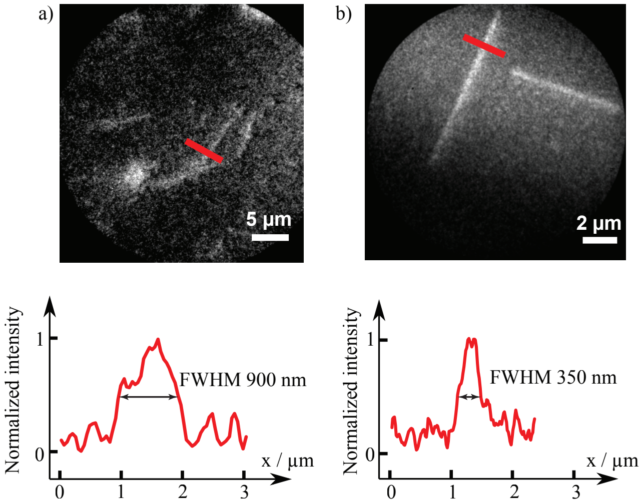

Figure 5.1: PEEM images of 200 nm thick Ag nanowires taken with: a) 1 kHz repetition rate HHG system (400 s exposure time) and b) 200 kHz OPCPA system (3 s exposure time).

The same type of nanowire was imaged by using HHG radiation obtained with the OPCPA laser (see Figure 5.1b). The exposure time was decreased by more than a factor of ten while an image quality improvement by a factor of 2-3 was observed. Future studies are necessary to confirm that using the high repetition rate HHG source we can reach the resolution limit of our electron microscope.

Furthermore, steps have been taken towards combining the high spatial resolution of the PEEM with attosecond time resolution. For this purpose an IR-pump – XUV-probe setup is under construction. The setup will be a Mach-Zehnder-type interferometer with the splitting and recombination realized by holey mirrors. First tests show that the energy provided by the OPCPA system is sufficient even if 50% of the laser power is taken from the generation arm into the probe arm. Nevertheless, an upgrade of the OPCPA system is planned, which should significantly increase the laser energy, and make pump-probe applications much easier. Furthermore, as was presented in *Paper* **I**, a beam amplified by the OPA process is exposed to parasitic nonlinear conversions and spatio-temporal distortions, which might lead to a reduced HHG efficiency. Thus, a combination of spatio-temporal diagnostics together with simulations is foreseen to address the problem. It is also planned to increase the pressure in the gas jet in order to achieve phase-matching.

The high-power HHG source has been recently rebuilt to facilitate very loose focusing geometry. Now, a focusing geometry of 9 m is used, which according to the scaling described in this thesis allows the exploitation of a higher laser pulse energy. First experimental measurements give a HHG pulse energy in Ar above the 11^{th} harmonic of approximately 2 μJ. Simultaneously, the setup is prepared for high-intensity applications. For this purpose a refocusing system based on a Wolter-type assembly of two toroidal mirrors has been installed. The setup is able to focus the XUV radiation to a spot size of 3 μm. Using the above values, an intensity of 4×10^{14} W/cm^2 per harmonic pulse could be reached, assuming 20 fs duration, and 30% transmission through Al filters. Further increase of the energy could be achieved by enhancement of the single atom response following a two-cell generation principle, as discussed in *Paper* **VI**.

COMMENTS ON THE PAPERS

I **Temporal and spatial effects inside a compact and CEP-stabilized, few cycle dual-stage OPCPA system at high repetition rates**
We describe an OPCPA system and study the parametric process in terms of temporal and spatial pulse shapes. I worked on the construction of the OPA part of the system and f-to-2f interferometer during my secondment at Venteon in the spring 2012 (three months) as well as after the system was installed in Lund. I contributed to the manuscript by feedback and discussions.

II **Compression of TW class laser pulses in a planar hollow waveguide for applications in strong-field physics**
We present a post-compression scheme for high-energy CPA laser systems. The compression allowed us to obtain <15 fs pulses with energy up to 40 mJ with our TW scale system. The post-compressed pulses were used for HHG. I took part in the optimization of the laser system, in the pulse post-compression, and HHG experiments.

III **A high-flux high-order harmonic source**
We present a source of high-flux high-order harmonics generated in gases. Moreover, we theoretically examine the macroscopic conditions for absorption-limited conversion efficiency and optimization of the HHG source output energy for high-energy laser systems. I took a major role in the optimization of the driving laser system, construction of the HHG setup, acquisition of data, and their analyses. I wrote the manuscript.

IV **Carrier-envelope phase dependent high-order harmonic generation with a high-repetition rate OPCPA-system**
We present a high-repetition rate high-order harmonic source driven by the Lund OPCPA laser system. HHG is studied as a function of the driving pulse CEP. I led the experimental activity, analyzed the data, and partly drafted the manuscript.

V **Conceptual Design Report for a gas HHG beamline at ELI-ALPS**
We present a conceptual design for a gas beamline at the Extreme Light Infrastructure (ELI) - Attosecond Light Pulse Source (ALPS) facility. I was responsible for proposing a gating technique for single attosecond pulse generation at two phases of the facility development. I wrote the corresponding part of the report.

VI **Efficient high-order harmonic generation boosted by below-threshold harmonics**
We demonstrate an enhancement method for the high-order harmonic process. I took a major role in the experimental part of the work: design of an interferometric setup, data acquisition, and analysis of the data from both two-cell and interferometric experiments. I performed classical simulations, which led to the interpretation of the enhancement process. I participated in writing the manuscript.

VII **Macroscopic Phase Effects in Noncollinear High-order Harmonic Generation**
We study high-order harmonic generation in a two-color non-collinear geometry. The technique allows the measurement and control of macroscopic phase-matching effects. I took part in the preparation of the experimental setup and data acquisition. I contributed to the writing of the paper through feedback and discussions.

VIII **Digital in-line holography on amplitude and phase objects prepared with electron beam lithography**
We demonstrate a method to produce samples with arbitrary phase and amplitude properties, and to measure of these properties in digital in-line holography. I worked on the optimization of the HHG source parameters, especially preparing the driving laser system for the experiment. I have contributed to the writing of the paper through feedback.

IX **Imaging localized surface plasmons by femtosecond to attosecond time-resolved Photoelectron Emission Microscopy - "ATTO-PEEM"**
In this book chapter experiments towards imaging of localized surface plasmons with attosecond temporal resolution are reviewed. I took part in the work by providing the OPCPA and HHG beams to the experiment, including the refocused HHG beam into the PEEM experiment. I contributed to the writing of the manuscript through feedback.

ACKNOWLEDGEMENTS

Contributions from many different people, in many different ways, have made this work possible.

First, I would like to express my gratitude to my supervisor Anne L'Huillier for providing me with the opportunity to join the group in Lund. Thank you for your confidence and trust in me. I had great freedom to plan and execute my ideas for research. Your constant motivation, support, and encouragement throughout my graduate studies have always kept me going forwards. I can only say a proper thanks to you through my future work.

Merci beaucoup!

I am also deeply grateful to my co-supervisor Anders Person for help, cooperation and support during my work with the laser systems. I always ended up with confidence, and full of energy, after discussions with you.

Tack så mycket!

I would like to offer my special thanks to my co-supervisor Cord Arnold. Your hard work and attitude to research is very motivating to me. Thank you for all your help. I am also grateful to Thomas Fordell for his co-supervision and support at the beginning of my studies.

Vielen Dank!, Paljon kiitoksia!

I would like to thank all my supervisors for reading drafts of this thesis and providing many valuable comments to improve the presentation and contents of this dissertation.

Probably, I would not be a Ph.D. student in Lund if not for Rafał Rakowski. Thanks to him I was able to visit Lund in 2009, and meet the group and my future supervisors. When I started my Ph.D. project, I worked together with Rafał, Christoph Heyl, Jörg Schwenke and later Fernando Brizuela on the high-intensity beamline. This work reassured me that physics is nothing else but fun. The friendly atmosphere and enjoyable time spent in the lab, especially with Christoph and Fernando, has led to many interesting good-spirited discussions, and to great results.

Further development of the laboratory is to the credit of other people from the group: Linnea Rading, Bastian Manschwetus, Filippo Campi, Byunghoon Kim and Per Johnsson. I also had the pleasure to work with Amélie Jarnac and Aurélien

Houard from Laboratoire d'Optique Appliquée (LOA) on the high-power system post-compression.

When the OPCPA system came to Lund a new chapter of work started with another excellent team: Anne Hart, Eleonora Lorek, Miguel Miranda (I would like to offer my special thanks to the three of you for spending your precious time to help me, especially during the last week of writing the thesis), Chen Guo, Anders Mikkelsen and Erik Mårsell. I am grateful for all the support I have received from you.

It would not have been possible to write this thesis without the help and support of the kind people around me: Samuel Bengtsson, Stefanos Carlström (all my knowledge of Swedish history is from him), Mathieu Gisselbrecht, Diego Guénot, David Kroon, Jana Preclíková, Esben Witting Larsen, Maité Louisy, Johan Mauritsson, Jenny Karlsson, Andreas Walther, Diana Serrano, Lovisa Senje, Martin Hansson. And those who are not in Lund anymore: Kathrin Klünder, Aaron von Conta, Marcus Dahlström, Mahmood Sabooni. You all have a great spirit and knowledge, which is the key to great results.

The burden of these Ph.D. studies was lessened substantially by the support and humor of my roommates: Erik Mansten, Marija Kotur and Filippo Campi. Thanks for being awesome!

The Atomic Physic Division would not be such a pleasant place to work in if not the Head of the Division Claes-Göran Wahlström and the technical and administrative staff: Minna Ramkull, Camilla Nilsson, Hariett Lindahl, Anne Petersson Jungbeck, Bertil Hermansson, and Åke Johansson (Hi-Fi specialist).

During my studies I had the opportunity to visit Venteon in Hanover and work with Thomas Binhammer, Jan Matyschok, Oliver Prochnow, and Stefan Rausch, whom I would like to thank for their patience when I had thousands of questions about OPCPA. The visit turned into a great time spent with them and also with people from Uwe Morgner's group: Moritz Emons, Heiko Kurz, Tino Lang, Martin Kretschmar, and many others ...

My research was partly supported by the Marie Curie program ATTOFEL (ITN). In the network I came to know very devoted students from all around the world, working in the best laboratories in Europe. In particular: Faruk Krecinic, Aura Ines Gonzales, Emeric Balogh, Nan Lin, Fabian Lücking, Antoine Moulet, Dimitrios Rompotis and Tran Trung Luu, and my ATTOFEL network supervisor Pierre-Mary Paul from Amplitude Technology.

Thank you very much!

Dziękuję również mojej Rodzinie oraz Przyjaciołom (w szczególności Michałowi Petryszakowi), którzy w różny sposób wspierali mnie przez cały ten czas.

Nothing would be possible without my beloved wife Agnieszka. She has supported me for every single second of the four years of this Ph.D. project, and for long before that.

Bardzo Dziękuję!

References

1. A. McPherson, G. Gibson, H. Jara, U. Johann, T. S. Luk, I. A. McIntyre, K. Boyer and C. K. Rhodes. *Studies of multiphoton production of vacuum-ultraviolet radiation in the rare gases.* J. Opt. Soc. Am. B **4**, 595 (1987).

2. M. Ferray, A. L'Huillier, X. F. Li, G. Mainfray and C. Manus. *Multiple-harmonic conversion of 1064 nm radiation in rare gases.* J. Phys. B **21**, L31 (1988).

3. F. Krausz and M. Ivanov. *Attosecond physics.* Reviews of Modern Physics **81**, 163–234 (2009).

4. E. Goulielmakis, Z. Loh, A. Wirth, R. Santra, N. Rohringer, V. S Yakovlev, S. Zherebtsov, T. Pfeifer, A. M. Azzeer, M. F. Kling, S. R. Leone and F. Krausz. *Real-time observation of valence electron motion.* Nature **466**, 739–743 (2010).

5. M. Schultze, M. Fieß, N. Karpowicz, J. Gagnon, M. Korbman, M. Hofstetter, S. Neppl, A. L. Cavalieri, Y. Komninos, Th. Mercouris, C. A. Nicolaides, R. Pazourek, S. Nagele, J. Feist, J. Burgdörfer, A. M. Azzeer, R. Ernstorfer, R. Kienberger, U. Kleineberg, E. Goulielmakis, F. Krausz and V. S. Yakovlev. *Delay in Photoemission.* Science **328**, 1658–1662 (2010).

6. K. Klünder, J. M. Dahlström, M. Gisselbrecht, T. Fordell, M. Swoboda, D. Guénot, P. Johnsson, J. Caillat, J. Mauritsson, A. Maquet, R. Taïeb and A. L'Huillier. *Probing Single-Photon Ionization on the Attosecond Time Scale.* Phys. Rev. Lett. **106**, 143002 (2011).

7. Richard L. Sandberg, Changyong Song, Przemyslaw W. Wachulak, Daisy A. Raymondson, Ariel Paul, Bagrat Amirbekian, Edwin Lee, Anne E. Sakdinawat, Chan La-O-Vorakiat, Mario C. Marconi, Carmen S. Menoni, Margaret M. Murnane, Jorge J. Rocca, Henry C. Kapteyn and Jianwei Miao. *High numerical aperture tabletop soft x-ray diffraction microscopy with 70-nm resolution.* Proceedings of the National Academy of Sciences **105**, 24–27 (2008).

8. G. Lambert, T. Hara, D. Garzella, T. Tanikawa, M. Labat, B. Carre, H. Kitamura, T. Shintake, M. Bougeard, S. Inoue, Y. Tanaka, P. Salieres, H. Merdji, O. Chubar, O. Gobert, K. Tahara and M.-E. Couprie. *Injection of harmonics generated in gas in a free-electron laser providing intense and coherent extreme-ultraviolet light.* Nat Phys **4**, 296–300 (2008).

9. E. P. Benis, D. Charalambidis, T. N. Kitsopoulos, G. D. Tsakiris and P. Tzallas. *Two-photon double ionization of rare gases by a superposition of harmonics.* Phys. Rev. A **74**, 051402 (2006).

10. Kenichi Ishikawa and Katsumi Midorikawa. *Two-photon ionization of* He^+ *as a nonlinear optical effect in the soft-x-ray region.* Phys. Rev. A **65**, 043405 (2002).

11. Kun Zhao, Qi Zhang, Michael Chini, Yi Wu, Xiaowei Wang and Zenghu Chang. *Tailoring a 67 attosecond pulse through advantageous phase-mismatch.* Opt. Lett. **37**, 3891–3893 (2012).

12. E. Goulielmakis, M. Schultze, M. Hofstetter, V. S. Yakovlev, J. Gagnon, M. Uiberacker, A. L. Aquila, E. M. Gullikson, D. T. Attwood, R. Kienberger, F. Krausz and U. Kleineberg. *Single-Cycle Nonlinear Optics.* Science **320**, 1614 (2008).

13. R. A. Bartels, A. Paul, H. Green, H. C. Kapteyn, M. M. Murnane, S. Backus, I. P. Christov, Y. Liu, D. Attwood and C. Jacobsen. *Generation of Spatially Coherent Light at Extreme Ultraviolet Wavelengths.* Science **297**, 376 (2002).

14. Yusuke Tamaki, Jiro Itatani, Minoru Obara and Katsumi Midorikawa. *Highly Coherent Soft X-Ray Generation by Macroscopic Phase Matching of High-Order Harmonics.* Japanese Journal of Applied Physics **40**, L1154–L1156 (2001).

15. Z. Chang, A. Rundquist, H. Wang, M. M. Murnane and H. C. Kapteyn. *Generation of Coherent Soft X Rays at 2.7 nm Using High Harmonics.* Phys. Rev. Lett. **79**, 2967 (1997).

16. Ch. Spielmann, N. H. Burnett, S. Sartania, R. Koppitsch, M. Schnürer, C. Kan, M. Lenzner, P. Wobrauschek and F. Krausz. *Generation of Coherent X-rays in the Water Window Using 5-Femtosecond Laser Pulses.* Science **278**, 661 (1997).

17. M. Schnürer, Z. Cheng, M. Hentschel, F.Krausz, T.Wilhein, D.Hambach, G. Schmahl, M. Drescher, Y. Lim and U. Heinzmann. *Few-cycle-driven XUV laser harmonics: generation and focusing.* Appl. Phys. B **70**, S227 (2000).

18. A. Paul, R. A. Bartels, R. Tobey, H. Green, S. Weiman, I. P. Christov, M. M. Murnane, H. C. Kapteyn and S. Backus. *Quasi-phase-matched generation of coherent extreme-ultraviolet light.* Nature **421**, 51 (2003).

19. E. Seres, J. Seres, F. Krausz and C. Spielmann. *Generation of Coherent Soft-X-Ray Radiation Extending Far Beyond the Titanium L Edge.* Phys. Rev. Lett. **92**, 163002 (2004).

20. E. J. Takahashi, P. Lan, O. D. Mücke, Y. Nabekawa and Katsumi Midorikawa. *Attosecond nonlinear optics using gigawatt-scale isolated attosecond pulses.* Nature Communications **4** (2013).

21. Erik P. Månsson, Diego Guénot, Cord L. Arnold, David Kroon, Susan Kasper, J. Marcus Dahlström, Eva Lindroth, Anatoli S. Kheifets, Anne L'Huillier, Stacey L. Sorensen and Mathieu Gisselbrecht. *Double ionization probed on the attosecond timescale.* Nat Phys **10** (2014).

22. A. Mikkelsen, J. Schwenke, T. Fordell, G. Luo, K. Klünder, E. Hilner, N. Anttu, A. A. Zakharov, E. Lundgren, J. Mauritsson, J. N. Andersen, H. Q. Xu and A. L'Huillier. *Photoemission electron microscopy using extreme ultraviolet attosecond pulse trains.* Revew of Scientific Instruments **80**, 123703 (2009).

23. Erik Mårsell, Cord L. Arnold, Eleonora Lorek, Diego Guenot, Thomas Fordell, Miguel Miranda, Johan Mauritsson, Hongxing Xu, Anne L'Huillier and Anders Mikkelsen. *Secondary electron imaging of nanostructures using Extreme Ultra-Violet attosecond pulse trains and Infra-Red femtosecond pulses.* Annalen der Physik **525**, 162–170 (2013).

24. Manuel Krebs, Steffen Hädrich, Stefan Demmler, Jan Rothhardt, Amelle Zaïr, Luke Chipperfield, Jens Limpert and Andreas Tünnermann. *Towards isolated attosecond pulses at megahertz repetition rates.* Nature Photonics **7**, 555–559 (2013).

25. Marcel Schultze, Thomas Binhammer, Andy Steinmann, Guido Palmer, Moritz Emons and Uwe Morgner. *Few-cycle OPCPA system at 143 kHz with more than 1 μJ of pulse energy.* Opt. Express **18**, 2836–2841 (2010).

26. Marcel Schultze, Thomas Binhammer, Guido Palmer, Moritz Emons, Tino Lang and Uwe Morgner. *Multi-μJ, CEP-stabilized, two-cycle pulses from an OPCPA system with up to 500 kHz repetition rate.* Opt. Express **18**, 27291–27297 (2010).

27. F. Tavella, A. Willner, J. Rothhardt, S. Hädrich, E. Seise, S. Düsterer, T. Tschentscher, H. Schlarb, J. Feldhaus, J. Limpert, A. Tünnermann and J. Rossbach. *Fiber-amplifier pumped high average power few-cycle pulse non-collinearOPCPA.* Opt. Express **18**, 4689–4694 (2010).

28. Anne Harth, Marcel Schultze, Tino Lang, Thomas Binhammer, Stefan Rausch and Uwe Morgner. *Two-color pumped OPCPA system emitting spectra spanning 1.5 octaves from VIS to NIR.* Opt. Express **20**, 3076–3081 (2012).

29. Henry N. Chapman, Anton Barty, Michael J. Bogan, Sébastien Boutet, Matthias Frank, Stefan P. Hau-Riege, Stefano Marchesini, Bruce W. Woods, Saa Bajt, W. Henry Benner, Richard A. London, Elke Plönjes, Marion Kuhlmann, Rolf Treusch, Stefan Düsterer, Thomas Tschentscher, Jochen R. Schneider, Eberhard Spiller, Thomas Möller, Christoph Bostedt, Matthias Hoener, David A. Shapiro, Keith O. Hodgson, David van der Spoel, Florian Burmeister, Magnus Bergh, Carl Caleman, Gösta Huldt, M. Marvin Seibert, Filipe R. N. C. Maia, Richard W. Lee, Abraham Szöke, Nicusor Timneanu and Janos Hajdu. *Femtosecond diffractive imaging with a soft-X-ray free-electron laser.* Nature Physics **2**, 839–843 (2006).

30. Tenio Popmintchev, Ming-Chang Chen, Dimitar Popmintchev, Paul Arpin, Susannah Brown, Skirmantas Alisauskas, Giedrius Andriukaitis, Tadas Balciunas, Oliver D. Mücke, Audrius Pugzlys, Andrius Baltuska, A.ka, Bonggu Shim, Samuel E. Schrauth, Alexander Gaeta, Carlos Hernández-Garcia, Luis Plaja, Andreas Becker, Agnieszka Jaron-Becker, Margaret M. Murnane and Henry C. Kapteyn. *Bright Coherent Ultrahigh Harmonics in the keV X-ray Regime from Mid-Infrared Femtosecond Lasers.* Science **336**, 1287–1291 (2012).

31. G. Genoud, O. Guilbaud, E. Mengotti, S.-G. Pettersson, E. Georgiadou, E. Pourtal, C.-G. Wahlström, and A. L'Huillier. *XUV digital in-line holography using high-order harmonics.* Appl. Phys. B **90**, 533–538 (2008).

32. J. Schwenke, A. Mai, M. Miranda, X. He, G. Genoud, A. Mikkelsen, S.-G. Pettersson, A. Persson and A. L'Huillier. *Single-shot holography using high-order harmonics.* Journal of Modern Optics **55**, 2723–2730 (2008).

33. S. H. Chew, F. Süssmann, C. Späth, A. Wirth, J. Schmidt, S. Zherebtsov, A. Guggenmos, A. Oelsner, N. Weber, J. Kapaldo, A. Gliserin, M. I. Stockman, M. F. Kling and U. Kleineberg. *Time-of-flight-photoelectron emission microscopy on plasmonic structures using attosecond extreme ultraviolet pulses.* Applied Physics Letters **100** (2012).

34. A. Zewail. *Femtochemistry: Atomic-Scale Dynamics of the Chemical Bond.* J. Phys. Chem. A **104**, 5660 (2000).

35. Press Release: The 1999 Nobel Prize in Chemistry (1999). [online, accessed 21 Apr 2012].

36. W Denk, JH Strickler and WW Webb. *Two-photon laser scanning fluorescence microscopy.* Science **248**, 73–76 (1990).

37. Frits Zernike and Paul R. Berman. *Generation of Far Infrared as a Difference Frequency.* Phys. Rev. Lett. **15**, 999–1001 (1965).

38. J.-C. Diels and W. Rudolph. *Ultrashort laser pulse phenomena.* Academic Press (1996).

39. B. E. A. Saleh and M. C. Teich. *Fundamentals of Photonics.* John Wiley and Sons (2007).

40. Rick Trebino. *Frequency-resolved optical gating: the measurement of ultrashort laser pulses.* Kluwer Academic Publishers (2000).

41. Selcuk Akturk, Xun Gu, Pamela Bowlan and Rick Trebino. *Spatio-temporal couplings in ultrashort laser pulses.* Journal of Optics **12**, 093001 (2010).

42. G. Pretzler, A. Kasper and K.J. Witte. *Angular chirp and tilted light pulses in CPA lasers.* Applied Physics B **70**, 1–9 (2000).

43. Z. Bor. *Distortion of Femtosecond Laser Pulses in Lenses and Lens Systems.* Journal of Modern Optics **35**, 1907–1918 (1988).

44. Z. Bor. *Distortion of femtosecond laser pulses in lenses.* Opt. Lett. **14**, 119–121 (1989).

45. L. E. Hargrove, R. L. Fork and M. A. Pollack. *Locking of HeNe laser modes induced by synchronous intracavity modulation.* Applied Physics Letters **5**, 4–5 (1964).

46. A.J. DeMaria, W.H. Glenn Jr., M.J. Brienza and M.E. Mack. *Picosecond laser pulses.* Proceedings of the IEEE **57**, 2 – 25 (1969).

47. E.P. Ippen, C.V. Shank and A. Dienes. *Passive mode locking of the cw dye laser.* Applied Physics Letters **21**, 348–350 (1972).

48. GT Advanced Technologies (2013).

49. P. F. Moulton. *Spectroscopic and laser characteristics of Ti:*Al_2O_3. J. Opt. Soc. Am. B **3**, 125–133 (1986).

50. Andrius Baltuška, Takao Fuji and Takayoshi Kobayashi. *Controlling the Carrier-Envelope Phase of Ultrashort Light Pulses with Optical Parametric Amplifiers.* Phys. Rev. Lett. **88**, 133901 (2002).

51. C. Vozzi, G. Cirmi, C. Manzoni, E. Benedetti, F. Calegari, G. Sansone, S. Stagira, O. Svelto, S. De Silvestri, M. Nisoli and G. Cerullo. *High-energy, few-optical-cycle pulses at 1.5 μm with passive carrier-envelope phase stabilization.* Opt. Express **14**, 10109–10116 (2006).

52. Claude Rulliere. *Femtosecond Laser Pulses:principles and experiments.* Springer (2003).

53. C. Iaconis and I. A. Walmsley. *Spectral phase interferometry for direct electric field reconstruction of ultrashort optical pulses.* Opt. Lett. **23**, 792 (1998).

54. H. R. Telle, G. Steinmeyer, A. E. Dunlop, J. Stenger, D. H. Sutter and U. Keller. *Carrier-envelope offset phase control: A novel concept for absolute optical frequency measurement and ultrashort pulse generation.* Appl. Phys. B **69**, 327 (1999).

55. L. Xu, Ch. Spielmann, A. Poppe, T. Brabec, F. Krausz and T. W. Hänsch. *Route to phase control of ultrashort light pulses.* Opt. Lett. **21**, 2008 (1996).

56. Takao Fuji, Jens Rauschenberger, Alexander Apolonski, Vladislav S. Yakovlev, Gabriel Tempea, Thomas Udem, Christoph Gohle, Theodor W. Hänsch, Walter Lehnert, Michael Scherer and Ferenc Krausz. *Monolithic carrier-envelope phase-stabilization scheme.* Opt. Lett. **30**, 332–334 (2005).

57. Miguel Miranda, Thomas Fordell, Cord Arnold, Anne L'Huillier and Helder Crespo. *Simultaneous compression and characterization of ultrashort laser pulses using chirped mirrors and glass wedges.* Opt. Express **20**, 688–697 (2012).

58. Miguel Miranda, Cord L. Arnold, Thomas Fordell, Francisco Silva, Benjamín Alonso, Rosa Weigand, Anne L'Huillier and Helder Crespo. *Characterization of broadband few-cycle laser pulses with the d-scan technique.* Opt. Express **20**, 18732–18743 (2012).

59. A Brun, P Georges, G Le Saux and F Salin. *Single-shot characterization of ultrashort light pulses.* Journal of Physics D: Applied Physics **24**, 1225 (1991).

60. R. W. Boyd. *Nonlinear Optics.* Academic Press (2003).

61. W. Sibbett, A. A. Lagatsky and C. T. A. Brown. *The development and application of femtosecond laser systems.* Opt. Express **20**, 6989–7001 (2012).

62. G. Cerullo, S. De Silvestri, V. Magni and L. Pallaro. *Resonators for Kerr-lens mode-locked femtosecond Ti:sapphire lasers.* Opt. Lett. **19**, 807–809 (1994).

63. Stefan Rausch, Thomas Binhammer, Anne Harth, Emilia Schulz, Martin Siegel and Uwe Morgner. *Few-cycle oscillator pulse train with constant carrier-envelope- phase and 65 as jitter.* Opt. Express **17**, 20282–20290 (2009).

64. U. Morgner, F. X. Kärtner, S. H. Cho, Y. Chen, H. A. Haus, J. G. Fujimoto, E. P. Ippen, V. Scheuer, G. Angelow and T. Tschudi. *Sub-two-cycle pulses from a Kerr-lens mode-locked Ti:sapphire laser.* Opt. Lett. **24**, 411 (1999).

65. D. H. Sutter, G. Steinmeyer, L. Gallmann, N. Matuschek, F. Morier-Genoud, U. Keller, V. Scheuer, G. Angelow and T. Tschudi. *Semiconductor saturable-absorber mirror-assisted Kerr-lens mode-locked Ti:sapphire laser producing pulses in the two-cycle regime.* Opt. Lett. **24**, 631 (1999).

66. H. M. Crespo, J. R. Birge, E. L. Falcão-Filho, M. Y. Sander, A. Benedick and F. X. Kärtner. *Nonintrusive phase stabilization of sub-two-cycle pulses from a prismless octave-spanning Ti:sapphire laser.* Opt. Lett. **33**, 833–835 (2008).

67. D. Strickland and G. Mourou. *Compression of amplified chirped optical pulses.* Opt. Commun. **56**, 219 (1985).

68. C.E. Cook. *Pulse Compression-Key to More Efficient Radar Transmission.* Proceedings of the IRE **48**, 310–316 (1960).

69. R. Szipöcs, K. Ferencz, Ch. Spielmann and F. Krausz. *Chirped multilayer coatings for broadband dispersion control in femtosecond lasers.* Opt. Lett. **19**, 201 (1994).

70. Nicolai Matuschek, Franz X. Kärtner and Ursula Keller. *Theory of Double-Chirped Mirrors.* IEEE Journal of Selected Topics in Quantum Electronics **4**, 197 (1998).

71. G. Cheriaux, P. Rousseau, F. Salin, J. P. Chambaret, Barry Walker and L. F. Dimauro. *Aberration-free stretcher design for ultrashort-pulse amplification.* Opt. Lett. **21**, 414–416 (1996).

72. E. Treacy. *Optical pulse compression with diffraction gratings.* Quantum Electronics, IEEE Journal of **5**, 454 – 458 (1969).

73. O. E. Martinez. *Grating and prism compressors in the case of finite beam size.* J. Opt. Soc. Am. B **3**, 929 (1986).

74. A. Galvanauskas, M. E. Fermann, D. Harter, K. Sugden and I. Bennion. *All-fiber femtosecond pulse amplification circuit using chirped Bragg gratings.* Applied Physics Letters **66**, 1053–1055 (1995).

75. Kai-Hsiu Liao, Ming-Yuan Cheng, Emilie Flecher, Vadim I. Smirnov, Leonid B. Glebov and Almantas Galvanauskas. *Large-aperture chirped volume Bragg grating based fiber CPA system.* Opt. Express **15**, 4876–4882 (2007).

76. S. Kane and J. Squier. *Grism-pair stretcher-compressor system for simultaneous second- and third-order dispersion compensation in chirped-pulse amplification.* Journal of the Optical Society of America B-Optical Physics **14**, 661–665 (1997).

77. Walter Koechner. *Solid-State Laser Engineering.* Springer (2006).

78. O. Svelto. *Principles of Lasers.* Plenum Press, New York (1998).

79. C. Thaury, F. Quere, J.-P. Geindre, A. Levy, T. Ceccotti, P. Monot, M. Bougeard, F. Reau, P. D'Oliveira, P. Audebert, R. Marjoribanks and P. H. Martin. *Plasma mirrors for ultrahigh-intensity optics.* Nature Physics **3**, 424–429 (2007).

80. Fabio Giambruno, Christophe Radier, Gilles Rey and Gilles Chériaux. *Design of a 10 PW (150 J/15 fs) peak power laser system with Ti:sapphire medium through spectral control.* Appl. Opt. **50**, 2617–2621 (2011).

81. L. Antonucci, J.P. Rousseau, A. Jullien, B. Mercier, V. Laude and G. Cheriaux. *14-fs high temporal quality injector for ultra-high intensity laser.* Optics Communications **282**, 1374 – 1379 (2009).

82. B. Lyot. *Optical apparatus with wide field using interference of polarized light.* C. R. Acad. Sci. Paris (1933).

83. F. Verluise, V. Laude, Z. Cheng, C. Spielmann and P. Tournois. *Amplitude and Phase Control of Ultrashort Pulses by Use of an Acousto-Optic Programmable Dispersive Filter: Pulse Compression and Shaping.* Opt. Lett. **25**, 575–577 (2000).

84. T. Fordell, M. Miranda, A. Persson and A. L'Huillier. *Carrier-envelope phase stabilization of a multi-millijoule, regenerative-amplifier-based chirped-pulse amplifier system.* Opt. Express **17**, 21091–21097 (2009).

85. Jochen Dörring, Alexander Killi, Uwe Morgner, Alexander Lang, Max Lederer and Daniel Kopf. *Period doubling and deterministic chaos in continuously pumped regenerative amplifiers.* Opt. Express **12**, 1759–1768 (2004).

86. Xiaoshi Zhang, Eric Schneider, Greg Taft, Henry Kapteyn, Margaret Murnane and Sterling Backus. *Multi-microjoule, MHz repetition rate Ti:sapphire ultrafast regenerative amplifier system.* Opt. Express **20**, 7015–7021 (2012).

87. Aurélien Dantan, Julien Laurat, Alexei Ourjoumtsev, Rosa Tualle-Brouri and Philippe Grangier. *Femtosecond Ti:sapphire cryogenic amplifier with high gain and MHzrepetition rate.* Opt. Express **15**, 8864–8870 (2007).

88. M. Nisoli, S. De Silvestri and O. Svelto. *Generation of high energy 10 fs pulses by a new pulse compression technique.* Appl. Phys. Lett. **68**, 2793 (1996).

89. C L Arnold, B Zhou, S Akturk, S Chen, A Couairon and A Mysyrowicz. *Pulse compression with planar hollow waveguides: a pathway towards relativistic intensity with table-top lasers.* New Journal of Physics **12**, 073015 (2010).

90. A. Couairon, S. Tzortzakis, L. Bergé, M. Franco, B. Prade and A. Mysyrowicz. *Infrared femtosecond light filaments in air: simulations and experiments.* J. Opt. Soc. Am. B **19**, 1117 (2002).

91. Selcuk Akturk, Cord L. Arnold, Bing Zhou and Andre Mysyrowicz. *High-energy ultrashort laser pulse compression in hollow planar waveguides.* Opt. Lett. **34**, 1462–1464 (2009).

92. S. A Akhmanov, A. I. Kovrigin, A. S. Piskarskas, V. V. Fadeev and R. V. Khokhlov. *Observation of Parametric Amplification in the Optical Range.* JETP Letters **2**, 191 (1965).

93. T. H. Maiman. *Stimulated optical radiation in Ruby.* Nature **187**, 493 (1960).

94. A. Dubietis, G. JonuÅ¡auskas and A. Piskarskas. *Powerful femtosecond pulse generation by chirped and stretched pulse parametric amplification in BBO crystal.* Optics Communications **88**, 437 – 440 (1992).

95. R. Butkus, R. Danielius, A. Dubietis, A. Piskarskas and A. Stabinis. *Progress in chirped pulse optical parametric amplifiers.* Applied Physics B **79**, 693–700 (2004).

96. Giulio Cerullo and Sandro De Silvestri. *Ultrafast optical parametric amplifiers.* Review of Scientific Instruments **74**, 1–18 (2003).

97. Giedrius Andriukaitis, Tadas Balčiūnas, Skirmantas Ališauskas, Audrius Pugžlys, Andrius Baltuška, Tenio Popmintchev, Ming-Chang Chen, Margaret M. Murnane and Henry C. Kapteyn. *90 GW peak power few-cycle mid-infrared pulses from an optical parametric amplifier.* Opt. Lett. **36**, 2755–2757 (2011).

98. A. Baltuška, T. Fuji and T. Kobayashi. *Visible pulse compression to 4 fs by optical parametric amplification and programmable dispersion control.* Opt. Lett. **27**, 306 (2002).

99. I.N. Ross, P. Matousek, M. Towrie, A.J. Langley and J.L. Collier. *The prospects for ultrashort pulse duration and ultrahigh intensity using optical parametric chirped pulse amplifiers.* Opt. Commun. **144**, 125 (1997).

100. L. J. Waxer, V. Bagnoud, I. A. Begishev, M. J. Guardalben, J. Puth and J. D. Zuegel. *High-conversion-efficiency optical parametric chirped-pulse amplification system using spatiotemporally shaped pump pulses.* Opt. Lett. **28**, 1245–1247 (2003).

101. D. A. Kleinman. *Theory of Optical Parametric Noise.* Phys. Rev. **3**, 1027–1041 (1968).

102. F Tavella, A Marcinkevicius and F Krausz. *Investigation of the superfluorescence and signal amplification in an ultrabroadband multiterawatt optical parametric chirped pulse amplifier system.* New Journal of Physics **8**, 219 (2006).

103. J. A. Giordmaine and Robert C. Miller. *Tunable Coherent Parametric Oscillation in LiNbO3 at Optical Frequencies.* Phys. Rev. Lett. **14**, 973–976 (1965).

104. Franz Tavella. *Multiterawatt few-cycle pulse OPCPA for applications in high-field physics.* PhD thesis Fakultat fur Physik der Ludwig - Maximilians - Universitat Munchen (2007).

105. A. Shirakawa, I. Sakane, M. Takasaka and T. Kobayashi. *Sub-5-fs visible pulse generation by pulse-front-matched noncollinear optical parametric amplification.* Applied Physics Letters **74**, 2268–2270 (1999).

106. Akira Shirakawa, Isao Sakane and Takayoshi Kobayashi. *Pulse-front-matched optical parametric amplification for sub-10-fs pulse generation tunable in the visible and near infrared.* Opt. Lett. **23**, 1292–1294 (1998).

107. Howe-Siang Tan, Elmar Schreiber and Warren S. Warren. *High-resolution indirect pulse shaping by parametric transfer.* Opt. Lett. **27**, 439–441 (2002).

108. T. Lang, A. Harth, J. Matyschok, T. Binhammer, M. Schultze and U. Morgner. *Impact of temporal, spatial and cascaded effects on the pulse formation in ultra-broadband parametric amplifiers.* Opt. Express **21**, 949–959 (2013).

109. P. M. Paul, E. S. Toma, P. Breger, G. Mullot, F. Augé, Ph. Balcou, H. G. Muller and P. Agostini. *Observation of a train of attosecond pulses from high harmonic generation.* Science **292**, 1689 (2001).

110. T. Brabec and F. Krausz. *Intense few-cycle laser fields: Frontiers of nonlinear optics.* Rev. Mod. Phys. **72**, 545 (2000).

111. Eiji J. Takahashi, Yasuo Nabekawa and Katsumi Midorikawa. *Low-divergence coherent soft x-ray source at 13 nm by high-order harmonics.* Appl. Phys. Lett. **84**, 4–6 (2004).

112. David M. Gaudiosi, Brendan Reagan, Tenio Popmintchev, Michael Grisham, Mark Berrill, Oren Cohen, Barry C. Walker, Margaret M. Murnane, Henry C. Kapteyn and Jorge J. Rocca. *High-Order Harmonic Generation from Ions in a Capillary Discharge.* Phys. Rev. Lett. **96**, 203001 (2006).

113. Eiji Takahashi, Yasuo Nabekawa, Tatsuya Otsuka, Minoru Obara and Katsumi Midorikawa. *Generation of highly coherent submicrojoule soft x rays by high-order harmonics.* Phys. Rev. A **66**, 021802– (2002).

114. E. Takahashi, Y. Nabekawa and K. Midorikawa. *Generation of 10-μJ coherent extreme-ultraviolet light by use of high-order harmonics.* Opt. Lett. **27**, 1920 (2002).

115. P. B. Corkum. *Plasma perspective on strong-field multiphoton ionization.* Phys. Rev. Lett. **71**, 1994 (1993).

116. K. J. Schafer, B. Yang, L. F. DiMauro and K. C. Kulander. *Above threshold ionization beyond the high harmonic cutoff.* Phys. Rev. Lett. **70**, 1599 (1993).

117. J. L. Krause, K. J. Schafer and K. C. Kulander. *High-order harmonic generation from atoms and ions in the high intensity regime.* Phys. Rev. Lett. **68**, 3535 (1992).

118. Henry Kapteyn, Oren Cohen, Ivan Christov and Margaret Murnane. *Harnessing Attosecond Science in the Quest for Coherent X-rays.* Science **317**, 775–778 (2007).

119. Tenio Popmintchev, Ming-Chang Chen, Oren Cohen, Michael E. Grisham, Jorge J. Rocca, Margaret M. Murnane and Henry C. Kapteyn. *Extended phase matching of high harmonics driven by mid-infrared light.* OPTICS LETTERS **33**, 2128–2130 (2008).

120. M. Lewenstein, P. Salières and A. L'Huillier. *Phase of the atomic polarization in high-order harmonic generation.* Phys. Rev. A **52**, 4747 (1995).

121. C. Lyngå, M. B. Gaarde, C. Delfin, M. Bellini, A. L'Huillier T. W. Hänsch and C.-G. Wahlström. *Studies of the temporal coherence of high-order harmonics.* Phys. Rev. A **60**, 4823 (1999).

122. M. Lewenstein, Ph. Balcou, M.Yu. Ivanov, A. L'Huillier and P. B. Corkum. *Theory of high-order harmonic generation by low-frequency laser fields.* Phys. Rev. A **49**, 2117 (1994).

123. G. Farkas and C. Tóth. *Proposal for attosecond light pulse generation using laser induced multiple-harmonic conversion processes in rare gases.* Phys. Lett. A **168**, 447 (1992).

124. S. E. Harris, J. J. Macklin and T. W. Hänsch. *Atomic scale temporal structure inherent to high-order harmonic generation.* Opt. Commun. **100**, 487 (1993).

125. Ph. Antoine, A. L'Huillier and M. Lewenstein. *Attosecond Pulse Trains Using High-Order Harmonics.* Phys. Rev. Lett. **77**, 1234 (1996).

126. J. Itatani, F. Quéré, G. L. Yudin, M. Yu. Ivanov, F. Krausz and P. B. Corkum. *Attosecond Streak Camera.* Phys. Rev. Lett. **88**, 173903 (2002).

127. E. Mansten, J. M. Dahlström, J. Mauritsson, T. Ruchon, A. L'Huillier, J. Tate, M. B. Gaarde, P. Eckle, A. Guandalini, M. Holler, F. Schapper, L. Gallmann and U. Keller. *Spectral Signature of Short Attosecond Pulse Trains.* Phys. Rev. Lett. **102**, 083002 (2009).

128. M. Kovacev, Y. Mariesse, E. Priori, H. Merdji, O. Tcherbakoff, P. Monchieourt, P. Breger, E. Mevel, E. Constant, P. Salieres, B. Carre and P. Agostini. *Temporal confinement of harmonic emission by polarization gating.* Eur. Phys. J. D **26**, 79 (2003).

129. Erik Mansten. *Measurement and control of attosecond ligh fields.* PhD thesis Lund University (2009).

130. A. L'Huillier, X. F. Li and L. A. Lompré. *Propagation effects in high-order harmonic generation in rare gases.* JOSA B **7**, 527–536 (1990).

131. S. Kazamias, S. Daboussi, O. Guilbaud, K. Cassou, D. Ros, B. Cros and G. Maynard. *Pressure-induced phase matching in high-order harmonic generation.* Phys. Rev. A **83** (2011).

132. S. Kazamias, D. Douillet, F.Weihe, C. Valentin, A. Rousse, S. Sebban, G. Grillon, F. Augé, D. Hulin and Ph. Balcou. *Global Optimization of High Harmonic Generation.* Phys. Rev. Lett. **90**, 193901 (2003).

133. M. Gaarde, F. Salin, E. Constant, Ph. Balcou, K. J. Schafer, K. C. Kulander and A. L'Huillier. *Spatiotemporal separation of high harmonic radiation into two quantum path components.* Phys. Rev. A **59**, 1367 (1999).

134. K. Varjú, Y. Mairesse, B. Carre, M. B. Gaarde, P. Johnsson, S. Kazamias, R. Lopez-Martens, J. Mauritsson, K. J. Schafer, Ph. Balcou, A. L'Huillier and P. Salières. *Frequency chirp of harmonic and attosecond pulses.* J. Mod. Opt. **52**, 379 (2005).

135. Xinkui He, M. Miranda, J. Schwenke, O. Guilbaud, T. Ruchon, C. Heyl, E. Georgadiou, R. Rakowski, A. Persson, M. B. Gaarde and A. L'Huillier. *Spatial and spectral properties of the high-order harmonic emission in argon for seeding applications.* Phys. Rev. A **79**, 063829 (2009).

136. P. Salières, A. L'Huillier and M. Lewenstein. *Coherence control of high-order harmonics.* Phys. Rev. Lett. **74**, 3776 (1995).

137. F. Ferrari, F. Calegari, M. Lucchini, C. Vozzi, S. Stagira and G. Sansoneand M. Nisoli. *High-energy isolated attosecond pulses generated by above-saturation few-cycle fields.* Nature Photonics **4**, 875–879 (2010).

138. C M Heyl, J Güdde, A L'Huillier and U Höfer. *High-order harmonic generation with μJ laser pulses at high repetition rates.* Journal of Physics B: Atomic, Molecular and Optical Physics **45**, 074020 (2012).

139. B.L. Henke, E.M. Gullikson and J.C. Davis. *X-Ray Interactions: Photoabsorption, Scattering, Transmission, and Reflection at E = 50-30,000 eV, Z = 1-92.* Atomic Data and Nuclear Data Tables **54**, 181 – 342 (1993).

140. E. Constant, D. Garzella, P. Breger, E. Mével, Ch. Dorrer, C. Le Blanc, F. Salin and P. Agostini. *Optimizing High Harmonic Generation in Absorbing Gases: Model and Experiment.* Phys. Rev. Lett. **82**, 1668 (1999).

141. J.-F. Hergott, M. Kovacev, H. Merdji, C. Hubert, Y. Mairesse, E. Jean, P. Breger, P. Agostini, B. Carré and P. Salières. *Extreme-ultraviolet high-order harmonic pulses in the microjoule range.* Phys. Rev. A **66**, 021801 (2002).

142. Erik Gustafsson and Thierry Ruchon. *Design of a kHz pulsed gas valve.* Lund Reports on Atomic Physics **366** (2006).

143. Attotech HB (2009).

144. S. Watanabe, K. Kondo, Y. Nabekawa, A. Sagisaka and Y. Kobayashi. *Two-Color Phase Control in Tunneling Ionization and Harmonic Generation by a Strong Laser Field and Its Third Harmonic.* Phys. Rev. Lett. **73**, 2692 (1994).

145. J. Mauritsson, P. Johnsson, E. Gustafsson, A. L'Huillier, K. J. Schafer and M. B. Gaarde. *Attosecond Pulse Trains Generated Using Two Color Laser Fields.* Phys. Rev. Lett. **97**, 013001 (2006).

146. H. Mashiko, S. Gilbertson, C. Li, S. D. Khan, M. M. Shakya, E. Moon and Z. Chang. *Double optical gating of high-order harmonic generation with carrier-envelope phase stabilized lasers.* Phys. Rev. Lett. **100**, 103906 (2008).

147. J. B. Bertrand, H. J. Wörner, H.-C. Bandulet, E. Bisson, M. Spanner, J.-C. Kieffer, D. M. Villeneuve and P. B. Corkum. *Ultrahigh-Order Wave Mixing in Noncollinear High Harmonic Generation.* Physical Review Letters **106** (2011).

148. Dror Shafir, Hadas Soifer, Barry D. Bruner, Michal Dagan, Yann Mairesse, Serguei Patchkovskii, Misha Yu. Ivanov, Olga Smirnova and Nirit Dudovich. *Resolving the time when an electron exits a tunnelling barrier.* Nature pages 343–346 (2012).

149. Kenichi L. Ishikawa. *Efficient photoemission and ionization of* He^{+} *by a combined fundamental laser and high-order harmonic pulse.* Phys. Rev. A **70**, 013412 (2004).

150. K. J. Schafer, M. B. Gaarde, A. Heinrich, J. Biegert and U. Keller. *Strong Field Quantum Path Control Using Attosecond Pulse Trains.* Phys. Rev. Lett. **92**, 23003 (2004).

151. A Heinrich, W Kornelis, M P Anscombe, C P Hauri, P Schlup, J Biegert and U Keller. *Enhanced VUV-assisted high harmonic generation.* Journal of Physics B: Atomic, Molecular and Optical Physics **39**, S275 (2006).

152. Eiji J. Takahashi, Tsuneto Kanai, Kenichi L. Ishikawa, Yasuo Nabekawa and Katsumi Midorikawa. *Dramatic Enhancement of High-Order Harmonic Generation.* Physical Review Letters **99**, 053904 (2007).

PAPERS

PAPER I

Temporal and spatial effects inside a compact and CEP-stabilized, few cycle dual-stage OPCPA system at high repetition rates

J. Matyschok, T. Lang, T. Binhammer, O. Prochnow, S. Rausch, M. Schultze, A. Harth, P. Rudawski, C. L. Arnold, A. L'Huillier and U. Morgner.

Opt. Express **21**, 29656–29665 (2013).

Temporal and spatial effects inside a compact and CEP stabilized, few-cycle OPCPA system at high repetition rates

**Jan Matyschok,[1,2,*] Tino Lang,[1,3] Thomas Binhammer,[2] Oliver Prochnow,[2]
Stefan Rausch,[2] Marcel Schultze,[1] Anne Harth,[1,3] Piotr Rudawski,[4]
Cord L. Arnold,[4] Anne L'Huillier,[4] and Uwe Morgner[1,3,5]**

[1]*Institute of Quantum Optics, Leibniz Universität Hannover, Welfengarten 1, D-30167 Hannover, Germany*
[2]*VENTEON Laser Technologies GmbH, Hertzstraße 1b, D-30827 Garbsen, Germany*
[3]*Centre for Quantum Engineering and Space-Time Research (QUEST), Welfengarten 1, D-30167 Hannover, Germany*
[4]*Department of Physics, Lund University, P.O. Box 118, SE-221 00 Lund, Sweden*
[5]*Laser Zentrum Hannover (LZH), Hollerithallee 8, D-30419 Hannover, Germany*
[*]*matyschok@iqo.uni-hannover.de*

Abstract: We present a compact and ultra-stable few-cycle OPCPA system. In two non-collinear parametric amplification stages pulse energies up to 17 µJ at 200 kHz repetition rate are obtained. Recompression of the broadband pulses down to 6.3 fs is performed with chirped mirrors leading to peak powers above 800 MW. The parametric amplification processes were studied in detail employing (2 + 1) dimensional numerical simulations and compared to experimental observations in terms of spectral shapes, pulse energy, spatial effects as well as delay dependent nonlinear mixing products. This gives new insights into the parametric process and design guidelines for high repetition rate OPCPA systems.

OCIS codes: (190.0190) Nonlinear optics; (190.4410) Nonlinear optics, parametric processes; (190.4970) Parametric oscillators and amplifiers; (320.7090) Ultrafast lasers.

References and links

1. A. Dubietis, R. Butkus, and A. P. Piskarskas, "Trends in chirped pulse optical parametric amplification," IEEE J. Sel. Top. Quantum Electron. **12**(2), 163–172 (2006), http://ieeexplore.ieee.org/stamp/stamp.jsp?tp=&arnumber=1632161&isnumber=34227.
2. G. Cerullo, A. Baltuška, O. D. Mücke, and C. Vozzi, "Few-optical-cycle light pulses with passive carrier-envelope phase stabilization," Laser Photon. Rev. **5**(3), 323–351 (2011), doi:10.1002/lpor.201000013.
3. D. Herrmann, L. Veisz, R. Tautz, F. Tavella, K. Schmid, V. Pervak, and F. Krausz, "Generation of sub-three-cycle, 16 TW light pulses by using noncollinear optical parametric chirped-pulse amplification," Opt. Lett. **34**(16), 2459–2461 (2009), doi:10.1364/OL.34.002459.
4. S. Adachi, N. Ishii, T. Kanai, A. Kosuge, J. Itatani, Y. Kobayashi, D. Yoshitomi, K. Torizuka, and S. Watanabe, "5-fs, multi-mJ, CEP-locked parametric chirped-pulse amplifier pumped by a 450-nm source at 1 kHz," Opt. Express **16**(19), 14341–14352 (2008), doi:10.1364/OE.16.014341.
5. D. Brida, C. Manzoni, G. Cirmi, M. Marangoni, S. Bonora, P. Villoresi, S. De Silvestri, and G. Cerullo, "Few-optical-cycle pulses tunable from the visible to the mid-infrared by optical parametric amplifiers," J. Opt. **12**(1), 013001 (2010), doi:10.1088/2040-8978/12/1/013001.
6. A. Thai, M. Hemmer, P. K. Bates, O. Chalus, and J. Biegert, "Sub-250-mrad, passively carrier-envelope-phase-stable mid-infrared OPCPA source at high repetition rate," Opt. Lett. **36**(19), 3918–3920 (2011), doi:10.1364/OL.36.003918.
7. A. Shirakawa, I. Sakane, M. Takasaka, and T. Kobayashi, "Sub-5-fs visible pulse generation by pulse-front-matched noncollinear optical parametric amplification," Appl. Phys. Lett. **74**(16), 2268 (1999), doi:10.1063/1.123820.
8. A. Harth, M. Schultze, T. Lang, T. Binhammer, S. Rausch, and U. Morgner, "Two-color pumped OPCPA system emitting spectra spanning 1.5 octaves from VIS to NIR," Opt. Express **20**(3), 3076–3081 (2012), doi:10.1364/OE.20.003076.
9. S. Huang, G. Cirmi, J. Moses, K. Hong, S. Bhardwaj, J. R. Birge, L. Chen, E. Li, B. Eggleton, G. Cerullo, and F. X. Kärtner, "High-energy pulse synthesis with sub-cycle waveform control for strong-field physics," Nat. Photonics **5**(8), 475–479 (2011), doi:10.1038/nphoton.2011.140.

#198267 - $15.00 USD Received 24 Sep 2013; revised 17 Oct 2013; accepted 25 Oct 2013; published 22 Nov 2013
(C) 2013 OSA 2 December 2013 | Vol. 21, No. 24 | DOI:10.1364/OE.21.029656 | OPTICS EXPRESS 29656

10. G. G. Paulus, F. Grasbon, H. Walther, P. Villoresi, M. Nisoli, S. Stagira, E. Priori, and S. De Silvestri, “Absolute-Phase phenomena in photoionization with few-cycle laser pulses,” Nature **414**(6860), 182–184 (2001).
11. A. Baltuška, M. Uiberacker, E. Goulielmakis, R. Kienberger, V. S. Yakovlev, T. Udem, T. W. Hänsch, and F. Krausz, “Phase-Controlled Amplification of Few-Cycle Laser Pulses,” IEEE J. Sel. Top. Quantum Electron. **9**(4), 972–989 (2003).
12. A. Mikkelsen, J. Schwenke, T. Fordell, G. Luo, K. Klünder, E. Hilner, N. Anttu, A. A. Zakharov, E. Lundgren, J. Mauritsson, J. N. Andersen, H. Q. Xu, and A. L’Huillier, “Photoemission electron microscopy using extreme ultraviolet attosecond pulse trains,” Rev. Sci. Instrum. **80**(12), 123703 (2009), doi:10.1063/1.3263759.
13. A. Thai, M. Baudisch, M. Hemmer, and J. Biegert, “20 µJ, few-cycle pulses at 3.1 µm and 160 kHz repetition rate from mid-IR OPCPA,” in Conference on Lasers and Electro-Optics 2012, OSA Technical Digest (online) (Optical Society of America, 2012), paper CM1B.2.
14. M. Schultze, T. Binhammer, G. Palmer, M. Emons, T. Lang, and U. Morgner, “Multi-µJ, CEP-stabilized, two-cycle pulses from an OPCPA system with up to 500 kHz repetition rate,” Opt. Express **18**(26), 27291–27297 (2010), doi:10.1364/OE.18.027291.
15. J. Rothhardt, S. Demmler, S. Hädrich, J. Limpert, and A. Tünnermann, “Octave-spanning OPCPA system delivering CEP-stable few-cycle pulses and 22 W of average power at 1 MHz repetition rate,” Opt. Express **20**(10), 10870–10878 (2012), doi:10.1364/OE.20.010870.
16. J. Rothhardt, S. Demmler, S. Hädrich, T. Peschel, J. Limpert, and A. Tünnermann, “Thermal effects in high average power optical parametric amplifiers,” Opt. Lett. **38**(5), 763–765 (2013), doi:10.1364/OL.38.000763.
17. M. Krebs, S. Hädrich, S. Demmler, J. Rothhardt, A. Zaïr, L. Chipperfield, J. Limpert, and A. Tünnermann, “Towards isolated attosecond pulses at megahertz repetition rates,” Nat. Photonics **7**(7), 555–559 (2013), doi:10.1038/nphoton.2013.131.
18. A. Vernaleken, J. Weitenberg, T. Sartorius, P. Russbueldt, W. Schneider, S. L. Stebbings, M. F. Kling, P. Hommelhoff, H. D. Hoffmann, R. Poprawe, F. Krausz, T. W. Hänsch, and T. Udem, “Single-pass high-harmonic generation at 20.8 MHz repetition rate,” Opt. Lett. **36**(17), 3428–3430 (2011), doi:10.1364/OL.36.003428.
19. C.-T. Chiang, A. Blattermann, M. Huth, J. Kirschner, and W. Widdra, “High-order harmonic generation at 4 MHz as a light source for time-of-flight photoemission spectroscopy,” Appl. Phys. Lett. **101**(7), 071116 (2012), doi:10.1063/1.4746264.
20. T. Lang, A. Harth, J. Matyschok, T. Binhammer, M. Schultze, and U. Morgner, “Impact of temporal, spatial and cascaded effects on the pulse formation in ultra-broadband parametric amplifiers,” Opt. Express **21**(1), 949–959 (2013), doi:10.1364/OE.21.000949.
21. S. Hädrich, J. Rothhardt, M. Krebs, S. Demmler, J. Limpert, and A. Tünnermann, “Improving carrier-envelope phase stability in optical parametric chirped-pulse amplifiers by control of timing jitter,” Opt. Lett. **37**(23), 4910–4912 (2012), doi:10.1364/OL.37.004910.

1. Introduction

In recent years the number of scientific applications requiring intense few-cycle laser pulses with a stable Carrier Envelope Phase (CEP) has rapidly grown. During the last ten years Ti:sapphire-based amplifier systems with subsequent pulse compression stages have been the workhorses especially in the field of High Harmonic Generation (HHG) and attosecond physics. Meanwhile this technique has reached limitations with little potential for further scaling in average power or repetition rate. A lot of effort is presently devoted to the development of the alternative approach of parametric amplifier systems [1, 2]. Optical Parametric Chirped Pulse Amplification (OPCPA) systems are able to directly provide a broad amplification bandwidth and are scalable in terms of output power and repetition rate. Direct amplification of few-cycle laser pulses into the mJ-regime [3, 4] has been shown in a variety of wavelength regimes from the visible to the mid-infrared [5–7]. Combining several Optical Parametric Amplifier (OPA) stages, even the single cycle limit comes within reach and pulse durations well below 5 fs have been demonstrated [8, 9]. The CEP of few-cycle pulses is an important parameter for applications such as photoionization [10] or HHG [11], and furthermore many experimental applications (e.g. photoemission electron microscopy [12]) will benefit from a higher repetition rate due to shorter integration times, higher photon flux, and increased statistics. In the range from 100 kHz up to 1 MHz some multi-µJ systems have been reported [13, 14], emitting up to 22 W of average power with elaborate laboratory set-ups [15]. Although in principle thermal effects are negligible in OPA based systems, absorption of the infrared idler or multi-photon absorption can lead to limitations of average power [16]. CEP-stable few-cycle OPCPA systems operated above 100 kHz have recently been used successfully for HHG into the cutoff regions [17] showing the potential of this technology. Even lower energies in the µJ range have been shown to be sufficient for HHG with few-cycle pulses [18, 19]. As experiments for XUV and attosecond spectroscopy are getting more and more complex, there is a strong need for reliable, long-term stable, and user-friendly light sources.

In this paper we present a compact OPCPA system at 200 kHz repetition rate which is able to deliver CEP-stable few-cycle pulses with high peak power. The setup is designed for maximum compactness, low complexity, and low noise in order to bring the OPCPA technology to the next step towards compact and reliable light sources, ideally suited for many types of nonlinear light-matter interaction experiments. The easy and robust setup provides excellent noise performance and CEP stability with pulse durations as shot as 6.3 fs. A CEP stabilized octave-spanning seed oscillator provides the ultra-broadband signal and the narrowband seed for the Yb-based pump amplifier without further nonlinear spectral shifting. After two subsequent Non-collinear Optical Parametric Amplifier (NOPA) stages up to 17 µJ of pulse energy is demonstrated. The NOPA design in the case of high pulse repetition rates with moderate pump energies requires tight focal spot sizes and comparably large crystal lengths for efficient parametric amplification. Therefore, the influence of spatial as well as walk-off effects has to be taken carefully into account. To investigate various experimentally observed spatial phenomena occurring along with the NOPA in the chosen Poynting-Vector-Walk-off Compensation (PVWC) geometry we used our (2 + 1) dimensional propagation simulation code [20]. Temporal, spatial, and cascaded effects were investigated and compared to the experimental results. Additionally the influence of the temporal delay between signal and pump pulse in the OPA to the spatially observed nonlinear mixing products are examined. These features might be useful for future novel stabilization schemes (see e.g [21].). The remarkable agreement between simulation and experimental results increases the confidence in the (2 + 1) dimensional approximation which can provide vital support for designing future OPCPA systems.

2. Experimental setup

An overview of the experimental setup of the OPCPA system is given in Fig. 1. It consists of a CEP stabilized broadband Ti:sapphire oscillator, and an ytterbium doped fiber preamplifier seeding two separate rod-type fiber amplifiers which are operated in parallel. After pulse compression and Second Harmonic Generation (SHG), they individually pump the two parametric amplifier stages which are followed by a chirped mirror compressor and an f-to-2f interferometer. The whole system fits on a compact footprint (150 x 210 cm) and is boxed for low amplitude and CEP noise. The Ti:sapphire oscillator (VENTEON | PULSE: ONE OPCPA SEED) delivers an octave spanning spectrum from 600 nm – 1200 nm with an average output power of 240 mW at 80 MHz. The outer edges of this spectrum are filtered and sent into a self-referencing f-to-2f interferometer for CEP stabilization. The feedback to the oscillator is implemented by pump power modulation via an acousto-optic modulator, whereas slow drifts are corrected by moving the intra-cavity wedge pair by a motorized stage. This way, a low rms phase noise of 80 mrad (3 Hz – 1 MHz) and a long-term locking for more than 12 hours can be achieved. After filtering for CEP locking, more than 90% of the output power is still available. A dichroic filter extracts the long wavelength part, centered at 1030 nm, from the oscillator spectrum to seed the fiber amplifier. Due to the large fundamental bandwidth, no external spectral shifting in e.g. nonlinear fibers is required to reach the fiber amplification band with sufficient seed energy of more than 40 pJ, which greatly enhances the noise performance and long-term stability of the amplifier seed. In addition, no coupling or soliton effects are affecting the timing jitter between pump and signal pulses of the OPCPA, which is especially important when using pump pulses below 1 ps. The main spectral region from 650 nm – 1020 nm, which still supports sub-6 fs pulses, with 2.5 nJ of pulse energy is used as signal radiation for the subsequent NOPA stages.

#198267 - $15.00 USD Received 24 Sep 2013; revised 17 Oct 2013; accepted 25 Oct 2013; published 22 Nov 2013

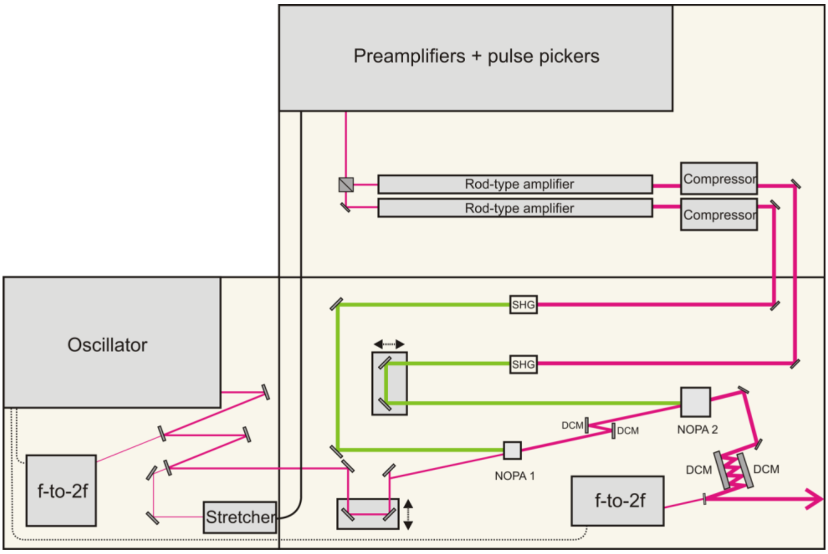

Fig. 1. Experimental setup of the OPCPA system: SHG: Second Harmonic Generation; NOPA: Non-collinear Optical Parametric Amplifier; DCM: Double Chirped Mirrors; f-to-2f: interferometer for the carrier envelope phase measurement.

Before coupling into the three-stage fiber preamplifier which includes two pulse pickers, the infrared light centered at 1030 nm is spectrally filtered and temporally stretched by a Chirped Volume Bragg Grating (CVBG, 27 ps/nm, 16 nm FWHM) with an efficiency of 75%. The advantages of this approach are the monolithic and thereby drift-free design and the small footprint of the stretcher arrangement, which can be implemented within the oscillator housing. After preamplification to about 300 mW at 200 kHz repetition, the output of the preamplifier is divided into two beam lines for seeding two independent 80 cm long rod-type fibers (NKT, DC 285/100 PM-Yb-ROD) for power amplification. The advantages of this parallel approach are the reduced pulse energy and average power in each main amplification stage compared to a one-stage amplifier, and the possibility to optimize the pump pulse energies and pulse durations for the NOPA stages independently. The fiber main amplifiers deliver an average power of 20 W for the first and 23 W for the second amplification stage before compression. Nevertheless, the stretched pump pulse duration obtained from the CVBG limits the pulse energy in the fiber amplifier due to nonlinear effects. While in the present implementation the focus was on compactness and reduced complexity of the stretcher unit, further energy scaling could therefore be realized in the future by implementing a different stretching concept, e.g. with a much less compact and stable grating sequences. Pulse compression is optimized to maximum parametric yield and performed by a second CVBG matched to the stretcher with an efficiency of 57% (first stage) and by a GRISM with 67% efficiency (second stage). The GRISM was used instead of a designated third CVBG due to the higher efficiency together with the better pulse and beam quality. After frequency doubling, pump energies of 27 µJ are available for the first stage and 44 µJ for the second stage, with pulse durations of around 500 fs as derived from the measured intensity autocorrelations of the compressed infrared pulses.

Parametric amplification of the seed pulses takes place in two BBO crystals whereby broadband phase matching is achieved by non-collinear interaction of pump and signal beam in the crystals. For the first parametric amplification stage, the temporal overlap of signal and pump pulses are controlled by a translation stage, while the pulse duration of the broadband Ti:sapphire signal is adapted to the pump pulse duration. Subsequently, the chirp of the signal

#198267 - $15.00 USD Received 24 Sep 2013; revised 17 Oct 2013; accepted 25 Oct 2013; published 22 Nov 2013

pulse is reduced with chirped mirrors to optimize the pulse duration for optimum temporal overlap in the second BBO crystal. After both NOPA stages, a chirped mirror compressor with more than 80% efficiency is used to compress the pulses down to the final pulse duration.

3. Experimental results

In the first NOPA the pump beam is focused down to a $1/e^2$-beam radius of 175 µm and temporally and spatially overlapped with the signal which exhibits a slightly smaller radius of 110 µm. The angle between signal and pump corresponds to 2.4° to achieve the most broadband phase matching. For the given pump energy, the PVWC geometry was chosen with a crystal length of 5 mm. Amplification from 1.25 nJ (at 80 MHz) up to 4.5 µJ (at 200 kHz) was achieved. Due to the temporal stretching of the broadband signal in glass, air and BBO, the pulse duration after the first stage is stretched to 420 fs (measured with SPIDER). The positive chirp of the seed is slightly reduced using two bounces on a chirped mirror pair (VENTEON, 600-1200 nm, -120 fs^2 / pair at 800 nm).

The second NOPA is operated with the same crystal parameters with approximately 270 fs input pulse duration and 3.4 µJ pulse energy of the signal. The input beam is focused down to 170 µm radius. For the pump, with energy of 44 µJ, a slightly larger spot size of 270 µm was chosen to keep the intensity on the BBO crystal below 100 GW/cm^2 to avoid crystal damages. Here, amplification up to 17 µJ is achieved, corresponding to an optical-to-optical power conversion efficiency of 31% from pump to signal. The spectral bandwidth after the second NOPA spans more than 450 nm (at -10 dBc) (see Fig. 2(a)) and supports a pulse duration of 4.9 fs. Due to short pump pulses and corresponding moderate stretching, pulse compression with a chirped mirror compressor is possible. The simple, compact, and drift-free compressor uses 12 reflections in double-pass configuration and shows an overall throughput above 80%. The mirror dispersion is designed for compensation of the BBO crystal, air, and fused silica. The pulse duration after compression is measured as 6.3 fs (see Fig. 2(b)) using a commercial SPIDER system (VENTEON | PULSE: FOUR SPIDER).

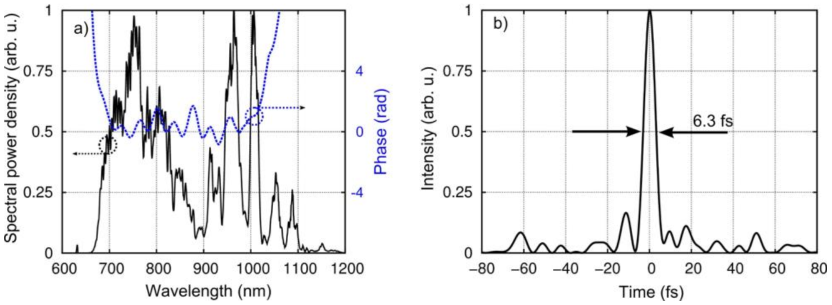

Fig. 2. a) Measured spectrum from the compressed pulse after the second NOPA stage (black) together with the spectral phase (dotted blue) from the SPIDER measurement. b) Reconstructed pulse from the SPIDER measurement.

After pulse compression, a small fraction of the beam (approx. 300 nJ) is separated and sent to an f-to-2f interferometer. The interference pattern (see Fig. 3(a); approx. 4000 spectra from an USB-spectrometer, Avantes AVASPEC-2048-USB2) allows to determine directly the CEP. With a slow feedback loop for thermal drift compensation, an excellent stability of 68 mrad over 15 min could be reached (see Fig. 3(b)), showing the high intrinsic stability of the compact system.

The low noise of the fiber-based amplifier in combination with a low timing jitter between signal and pump pulses result in high stability of the average output power which is measured to be below 0.5% over 100 min after a certain warm up time. CEP and power stability measurements are performed without any active delay stabilization. This intrinsic stability

#198267 - $15.00 USD Received 24 Sep 2013; revised 17 Oct 2013; accepted 25 Oct 2013; published 22 Nov 2013

was obtained by the optical synchronization between signal and pump pulse, the single pass pump amplification, the completely boxed and compact setup in combination with water cooling at several points of the system to enhance the thermal stability.

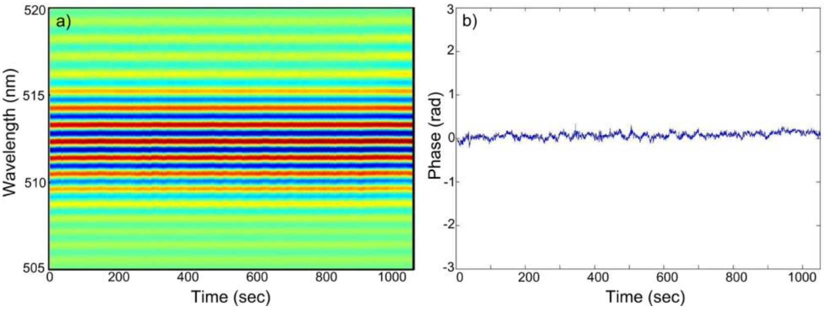

Fig. 3. a) Interference pattern measured with the f-to-2f interferometer after the second parametric amplification stage and the chirped mirror compressor controlled with the second feedback loop. The spectra were recorded with 3 ms integration time and an average over 10 spectra respectively. b) Phase of the fringe pattern given in Fig. 3(a) corresponding to an rms noise < 70 mrad.

The combination of µJ-level energy with high repetition rate and few-cycle pulses with excellent CEP stability makes this system an ideal source for high-intensity applications such as ionization or HHG.

4. Numerical simulations and spatial effects

For a better understanding of the temporal and spatial effects during the parametric amplification, we performed extensive numerical modeling of the amplification process including two spatial as well as the time dimension. This simulation is based on solving the linear and nonlinear propagation equations for the ordinary and extraordinary polarized waves. The spatial behavior is treated in two dimensions in order to describe the non-collinear propagation, including phase matching, as well as walk-off and focusing/diffraction effects. Further details about the numeric are given in a previous publication [20]. The parameters for the simulation of the two amplification stages, such as spot sizes, pump energies, and pulse durations are taken from the experiment. The seeding signal field for the first NOPA was taken from the measured spectral amplitude and phase from the Ti:sapphire oscillator. The phase matching angle Θ can be precisely chosen to reproduce the experimental situation e.g. via the spectral position of the distinctive dip caused by the parasitic SHG. The non-collinear angle α between signal and pump as well as the delay between both pulses are adapted in the simulation to reproduce the experimentally observed spectrum.

A comparison between the experimental results and the results from the simulation are shown in Fig. 4(a). For angles $\Theta = 24.35°$ and $\alpha = 2.43°$, the spectral structures as well as the spectral bandwidth match very well the experimental results. For a quantitative extraction of pulse energies from the calculations, radial symmetry of the beam is assumed, and the signal beam radius is taken to be the measured one. For 27 µJ of pump energy, an amplification from 1.25 nJ to 4.4 µJ is calculated which is very close to the 4.1 µJ obtained in the experiment. The energy slopes from simulation and experiment are compared in Fig. 4(b). Again the simulation is capable to predict the output of the OPCPA stage with high accuracy.

The results from the first NOPA together with the dispersion of the chirped mirrors in between both stages are used as input with the measured beam sizes for modeling the second amplification stage. For the second stage $\Theta = 24.2°$ and $\alpha = 2.36°$ lead to the best match between experimental and simulated spectra with optimized temporal delay (see Fig. 4(a)). The simulation is able to reproduce the spectral shape and bandwidth of the signal. Also for

#198267 - $15.00 USD Received 24 Sep 2013; revised 17 Oct 2013; accepted 25 Oct 2013; published 22 Nov 2013

the second amplification stage, the signal vs. pump energy slope is comparable to the measurement (see Fig. 4(b)).

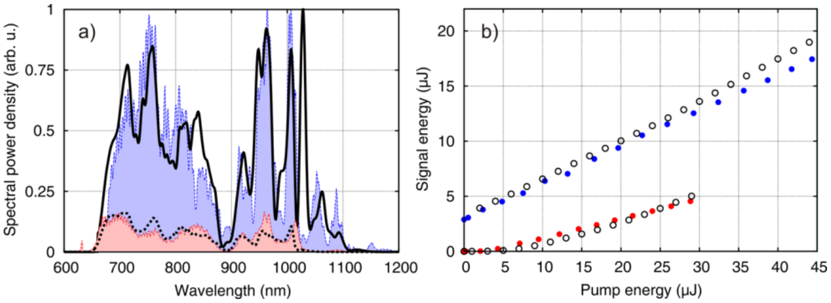

Fig. 4. a) Measured spectra obtained from the first (shadowed red) and second (shadowed blue) NOPA stage together with the calculated spectra from the numerical simulation of the first (dashed line) and second (black line) NOPA. b) Measured (red first NOPA, blue second NOPA) and calculated (black circles) pulse energy after each amplification stage for different pump energies.

The agreement between the simulation and experiment prove the correctness of the algorithm and allows for predicting the performance of the OPCPA in different situations. This is especially helpful in finding optimum beam waists for signal and pump or comparing both Tangential Phase Matching (TPM) and PVWC geometry with respect to efficiency, beam profile, and compressibility. The numerical model indicates that with 27 µJ of pump energy a crystal length of 5 mm is required to reach a conversion efficiency of > 10%. For such crystal lengths the PVWC geometry is preferable due to better compressibility around 650 nm. Furthermore, in TPM there is a strong angular deviation from the collimated signal beam in this spectral region which leads to a distorted beam profile of the signal. This spatial distortion makes the TPM geometry less favorable for the chosen crystal length and given pump energies.

Since the model predicts the angular distributions of signal and idler beams as well as of all other phase matched mixing products, we are able – for the first time to our knowledge – to perform a direct comparison between experiment and simulations of the non-collinear parametric process including spatial angle distribution and delay dependence including all mixing products. This provides unprecedented insight into the different processes. In Fig. 5, the simulated angle and frequency distribution of the first parametric amplification stage in the chosen PWVC geometry is shown. For experimental access, a screen with a hole for the intense pump beam is placed behind the first parametric amplification stage, and the angular distribution for several delays is recorded with a digital camera (Nikon D300, see inset Fig. 5 and Fig. 6(c)). The angle axes of these pictures are rescaled to the propagation angles inside the nonlinear crystal by compensating for the BBO surface refraction.

The transversal spatial dimension of the model is indicated as the central line (CL) of the photograph (see inset Fig. 5 marked with white dots). The other dimension of the image belongs to the third spatial dimension which is not included in the simulation. Identification of the observed features in Fig. 5 can be easily done in the model by turning on and off the different nonlinear effects and the separate consideration of the ordinary (o) and extraordinary (e) polarization within the simulation. The feature (A, e) around alpha = 0° is attributed to the intensive pump at 515 nm (0.58 PHz) not visible on the photo due to the hole in the screen. At $\alpha = 2.5°$ the broadband amplified signal spanning from 0.27 PHz to 0.46 PHz (B, o) with the likewise phase matched parasitic SHG to 0.68 PHz (C, e) is visible in the simulated data corresponding to a bright white signal spot in the photograph from the experiment. Due to energy and momentum conservation the corresponding idler is generated in the infrared between 0.12 PHz and 0.33 PHz and spatially dispersed between $\alpha = –2.5°$ to –10° (D, o). This idler wave is broadband phase matched for a SHG process, which leads to the bright green to red feature in the visible wavelength region between −2.5° and −5° (E, e). The predicted colors and angles from the simulation fit well with the observations from the experiment.

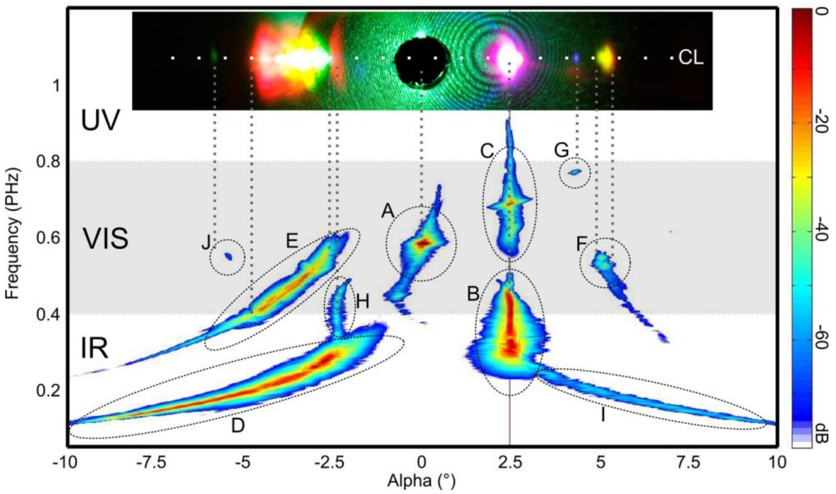

Fig. 5. Results of the numerical model with the parameters from the first parametric amplification stage. For comparison the visible wavelength range are shaded. The picture shows the 515 nm pump (feature A) at alpha = 0°, the broadband seed (between 0.27 - 0.46 PHz, B) with the parasitic SHG at 0.7 PHz (C). Also visible is the spectral dispersive idler wave in the infrared (IR) region (D) at negative angles with frequency doubling to the visible (VIS) region (E) together with further mixing products in the visible (F, G, J). The inset shows a photograph taken from a screen behind the first BBO crystal with a hole for the pump light.

Apart from these well-known beams also a few other mixing products show up in good agreement with experimental observations; now, their origin can be identified: **i**) The visible feature at α = 5.1° (F, o) is explained by a simultaneously phase matched DFG process where the parasitic SHG (C) around 0.68 PHz of the signal (B) at α = 2.5° serves as pump radiation and the infrared idler (D) around −6.8° as seeded idler. The extension from feature (F) to larger angles and lower frequencies is following the corresponding phase matching curve. **ii**) A phase matched SFG process of the part of feature (F) around 5.4° and 0.48 PHz with the infrared part of the signal (B) around 0.29 PHz and 2.5° leads to the small blue spot (G, e) visible at 4.3°. **iii**) The red feature (H, o) located next to the SHG of the idler at α = −2.5° can be explained as super-fluorescence and occurs in the simulation only by adding white noise resulting in a signal following the phase matching curve with the corresponding infrared idler (I, o) at positive angles between 2.5° and 10°. **iv**) No clear explanation has been found for the tiny green spot (J, e) around −5.4° which occurs in both experiment and simulation with a slight angular offset. The offset can be attributed to the re-scaling of the photograph (see Fig. 5 inset and Fig. 6(c)) to match the internal angles, where the difference between ordinary and extraordinary refractive index was neglected. Furthermore the change of the refractive index for the different propagation angles in the extraordinary polarization was neglected in the conversion from the spatial frequencies used in the simulation to the propagation angles in Fig. 5 and Fig. 6(a).

In Fig. 6 the temporal delay between signal and pump was changed between −500 and + 600 fs in steps of 67 fs, and for each delay the angular intensity distribution was determined by integration over the visible spectral region (shaded area in Fig. 5). The results are shown in Fig. 6(a) and compared to a series of photographs as in Fig. 5. The zero position of the delay axis is chosen to match the simulation. In the simulation, zero delay means signal and pump pulse ideally overlapping in time at the beginning of the crystal. Positive delay means that the signal is ahead of the pump pulse. Due to the different dispersion properties of ordinary and extraordinary propagation, a delay of around + 200 fs leads to the optimum amplification. By integration over the three color channels from the central line of each photograph shown in Fig. 6(c), a more quantitative representation of the angular distribution can be extracted (see Fig. 6(b)). Due to saturation/nonlinear response of the photo camera sensor, no robust statements concerning relative intensities can be extracted, but still the overall agreement is quite remarkable; several mixing products only appear around the optimal delay where signal and idler are most broadband and intense. At large negative delays, the super-fluorescence signal at α = –2.5° is most prominent and almost vanishes at the ideal delay. The green spot at α = –6° also shows a strong delay dependence, and is only present in a range of + 100 fs up to + 600 fs.

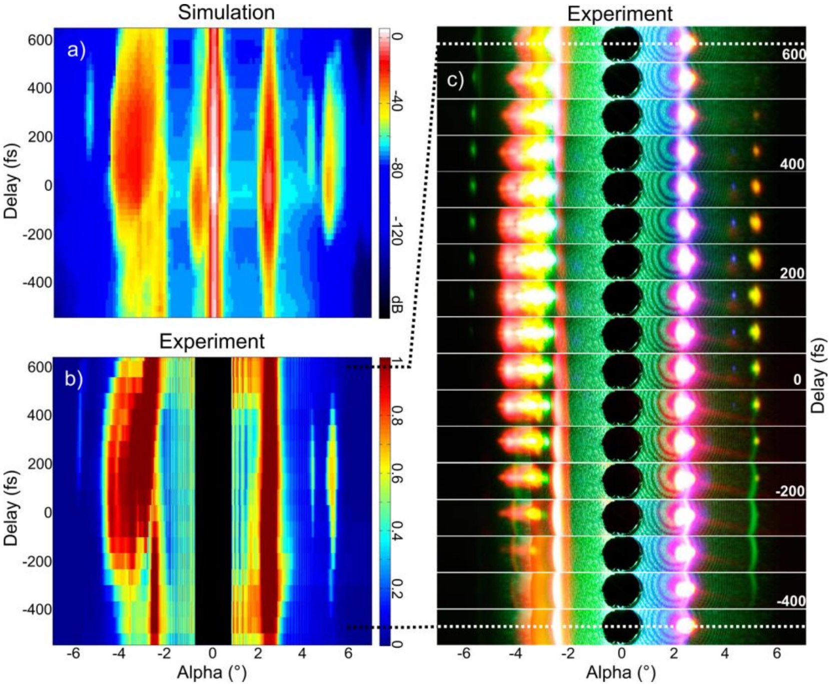

Fig. 6. a) Integration over the spatial power distribution of the visible wavelength range given from the results of the numerical simulation of the first amplification stage as a function of the relative delay between signal and pump. b) Shows the evaluation of the photographs from the experiment (given in 6c) taken from the experiment after the first parametric amplification stage with delay variation in steps of 67 fs between signal and pump.

The spatially and temporally resolved analysis presented here can be easily extended to the TPM geometry. There, it has been shown in [21], that some mixing products can be successfully used for stabilization of the relative delay or the CEP of the amplifier output. For the PVWC geometry, so far no nonlinear mixing product usable for CEP stabilization has been identified. Delay stabilization can be most easily done by detecting the spectral wings of the second harmonic of the idler which show an opposite dependence on delay for the high and low frequency edges (see Fig. 6(b)). Figure 6 reveals even more delay dependent signals, but their usability for stabilization has to be further investigated.

5. Conclusion

In this work an OPCPA system with high repetition rate and few-cycle CEP-stable pulses has been presented. Energies of more than 10 µJ have been generated with high conversion efficiency. Due to the compact and robust system design, low noise below 0.5% rms for the output power and below 70 mrad for the CE phase error could be obtained. The system is thus ideally suited for applications requiring high peak power such as HHG or photoionization. Further up-scaling of the system is possible by extending the stretching of the pump pulses into the ns-regime. For the given pump energy of 27 µJ for the first and 44 µJ for the second pump stage, 5 mm long BBO crystals and relatively small focal sizes are required for high conversion efficiencies. In this case the PVWC geometry is favorable. Extensive numerical simulations with the model from [20] show a remarkable agreement with the experimental observations. Both, angular distributions as well as the energy scaling curves are well predicted. A complete comparison of the numerically calculated and experimentally observed angular distribution of all phase matched nonlinear mixing products within the parametric process has been presented. The investigation of the delay dependence of the observed signals might lead to useful delay or CEP stabilization schemes.

The agreement between experiment and simulation reveals the potential of the model to establish design criteria for future short pulse OPCPA systems. As the simulation is easily adapted to different nonlinear crystals and wavelength ranges, it allows for novel insights into phase matching conditions and the expected nonlinear mixing products while providing the best geometry and focal sizes for the respective experimental parameters. This is especially important for high repetition rate OPCPA systems with limited pump energy, smaller focal sizes, and longer crystals. The analysis emphasizes the importance of spatial effects and gives some novel insight into the colorful and rich physics involved in the nonlinear process.

Acknowledgments

This work was funded by Deutsche Forschungsgemeinschaft within the Cluster of Excellence QUEST, Centre for Quantum Engineering and Space-Time Research, within the contract Mo850/15-1, the Swedish Research Council, the Knut and Alice Wallenberg Foundation (Wallenberg Scholar), the European Research Council (Advanced Research Grant ALMA), and the Open Access Publishing Fund of the Leibniz Universität Hannover.

Paper II

Compression of TW class laser pulses in a planar hollow waveguide for applications in strong-field physics

A. Jarnac, F. Brizuela, C. M. Heyl, P. Rudawski, F. Campi, B. Kim, L. Rading, P. Johnsson, A. Mysyrowicz, A. L'Huillier, A. Houard, and C. L. Arnold.

(2014) *Manuscript in preparation.*

Compression of TW class laser pulses in a planar hollow waveguide for applications in strong-field physics

A. Jarnac,[1] F. Brizuela,[2] C. M. Heyl,[2] P. Rudawski,[2] F. Campi,[2] B. Kim,[2] L. Rading,[2]
P. Johnsson,[2] A. Mysyrowicz,[1] A. L'Huillier,[2] A. Houard,[1] and C. L. Arnold[2]

[1] *Laboratoire d'Optique Appliquée, ENSTA Paristech,*
École Polytechnique, CNRS, FR-91762 Palaiseau, France
[2] *Department of Physics, Lund University, P.O. Box 118, 22100 Lund, Sweden*

We demonstrate pulse post compression of a TW class chirped pulse amplification laser using a planar hollow waveguide scheme. A waveguide throughput of 80% was achieved for 50 mJ input pulse energy. Good focusability was found and after compression with chirped mirrors sub-15 fs pulse duration was obtained with SPIDER measurements. The viability of this post compression scheme for applications in strong-field physics is demonstrated by generating high-order harmonics in a pulsed Ar gas jet.

Few-cycle laser pulses, i.e. pulses so short that the pulse envelope encloses only a few (in the extreme just one) cycles of the carrier frequency, have become indispensable tools in optics and related sciences, such as high-order harmonic generation (HHG) [1] and attosecond science [2], strong-field physics [3], and acceleration of particles [4]. While low-energy, few-cycle pulses can today routinely be obtained from Titanium :Sapphire based ultrafast oscillators [5], the output of chirped pulse amplification (CPA) femtosecond lasers hardly reaches below 20 fs (FWHM) pulse duration, mostly due to gain-bandwidth-narrowing. Typical Titanium-Sapphire based CPA lasers, found in research laboratories today, have pulse duration in the range of 25-100 fs and pulse energies in the mJ to hundreds of mJ range. Thus, there is a strong need for pulse post compression.

The two most prominent schemes for pulse compression to the few-cycle regime are based on strong spectral broadening due to nonlinear propagation in either a noble gas filled hollow capillary [6] or in a self-guided filament [7] and subsequent compression with chirped mirrors. Few-cycle pulses from a hollow capillary compressor allowed for the first time the generation of single-attosecond pulses in the XUV spectral region via HHG [8]. Due to ionization inside the capillary and nonlinear coupling to higher order capillary modes with stronger attenuation the output pulse energy of a hollow capillary compressor rarely exceeds 1 mJ. Attempts to increase the energy output of hollow capillary compressors require advanced optical engineering [9], or advanced capillary engineering [10], and often exhibit low efficiency [11].

Pulse compression employing self-guiding in a laser filament, which forms as consequence of a dynamic equilibrium between self-focusing and plasma defocusing [12], in practice is also limited to output pulse energies of about 1 mJ, mainly due to the onset of multiple filamentation, spatial chirp, and angular dispersion [13, 14]. Consequently, only the center of the output beam is spectrally homogeneous and can be recompressed to a few-cycle pulse.

A scheme that potentially scales much more favorably to high pulse energy than hollow capillaries and filamentation was proposed by Nurhuda and Midorikawa [15]. By use of planar hollow waveguides for post compression the pulse energy can easily be up-scaled by increasing the beam size in one spatial direction, while keeping the intensity inside the waveguide at levels benefiting efficient self-phase modulation, but limiting ionization. In the first implementation, strong deterioration of the beam profile along the unguided direction was observed due to 1-dimensional self-focusing [16]. Shortly after, some of the current authors showed that by carefully controlling experimental parameters such as gas pressure and waveguide length, a balance between spectral broadening and beam deterioration can be achieved and demonstrated pulse compression at the 10 mJ level with up to 80 % wave guide throughput and good focusability [17–19]. A theoretical model describing a stability regime for further up-scaling of the planar hollow waveguide compression scheme was identified [18, 20].

In the current work, we present experimental results of pulse post compression of a TW class CPA laser in a gas-filled planar hollow waveguide with up 50 mJ input pulse energy. The compressed pulses were fully characterized in terms of beam profile, focusability, and pulse duration. The viability of the compressed pulses for applications in high-field physics is demonstrated by generating high-order harmonics in a pulsed Ar gas jet. The harmonic cut-off is significantly increased compared to using longer driving laser pulses without the post compressor.

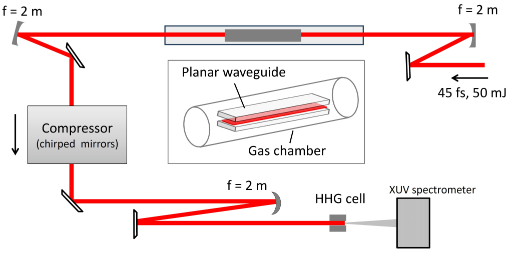

FIGURE 1. (color online). Sketch of the experimental setup.

Figure 1 sketches our experimental setup. Pulses of up to 50 mJ pulse energy at 10 Hz repetition rate and pulse duration of 45 fs, centered around 800 nm are focused with a cylindrical focusing mirror (f=2 m) onto the input of the planar hollow waveguide. The pulse energy can be adjusted by a $\lambda/2$-plate and a polarizer installed before the grating compressor of the CPA chain. The waveguide is comprised of two parallel, highly polished slabs (Plan Optik GmbH) made of Borofloat glass with dimensions 500x40x10 mm^3 with a gap of $2a = 127\,\mu m$ between them. The gap is matched to the width of the line-shaped laser beam at the waveguide entrance $w_{\text{foc}} \approx 0.735a$, where w_{foc} is the Gaussian half-width $(1/e^2)$; this condition facilitates maximum coupling efficiency into the fundamental waveguide mode. The waveguide is located inside a gas cell with thin (2.2 mm), broadband anti-reflection coated fused silica windows in both ends. The gas cell is approximately 3 m long in order to avoid detrimental nonlinear interaction with the windows. After the gas cell, the output beam of the waveguide is collimated with an identical cylindrical mirror and passed through a chirped mirror compressor. After compression the beam is sent to a high-order harmonic generation setup and generated harmonic spectra are recorded with a flat-field, XUV photon spectrometer.

The gas cell, in which the waveguide is located, was filled with Ar at pressures up to one atmosphere. The waveguide throughput is higher than 80% in vacuum, proving good coupling to the fundamental mode. The theoretical throughput for a 50 cm long waveguide with 127 μm separation is 86% for the fundamental mode. The throughput does not decrease up to 400 mbar of Ar, indicating that losses due to ionization and nonlinear coupling to higher order modes are small. For Ar pressure beyond 500 mbar the transverse mode breaks into a number of filaments, unusable for pulse compression. At the same time, the waveguide throughput drops, reflecting increased losses due to stronger nonlinear propagation effects and stronger ionization.

Fig. 2a) shows the spectra observed at the input and output of the waveguide for pulse energy of 50 mJ at vacuum and 200 mbar and 400 mbar of Ar. For the evacuated gas cell, the spectrum slightly broadens probably due to parasitic nonlinear interaction with the windows, which thus should be located as far away from the waveguide as possible. When the gas cell is filled to 400 mbar of Ar, an about four-fold increase of the spectral width is observed with the spectral wings spanning from 700-900 nm. The broadening is only slightly blue-shifted, identifying self-phase modulation as the main source of spectral broadening with only small contribution from plasma related blue-shifting [21]. The spectrum obtained at 400 mbar of Ar supports a transform limited pulse duration of 13 fs. The spectra were measured at the center of the output beam. It should be noted that along the unguided waveguide direction, spectral broadening is maximum at the beam center and smaller at the wings. The inhomogeneous spectral broadening also leads to different transverse pulse duration after compression, with the shortest pulse obtained at the beam center and longer pulse duration at the wings [18].

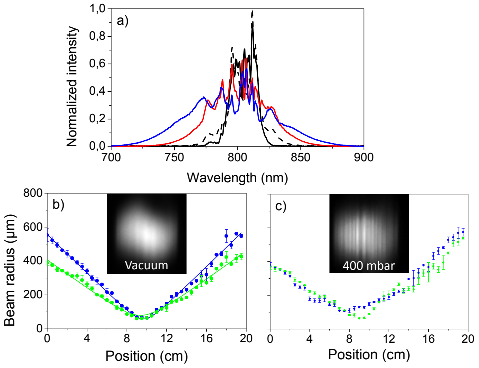

FIGURE 2. a) Spectra observed at the waveguide input (solid black) and output (dashed) for the case of evacuated waveguide and for 200 mbar (blue) and 400 mbar (purple) of Ar. b, c) Focusability of the guided (green) and free (blue) waveguide directions, illustrated in terms of beam caustics for the waveguide under vacuum (b) and filled with 400 mbar of Ar (c). The displayed beam sizes correspond to second order moments. The left insets shows the output mode at vacuum and the right at 400 mbar of Ar.

Before moving on to measuring the pulse duration after compression, we study the transverse beam profile and focusability of the waveguide output, which both are important criteria for pulse compression in planar hollow waveguides. If the waveguide output is not focusable to a small spot size, pulse post compression will not result in an increase of the focusable peak intensity. As discussed in [18], the focusability in the non-guided waveguide direction inevitably diminishes; first, due to the spatially inhomogeneous spectrum and second due to a pulse front deformation resulting from the beam center propagating slower (due to the Kerr-effect) than the wings. The second effect is essentially introducing an astigmatism, which however can easily be compensated by translating the collimating cylindrical mirror. The insets in Fig. 2b) and 2c) show the transverse mode observed at the output of the gas cell in case of vacuum (b) and 400 mbar of Ar (c). Modulational instability due to 1-dimensional self-focusing deteriorates the mode along the unguided waveguide direction. As self-phase modulation and self-focusing are the spectral and spatial manifestations of the Kerr-nonlinearity, transverse break-up of the mode ultimately limits the maximum spectral broadening and thus the shortest achievable compressed pulse duration [18]. To delay the onset of mode break-up, the laser beam profile was spatially filtered before the grating compressor of our CPA chain by focusing onto a conical pinhole made of fused silica. The transverse mode structure does not reduce the focusable intensity significantly

[18].

The focusability is investigated, after carefully attenuating the beam with reflections from uncoated wedges, by focusing the beam with a thin f=2 m focal length lens onto the chip of a CCD camera, which is moved along the optical axis in the vicinity of the geometrical focus. Fig. 2b) and c) show the beam radius as function of position for the guided and the free waveguide directions for the evacuated waveguide (b) and filled with 400 mbar of Ar (c). The beam size is extracted from the images by computing second order moments $\sigma_{x,y}$. For Gaussian beams $2\sigma_{x,y} = w_{x,y}$, where $w_{x,y}$ is the Gaussian beam radius ($1/e^2$). Indeed, the beam sizes obtained by moment theory are very close to beam sizes obtained from fitting a Gaussian profile, indicating that the focal spot is single-peaked and close to Gaussian shape. The focusability in terms of a M^2-parameter is obtained by fitting a parabola to the beam caustic (beam size vs. propagation direction) [22]. For the case of vacuum, fitting the caustics gives $M^2 \approx 1.28$ and $M^2 \approx 1.32$ in the guided and free waveguide directions, respectively. While for the guided direction, due to spatial cleaning from the waveguide, very good focusability can be expected, the focusability in the free waveguide direction is extraordinary good for a TW class laser system. For a filling pressure of 400 mbar, the focusability in the guided direction remains approximately unchanged, while in the free direction the minimum beam size increases by a factor of ≈ 1.6. At the same time, the focal position moves towards the lens, exhibiting a slight astigmatism, which however is easily removed by moving the cylindrical collimation mirror behind the waveguide.

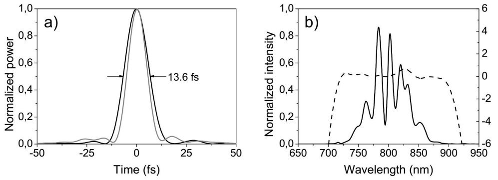

FIGURE 3. (left) Typical temporal pulse profile (black) obtained from SPIDER measurements compared to simulations (grey). (right) Spectrum and spectral phase from SPIDER measurement. $E_i = 50$ mJ, 400 mbar Ar.

The waveguide output is compressed by passing the beam through a chirped mirror compressor, comprised of four chirped mirrors (Layertec, 2") with eight bounces in total and six bounces from custom made mirrors (VENTEON, $20 \times 30\,\mathrm{mm}^2$). After careful attenuation, the compressed pulses are characterized with a commercial few-cycle SPIDER (VENTEON). Dispersion can be fine tuned by transmitting the beam through a pair of AR-coated fused silica wedges. Note that the wedges can only be put after strongly attenuating the beam. If put between the collimating cylindrical mirror and the chirped mirror compressor, filaments form inside the wedges. Thus, for actual experiments with the waveguide output, dispersion has to be coarsely adjusted by the number of bounces from the chirped mirrors without fine dispersion control. Fig. 3a) shows a typical SPIDER retrieval of the compressed temporal pulse profile (black) in optimized conditions for 50 mJ pulse energy at the waveguide input and a filling of 400 mbar Ar. Individual measurements exhibit a large spread in retrieved pulse duration due to shot-to-shot pulse energy fluctuations, typical for low repetition rate TW class lasers. We performed ten SPIDER measurements, with retrieved duration spreading from 13.4 fs to 17 fs ; the average pulse duration was 14.3 fs. Fig. 3b) shows the retrieved spectrum together with the spectral phase. The spectral phase is reasonably flat, indicating that the chirped mirror compressor is well suited to compress the waveguide output.

After having demonstrated strong spectral broadening, high throughput, good focusability, and sub-15 fs pulse duration, we use the compressed pulses to drive HHG, where short pulse duration and high focal intensity (exceeding $10^{14}\,\mathrm{Wcm}^{-2}$) are inevitable ingredients. High-order harmonic generation essentially is a strong-field effect and is most easily explained by the semi-classical three-step model [23], where first, close to each peak of the incident electric field an electron wavepacket is born in the continuum after tunnelling through the potential barrier, formed by the superposition of the Coulomb potential and the laser field. Second, the wavepacket picks up kinetic energy in the laser field and finally, as it eventually returns to the parent ion and recombines, its kinetic energy is emitted as high-energy XUV photon. The process repeats every half-cycle of the driving laser field, corresponding to the emission of a train of attosecond pulses. The spectrum is comprised of discrete odd order harmonics of the driving field frequency, whereas the spectral width of individual harmonics decreases with increasing number of contributing half-cycles. The highest energy $E_{\max}$ in a HHG spectrum is related to the driving field intensity by the cut-off law $E_{\max} = 3.17U_P + I_P$, where U_P is the ponderomotive energy (average energy of an electron in an AC field with $U_P \propto I_{\max}$), I_P is the ionization potential of the gas, and $I_{\max}$ is the peak intensity of the driving field.

In practice, for multi-cycle generating pulses the cut-off energy is rather determined by macroscopic phase-matching and propagation effects. Strong ionization of the gas medium leads both to reshaping of the fundamental field due to plasma-defocusing as well as to termination of HHG due to plasma-related unfavorable phase-matching conditions. Thus generating with shorter pulses, two main effects should be observed : first, a broadening of the individual harmonics due to less half-cycles contributing to the generation process and second a higher cut-off energy due to higher peak intensity as well as due to plasma-related effects setting in later for shorter pulses.

The chirped mirror compressor was slightly changed for high-order harmonic generation. In total eight

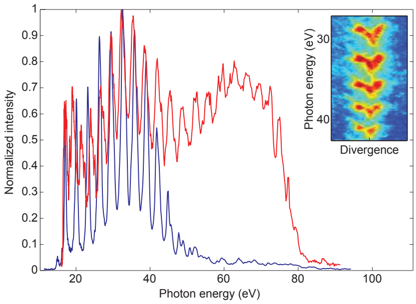

FIGURE 4. HHG spectrum with (red) and without (blue) waveguide compressor at ≈20 mJ input energy. The inset shows the spatial shape for a range of harmonics generated from the waveguide compressed pulses.

bounces from the Layertec CMs and two bounces from Venteon CMs were used, respectively to accommodate for 2.7 mm of fused silica (output window of the gas cell and input window of the harmonic generation setup) and for about five meters of air, required to collimate the waveguide output, compress the pulses, and enter the harmonic generation setup. It should be noted that the compressed pulse energy reaching at the harmonic setup was distinctively lower than the waveguide output. While ≈ 40 mJ can be observed at the output of the waveguide (50 mJ at the input), the compressed pulse energy available for harmonic generation was ≈ 20 mJ. The losses are mostly due to cutting on the limited apertures of vacuum windows and chirped mirrors. The compressed waveguide output is loosely focused with a spherical mirror (f=2 m) into a dilute Ar gas jet. The harmonic spectrum is recorded with a flat-field XUV photon spectrometer. Fig. 4 shows HHG spectra obtained in two different situations, using long pulses ≈45 fs circumventing the waveguide setup (blue) and using the waveguide filled with 400 mbar of Ar (red). The pulse energy in both cases was ≈20 mJ. The result is obvious; with increased gas pressure in the waveguide, the individual harmonics become broader and the cut-off energy increases, indicating that the pulse from the waveguide compressor is significantly shorter and more intense. Furthermore, the harmonics generated from waveguide compressed pulses feature rich transverse spatial structure (see inset), where each of the harmonics exhibits a triangular shape with higher XUV photon energy on-axis compared to the wings. Such behavior is not observed with the long pulses. We believe that this behavior is related to a spatial variation in the dipole phase or to propagation effects [24]. As the waveguide output features a transversely inhomogeneous spectral broadening and consequently transversely varying pulse duration, the pulse might undergo complicated spatio-temporal couplings upon focusing in combination with nonlinear propagation. Although interesting in itself the particular shape of the harmonics is beyond the scope of this article and might be discussed in another publication.

In conclusion, we have demonstrated that pulse post compression in planar hollow waveguides is a viable tool to approach the few-cycle pulse duration regime with typical TW CPA lasers, which are currently operated in laboratories around the world. In this work 50 mJ input pulses could be compressed to sub-15 fs pulse duration. A carefully designed chirped mirror compressor should in the future allow for 70% total energy efficiency (input-to-output). The pulse energy range presented here currently is and most likely will remain not easily accessible with competing compression schemes, such as hollow capillaries or filamentation. Furthermore, the planar hollow waveguide still bares large potential for energy up-scaling. Up-scaling can most easily be discussed in terms of the B-integral acquired by the beam during nonlinear propagation inside the waveguide,

$$B = \int_{z=0}^{L} k_0 I\left(z\right) n_2 P z dz \approx k_0 I_0 n_2 P L \qquad (1)$$

where k_0 is the wavenumber at the carrier frequency, I_0 is the intensity at the waveguide input, n_2 is the nonlinear refractive index for Ar at atmospheric pressure, P is the gas pressure given in atmospheres, and L is the length of the waveguide. For the current experiment, the B-integral accumulated in the waveguide is $B \approx 8$. While a higher B-integral would lead to stronger spectral broadening, inevitably the transverse beam profile would disintegrate, resulting in an unusable beam. Consequently, energy up-scaling must be achieved, while keeping the B-integral constant. Obviously, increasing the beam size in the unguided direction provides a trivial way to up-scale the pulse energy; further control knobs are intensity, gas pressure, length of the waveguide, and type of gas. The intensity however should be kept below a level of strong ionization ($\approx 7 \times 10^{13}$ Wcm^{-2} in the current experiment) in order to avoid plasma-related absorption and nonlinear coupling to higher waveguide modes. By *e.g.* using generalized Keldysh PPT theory [25] to calculate the amount of ionization one can estimate that the intensity for the case of Ne or He can be increased by factors of ≈3 and ≈5, respectively. The lower nonlinearity (≈7 times for Ne and ≈33 times for He) has to be compensated by higher pressure inside the waveguide. Considering the degrees of freedom sketched above, an up-scaling to input pulse energies in the range of hundreds of mJ seems straight forward, offering a possibility to expand the concept of pulse post compression to lasers with tens of TW peak power.

Acknowledgments

This research was supported by the European Research Council (ALMA, PALP), the Swedish Research Council, the Crafoord Foundation, and the Knut and Alice Wallenberg Foundation. A.J. and A.H. acknowledge support from DGA, the European Science Foundation (SILMI) and the European Cooperation in Science and Technology (COST).

[1] A. L'Huillier *et al.*, J. Nonl. Opt. Phys. Mat. **4**, 647 (1995).
[2] F. Krausz and M. I. Stockman, Nature Phot. **8**, 205 (2014).
[3] T. Brabec and F. Krausz, Rev. Mod. Phys. **72**, 545 (2000).
[4] E. Esarey, C. B. Schroeder, and W. P. Leemans, Rev. Mod. Phys. **81**, 1229 (2009).
[5] S. Rausch *et al.*, Opt. Express **17**, 14341 (2009).
[6] M. Nisoli *et al.*, Opt. Lett. **22**, 522 (1997).
[7] C. Hauri *et al.*, Appl. Phys. B **79**, 673 (2004).
[8] M. Hentschel *et al.*, Nature **414**, 509 (2001).
[9] X. Chen *et al.*, Fib. Opt. **21**, 198 (2011).
[10] S. Bohman *et al.*, Opt. Express **16**, 10684 (2008).
[11] C. Fourcade Dutin *et al.*, Opt. Lett. **35**, 253 (2010).
[12] A. Couairon and A. Mysyrowicz, Physics Reports **441**, 47 (2007).
[13] A. Couairon *et al.*, J. Mod. Optics **53**, 75 (2006).
[14] A. Zair *et al.*, Opt. Express **15**, 5394 (2007).
[15] M. Nurhuda *et al.*, Phys. Rev. Lett. **97**, 153902 (2006).
[16] J. Chen *et al.*, Opt. Lett. **33**, 2992 (2008).
[17] S. Akturk *et al.*, Opt. Lett. **34**, 1462 (2009).
[18] C. L. Arnold *et al.*, N. J. Phys. **12**, 073015 (2010).
[19] S. Chen *et al.*, J. Opt. Soc. Am. B **28**, 1009 (2011).
[20] C. L. Arnold *et al.*, Opt. Express **17**, 11122 (2009).
[21] A. Brodeur and S. L. Chin, Phys. Rev. Lett **80**, 4406 (1998).
[22] A. Siegman, OSA TOPS **17**, 184 (1997).
[23] P. B. Corkum, Phys. Rev. Lett **71**, 1994 (1993).
[24] E. Constant *et al.*, J. Phys. B **45**, 074018 (2012).
[25] A. M. Perelomov, V. S. Popov, and M. V. Terent'ev, Sov. Phys. JETP **23**, 924 (1966).

Paper III

A high-flux high-order harmonic source

P. Rudawski, C. M. Heyl, F. Brizuela, J. Schwenke, A. Persson,
E. Mansten, R. Rakowski, L. Rading, F. Campi, B. Kim, P. Johnsson,
and A. L'Huillier.

Rev. Sci. Instrum. **84**, 073103 (2013).

A high-flux high-order harmonic source

P. Rudawski,[1,a)] C. M. Heyl,[1] F. Brizuela,[1] J. Schwenke,[1] A. Persson,[1] E. Mansten,[2]
R. Rakowski,[1] L. Rading,[1] F. Campi,[1] B. Kim,[1] P. Johnsson,[1] and A. L'Huillier[1]
[1]*Department of Physics, Lund University, P.O. Box 118, SE-221 00 Lund, Sweden*
[2]*MAX-lab, Lunds Universitet, P.O. Box 118, SE-221 00 Lund, Sweden*

(Received 12 March 2013; accepted 11 June 2013; published online 9 July 2013)

We develop and implement an experimental strategy for the generation of high-energy high-order harmonics (HHG) in gases for studies of nonlinear processes in the soft x-ray region. We generate high-order harmonics by focusing a high energy Ti:Sapphire laser into a gas cell filled with argon or neon. The energy per pulse is optimized by an automated control of the multiple parameters that influence the generation process. This optimization procedure allows us to obtain energies per pulse and harmonic order as high as 200 nJ in argon and 20 nJ in neon, with good spatial properties, using a loose focusing geometry ($f_\# \approx 400$) and a 20 mm long medium. We also theoretically examine the macroscopic conditions for absorption-limited conversion efficiency and optimization of the HHG pulse energy for high-energy laser systems. [http://dx.doi.org/10.1063/1.4812266]

I. INTRODUCTION

High-order harmonics generated by the nonlinear interaction of an intense ultrashort laser pulse with atoms or molecules are now used in many fields of physics. The interest in the generated radiation results from unique features like tunability over the extreme ultraviolet (XUV) and soft x-ray (SXR) spectral regions (reaching several keV[1,2]), excellent beam quality,[3] and ultrashort pulse duration down to the attosecond range.[4] High-order harmonic generation (HHG) sources are well established in many research areas such as attosecond science[5] or femtosecond spectroscopy[6] and have become interesting for high-resolution imaging,[7,8] free-electron-laser seeding,[9] and nonlinear optics in the XUV range.[10,11]

Most applications of HHG sources benefit from harmonic pulses with high pulse energy. This requirement is difficult to achieve due to the low conversion efficiency of the generation process. Since the discovery of the HHG process over two decades ago,[12,13] its conversion efficiency has been progressively improved by optimizing the macroscopic phase-matching conditions and the microscopic single atom response. High-order harmonic generation has been carried out in different conditions, such as high-pressure jets,[14] gas cells,[15] semi-infinite media, and capillaries.[16] Phase-matching optimization using loosely focused (possibly self-guided) fundamental fields has led to conversion efficiencies of $\sim 10^{-7}$ in neon,[15] $\sim 10^{-5}$ in argon,[17] and slightly below 10^{-4} in xenon.[18,19] By modifying the generation field, e.g., by combining the fundamental field with one or more of its harmonics, the microscopic single atom response has been controlled on the subcycle level leading to enhanced HHG signals and/or generation of even-order harmonics.[20–22]

In this article, we describe a high-flux HHG source operating in the photon energy range up to 100 eV. The HHG setup is designed to work in a loose focusing geometry (up to 5 m focal length) and is driven by a high energy femtosecond laser system delivering up to 100 mJ per pulse. The optimization of the signal is performed using an automated scan of the main parameters that contribute to phase-matching (e.g., driving pulse intensity, gas pressure, etc.). Using this technique we have obtained a total energy per pulse in argon of a microjoule and a few hundred nJ in neon, in a geometry with an f-number $f_\# = f/D \approx 400$ and $f_\# \approx 133$, respectively, and a 20 mm long gas cell. Beam profiles were measured using an XUV-camera and the coherence properties were estimated in a Young's double-slit experiment. The article is organized as follows. Section II presents theoretical considerations for HHG under loose focusing. The HHG setup together with the methods for characterization and optimization are described in Sec. III. Results obtained with the high-energy, ultrashort laser system at the Lund Laser Centre are presented in Sec. IV. Section V presents a summary of the work and a discussion about scaling to extremely long focal lengths.

II. MODEL FOR LOOSE FOCUSING HHG

High-order harmonic generation with high conversion efficiency requires optimization of both the microscopic and macroscopic properties of the process. The microscopic response is well described by a semi-classical three-step model.[23,24] In every half-cycle of the driving wave, electrons can tunnel through the distorted atomic potential barrier, being then accelerated in the intense laser field. Depending on the release time into the continuum, the electrons may return to the parent ion and recombine, emitting an XUV photon. The trajectories of these electrons can be divided into two groups called short and long, depending on the excursion time in the continuum. HHG requires laser intensities in the range of 10^{14} W/cm^2–10^{15} W/cm^2 depending on the selected gas.

[a)]Electronic mail: piotr.rudawski@fysik.lth.se

Macroscopically, the total HHG signal is a coherent sum of the photons emitted from different atoms in the medium. For a given harmonic order q, constructive addition occurs along the propagation direction over the so-called coherence length $L_{\mathrm{coh}} = \pi/\Delta k$. Here, $\Delta k = qk_1 - k_{\mathrm{q}}$ is the wave-vector mismatch along the propagation direction between the generated field and the laser-induced polarization at frequency $q\omega$. In order to maximize the coherence length, the wave-vector mismatch must be minimized. In a non-guiding focus geometry this can be done through the interplay between the four sources of wave-vector mismatch,

$$\Delta k = \underbrace{\Delta k_{\mathrm{g}}}_{<0} + \underbrace{\Delta k_{\mathrm{n}}}_{>0} + \underbrace{\Delta k_{\mathrm{p}}}_{<0} + \underbrace{\Delta k_{\mathrm{d}}}_{\substack{<0 \text{ for } z<0 \\ >0 \text{ for } z>0}} . \tag{1}$$

The negative contribution Δk_{g} originates from the Gaussian beam phase gradient along the propagation direction (z). Δk_{n} and Δk_{p} describe the neutral and free-electron dispersion which have opposite sign and are proportional to the gas pressure. To explicitly outline this linear dependence, we write $\Delta k_{\mathrm{n,\,p}} = p\,\partial(\Delta k_{\mathrm{n,\,p}})/\partial p$, where the partial derivative is now pressure independent in the following. Δk_{d} is the gradient of the so-called dipole phase which is proportional to the intensity gradient and is small for the short trajectories but large for the long ones.[25]

Under our experimental conditions, the short trajectories dominate the HHG process. If only these trajectories are considered in Eq. (1), the dipole phase contribution can be neglected and the wave-vector mismatch can be minimized by canceling the plasma dispersion and Gaussian beam phase gradient with the neutral dispersion. For a fixed generation geometry, the degree of ionization in the medium determines the pressure, p_{match}, for which the system is phase matched.[26,27] For each harmonic order, p_{match} is defined as

$$p_{\mathrm{match}} = -\frac{\Delta k_{\mathrm{g}}}{\frac{\partial(\Delta k_{\mathrm{n}})}{\partial p} + \frac{\partial(\Delta k_{\mathrm{p}})}{\partial p}} . \tag{2}$$

For a given medium, harmonic order, and focal length, the only variable parameter is the free-electron contribution which is proportional to the degree of ionization ($\partial\Delta k_{\mathrm{p}}/\partial p \propto r_{\mathrm{ion}}$), and consequently can be adjusted by changing the laser intensity. The equation requires the intensity to be low enough so that the contribution due to neutral dispersion dominates over the free-electron dispersion. This defines a maximum ionization degree ($r_{\mathrm{ion}}^{\mathrm{max}}$), typically a few percent, above which phase-matched generation is not possible.

Figure 1 shows the variation of p_{match} in argon as a function of the degree of ionization for three harmonic orders and two different focusing geometries. p_{match} tends towards infinity when r_{ion} reaches $r_{\mathrm{ion}}^{\mathrm{max}}$. At low degree of ionization, the phase-matching pressure varies little both with pressure and with harmonic order. Considering that the dipole response is highest at the highest intensity, one could assume that the most efficient generation is possible at high pressures and at intensities that support an ionization degree around $r_{\mathrm{ion}}^{\mathrm{max}}$. High intensities, however, lead to steep gradients of r_{ion} in the longitudinal and radial directions within the generation volume, confining phase-matched generation to a small volume and leading to transient phase-matching.[27] In spite of a higher single atom response at high intensity, those effects can reduce the overall efficiency. An optimum ionization degree should assure phase-matched HHG over a broad bandwidth and a large volume. The ionization level should be such that the phase-matching pressure is approximately constant for a broad range of high-order harmonics, potentially leading to short and intense attosecond pulses. This phase-matching bandwidth increases with decreasing ionization degree yet at the same time the single atom response as well as the conversion efficiency decrease. As a rule of thumb, the optimum value for the ionization degree can be taken as $\sim r_{\mathrm{ion}}^{\mathrm{max}}/2$ for the highest harmonic in the considered HHG bandwidth. Under the conditions of Figure 1, this corresponds to $\sim$2% ionization and a laser intensity of $\sim 1.1 \times 10^{14}$ W/cm^2.

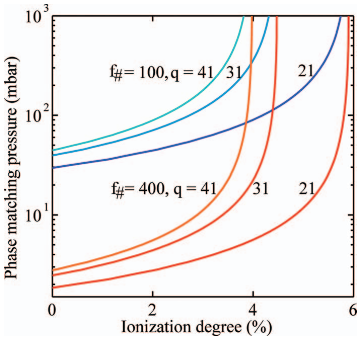

FIG. 1. Phase matching pressure in Ar as a function of ionization degree for different harmonic orders, q, and different focus geometries $f_{\#} = 100$, blue, and $f_{\#} = 400$, red. The central wavelength is 800 nm and the generation cell is placed at the focus of the fundamental beam.

When the coherence length, L_{coh}, is maximized, the harmonic emission is limited by re-absorption in the generation gas. The absorption length, L_{abs}, is defined by

$$L_{\mathrm{abs}}(p) = \frac{kT}{p\sigma_{\mathrm{ion}}}, \tag{3}$$

where k is the Boltzmann constant, T the temperature, and σ_{ion} the ionization cross-section. Following the argumentation of Constant *et al.*,[28] the harmonic yield is then maximized when the medium length, L_{med}, is at least three times the absorption length. This allows to define an optimum medium length under phase-matched conditions, $L_{\mathrm{med}}^{\mathrm{opt}} = 3L_{\mathrm{abs}}(p_{\mathrm{match}})$. For example for the 21st harmonic in Ar, and $f_{\#} = 400$, $T = 300$ K, $\sigma_{\mathrm{ion}} = 2 \times 10^{-21}$ m^2, $p_{\mathrm{match}} \approx 5$ mbar, and consequently $L_{\mathrm{med}}^{\mathrm{opt}}$ should be chosen to be at least 12 mm.

For high-energy laser systems, an increase of the absorption-limited HHG intensity can be achieved by scaling up the $f_{\#}$, i.e., by increasing the focal length for a certain initial beam diameter. The conversion efficiency can be held constant when changing the focal length if the laser pulse energy, the gas pressure, and the medium length are scaled appropriately. Using Gaussian optics and Eqs. (2) and (3), we derive the following scaling relations: E_f (laser energy) $\propto f^2$ in order to keep the same intensity at focus, $p_{\mathrm{match}} \propto 1/f^2$ since $\Delta k_{\mathrm{g}} \propto 1/f^2$, and $L_{\mathrm{med}} \propto f^2$. This ensures constant conversion

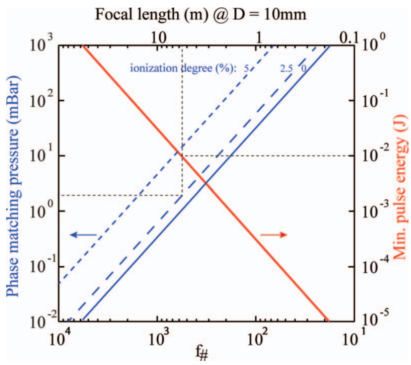

FIG. 2. Scaling of the phase matching pressure and the required laser pulse energy with focal length (or $f_\#$) for different ionization levels in argon. The corresponding minimum laser pulse energy required is shown in red. For the simulations, the following parameters were used: beam diameter before focusing: $D = 10$ mm, gas cell position: at the focus, central wavelength of 800 nm, harmonic order $q = 21$. The required pulse energy was calculated assuming a peak intensity of 1.5×10^{14} W/cm^2 and a pulse length of 45 fs.

efficiency, independent of the focusing geometry,[27] and the harmonic energy $E_h \propto f^2$.

Figure 2 illustrates these scaling relations in the case of argon, with the following parameters: 800 nm wavelength, a 45 fs pulse duration, an intensity of 1.5×10^{14} W/cm^2 at focus, and an initial beam diameter of 10 mm. A laser pulse energy of 10 mJ requires a focal length of approximately 5 m and a generation pressure of a few mbar to efficiently generate harmonics.

III. HIGH-ORDER HARMONIC EXPERIMENTAL SETUP

Our HHG setup consists of three sections: generation, diagnostics, and application (see Figure 3). The sections are connected by vacuum tubes with a diameter $\phi = 40$ mm. The generation section is mounted on stiffly connected optical tables. The diagnostics section together with the application chamber are mounted on a rail system. This allows us to adjust the distance between the vacuum chambers depending on the focusing geometry in order to avoid damage of optical elements placed after the generation by the fundamental laser field. It also provides vibration isolation and high stability.

High-order harmonics are generated by loosely focusing a high energy laser beam into a noble gas. The fundamental laser beam is apertured down by a variable diameter iris (I), typically between 9 and 30 mm and focused by a lens (L). Control of the beam size allows for re-adjustments of the focusing geometry ($f_\#$) as well as laser energy and intensity distribution at focus. Thus it allows us to optimize phase-matching in a simple way. Directly after the focusing optics, the beam enters the generation chamber. The entrance UV fused silica window is mounted at a small angle to avoid back propagation of the reflected light to the laser system. The beam propagates inside a 100 mm diameter vacuum tube and is folded by mirrors (M) mounted on small breadboards placed in 6-way crosses. Alternatively, the laser beam can be focused by a mirror at near-normal incidence placed in one of the vacuum crosses. The focused beam interacts with the noble gas confined in a cell (PGC). The cylindrical cell has a diameter of typically 0.5 mm and a length between 3 mm and 20 mm. The gas is released at the repetition rate of the laser by a valve[29] driven by a piezo-electric actuator and synchronized with the laser pulse. The opening and closing times are optimized for maximum harmonic signal. Simulating the gas distribution in the cell, we found a small pressure gradient from the middle of the cell, where the gas is injected, towards the ends of the cell, where the pressure abruptly drops. The cell is mounted on an XY motorized stage. Additionally, two motorized actuators control the tilt of the cell with respect to the incoming beam. In order to optimize the position of the cell relative to the laser focus the gas cell is additionally placed on a 6 cm long-range translation stage moving along the propagation direction (Z).

The generation chamber is designed to work simultaneously with up to two gas cells. The cells can be mounted in parallel or in series. The parallel configuration allows for the generation of two independent harmonic beams[30] while the serial configuration can be used for the enhancement of the HHG process using low-order harmonics generated in the first cell.[22] In both configurations, the generated harmonic beam propagates collinearly with the fundamental radiation in vacuum (10^{-6} mbar) to the diagnostics chamber. Elimination

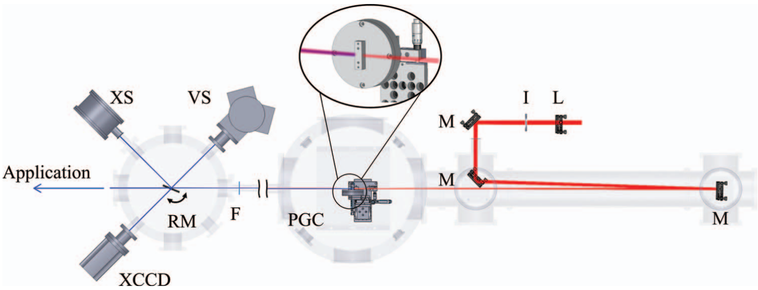

FIG. 3. HHG setup in the 4 m focusing configuration; L - focusing lens, I - iris, M - folding mirrors, PGC - pulsed gas cell, F - aluminum filters, RM - rotating mirror, XS - XUV spectrometer, VS - VUV spectrometer, and XCCD - XUV CCD camera.

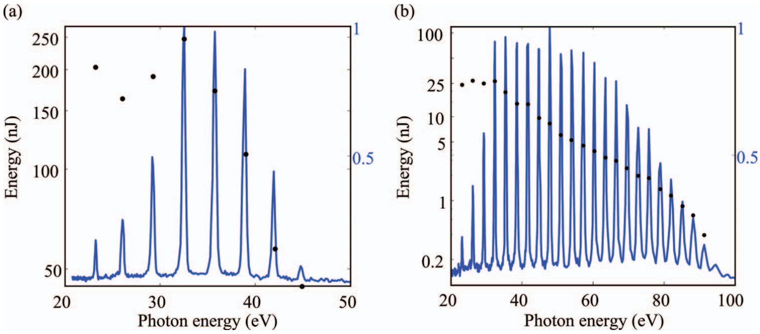

FIG. 4. High-order harmonic spectra in argon (a) and neon (b) gas. The pulse energy per individual harmonics, shown as dots, was obtained by combining total energy measurements with the spectral response from the XUV spectrometer.

of the fundamental is achieved by using 200 nm thick aluminum filters (F). The filters are mounted on a manual translation stage placed at the entrance of the diagnostics chamber, and controlled from the outside of the vacuum chamber.

The alignment of the setup is based on the beam position at the entrance iris and a reference point inside the diagnostics chamber. The precise alignment of the gas cell with respect to the laser beam is done by motorized control of the cell's four axes (XY and two tilts). The reference point and gas cell are monitored by cameras equipped with variable focal length objectives.

At the center of the diagnostics chamber, a gold-coated flat mirror (RM) mounted on a rotation stage is used to send the XUV beam to the different instruments or, when the mirror is removed, towards the application chamber (Fig. 3). The HHG spectra are measured by a flat-field grating spectrometer (XS, Jobin-Yvon PGM-PGS 200). The spectrometer detects spectrally-resolved far-field spatial profiles of individual high-order harmonics in the XUV spectral range. Low-order harmonics are detected using a vacuum ultraviolet monochromator (VS, McPherson 234/302). The vacuum ultraviolet spectrometer is equipped with an MCP detector coated with CsI allowing HHG diagnostics in a range from 50 to 250 nm. Additionally, spatial profiles and energy measurements are carried out using a back-illuminated XUV-CCD (Andor iKon-L) camera (XCCD). To attenuate the HHG beam for these measurements we use one or two 200 nm thick aluminum filters.

IV. RESULTS

This section presents measurements of high-order harmonics generated in argon and neon. The driving laser system is a high-power Ti:Sapphire chirped-pulse-amplification-based laser system delivering 45 fs pulses with up to 100 mJ energy at 10 Hz repetition rate. Before compression, the laser beam is spatially filtered with a conical pinhole mounted in a vacuum chamber. The pinhole waist, approximately 500 μm, is placed in a focal plane of a 1.7 m focal length lens. The laser beam diameter is 30 mm at the entrance to the harmonic setup. The laser beam position and angle are actively stabilized.

Figure 4 presents typical integrated harmonic spectra for (a) argon and (b) neon, recorded by the XUV spectrometer. The driving laser beam, with 20 mJ energy in case of argon and 24 mJ in case of neon, was focused by a 4 m lens in a 20 mm long cell. The HHG cut-off energy is 45 eV (29th harmonic) in argon whereas in neon it reaches 91.5 eV (59th harmonic). Under these conditions the total measured harmonic energy per laser shot is 1.15 μJ for argon and 0.23 μJ for neon. These values correspond to conversion efficiencies of 5×10^{-5} for argon and 8×10^{-6} for neon. Due to the high sensitivity of the XUV camera to the infrared radiation, the harmonic beam energy is measured within the aluminum filter's transmission window, i.e., between 14 eV and 71 eV, corresponding to harmonic orders between 11 and 45. The measurement procedure, similar to the one described by Erny *et al.*,[31] is based on XUV-CCD recorded background-subtracted images. The images are integrated to obtain the total number of counts. The total number of photons is estimated based on a calibration curve from the manufacturer. The individual harmonic energy is obtained by multiplying the total HHG beam energy with the relative intensity of each harmonic measured by the spectrometer. The spectrum is corrected for the folding mirror reflection (based on data from Henke *et al.*[32]), the grating efficiency, and the measured aluminum filter transmission. The estimated pulse energy per harmonic is shown as dots in Figure 4. The most prominent harmonic, both in argon and neon is the 21st harmonic (32.5 eV). Its energy is 250 nJ in argon and 30 nJ in neon. These values are comparable to previous results obtained by Takahashi *et al.*[15,17]

To find the optimum high-order harmonic energies an automated optimization procedure was carried out. This procedure is briefly summarized here. The important parameters to control are: fundamental beam energy and diameter (before focusing), gas pressure, and gas cell position relative to the laser focus. The energy of the fundamental beam is varied by an attenuator consisting of a half-wave plate mounted on a motorized rotation stage and a polarizer. We use a motorized

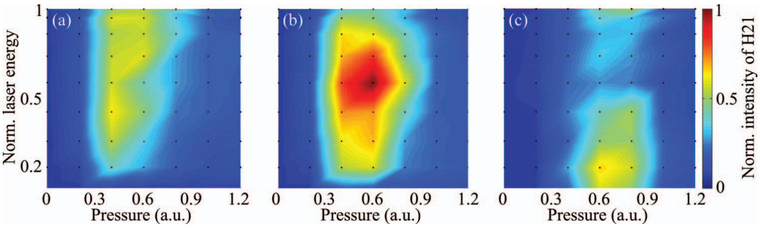

FIG. 5. Intensity of the 21st harmonic generated in argon as a function of driving laser energy and generation gas pressure. The measurements were carried out for a gas cell placed at the laser focus for three iris sizes: (a) $\phi = 22$ mm, (b) $\phi = 24$ mm, and (c) $\phi = 32$ mm. The values of a harmonic intensity between the measured points, shown as black dots, were interpolated.

variable iris to change the diameter of the fundamental beam before focusing. The distance between the center of the cell and the fundamental beam waist is varied by moving the cell. Finally, the gas pressure in the cell is adjusted by controlling a voltage applied to the cell nozzle's piezoelectric disks. We record a set of harmonic spectra while varying these four parameters in an automated way. Either the total HHG energy or the energy of a single harmonic can be optimized. Our optimization procedure allows us to routinely obtain HHG energies at the level of several hundred nJ in argon and a few tens of nJ in neon.

An example of the automated optimization is presented in Figure 5, where we investigated the dependence of the intensity of the 21st harmonic generated in argon as a function of the laser energy and gas pressure for three iris diameters. The signal is normalized to the maximum obtained for 21st harmonic. The recorded data show that for increasing iris size (decreasing $f_{\#}$), the required laser energy decreases and the phase matching pressure increases in agreement with our model prediction (see Fig. 1). Similar optimization in neon shows, as expected, a higher p_{match}. The optimum iris diameter corresponds to the longest Rayleigh range (the highest $f_{\#}$) for which the phase-matching conditions can be achieved, while keeping a high enough intensity at focus. It assures the highest HHG beam energy as is shown in Sec. II.

Figure 6(a) shows the spatial profile of high-order harmonics generated in argon and transmitted through an aluminum filter. The corresponding orders are between 11 and 45. The back-panel shows that the intensity distribution is almost perfectly Gaussian. Similar high quality Gaussian beams were generated in neon. The high spatial quality of the generated beams is due partly to the spatial quality of the driving beam, and partly to optimized phase-matching along the propagation axis. In our conditions, IR and XUV beams distortion due to nonlinear and plasma effects are negligible.

The generated beams divergence carries information about the contribution from the electronic trajectories. The divergence of the "short trajectory" harmonic beam is usually much smaller than for the "long trajectory" harmonics. For the 21st harmonic generated in argon, the divergence of the beam resulting from the long trajectory is 14 times higher than that from the short trajectory.[36] The different divergence is a consequence of a larger accumulated phase on the long trajectories. The analysis of the harmonic beam divergence shows that the main contribution to HHG in our conditions comes from the short trajectories. The contribution from the long trajectories is visible on the analyzed CCD images as a weak background.[30]

To estimate the spatial coherence of the HH beam, we performed a double-slit experiment. The degree of coherence of the HHG beam can be estimated from the fringe contrast in the diffraction pattern.[33,34] The slits used in this experiment had a width of 40 μm, a slit separation of 400 μm, and were located 1.5 m from the source. Figure 6(b) shows a cross-section of the double-slit diffraction pattern obtained with a single shot exposure. The experimental data were fitted with

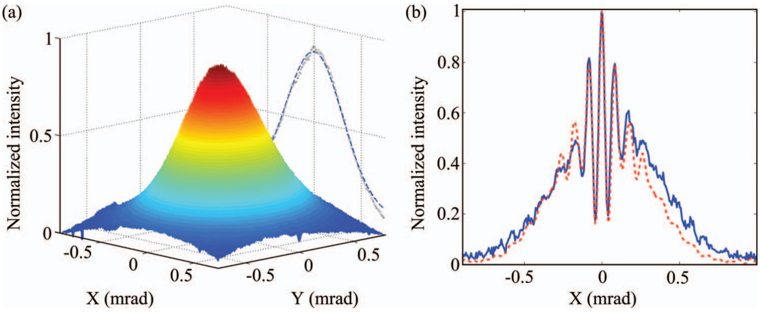

FIG. 6. (a) Spatial profile of the harmonic beam generated in Ar by focusing fundamental radiation with 2 m focal length lens into a 10 mm long cell, recorded with an x-ray CCD camera. The back-panel shows the cross-section of the beam (gray, dotted line), and a fitted intensity distribution (blue, dashed line), (b) Diffraction pattern created in a double-slit experiment, experimental data (blue, solid line), and fitted intensity distribution (red, dashed line).

a theoretical intensity function formed by the sum of diffraction patterns of the different harmonic wavelengths within the transmission window of the filter. The best fit was found with a degree of coherence of 0.8, in good agreement with previous measurements.[35]

V. SUMMARY AND OUTLOOK

We have developed a high-energy HHG setup, working in a loose focusing geometry, generating a total energy per laser pulse of a microjoule in argon and a few hundred nJ in neon. The source is designed for future studies of nonlinear processes in the XUV spectral range. The high harmonic pulse energies together with their high spatial coherence allow us to reach high peak intensities. For example, an intensity of 2×10^{14} W/cm^2 per harmonic pulse could be reached by focusing the HHG beam generated in argon using a broadband grazing-incident mirror, assuming a 3 μm focal spot size, 20 fs duration, and 30% transmission after reflection and filtering by an Al filter.

Our theoretical analysis of phase-matching in the absorption-limited case provides a simple guide for scaling HHG properties to high laser energies. For example we estimate that with $E_\mathrm{f} = 1$ J, $f = 50$ m, $p = 0.01$ mbar, and $L_\mathrm{med} = 6$ m, harmonic pulses with energy as high as 70 μJ could be reached.

Further increase in energy could be achieved by modifying the single atom response, e.g., using a double-cell scheme.[22] Our current beam line includes the option to drive the HHG process with two cells or to use an interferometric setup in order to combine the fundamental with itself, its second or third harmonic (ω/ω, $\omega/2\omega$, and $\omega/3\omega$), thus providing a large range of options for modifying the driving field.

Our experimental results combined with the above considerations show that HHG has the potential to provide intense ultrashort pulses reaching the intensity levels required for nonlinear experiments in the XUV spectral range.

ACKNOWLEDGMENTS

This research was supported by the Marie Curie program ATTOFEL (ITN), the European Research Council (ALMA), the Joint Research Programme ALADIN of Laserlab-Europe II, the Swedish Research Council, the Swedish Foundation for Strategic Research, and the Knut and Alice Wallenberg Foundation.

[1] C. Spielmann, N. H. Burnett, S. Sartania, R. Koppitsch, M. Schnürer, C. Kan, M. Lenzner, P. Wobrauschek, and F. Krausz, "Generation of coherent x-rays in the water window using 5-femtosecond laser pulses" Science **278**, 661 (1997).

[2] T. Popmintchev, M.-C. Chen, D. Popmintchev, P. Arpin, S. Brown, S. Alisauskas, G. Andriukaitis, T. Balciunas, O. D. Mücke, A. Pugzlys, A. Baltuska, B. Shim, S. E. Schrauth, A. Gaeta, C. Hernández-García, L. Plaja, A. Becker, A. Jaron-Becker, M. M. Murnane, and H. C. Kapteyn, "Bright coherent ultrahigh harmonics in the keV x-ray regime from mid-infrared femtosecond lasers," Science **336**, 1287–1291 (2012).

[3] Y. Tamaki, J. Itatani, M. Obara, and K. Midorikawa, "Highly coherent soft x-ray generation by macroscopic phase matching of high-order harmonics," Jpn. J. Appl. Phys. **40**, L1154–L1156 (2001).

[4] E. Goulielmakis, M. Schultze, M. Hofstetter, V. S. Yakovlev, J. Gagnon, M. Uiberacker, A. L. Aquila, E. M. Gullikson, D. T. Attwood, R. Kienberger, F. Krausz, and U. Kleineberg, "Single-cycle nonlinear optics," Science **320**, 1614 (2008).

[5] F. Krausz and M. Ivanov, "Attosecond physics," Rev. Mod. Phys. **81**, 163–234 (2009).

[6] S. L. Sorensen, O. Bjorneholm, I. Hjelte, T. Kihlgren, G. Ohrwall, S. Sundin, S. Svensson, S. Buil, D. Descamps, and A. L'Huillier, "Femtosecond pump-probe photoelectron spectroscopy of predissociative states in acetylen," J. Chem. Phys. **112**, 8038 (2000).

[7] R. L. Sandberg, C. Song, P. W. Wachulak, D. A. Raymondson, A. Paul, B. Amirbekian, E. Lee, A. E. Sakdinawat, C. La-O-Vorakiat, M. C. Marconi, C. S. Menoni, M. M. Murnane, J. J. Rocca, H. C. Kapteyn, and J. Miao, "High numerical aperture tabletop soft x-ray diffraction microscopy with 70-nm resolution," Proc. Natl. Acad. Sci. U.S.A. **105**, 24–27 (2008).

[8] J. Schwenke, E. Lorek, R. Rakowski, X. He, A. Kvennefors, A. Mikkelsen, P. Rudawski, C. M. Heyl, I. Maximov, S.-G. Pettersson, A. Persson, and A. L'Huillier, "Digital in-line holography on amplitude and phase objects prepared with electron beam lithography," J. Microsc. **247**, 196–201 (2012).

[9] G. Lambert, T. Hara, D. Garzella, T. Tanikawa, M. Labat, B. Carre, H. Kitamura, T. Shintake, M. Bougeard, S. Inoue, Y. Tanaka, P. Salieres, H. Merdji, O. Chubar, O. Gobert, K. Tahara, and M.-E. Couprie, "Injection of harmonics generated in gas in a free-electron laser providing intense and coherent extreme-ultraviolet light," Nat. Phys. **4**, 296–300 (2008).

[10] E. P. Benis, D. Charalambidis, T. N. Kitsopoulos, G. D. Tsakiris, and P. Tzallas, "Two-photon double ionization of rare gases by a superposition of harmonics," Phys. Rev. A **74**, 051402(R) (2006).

[11] K. Ishikawa and K. Midorikawa, "Two-photon ionization of He$^+$ as a nonlinear optical effect in the soft-x-ray region," Phys. Rev. A **65**, 043405 (2002).

[12] M. Ferray, A. L'Huillier, X. F. Li, G. Mainfray, and C. Manus, "Multiple-harmonic conversion of 1064 nm radiation in rare gases," J. Phys. B **21**, L31 (1988).

[13] A. McPherson, G. Gibson, H. Jara, U. Johann, T. S. Luk, I. A. McIntyre, K. Boyer, and C. K. Rhodes, "Studies of multiphoton production of vacuum-ultraviolet radiation in the rare gases," J. Opt. Soc. Am. B **4**, 595 (1987).

[14] T. Brabec and F. Krausz, "Intense few-cycle laser fields: Frontiers of nonlinear optics," Rev. Mod. Phys. **72**, 545 (2000).

[15] E. J. Takahashi, Y. Nabekawa, and K. Midorikawa, "Low-divergence coherent soft x-ray source at 13 nm by high-order harmonics," Appl. Phys. Lett. **84**, 4–6 (2004).

[16] T. Popmintchev, M. C. Chen, P. Arpin, M. M. Murnane, and H. C. Kapteyn, "The attosecond nonlinear optics of bright coherent x-ray generation," Nat. Photonics **4**, 822–832 (2010).

[17] E. Takahashi, Y. Nabekawa, T. Otsuka, M. Obara, and K. Midorikawa, "Generation of highly coherent submicrojoule soft x rays by high-order harmonics," Phys. Rev. A **66**, 021802(R) (2002).

[18] E. Takahashi, Y. Nabekawa, and K. Midorikawa, "Generation of 10-μJ coherent extreme-ultraviolet light by use of high-order harmonics," Opt. Lett. **27**, 1920 (2002).

[19] J.-F. Hergott, M. Kovacev, H. Merdji, C. Hubert, Y. Mairesse, E. Jean, P. Breger, P. Agostini, B. Carré, and P. Salières, "Extreme-ultraviolet high-order harmonic pulses in the microjoule range," Phys. Rev. A **66**, 021801(R) (2002).

[20] J. Mauritsson, P. Johnsson, E. Gustafsson, A. L'Huillier, K. J. Schafer, and M. B. Gaarde, "Attosecond pulse trains generated using two color laser fields," Phys. Rev. Lett. **97**, 013001 (2006).

[21] D. Shafir, H. Soifer, B. D. Bruner, M. Dagan, Y. Mairesse, S. Patchkovskii, M. Yu. Ivanov, O. Smirnova, and N. Dudovich, "Resolving the time when an electron exits a tunneling barrier," Nature (London) **485**, 343–346 (2012).

[22] F. Brizuela, C. M. Heyl, P. Rudawski, D. Kroon, L. Rading, J. M. Dahlström, J. Mauritsson, P. Johnsson, C. L. Arnold, and A. L'Huillier, "Efficient high-order harmonic generation boosted by below-threshold harmonics," Sci. Rep. **3**, 1410 (2013).

[23] P. B. Corkum, "Plasma perspective on strong-field multiphoton ionization," Phys. Rev. Lett. **71**, 1994 (1993).

[24] K. J. Schafer, B. Yang, L. F. DiMauro, and K. C. Kulander, "Above threshold ionization beyond the high harmonic cutoff," Phys. Rev. Lett. **70**, 1599 (1993).

[25] P. Salières, A. L'Huillier, and M. Lewenstein, "Coherence control of high-order harmonics," Phys. Rev. Lett. **74**, 3776 (1995).

[26] S. Kazamias, D. Douillet, F. Weihe, C. Valentin, A. Rousse, S. Sebban, G. Grillon, F. Augé, D. Hulin, and P. Balcou, "Global optimization of high harmonic generation," Phys. Rev. Lett. **90**, 193901 (2003).

[27]C. M. Heyl, J. Güdde, A. L'Huillier, and U. Höfer, "High-order harmonic generation with μJ laser pulses at high repetition rates," J. Phys. B **45**, 074020 (2012).

[28]E. Constant, D. Garzella, P. Breger, E. Mével, C. Dorrer, C. L. Blanc, F. Salin, and P. Agostini, "Optimizing high harmonic generation in absorbing gases: Model and experiment," Phys. Rev. Lett. **82**, 1668 (1999).

[29]Attotech HB.

[30]C. Lyngå, M. B. Gaarde, C. Delfin, M. Bellini, A. L'Huillier, T. W. Hänsch, and C.-G. Wahlström, "Studies of the temporal coherence of high-order harmonics," Phys. Rev. A **60**, 4823 (1999).

[31]C. Erny, E. Mansten, M. Gisselbrecht, J. Schwenke, R. Rakowski, X. He, M. B. Gaarde, S. Werin, and A. L'Huillier, "Metrology of high-order harmonics for free-electron laser seeding," New J. Phys. **13**, 073035 (2011).

[32]B. L. Henke, E. M. Gullikson, and J. C. Davis, "X-ray interactions: Photoabsorption, scattering, transmission, and reflection at $E = 50$-30000 ev, $Z = 1$–92," At. Data Nucl. Data Tables **54**, 181–342 (1993).

[33]M. Born and E. Wolf, *Principles of Optics* (Cambridge University Press, 1999).

[34]B. E. A. Saleh and M. C. Teich, *Fundamentals of Photonics* (John Wiley and Sons, 2007).

[35]R. A. Bartels, A. Paul, H. Green, H. C. Kapteyn, M. M. Murnane, S. Backus, I. P. Christov, Y. Liu, D. Attwood, and C. Jacobsen, "Generation of spatially coherent light at extreme ultraviolet wavelengths," Science **297**, 376 (2002).

[36]X. He, M. Miranda, J. Schwenke, O. Guilbaud, T. Ruchon, C. Heyl, E. Georgadiou, R. Rakowski, A. Persson, M. B. Gaarde, and A. L'Huillier, "Spatial and spectral properties of the high-order harmonic emission in argon for seeding applications," Phys. Rev. A **79**, 063829 (2009).

Paper IV

Carrier-envelope phase dependent high-order harmonic generation with a high-repetition rate OPCPA-system

P. Rudawski, A. Harth, C. Guo, E. Lorek, M. Miranda, C. M. Heyl,
J. Matyschok, T. Binhammer, U. Morgner, J. Mauritsson,
A. L'Huillier, and C. Arnold.

(2014) *Manuscript in preparation.*

Carrier-envelope phase dependent high-order harmonic generation with a high-repetition rate OPCPA-system

P. Rudawski[1], A. Harth[1], C. Guo[1], E. Lorek[1], M. Miranda[1], C. M. Heyl[1], J. Matyschok[2], T. Binhammer[2], U. Morgner[3], J. Mauritsson[1], A. L'Huillier[1], C. L. Arnold[1]

[1] Department of Physics, Lund University, P. O. Box 118, SE-22100 Lund, Sweden
[2] VENTEON Laser Technologies GmbH, Hertzstrasse 1b, D-30827, Garbsen, Germany
[3] Institut für Quantenoptik, Universität Hannover, Welfengarten 1, D-30167 Hannover, Germany

E-mail: `Piotr.Rudawski@fysik.lth.se`

Abstract. We perform high-order harmonic generation experiments using a high-repetition rate (200 kHz) laser system based upon optical-parametric chirped pulse amplification. The system delivers carrier-envelope-phase-stable 8 fs 10 μJ pulses at a central wavelength of 850 nm. High-order harmonics, generated in a high-pressure Ar jet, exhibit a strong CEP-dependence over the whole spectral range. The interference structures are analyzed and compared with single-atom simulations performed with the strong field approximation.

PACS numbers: 32.80.Qk, 32.80.Wr

Keywords: High-order harmonic generation, optical-parametric amplification, carrier-envelope phase, extreme nonlinear optics

Contents

1. Introduction

High-order harmonic generation (HHG) is a well-established method for the production of extreme ultraviolet (XUV) light pulses with attosecond duration [1]. This unique time scale has allowed a large number of groundbreaking experiments, such as the observation of the motion of valence electrons [2] or the measurement of photoionization time delays [3, 4] (see [1] for a more extensive review of possible applications).

The development of attosecond science strongly relies on the progress of ultrafast laser sources. Over more than twenty years, Chirped-Pulse Amplification (CPA) systems based on Ti:Sapphire technology have been used to drive XUV attosecond sources at repetition rates up to a few kHz. Many applications in attosecond science will however strongly benefit from attosecond sources operating at higher repetition rates, *i.e.* in the MHz range [5, 6, 7]. Examples of such applications are measurement schemes involving coincidence detection of two or more particles, which requires a low number of events per laser shot [8], but a large number of events per second to build up statistics. A different kind of application is in the field of surface science [9] where often space charge effects, in particular in applications involving imaging can be a serious obstacle. To compensate for this limitation, it is advantageous to operate at lower peak photon flux but higher average photon flux, *i.e.* higher repetition rate.

Optical parametric chirped pulse amplification (OPCPA) systems [10] are based on four-wave mixing in a nonlinear crystal, using as input waves, a stretched seed pulse and pump pulses of matched duration. The seed pulse is amplified while an idler pulse is generated. The current limitations in conventional amplifiers, such as gain narrowing and thermal lensing, are avoided in parametric amplification. OPCPA systems are especially advantageous for the production of low-energy, high-repetition rate pulses (1 MHz) [11, 12, 13] but are also developed for the production of few-cycle pulses with tens of mJ energy [14].

In this paper we present a HHG source driven by a compact OPCPA laser producing CEP-stable 8 fs, 10 μJ pulses, at 850 nm central wavelength, and 200 kHz repetition rate. To achieve intensities sufficient for efficient HHG, we focus the laser beam using an achromatic lens with 5 cm focal length into a high pressure gas jet. We observe a harmonic spectrum, which exhibits a strong CEP-dependence in the whole range. The results are compared to simulations based upon the Strong Field Approximation (SFA). The OPCPA system and HHG source are described in Section 1 and 2. The results are shown and discussed in Section 3.

2. Optical Parametric Chirp Pulse Amplification system

The laser system, sketched in Fig. 1, is composed of three parts: a broadband Ti:Sapphire oscillator, an Yb-based fiber amplifier, and a two-stage Non-collinear Optical-Parametric Amplifier (NOPA). The Ti:Sapphire oscillator produces an octave-spanning spectrum supporting pulses with durations below 5 fs at a repetition rate of 80 MHz. The spectral wings (blue boxes in the oscillator spectrum in Fig. 1) are filtered out and sent into an f-to-2f interferometer for CEP stabilization. A fast loop assures a CEP stability over more than 12 hours with an error below 80 mrad (3 Hz - 1 MHz). A small part of the oscillator spectrum around 1030 nm (10 nm bandwidth and 40 pJ of pulse energy) serves as seed for the fiber pump laser. Note that optical seeding of the fiber pump laser intrinsically synchronizes pump and seed in the NOPA stages leading to a small residual drift (tens of fs) due to slow refractive index changes. The main part of the spectrum (600 to 1020 nm, 2.5 nJ) seeds the OPCPA.

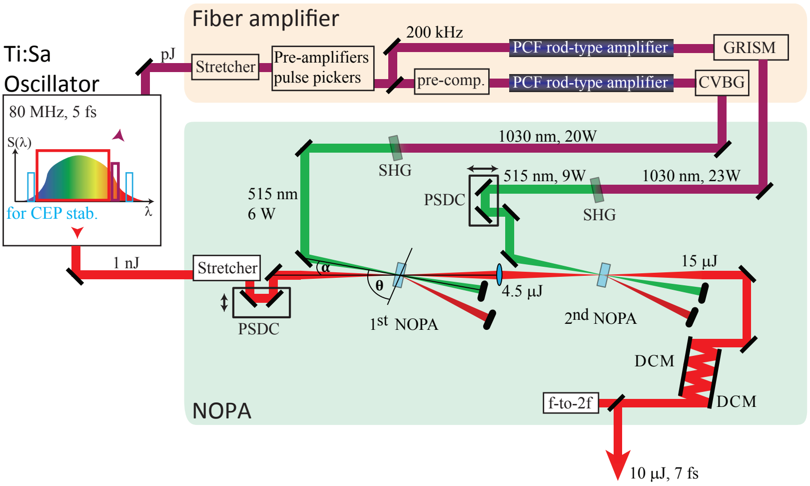

Figure 1. The OPCPA system; PCF - photonic crystal fiber, CVBG - chirp volume Bragg grating, SHG - second harmonic generation in BBO crystals, PSDC - pump-signal delay control, NOPA non-collinear optical parametric amplification in BBO crystals, α - non-collinear angle, θ - phase-matching angle, DCM - double chirp mirror.

The fiber amplifier is based on chirped-pulse amplification. The seed pulse from the oscillator is stretched to 250 ps in a Chirped Volume Bragg Grating (CVBG, 27 ps/nm) before it enters a pre-amplifier unit. The pre-amplifier consists of three fiber amplifiers. Two pulse pickers (an electro-optical and an acousto-optical) located between the three amplifiers are used to break down the repetition rate from 80 MHz to 200 kHz. After pre-amplification, the pulses are split into two independent main amplifier arms. Each arm incorporates a Yb-based photonic crystal rod-type fiber (NKT, DC 285/100, PM-Yb-ROD) and a compressor. The beam, from the first rod-type amplifier, is compressed with a CVBG with a dispersion curve opposite from that of the stretcher. An additional compressor, located before the rod-type fiber, compensates the dispersion the pre-amplifier and the rod-type amplifier. The beam out of the second rod-type amplifier is compressed with a GRISM (GRating-prISM combination). The two stages provide 20 and 23 W IR-average power respectively.

The fiber output is frequency doubled in two BBO crystals to 6.5 and 8.9 W, corresponding to 27 and 44 μJ energy per pulse (at 200 kHz). The two beams at 515 nm (pulse duration approximately 500 fs) pump the two parametric stages, amplifying the signal pulse from the Ti:Sapphire oscillator. For each NOPA stage, the delay between the seed and the pump is controlled by a manual translation stage (PSDC). Additionally, the first stage includes a motorized delay stage for automatic delay stabilization. To achieve a large amplification bandwidth, the seed and pump beams are non-collinearly crossed at an angle of about 2.4 deg in a 5 mm long Type-I BBO crystals. Phase-matching is achieved by choosing an angle of 24 deg between the pump beam (with polarization along the extraordinary axis) and the optical axis of the crystal. Since the seed, with polarization along the ordinary axis, propagates between the optical axis and the pump, the pump experiences an spatial walk-off towards the seed. This configuration, called Poynting-Vector-Walk-off Compensation (PVWC) geometry, is advantageous compared to non-PVWC geometry since it reduces the spatial distortion of the amplified beam as well as increases the compressibility [15]. The seed pulse is stretched to about 420 fs by transmission through a pair of BK7 wedges, the dispersion of the air path between the oscillator and the first NOPA stage and the dispersion of the first BBO crystal. After the amplification in the first NOPA-crystal (4.5 μJ), the pulse is pre-compressed by two reflections at a Double Chirp Mirror pair (-120 fs^2) to approximately 200 fs. The second NOPA-stage amplifies the signal to 15 μJ and the final compressor, based on the same type of DCMs, compresses the pulse in 16 bounces to below 7 fs [16]. A small part of the compressed beam (< 60 mW) can be used for a second f-to-2f interferometer to correct for slow CEP changes, caused mostly by thermal variations. The compressed output beam has an energy of 10 μJ per pulse at 200 kHz repetition rate.

3. High-order harmonic generation setup

The CEP-stable pulses from the OPCPA are sent into an HHG setup, illustrated in Figure 2. The setup comprises two chambers, one for the generation and one for the detection, separated by a small conical expanding hole used for differential pumping. Thus, the pressure in the generation chamber can be as high as 10^{-2} mbar (with a gas load), while that in the detection chamber remains below 10^{-7} mbar.

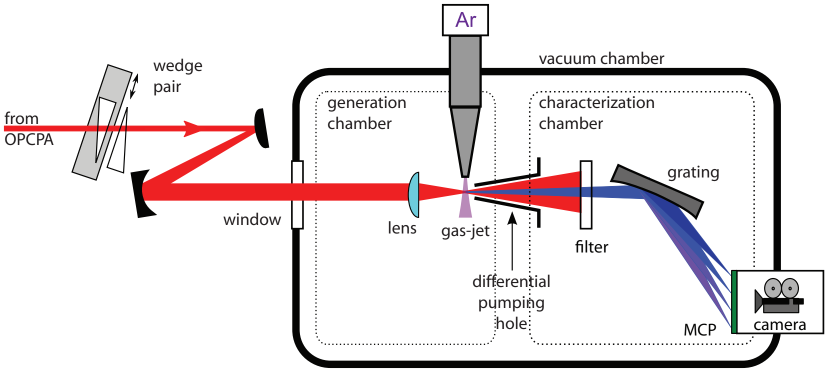

Figure 2. Experimental setup for HHG including a wedge pair, a telescope, and a vacuum chamber composed of a generation chamber and a characterization chamber hosting the XUV spectrometer.

The fundamental pulses are negatively chirped to pre-compensate additional dispersion of optical components used in the HHG setup, *i.e.* the vacuum window and the focusing lens. Fine tuning of the dispersion is carried out by a pair of BK7, anti-reflection coated, wedges mounted on a motorized translation stage. After the wedge-pair, the beam propagates through an all-reflective telescope, where the beam diameter is expanded from 2 to 5 mm and enters the vacuum chamber through a 0.5 mm-thick anti-reflection coated window. The fundamental beam is focused with an achromatic lens (f = 5 cm) into an effusive Ar-gas jet. However due to the large bandwidth of the pulses a small effect of chromatic aberration remains. According to the design data of the lens, the position of the focus varies by about 60 μm within a wavelength range from 650 to 1000 nm, which is comparable to the estimated Rayleigh length (50 μm). Figure 3 shows the spectral phase of the pulse obtained from a dispersion-scan measurement [17] after the lens and its reconstructed temporal pulse profile. With the central wavelength of 850 nm and a measured pulse duration of 8.4 fs the pulse includes 3 optical cycles under the full width at half maximum.

The Ar-gas jet exits a 90 μm wide nozzle, with a 4 bar backing pressure. The nozzle is located as close as possible to the laser beam by using a three-axis translation stage. A short focal length implies a small interaction volume and a steep Gouy-phase gradient across the focus with consequences for HHG phase matching. In order to compensate for both small volume and steep Gouy-phase gradient, a high gas density is needed. Focusing the fundamental beam with an f-number around 10 implies that a generation pressure $\mathrm{P_{opt}}$ of a few bars is needed to achieve phase matching [5]. The gas pressure

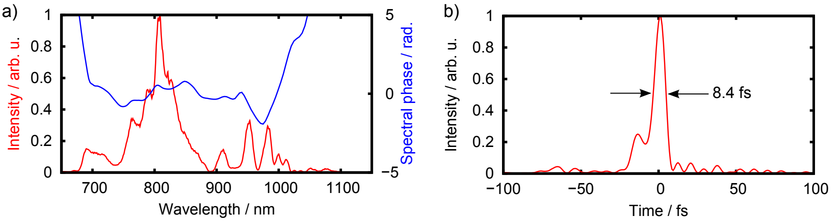

Figure 3. a) Spectral phase of the IR-pulse obtained from a d-scan measurement (blue) and power spectral density of the pulse (red). b) Reconstructed temporal pulse with a full width at half maximum of 8.4 fs.

used in the present setup is limited by the pumping system and is estimated to be below 1 bar. Thus, high-order harmonics are not generated phase-matched and a large contribution from the long electron trajectory emission is expected if the gas target is placed at the laser focus [18]. The gas target is therefore located behind the laser focus, so that the short trajectory contribution to HHG is selected.

The generated high-order harmonic radiation and the fundamental IR laser pulses enter the characterization chamber through the differential pump hole. The HHG beam can be separated from the fundamental by metallic filters, e.g. 200 nm-thick aluminum or titanium filters installed in a motorized filter mount. The XUV radiation is characterized with a spectrometer equipped with a cylindrical diffraction grating (Hitachi, 600 lines/mm), a Micro Channel Plate (MCP), and a phosphor screen. The MCP is coated with a CsI layer in order to extend its sensitivity range in the VUV region. Spatially-resolved harmonic spectra are recorded by imaging the phosphor screen with a CCD camera. The spectra are calibrated in photon energy using the well known transmission edges of different filters [19].

4. Results

Figure 4 (a) shows a typical harmonic spectrum in Ar from 25 to 50 eV. A spectrum integrated over the central region delimited by the dotted white lines is presented in Figure 4 (b). The harmonics are spectrally broad, with a continuous behavior above 40 eV (cut-off region).

In Figure 5, we present a HHG spectrum as a function of the wedge position (see wedge pair in Fig. 1). Moving the wedge pair changes the carrier-envelope phase of the IR-pulses, and the overall dispersion of the pulse, which affects the pulse duration and intensity. Such a scan takes less than a minute, so that laser instabilities (e.g. CEP fluctuations) are negligible. About 30 μm BK7 glass shifts the carrier-envelope phase by π while the change in pulse duration is negligible. The scan shown in Fig. 5 spans over a variable glass thickness of 1.6 mm and both CEP and intensity effects are visible. Below 1.8 and above 2.4 mm, the pulse is considerably chirped and the laser intensity is too

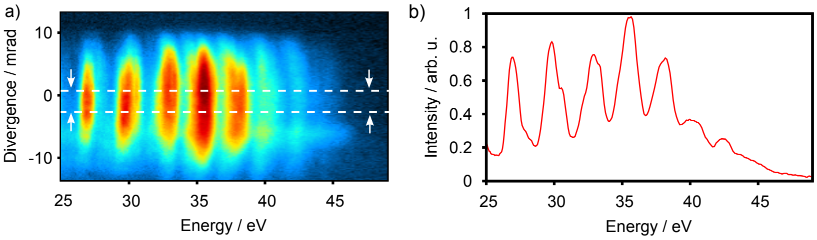

Figure 4. a) Spatial beam profile of high-order harmonics at the MCP phosphor screen after energy calibration of the lower axis. The integration of the spatial profile (using only the marked region) leads to the HHG spectrum shown in b).

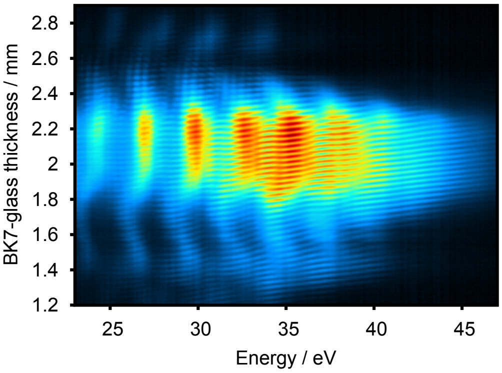

Figure 5. HHG spectrum scan over the BK7 wedge position. The influence of the change of the carrier-envelope phase over the whole HHG spectrum is clearly visible as well as the influence of the material dispersion on the IR pulse duration.

low to efficiently generate high-order harmonics. HHG is efficient with about 2.1 mm of BK7, corresponding to the shortest pulses. The most striking effect observed in these experiments is the strong CEP dependence over the whole energy range, leading to a complex interference structure.

CEP-dependent effects have been observed in previous works [20, 21, 22, 23, 7], but have been limited to specific spectral regions, such as the cut-off [20] or the region between consecutive harmonic spectral peaks [22, 23]. The effect observed in our experiment is shown in more detail in Fig. 6 (a) (extracted from Fig. 5) with a change in glass thickness limited to 0.3 mm so that the modification in pulse duration can be neglected. Fig. 6 (b) presents two lineouts from Fig. 6 (a) with a phase change of $\Delta\varphi = \pi/2$. Three different regions can be distinguished: In region I, close to the cut-off (45 eV), the spectrum shifts from odd to even harmonics as the CEP changes

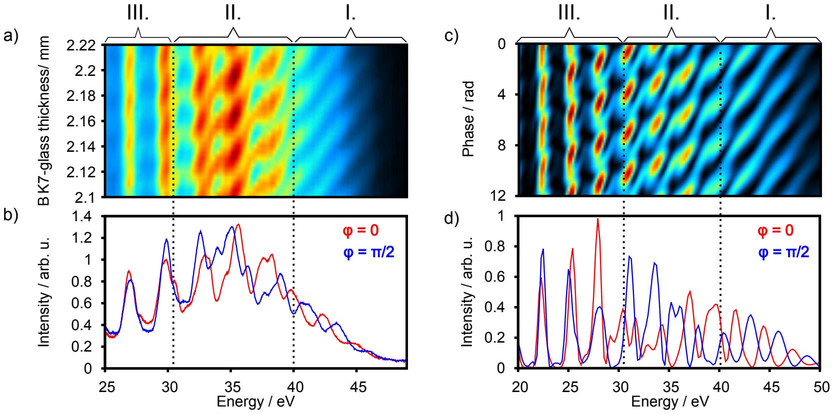

Figure 6. Measured a) and simulated c) HHG spectrum over the carrier-envelope phase. Corresponding to a), figure b) shows two single curves with a phase difference of $\pi/2$. The same goes for figure c) and d). Also three regions are marked in the figures: region I, II and III, which defines different types of CEP dependence.

by $\pi/2$. In region III, the position of the harmonic peaks does not change, but their amplitude depends on the CEP, in a non trivial manner. Finally, in region II, the harmonic spectrum becomes quite complex, with structures that are not located at multiple orders of the laser frequency.

A simulation of the HHG spectrum based on the Strong Field Approximation (SFA) [24] shows a similar behavior, as shown in Fig. 6 c) and d). The simulation calculates the single atom response, and does not include propagation effects. The fundamental field has a Gaussian envelope of 5 fs (FWHM), the central wavelength is 850 nm and the peak intensity 1.5×10^{14}W/cm^2. Although the spectral width of the harmonics is smaller than in the measurement, the behavior of the interference structure is very well reproduced.

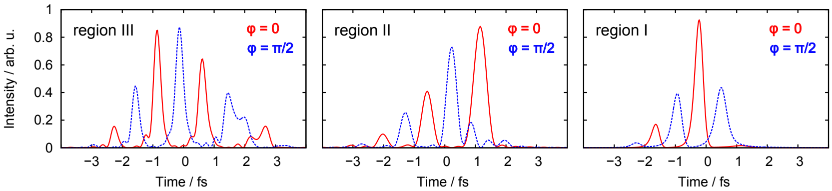

Figure 7. Analysis of the CEP dependent HHG spectrum in the time domain.

In order to understand the physics behind the observed interferences, we examine the temporal structure of the attosecond pulse trains in each of the regions indicated in

Fig. 6, by spectrally windowing and Fourier transforming the calculated dipole moment. The different regions can be distinguished by the number of contributing attosecond pulses. In region I, depending on the CEP, there are one main pulse and a satellite, or two pulses of comparable intensity. In region II, there are essentially two pulses with variable strength. Finally, in region III there are two or three pulses. The different spectral regions also differ by the variation of the dipole phase, which is traditionally written as

$$\Phi(\Omega, I) = -\alpha_\Omega I = -(\beta\Omega - \alpha_0)I \tag{1}$$

where β the slope of the (linear) variation of α_Ω with frequency ($\alpha_0 \simeq 0$). The phase variation for the short trajectory is almost zero at low frequency and increases towards the cut-off [25]. Changing the CEP changes the relative phase $\Phi(\Omega, I)$ of consecutive attosecond pulses. For a short train of pulses in the cut-off region, $\Phi(\Omega, I)$ differs between the leading edge and the maximum of the fundamental pulse, so that interferences become constructive at a different frequency. In contrast, for a longer train of pulses and at lower frequencies corresponding to the plateau region, the phase variation between consecutive attosecond pulses does not change the position of the interference structure. Region II shows an intermediate case, with an interesting, almost chaotic, spectral behavior, induced by a very regular phase variation.

5. Conclusion

The paper presents high-order harmonic generation driven by a high-repetition rate OPCPA system. In spite of the low energy per pulse (10 μJ), there is no difficulty in generating harmonics in Ar. This is done using a tight focusing geometry and a high pressure gas jet with a narrow aperture. The excellent CEP-stability of the system allows us to study in details the HHG spectrum as a function of CEP. Regular interference structures are observed over the whole spectrum. The spectrum evolves from harmonic peaks whose amplitude changes with the CEP, to a region which almost supports single attosecond pulses, showing an oscillation between even and odd harmonics.

Acknowledgments

This research was supported by the Marie Curie Research Training Network ATTOFEL, the European Research Council (ALMA, PALP), the Knut and Alice Wallenberg foundation and the Swedish Research Council.

References

[1] F. Krausz and M. Ivanov. Attosecond physics. *Reviews of Modern Physics*, 81(1):163–234, 2009.

[2] E. Goulielmakis, Z. Loh, A. Wirth, R. Santra, N. Rohringer, V. S Yakovlev, S. Zherebtsov, T. Pfeifer, A. M. Azzeer, M. F. Kling, S. R. Leone, and F. Krausz. Real-time observation of valence electron motion. *Nature*, 466:739–743, 2010.

[3] M. Schultze, M. Fieß, N. Karpowicz, J. Gagnon, M. Korbman, M. Hofstetter, S. Neppl, A. L. Cavalieri, Y. Komninos, Th. Mercouris, C. A. Nicolaides, R. Pazourek, S. Nagele, J. Feist, J. Burgdörfer, A. M. Azzeer, R. Ernstorfer, R. Kienberger, U. Kleineberg, E. Goulielmakis, F. Krausz, and V. S. Yakovlev. Delay in photoemission. *Science*, 328:1658–1662, 2010.

[4] K. Klünder, J. M. Dahlström, M. Gisselbrecht, T. Fordell, M. Swoboda, D. Guénot, P. Johnsson, J. Caillat, J. Mauritsson, A. Maquet, R. Taïeb, and A. L'Huillier. Probing single-photon ionization on the attosecond time scale. *Phys. Rev. Lett.*, 106:143002, 2011.

[5] C M Heyl, J Güdde, A L'Huillier, and U Höfer. High-order harmonic generation with μj laser pulses at high repetition rates. *Journal of Physics B: Atomic, Molecular and Optical Physics*, 45(7):074020, 2012.

[6] Johan Boullet, Yoann Zaouter, Jens Limpert, Stéphane Petit, Yann Mairesse, Baptiste Fabre, Julien Higuet, Eric Mével, Eric Constant, and Eric Cormier. High-order harmonic generation at a megahertz-level repetition rate directly driven by an ytterbium-doped-fiber chirped-pulse amplification system. *Opt. Lett.*, 34(9):1489–1491, May 2009.

[7] Manuel Krebs, Steffen Hädrich, Stefan Demmler, Jan Rothhardt, Amelle Zaïr, Luke Chipperfield, Jens Limpert, and Andreas Tünnermann. Towards isolated attosecond pulses at megahertz repetition rates. *Nature Photonics*, 7:555–559, 2013.

[8] Erik P. Månsson, Diego Guénot, Cord L. Arnold, David Kroon, Susan Kasper, J. Marcus Dahlström, Eva Lindroth, Anatoli S. Kheifets, Anne L'Huillier, Stacey L. Sorensen, and Mathieu Gisselbrecht. Double ionization probed on the attosecond timescale. *Nat Phys*, 10, 2014.

[9] A. Mikkelsen, J. Schwenke, T. Fordell, G. Luo, K. Klünder, E. Hilner, N. Anttu, A. A. Zakharov, E. Lundgren, J. Mauritsson, J. N. Andersen, H. Q. Xu, and A. L'Huillier. Photoemission electron microscopy using extreme ultraviolet attosecond pulse trains. *REVIEW OF SCIENTIFIC INSTRUMENTS*, 80:123703, 2009.

[10] A. Dubietis, R. Butkus, and A.P. Piskarskas. Trends in chirped pulse optical parametric amplification. *Selected Topics in Quantum Electronics, IEEE Journal of*, 12(2):163–172, March 2006.

[11] Jan Rothhardt, Stefan Demmler, Steffen Hädrich, Jens Limpert, and Andreas Tünnermann. Octave-spanning opcpa system delivering cep-stable few-cycle pulses and 22 w of average power at 1 mhz repetition rate. *Opt. Express*, 20(10):10870–10878, May 2012.

[12] Marcel Schultze, Thomas Binhammer, Guido Palmer, Moritz Emons, Tino Lang, and Uwe Morgner. Multi-μj, cep-stabilized, two-cycle pulses from an opcpa system with up to 500 khz repetition rate. *Opt. Express*, 18(26):27291–27297, Dec 2010.

[13] Anne Harth, Marcel Schultze, Tino Lang, Thomas Binhammer, Stefan Rausch, and Uwe Morgner. Two-color pumped opcpa system emitting spectra spanning 1.5 octaves from vis to nir. *Opt. Express*, 20(3):3076–3081, Jan 2012.

[14] Franz Tavella, Yutaka Nomura, Laszlo Veisz, Vladimir Pervak, Andrius Marcinkevičius, and Ferenc Krausz. Dispersion management for a sub-10-fs, 10 tw optical parametric chirped-pulse amplifier. *Opt. Lett.*, 32(15):2227–2229, Aug 2007.

[15] T. Lang, A. Harth, J. Matyschok, T. Binhammer, M. Schultze, and U. Morgner. Impact of temporal, spatial and cascaded effects on the pulse formation in ultra-broadband parametric amplifiers. *Opt. Express*, 21(1):949–959, Jan 2013.

[16] Jan Matyschok, Tino Lang, Thomas Binhammer, Oliver Prochnow, Stefan Rausch, Marcel Schultze, Anne Harth, Piotr Rudawski, Cord L. Arnold, Anne L'Huillier, and Uwe Morgner. Temporal and spatial effects inside a compact and cep stabilized, few-cycle opcpa system at high repetition rates. *Opt. Express*, 21(24):29656–29665, Dec 2013.

[17] Miguel Miranda, Thomas Fordell, Cord Arnold, Anne L'Huillier, and Helder Crespo. Simultaneous compression and characterization of ultrashort laser pulses using chirped mirrors and glass wedges. *Opt. Express*, 20(1):688–697, Jan 2012.

[18] C. M. Heyl, J. Guedde, U. Hoefer, and A. L'Huillier. Spectrally resolved maker fringes in high-order harmonic generation. *Physical Review Letters*, 107(033903), 2011.

[19] B.L. Henke, E.M. Gullikson, and J.C. Davis. X-ray interactions: Photoabsorption, scattering, transmission, and reflection at e = 50-30,000 ev, z = 1-92. *Atomic Data and Nuclear Data Tables*, 54(2):181 – 342, 1993.

[20] A. Baltuška, Th. Udem, M. Uiberacker, M. Hentschel, E. Goulielmakis, Ch. Gohle, R. Holzwarth, V. S. Yakovlev, A. Scrinzi, T. W. Hänsch, and F. Krausz. Attosecond control of electronic processes by intense light fields. *Nature*, **421**:611, 2003.

[21] E. Mansten, J. M. Dahlström, J. Mauritsson, T. Ruchon, A. L'Huillier, J. Tate, M. B. Gaarde, P. Eckle, A. Guandalini, M. Holler, F. Schapper, L. Gallmann, and U. Keller. Spectral Signature of Short Attosecond Pulse Trains. *Phys. Rev. Lett.*, 102(8):083002, Feb 2009.

[22] G. Sansone, C. Vozzi, S. Stagira, M. Pascolini, L. Poletto, P. Villoresi, G. Tondello, S. De Silvestri, and M. Nisoli. Observation of Carrier-Envelope Phase Phenomena in the Multi-Optical-Cycle Regime. *Phys. Rev. Lett.*, 92:113904, 2004.

[23] G. Sansone, E. Benedetti, J.-P. Caumes, S. Stagira, C. Vozzi, M. Pascolini, L. Poletto, P. Villoresi, S. De Silvestri, and M. Nisoli1. Measurement of Harmonic Phase Differences by Interference of Attosecond Light Pulses. *Phys. Rev. Lett.*, 94:193903, 2005.

[24] M. Lewenstein, Ph. Balcou, M.Yu. Ivanov, A. L'Huillier, and P. B. Corkum. Theory of high-order harmonic generation by low-frequency laser fields. *Phys. Rev. A*, 49:2117, 1994.

[25] K. Varjú, Y. Mairesse, B. Carre, M. B. Gaarde, P. Johnsson, S. Kazamias, R. Lopez-Martens, J. Mauritsson, K. J. Schafer, Ph. Balcou, A. L'Huillier, and P. Salières. Frequency chirp of harmonic and attosecond pulses. *J. Mod. Opt.*, 52:379, 2005.

Paper V

Conceptual Design Report for a gas HHG beamline at ELI-ALPS

C. M. Heyl, P. Rudawski, F. Brizuela, P. Johnsson, C. L. Arnold, and A. L'Huillier.

(2012) *Report ELI-ALPS*.

Conceptual Design Report for a gas HHG beamline at ELI-ALPS

Christoph M. Heyl, Piotr Rudawski, Fernando Brizuela, Per Johnsson,
Cord L. Arnold, and Anne L'Huillier
Physics Department, Lund University, PO Box 118, SE-221 00 Lund, Sweden,
November 21, 2012

1. Aim of the CDR

The aim of the CDR is specified below:

> Preparing a conceptual design of the gas HHG beamline to be driven by the SYLOS laser of the ELI-ALPS facility with the driver source parameters provided in two phases: *phase 1*: 1 kHz, ~30 mJ, <10 fs, CEP stabilized, *phase 2*: 1 kHz, ~100 mJ, <5 fs, CEP stabilized. If isolated attosecond pulses cannot be produced with the given parameters, gating techniques have to be foreseen. Characterization of the produced attosecond pulses has to be included. The design should address the question of HHG source development needs vs. user availability and that both types of experiments will have to be performed during facility operation. The design also involves a planned layout, laboratory space and supply requirement estimates, and a full equipment list including necessary diagnostic equipment.

Additional information was provided by ELI-ALPS during the confection of this CDR:

- Estimated laser beam diameter: 30 mm
- Estimated laser spatial profile quality: $M^2 = 1.1$
- Damage threshold for mirrors: 200 mJ/cm^2 for *phase 1* and 500 mJ/cm^2 for *phase 2*

The performance of the laser for the two phases is summarized in Table 1.

	Pulse energy (mJ)	Pulse duration (fs)	estimated beam diameter (mm)	repetition rate (kHz)	Average power (W)
phase 1	30	<10	30	1	30
phase 2	100	<5	30	1	100

Table 1: SYLOS laser parameters.

2. System overview and general requirements

The main layout of the proposed setup is shown in Figure 1. The system is separated into four units connected by vacuum tubes. The distances between the individual units can be changed in order to ensure the optimum performance of the system in its different phases (viz. *phase 1* and *2*). In the following, we make a few general comments on the laser beam requirements, followed by a brief overview of the system while a more detailed description of the individual units is given in Section 3.

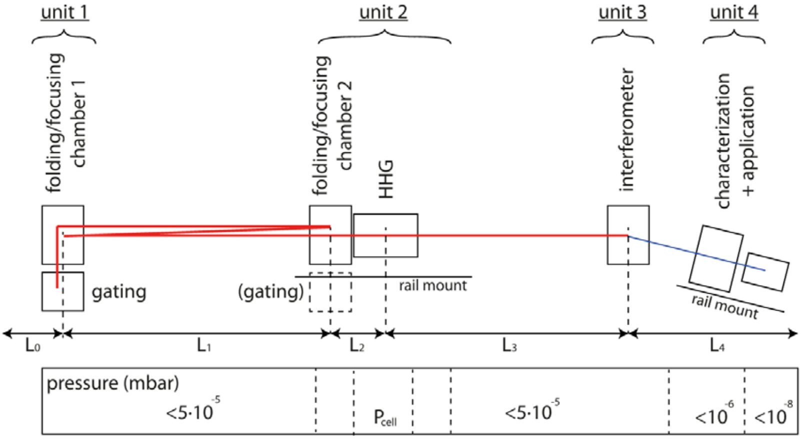

Figure 1: System overview and vacuum specifications. The given distances are labeled as follows: L_0: space before the first focusing/folding chamber to center of this chamber; L_1: center of first focusing/folding chamber to center second focusing/folding chamber; L_2: center of second focusing/folding chamber to HHG cell center; L_3: HHG cell center to center of interferometer chamber; L_4: center of interferometer chamber to end of the beamline (including characterization & application area).

The large scale of the system and the extreme laser parameters set high requirements for beam propagation and focusing, and on the reflective optics. Due to the high average power, a very good *heat transfer management* has to be ensured for all optics in the beam path. The long beam propagation distances will require high beam pointing stability. Since the distance from the laser output to the beamline is not defined, we define the pointing stability as a lateral displacement of the center of mass of the beam at the generation or application point, which should be kept below 100 µm. If such stability is not provided by the laser, an *active beam pointing stabilization* system should be implemented before entering the HHG setup. Further, *variation of the pulse energy* should be possible. The presented setup requires an *s-polarized* (vertically polarized) laser field (see also Section 3.3). A number of *alignment cameras* have to be foreseen along the beamline. As a minimum, we suggest two points to be imaged for alignment: one in *unit 4* (as described in Section 3.4) and another which images the entrance of the gas cell in *unit 2*. Both cameras can be mounted outside the vacuum system and image through viewports.

After the compressor, the laser beam should propagate under vacuum into a first vacuum chamber at *unit 1* where it can pass an optical setup modifying the beam for gating purposes (Section 3.2). Alternatively it can enter at *unit 2* (in this case, the gating setup would be located here), depending on the focusing geometry. Another vacuum chamber at *unit 1* contains a focusing mirror and beam folding mirror(s). The second part of the beam folding setup is located in the first vacuum chamber at *unit 2* which is connected to another chamber which acts as an entrance to the HHG gas cell. The HHG cell is located at the center of *unit 2* at the focus of the laser beam. Another vacuum chamber acts as the exit from the HHG cell. Both entrance and exit chambers ensure differential pumping between the gas cell and the connecting beamline tubes. The fundamental and harmonic beams co-propagate to *unit 3* which contains an interferometric setup as well as filters in order to be able to

(i) separate the fundamental and harmonic beams,
(ii) adjust the time delay between the fundamental and attosecond pulses,
(iii) filter the harmonic spectrum, and
(iv) possibly compress the attosecond pulses.

Unit 4 contains spectrometers and detectors to temporally, spectrally and spatially characterize the produced pulses. From *unit 4,* the generated attosecond pulses can be sent to user setups.

Besides the general layout, Figure 1 specifies upper limits for the vacuum pressure. Due to the relatively long beam propagation distances, the pressure inside the straight tube sections has to be kept at least below $5\cdot10^{-5}$mbar. The HHG cell pressure is discussed in Section 3.1. The pressure at *unit 4* should be seen as an upper limit for the characterization chamber. Depending on the application, a much lower pressure might be necessary in the application chamber.

In the following, we give a detailed description of our design, in four sections: Focusing and HHG cell, Gating, Interferometer, and Characterization.

3 Detailed description of the design

3.1 Focusing & HHG cell

The HHG beamline is based on a loose focusing concept allowing for the generation of attosecond pulses with high efficiency. Phase matching considerations suggest a long, non-guiding generation medium with low density[1]. The concept upscales well-known HHG beamline design considerations at much shorter focal geometries where short gas cells are typically used.

---

[1] Heyl, C. et al., J. Phys. B, **45**:074020 (2012).

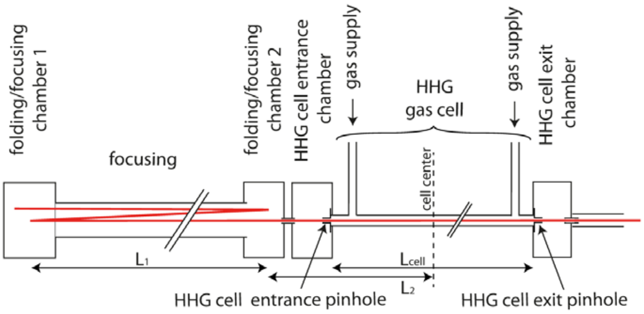

Figure 2: Focusing and gas cell layout. As an example, a beam folded into three sections (N = 3) is shown.

Focusing layout

We consider two different operation modes which imply different system optimization parameters in order to achieve single attosecond pulse generation *(operation mode 1)* or highest possible XUV flux *(operation mode 2).*
Operation mode 1, which is based on ionization gating[2] (Section 3.2), requires an intensity which is approximately one order of magnitude higher than for *operation mode 2*. We therefore consider different focusing geometries for the two operation modes in order to achieve the best efficiency. Further, different focusing geometries are considered for *phase 1* and *phase 2*. In the suggested design, a switch between the two modes is possible by changing the focal length and the cell length (L_{cell}), while adjusting the number of beam folding sections to keep the distances between the units fixed. In order to allow for very loose focusing geometry while limiting the total size of the system, the focused laser beam can be folded, as shown in Figure 2. Instead of folding the focused beam, a telescope setup could be used to reduce the beam size and reach a loose focusing geometry over a shorter distance. The main limitation in both configurations, which imposes the length of the focusing section L_1, is the intensity at the last optical element before the focus. A telescope setup does not provide any major advantages, but might complicate changing the focal geometry. We therefore suggest focusing with long focal length optics and folding the focused laser beam. In addition, a *variable aperture* should be placed before the focusing optics, to fine tune the focusing geometry. If the estimated beam quality parameter for the laser cannot be achieved, we suggest implementing *adaptive optics* (e.g. a mirror before the focusing element as well as a wave front sensor behind) to compensate for non-perfect focusing of the laser beam in the gas cell.

Generation cell

The generation cell consists of a straight tube, mounted between an entrance and an exit chamber. The beam enters and exits the cell through a short tube section with a diameter of a

---

[2] Ferrari, F. et al**.,** Nature Photonics, **4**:857 (2010).

few millimeters. We suggest using two short tube sections instead of simple pinholes in order to improve the differential pumping situation between the cell and the vacuum tubes. The width of the short tube sections (as well as of the cell in general) has to be chosen large enough to avoid clipping the laser beam, taking into account beam pointing fluctuations which are difficult to estimate at the current status. For differential pumping purposes and in order to limit the gas flow into the long connecting tube section along L_1, another thin tube section should separate the HHG cell entrance chamber and the last folding mirror chamber. A fourth thin tube section after the HHG cell exit chamber ensures a low gas pressure in the tube along L_3.

All chambers of *unit 2* (including the HHG cell) should be mounted on a rail system. The cell itself consists of either several tube sections or alternatively, a long bellow. Changing the cell length simply requires a movement of entrance and exit chamber plus adjustment of the relevant tubing. Further, the exact position of *unit 2* can easily be adjusted by moving the entire unit on the rail system. In the current design, considering the very loose focusing geometry, we expect only a very weak dependence of the generated XUV emission on the focus position. The focus is therefore placed in the center of the gas medium. Furthermore, due to this geometry, we expect that phase matching can be achieved without using quasi phase matching techniques or a guiding cell geometry. We therefore suggest a gas cell geometry with constant pressure and constant diameter that exceeds the size of the focused beam.

Pressure and gas cell length were estimated by scaling up known experimental parameters at much shorter focusing geometries[3] as well as by theoretical simulations. The given gas pressure should be considered as an approximate value, which should to be adjusted once the system is in operation. The gas pressure depends not only on the focusing geometry, but also on other parameters like the gas type (typically xenon, argon, neon, helium), the laser intensity, and the generated wavelength of interest.

System parameters

The estimated system parameters are listed in Table 2. The focal length for *operation mode 1* (*operation mode 2*) was calculated considering a peak intensity around $5{\cdot}10^{15}$ W/cm^2 ($5{\cdot}10^{14}$ W/cm^2), for a perfectly focused Gaussian beam. The required intensities for both operation modes are typically less than these values. We consider higher values in order to take into account non-perfect focusing.

---

[3] Heyl, C. et al., J. Phys. B, **45**:074020 (2012).

	focal length (m) ~ L_1 x N + L_2	L_1 (m)	number of folding sections (N)	L_2 (m)	gascell length (m)	peak fluence at last mirror (mJ/cm^2)	min L_3 (m)	expected XUV beam divergence (µrad)	P_{cell} (mbar)
phase 1									
Operation mode 1	~12	4,9	2	1,7	0,16	26	2	75	2
Operation mode 2	~36	4,9	7	1,7	1,4	170	6	25	0,2
phase 2									
Operation mode 1	~30	12,2	2	5	1	82	6	30	0,3
Operation mode 2	~90	12,2	7	5	9	428	15	10	0,03

Table 2: Main system parameters for the different phases and operation modes.

The folding geometry was chosen in order to

(i) minimize L_1 while keeping the peak fluence at the last folding mirror below the damage threshold values provided in Section 1,

(ii) ensure easy conversion[4] between *operation mode 1* and *2*, and

(iii) keep the focal length as long as possible in order to maximize the XUV flux.

The system layout can also accommodate intermediate situations between the two modes, by changing the number of folding sections and gas cell length.

As an estimate for the damage threshold, we assume the maximum peak fluence values given in Section 1. Two different values are considered since a further mirror development between *phase 1* and *phase 2* is planned. We further note that the peak fluence should only be seen as one limiting factor. Thermal load due to the very high average power must also be considered. The folding geometry as well as the length L_3 were calculated considering the above mentioned peak fluence values, assuming a 45º angle of incidence at the interferometer (see Section 3.3).

The conversion efficiency depends on the generation gas. In argon, for example, for *operation mode 1* we expect a conversion efficiency for each harmonic order of ~10^{-5}. For *operation mode 2*, where a continuum spectrum is generated, we expect a conversion efficiency of ~10^{-6} into the plateau region. Using lighter gases (Ne or He) which enable to achieve higher photon energies, the conversion efficiency is approximately one order of magnitude less.

3.2 Gating

Single attosecond pulse (SAP) generation requires the confinement of the high-order harmonic emission to only one half-cycle of the IR field (1.3 fs). We propose to use ionization gating[5] as the main technique for both *phase 1* and *phase 2*, based on the high laser intensity

---

[4] Conversion between operation modes requires changing the focusing optics, number of folding sections, and gas cell length, without changing the distances between the units.

[5] Ferrari, F. et al**.,** Nature Photonics, **4**:857 (2010).

and the short pulse duration of the source. The required peak intensity for ionization gating is well above the saturation intensity, at which most of the medium ionizes. In this regime, the field strength increases rapidly in the rising edge of the pulse, resulting in a steep ionization front. Only one half-cycle contributes significantly to HHG, whereas the generation from the following sub-cycles is suppressed due to depletion of the generation medium. There are two main requirements for the ionization gating technique:

(i) Short pulse duration and high laser intensity in order to allow for efficient HHG during only one half-cycle of the laser.
(ii) Selection by spectral filtering of the continuous part of the HHG spectrum.

Requirement (i) is easily achieved by the performance of the laser system. In *operation mode 1* the intensity in the gas cell largely exceeds that necessary for HHG. The description of the focusing geometry required for this *operation mode* for both phases was presented in Section 3.1. Requirement (ii) can be achieved either by using metallic filters (Section 3.3) or multilayer mirrors (Section 3.4).

As an alternative method for SAP generation in *phase 1*, we propose the Double Optical Gating (DOG)[6] technique, which combines polarization gating[7] and two-color HHG. The basic idea of polarization gating is that the fundamental field is made elliptical during most of the pulse except during a short time at the center of the pulse, thus suppresing HHG. Using a combination of fundamental and its second harmonic, attosecond pulses are generated in one half-cycle of the fundamental field[8]. The DOG technique requires thin transmissive optics (less than 0.5 mm to keep the B-integral below 1 in *phase 1*) making it unsuited for *phase 2*.

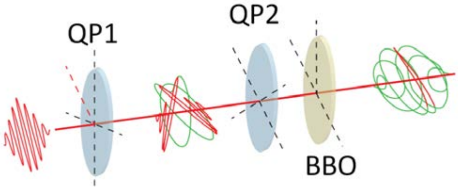

Figure 3: Double optical gating setup, from ref.[9]. QP1 and QP2 - quartz plates, BBO – barium borate crystal.

A DOG setup can easily inserted in the fundamental beam. Since it uses transmission optics, dispersion precompensation is required.

The experimental setup (Figure 3) includes two quartz plates (QP1 and QP2) and a barium borate crystal (BBO). The first quartz plate (QP1), with optical axis at 45° with respect to the incoming pulse, creates two orthogonally polarized and delayed components. When the two components overlap, the polarization is circular. The second quartz plate (QP2) combined with the BBO crystal act as a quarter waveplate, changing the linearly polarized part into

---

[6] Mashiko et al. Phys. Rev. Lett. **100**:103906 (2008).
[7] Tcherbakoff et al. Phys. Rev. A **68**:043804 (2003).
[8] Mauritsson et al. Phys. Rev. Lett. **97**:013001 (2006).
[9] Sansone et al. Nat. Phot. **5:**655 (2011).

circularly polarized and vice versa. The type I BBO crystal generates the second harmonic. Fine tuning of the sub-cycle delay is achieved by tilting the second quartz plate.

3.3 Interferometer

After HHG, the fundamental IR field must be separated from the harmonic beam. One way of efficiently doing so is by using fused silica plates with antireflection (AR) coatings for the infrared[10]. By using these plates near grazing incidence, the harmonic spectrum is reflected while the IR field is transmitted. Depending on the application, the harmonic spectra might need to be further filtered to remove low-order harmonics or to select cutoff spectral region in order to generate single attosecond pulses. This can be achieved through the use of thin metallic filters whose thickness and material composition determine the transmitted bandwidth[11]. These filters can also provide some temporal compression of attosecond pulses by compensating intrinsic HHG chirp[12]. The time duration of the attosecond pulses can be measured by cross correlation using a fraction of the residual IR field, with a variable delay relative to the attosecond pulses, as described in Section 3.4. We propose a compact (40 cm × 20 cm) interferometer to separate the harmonic spectrum from the IR, filter appropriately the spectrum, and combine the IR and XUV pulses with a controlled time delay. A schematic of this setup is shown in Figure 4.

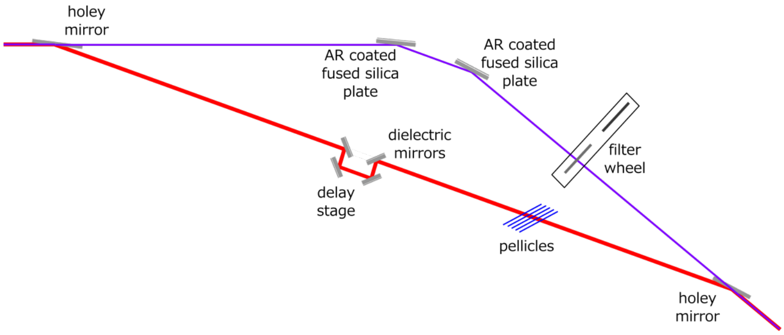

Figure 4: Interferometric setup for attosecond pulse generation and measurement.

The different divergence of the IR and harmonic beams provides a simple way of separating and recombining them using holey mirrors. In one arm of the interferometer, the harmonic beam, which is very collimated, passes through a hole in the mirror and is reflected off two AR-coated fused silica plates at grazing incidence (e.g. 10 degrees incidence angle). The hole should be larger than the expected XUV beam size at this point. The beam size for *Operation mode 2* should be considered in each phase to avoid changing the mirror when switching modes. The combination of the holey mirror and the two fused silica plates with AR coating for the fundamental, ensures the complete elimination of the IR beam in this arm. The XUV

---

[10] Gustafsson et al. Opt. Lett. **32**:1353 (2007).
[11] Bourassin-Bouchet et al. New J. Phys. **14**:023040 (2012).
[12] López-Martens et al. Phys. Rev. Lett. **94**:033001 (2005).

reflectivity of the coated fused silica plates ranges from 40% to 20% per reflection in the spectral range of 20 eV to 100 eV for a 10 degree incidence angle. After the second plate, a wheel with thin metallic film filters is placed providing appropriate filtering of the harmonic spectrum. The dielectric holey mirror reflects the more divergent IR beam in the second arm of the interferometer. In this arm, a piezo-controlled delay stage is added to adjust the optical path difference between the two arms. The delay stage should be able to scan 30 µm with a precision better than 5 nm during measurements. In the case of generating harmonics with the DOG technique described in Section 3.2, pellicles at Brewster angle can be added to this arm to remove the residual circularly polarized light which is unwanted in the cross correlation measurements (in the figure the pellicles have been drawn at a different angle for clarity). The distance between the generation cell and the interferometer is dictated by the damage threshold of the first holey mirror and fused silica plate and is listed as L_3 in Table 2 for the different stages and operation modes.

3.4 Characterization

This Section describes the spatial, spectral, and temporal characterization of the radiation produced in the generation chamber. The central element here is an arrangement of three (or more) mirrors, mounted on a translation and rotation stage, with the purpose of redirecting the incoming VUV, XUV, and IR radiation towards different application and characterization stations, arranged circularly around the deflection mirrors. In particular, single attosecond pulses (SAPs) as well as attosecond pulse trains (APTs) can be directly characterized at their application ports. The layout is sketched in Figure 5. For the purpose of redirecting the radiation to different ports, we envisage a metallic coated mirror (e.g. gold) which features a very broad reflection range in the VUV, visible, and IR spectral regions at both grazing and normal incidence and high reflectivity in the XUV at grazing incidence.

Furthermore, we suggest XUV multilayer coatings to, depending on the application, select a spectral region, extract a particular harmonic, or to temporally compress SAPs. The multilayer XUV mirrors which are designed for specific wavelength ranges and small angles (close to normal incidence) will direct the radiation to application ports 1 and 2. Metallic mirrors address the rest of the ports. The highest possible XUV flux is obtained at port 5, as no deflection is required; in this case the mirrors are moved completely out of the beam path. Ports 1 and 2 and ports 3 and 4, respectively are designed symmetrically, meaning that each pair of ports shares exactly the same properties. This offers great flexibility to users and operators, as *e.g.* the XUV radiation send to experiments in one application port can be characterized at its symmetric counterpart and vice versa. The total arrangement of five application and characterization ports provides a large variety of possibilities for user applications.

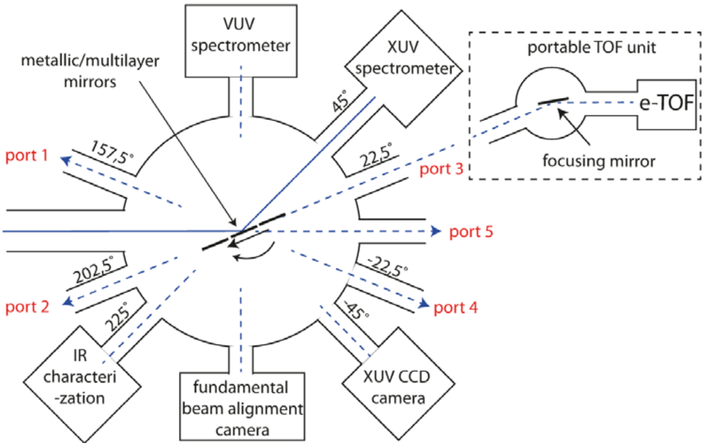

Figure 5: Beam characterization: Mirrors with different coatings on a rotation and translation stage send the incoming VUV, XUV, and IR radiation to different application and diagnostic end-stations.

For spectral characterization we envisage a VUV spectrometer (~ 5 – 20 eV) for low-order harmonics (sub ionization threshold harmonics) and a high resolution XUV spectrometer (20 – 200 eV) for high-order harmonics from different generation gases. A spectral resolution below 1 nm is sufficient for this application. The spectrometers should be one-dimensional imaging spectrometers, which provide valuable insight also into the spatial properties of the beam. Different suitable types of such imaging spectrometers are commercially available. A CsI-coated imaging MCP should be used as the detector for the VUV spectrometer. For the XUV spectrometer, either an imaging MCP or an XUV CCD can be used. These diagnostic tools will be important for tuning the gating parameters for the generation of single attosecond pulses. Moreover, we suggest a calibrated back-illuminated XUV CCD camera to characterize the spatial beam profile and to measure the XUV pulse energy[13]. We recommend a 2048 x 2048 array with a 13.5 µm pixel size, to ensure high spatial resolution and ample field of view.

Ionization cross-correlations with the IR field obtained from the pump-probe interferometer will be performed to characterize the temporal properties of the generated XUV single attosecond pulses and attosecond pulse trains. The generated photo-electron spectra are recorded with an electron time-of-flight (e-TOF) spectrometer while the IR field is temporally swept through the XUV field. A toroidal mirror at grazing incidence focuses the XUV and IR fields into the sensitive region of the e-TOF where a suitable detection gas is provided. The cross-correlations can be performed in different modes; the streaking method[14] will be applied to SAPs, while the RABBIT[15] scheme[16] will be used for attosecond pulse trains. The e-TOF should feature a narrow electron acceptance angle in order to perform reliable streaking

---

[13] Erny et al, N. J. Phys., **13**:073035 (2011).
[14] Hentschel et al, Nature, **414**:509 (2001).; Kienberger et al, Nature, **427**:817 (2004).
[15] RABBIT - Reconstruction of attosecond beating by interference of two-photon transitions
[16] Paul et al, Science **292**:1689 (2001).

measurements. In addition, it should provide an energy resolution better than 100 meV for photoelectrons with energies up to 100 eV. Depending on the length of the streaking trace, the single attosecond pulse and/or the IR streaking pulse can be reconstructed[17]. The unit composed of the toroidal mirror and subsequent e-TOF can be moved to different application and diagnosis ports. In this way the radiation at each port can be characterized either directly or at its symmetric counterpart.

Finally, we envisage two more ports for diagnostics: One port for alignment purposes, and another port from which the IR beam can be extracted and directed to characterization devices suited to measure the temporal profile of few- to single-cycle laser pulses, such as special versions of FROG[18] or SPIDER[19].

4 Summary

Laboratory space estimates

As shown in Figure 1, the entire system consists of several units, separated by connecting vacuum tubes. Little transversal space is needed for the straight tube sections. The main size limitation is the length of the system. Considering a length of L_0 = 2 m along the beamline before *unit 1*, L_1, L_2 and L_3 as discussed in Section 3.1 and a length of 8 m for L_4 (space for characterization and application area), a total length, L_{total}, of approximately 23 m and 42 m are needed for phase 1 and phase 2 respectively (Table 3). Our estimations include some work space around the system. The given values of L_1 and L_3 should be seen as an estimate of the minimum required lengths. This implies the possibility to increase these values for *phase 1* (while keeping the total focal length unchanged) in order to fit the dimensions for *phase 2*.

(m)	L_0	L_1	L_2	L_3	L_4	L_{total}
phase 1	2	4,9	1,7	6	8	22,6
phase 2	2	12,2	5	15	8	42,2

Table 3: System length.

We further note that it might be of interest from an application point of view to increase the beam propagation distance before the application area significantly (e.g. the distance between *unit 3* and *4*). This is especially relevant for applications where the XUV beam is refocused in order to reach a high XUV intensity. Minimizing the number of mirrors in the XUV beam while achieving a tight focus geometry requires the expansion of the divergent XUV beam before refocusing.

---

[17] Itatani et al, Phys. Rev. Lett., **88**(17):173903 (2002); Mairesse et al, Phys. Rev. A, **71**(1):011401 (2005); Quéré et al, J. Mod. Opt., 52(2-3):339 (2005).; Chini et al, Opt. Express, 18(12):13006 (2010).

[18] FROG - Frequency Resolved Optical Gating.

[19] SPIDER - Spectral Phase Interferometry for Direct Electric-field Reconstruction.

Our size estimations for the individual units are given in Table 4. Again, the actual chamber size plus some work space around are considered.

length x transverse size (m x m)	*Unit 1*	*Unit 2*	*Unit 3*	*Unit 4* (including application area)
phase 1	3 x 3	3 x 3	3 x 3	7 x 8
phase 2	3 x 3	10 x 3	3 x 3	7 x 8

Table 4: Dimensions of the individual sub-systems.

The minimum floor space required for each phase is schematically shown in Figure 6. The proposed floor plan fits within the laboratory space at ELI labeled 100KHZ-ISO 7, AU1-ISO 7, AU2-ISO 7, and AU3-ISO 7 in the 'Layout for Technology 2012.08.27' document. We also note that *unit 4* can be set up equivalently to the right or the left of the beamline. Changing from the left to the right requires building a mirrored interferometer (Figure 4).

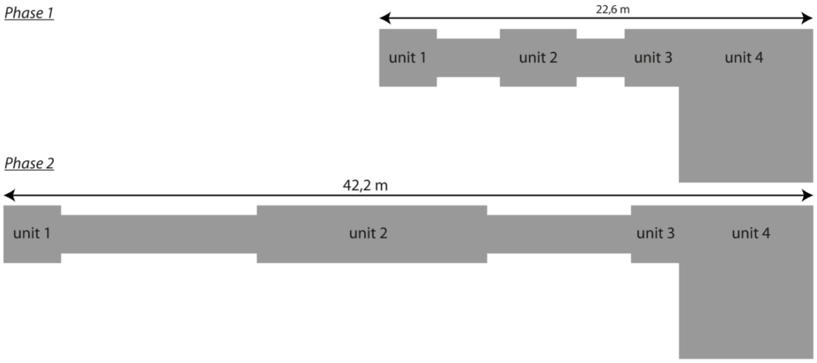

Figure 6: Estimated footprint of the setup for both phases

Source development needs and user availability

The system allows further source development even during operation periods dedicated for users. This is ensured by a design which allows fast switching between sending the generated attosecond pulses for characterization and to user stations.

The beamline dimensions and other system parameters greatly exceed the parameters of any known operating attosecond beamlines. We therefore foresee a large amount of time necessary for testing and initial source development during the first six months of the system operation. In the long run, 15% operation time for further source development should be sufficient.

Estimated construction time

We estimate a construction time of 17 man months for the detailed design, 8 months for delivery of all items, and 19 man months for setup and installation. This estimation does not include "testing and initial source development" mentioned above.

PAPER VI

Efficient high-order harmonic generation boosted by below-threshold harmonics

F. Brizuela, C. M. Heyl, P. Rudawski, D. Kroon, L. Rading,
J. M. Dahlström, J. Mauritsson, P. Johnsson, C. L. Arnold,
A. L'Huillier.

Scientific Reports **3**, 1410 (2013).

SCIENTIFIC REPORTS

OPEN

SUBJECT AREAS:
ATTOSECOND SCIENCE
NONLINEAR OPTICS
APPLIED PHYSICS
X-RAYS

Received
12 February 2013

Accepted
13 February 2013

Published
11 March 2013

Correspondence and requests for materials should be addressed to A.L. (anne.lhuillier@fysik.lth.se)

Efficient high-order harmonic generation boosted by below-threshold harmonics

F. Brizuela[1], C. M. Heyl[1], P. Rudawski[1], D. Kroon[1], L. Rading[1], J. M. Dahlström[2], J. Mauritsson[1],
P. Johnsson[1], C. L. Arnold[1] & A. L'Huillier[1]

[1]Department of Physics, Lund University, P. O. Box 118, SE-22100 Lund, Sweden, [2]Atomic Physics, Fysikum, Stockholm University, AlbaNova University Center, SE-10691 Stockholm, Sweden.

High-order harmonic generation (HHG) in gases has been established as an important technique for the generation of coherent extreme ultraviolet (XUV) pulses at ultrashort time scales. Its main drawback, however, is the low conversion efficiency, setting limits for many applications, such as ultrafast coherent imaging, nonlinear processes in the XUV range, or seeded free electron lasers. Here we introduce a novel scheme based on using below-threshold harmonics, generated in a "seeding cell", to boost the HHG process in a "generation cell", placed further downstream in the focused laser beam. By modifying the fundamental driving field, these low-order harmonics alter the ionization step of the nonlinear HHG process. Our dual-cell scheme enhances the conversion efficiency of HHG, opening the path for the realization of robust intense attosecond XUV sources.

The interaction of intense laser pulses with atomic or molecular gas media leads to the generation of harmonics of the laser light, up to very high orders[1]. These harmonics are locked in phase, giving rise to attosecond bursts of XUV light. The simplicity of the experimental technique, together with the progress in ultrafast laser technology, has promoted HHG sources as essential tools in many laboratories; opening, in particular, the field of attosecond science[2]. However, HHG suffers from low conversion efficiency, owing partly to phase mismatches in the nonlinear medium that prevent efficient build up of the macroscopic field[3–6], but mostly to the weak response of the individual atoms to the field.

The atomic response to an external driving field can be described by a three-step model [Fig. 1(a)]: First, a bound electron tunnel-ionizes into the continuum; second, it is accelerated by the laser field; and finally, it recombines with the parent ion upon field reversal, emitting an XUV photon[7,8]. The electron trajectories can be grouped in two families, named the long and the short, depending on the excursion time of the electron and generated in intervals II and III of Fig. 1(a), respectively. The most interesting from a practical point-of-view are the short trajectories, which lead to collimated and spectrally narrow emission. Unfortunately, these trajectories start at times close to the zero-crossings of the driving electric field, suffering from very low quantum-tunneling probability.

Altering the driving electric field at the subcycle level[9] provides a way of modifying the single atom response. This has been investigated mainly by adding the second harmonic field[10–13], thus breaking the symmetry between consecutive half cycles. In contrast, odd-order harmonics modify the HHG process while maintaining the half-cycle symmetry. In a pioneering work, Watanabe and coworkers[14] investigated the influence of the third harmonic (TH) on single ionization and HHG in Ar, obtaining an enhancement of up to a factor of ten for the 27–31 harmonics. Also, a few theoretical works discuss the influence of the TH on the enhancement of the yield[15,16] and/or the extension of the cutoff energy[17–19]. Another approach to enhance the signal by modify the single atom response is to control the time of ionization by using attosecond pulse trains to initialize the three-step process via single photon absorption[20–23].

In this letter, we demonstrate a simple and robust, yet powerful enhancement scheme based on a dual gas-cell setup [Fig. 1(b)]. We study HHG in neon using a high-energy (~20 mJ), near-infrared fundamental field, loosely focused in a long gas cell, resulting in high-order harmonics in the 40–100 eV range, with a typical energy of 10 nJ per harmonic order. The addition of a high-pressure Ar gas cell before the generation cell produces a large enhancement in the Ne signal, as seen in Fig. 1(c). We experimentally and theoretically show that the observed enhancement is due to below-threshold, low-order harmonics which modify the fundamental field in such a way that the contribution of the short trajectories is increased.

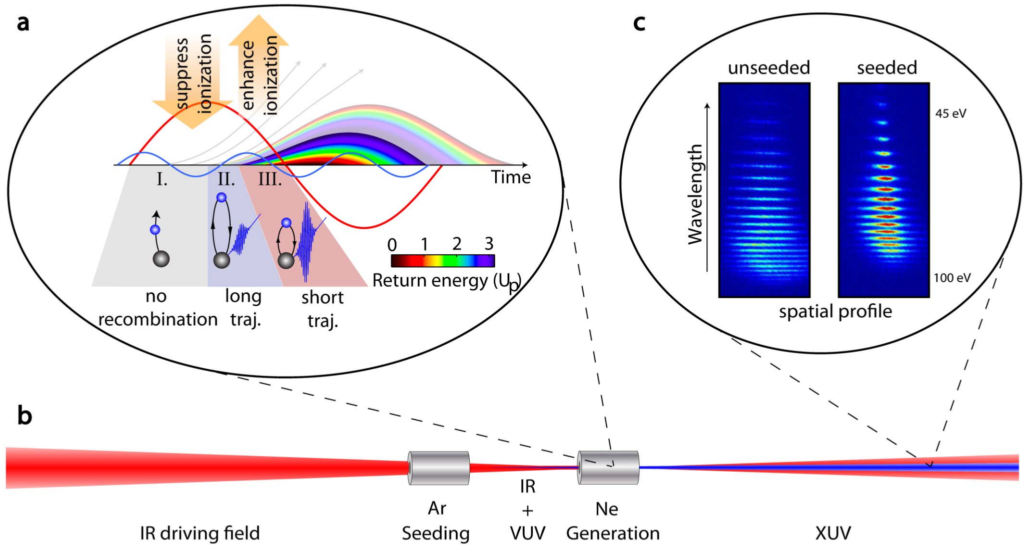

Figure 1 | HHG in a dual gas-cell. (a) Schematic classical trajectories for a sinusoidal driving field (red line). The colors indicate the return energy of the electrons in units of the ponderomotive energy U_p. Modifying the driving field by adding an odd harmonic field (blue line) can lead to an enhanced ionization probability for short trajectories (interval III) while suppressing the ionization of non-contributing electrons (intervals I and II), as indicated by the arrows. (b) Schematic experimental setup. Low-order harmonics generated in the seeding cell co-propagate with the fundamental into the generation cell and modify the HHG process. (c) Comparison of a typical HHG spectrum from a neon-filled generation cell obtained using only the fundamental field; and a spectrum obtained combining the fundamental field with low-order harmonics generated in the argon-filled seeding cell. In the latter case, the harmonic yield for the plateau harmonics is enhanced while the cutoff energy and the divergence are reduced.

Results

In our experiment, the generation cell is placed approximately at the laser focus while the seeding cell is located a few centimeters before (see Methods). The gas pressures in the cells can be independently adjusted and are typically a few mbar in the generation cell (Ne) and up to tens of mbar in the seeding cell (Ar). In Fig. 2(a–c), HHG spectra from neon are plotted as a function of the seeding pressure for three different driving intensities. When no gas is present in the seeding cell, standard Ne spectra are obtained. As the seeding pressure increases, the signal from the neon cell decreases until it is almost completely suppressed. At higher pressures, the neon spectra reappear and are significantly enhanced in the 50 – 80 eV region while the maximum photon energy slightly shifts to lower harmonic orders.

Figure 2(d) shows harmonics generated in the seeding cell. Harmonics with energies above the ionization threshold are not present at pressures where the enhancement in the generation cell occurs, and therefore are not responsible for the signal boost through single-photon ionization[20–23]. At these pressures, only low-order harmonics are efficiently generated in the seeding cell, indicating that they are responsible for the seeding process.

In order to validate our interpretation, we performed numerical simulations for both cells. In the generation cell, we simulated the seeded HHG process using the strong-field approximation

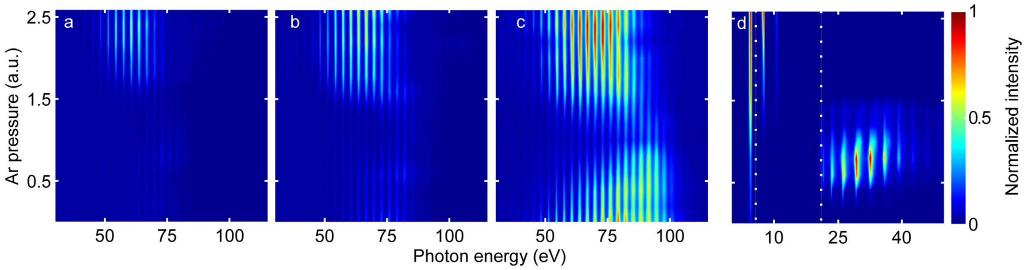

Figure 2 | Experimental HHG spectra. (a-c) Spectra from the generation cell as a function of the pressure in the seeding cell at three driving intensities 2.7, 3.5, and 4.4 × 10^{14} W/cm^2, respectively. The spectra were obtained using argon in the seeding cell and neon, at a fixed pressure, in the generation cell. The data were normalized to the most intense enhanced neon spectrum. (d) Low- (3–7) and high-order harmonics from the seeding cell as a function of Ar pressure. The dotted lines indicate regions measured independently with different detectors. Each region was normalized to the highest intensity in the corresponding spectral range.

(SFA)[15,16,24,25] (see Methods). The total field can be written as

$$E(t)=E_0\left[\sin(\omega t)+\sum_{q\omega<I_p} r_q \sin\left(q\omega t+\Delta\varphi_q\right)\right], \qquad (1)$$

where E_0 is the amplitude of the fundamental field, ω its frequency, I_p the ionization energy, r_q the ratio between the fundamental and qth harmonic field, and $\Delta\varphi_q$ their relative phase. Although all harmonics below the ionization threshold of Ar may influence the enhancement phenomenon, we considered only the TH, which is the most intense one (we omit the subscript 3 below). A simulated HHG spectrum in neon with $|r|^2 = 0.01$, is shown in Fig. 3(a) as a function of $\Delta\varphi$. A relative phase of ~1 rad leads to an enhanced ionization probability, since the electrical field is increased at the time where the short electron trajectories are born [interval III in Fig. 1(a)]. Furthermore, the electric field amplitude is reduced around the peak of the fundamental field leading to suppressed probability for non-contributing trajectories (intervals I, II) and to an improved macroscopic situation since plasma dispersion and depletion effects are minimized[4,5]. When $\Delta\varphi \approx 1 \pm \pi$, the situation is reversed and HHG is suppressed compared to the unseeded case.

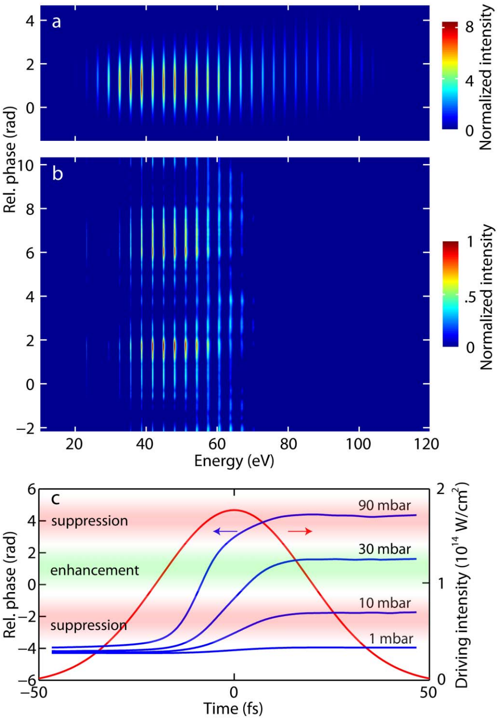

Figure 3 | Influence of the relative (ω, 3ω) phase in HHG. (a) SFA spectra as a function of $\Delta\varphi$ in the generation cell, normalized to the unseeded spectrum. Only the contribution of the short trajectory is considered. An effective grating response is included to mimic the experimental conditions. (b) Experimental results with the TH generated in a crystal, normalized to the highest signal. (c) Propagation simulations in the seeding cell: $\Delta\varphi$ at the exit of the cell as a function of time for different pressures.

We experimentally confirmed the dependence of the HHG signal on $\Delta\varphi$ by studying HHG using a combination of the fundamental and the TH generated in a crystal[14]. To control the delay between the two fields, we used a Michelson interferometer with the TH produced in one arm. Our results, plotted in Fig. 3(b), show a strong delay dependence of the harmonic yield. However, we could not increase the overall HHG efficiency compared to the dual-cell scheme, since a large fraction of the fundamental field was needed for the TH generation and consequently lost for HHG.

In the seeding cell, we examined the pressure dependence of both low-order and high-order harmonic generation. Our calculations[26] confirm the experimental observation that HHG in Ar peaks at a certain pressure (~10 mbar) which corresponds to optimized phase matching[27], while below-threshold harmonics continue to increase up to pressures as high as 100 mbar. We also investigated the propagation of the fundamental and TH fields in a high pressure cell[28] (see Methods). This allowed us to examine their phase relation after the seeding cell and to eliminate the relatively weak reshaping of the fundamental field in our experimental conditions as possible cause for the enhancement. As Fig. 3(c) shows, for high enough seeding pressures, $\Delta\varphi$ will be between 0 and 2 radians during part of the laser pulse, leading to a gated enhancement mechanism.

Discussion

As in any enhancement scheme, a key question is whether our method is advantageous over "usual" HHG optimization, which can be achieved for example by using looser focusing, optimizing the position of the focus in the cell, or adjusting the pressure in the gas cell[4,29,30]. Ideally, one would like to compare optimized HHG and optimized seeded HHG for a given fundamental pulse energy. This is not easy to realize experimentally, so we choose to benchmark seeded HHG against optimized unseeded HHG, with ~10 nJ at 63 eV (41st harmonic).

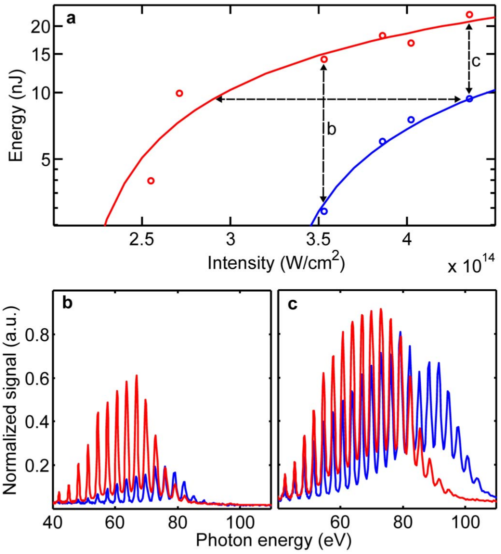

Figure 4 | Optimization of HHG. (a) 41st harmonic energy as a function of the driving intensity for seeded (red) and unseeded (blue) HHG. Unseeded HHG is optimized at the maximum intensity.
(b, c) Corresponding experimental spectra at 3.5 and 4.4 × 10^{14} W/cm^2, respectively.

Figure 4(a) compares the 41st harmonic signal in the seeded and unseeded cases as a function of the driving intensity. The intensity required for saturating seeded HHG is only half that needed for unseeded HHG. This explains the reduction of the cutoff energy and the lower divergence for the harmonics. The enhancement factor depends on the driving intensity [Fig. 4(b,c)]. For the 41st harmonic, it varies from five at 3.5×10^{14} W/cm^2 (and even higher at lower intensity) to two at 4.4×10^{14} W/cm^2. By further optimizing seeded HHG (e.g. by changing the focusing conditions) one should be able to obtain an even larger increase compared to unseeded HHG. The higher efficiency together with the lower divergence leads to a brighter source of XUV light.

In summary, we have studied the effect of seeding HHG using harmonics generated in a separate gas cell and showed that low-order harmonics are responsible for the resulting enhancement. The combined electric field preferentially enhances the short trajectories while suppressing depletion and plasma dispersion effects. The required phase difference between the fundamental and the low-order harmonics is obtained by adjusting the pressure in the seeding cell, thus modifying the free-electron dispersion. Our method is not limited to the gas combination presented here. Experimentally we have observed an increased harmonic yield for a variety of gas combinations, and even when the same gas is used in both cells. Our simulations show that the enhancement can be scaled far above one order of magnitude by increasing the low-order harmonic intensity, for example by using longer cells, higher pressures or gases with higher nonlinearities. This also leads to a shorter temporal gate, of interest for single attosecond pulse generation.

Methods

Experimental setup. The harmonics were generated using 45 fs pulses, centered at 800 nm. The gas cells used in this setup were 1 cm long with a diameter of 1 mm. The injection of gas into the cell was synchronized with the laser repetition rate (10 Hz) and the delay between the gas injection and the laser pulse was optimized for each cell. In the experiments, seeding cell pressure and pulse energy were the parameters investigated. The generation cell pressure was set for the best phase-matching conditions for Ne at the highest laser intensity intensity (4.4×10^{14} W/cm^2), corresponding to less than 10 mbar. The focus position was adjusted in order to optimize HHG in the generation cell. The cell separation was 15 mm with the generation-cell located at focus (f = 4 m). Nevertheless, larger separations, up to 50 mm yielded similar results. The cells were mounted on motor-controlled XYZ stages with motorized XY tilt capabilities. The cells could be removed completely from the IR field. A CCD camera was used to align each cell to the laser and observation of the spectra at the best phase-matching conditions were used to evaluate the tilt of each cell. The same Ne spectra from the generation cell could be obtained though the evacuated seeding cell or with the seeding cell removed from the beam path. The same was true for the seeding cell where Ar spectra could be obtained under both conditions. The pressure and intensity controls were automated to scan the region of interest. At each experimental condition 10 single-shot spectra were measured and averaged. The harmonic orders were calibrated using the absorption edge of an Al-foil filter. The fundamental intensity was estimated from the cutoff of the unseeded Ne spectra.

Numerical simulations. *Generation cell.* The influence of a weak third harmonic field on the HHG process was simulated by solving the time dependent Schrödinger Equation within the strong field approximation. The quasi-classical action for the electron motion in the continuum

$$S(\vec{p},t,t_0)=\int_{t_0}^{t} dt'\left(\frac{\left[\vec{p}-e\vec{A}(t')\right]^2}{2m}+I_p\right) \tag{2}$$

is calculated for a combined vector potential of the fundamental field and a weak parallel auxiliary field consistent with the field definition in Eq. (1). t_0 and t correspond to the tunneling and recombination times for an electron with canonical momentum $\vec{p}$, I_p is the ionization potential, and $\vec{A}$ the vector potential of the field. We approximate the HHG dipole as[24]

$$\begin{aligned} x(t)=i\int_0^{\infty} d\tau\left(\frac{\pi}{\epsilon+i\tau/2}\right)^{3/2} & d_x^*(p_{st}(t,\tau)-A_x(t)) \\ & \times d_x(p_{st}(t,\tau)-A_x(t-\tau))E(t-\tau) \\ & \times \exp[-iS_{st}(t,\tau)]F(\tau)+c.c., \end{aligned} \tag{3}$$

where a stationary phase approximation is performed over momentum, with $p_{st}(t,\tau) = [E(t) - E(t-\tau)]/\tau$, where $\tau = t - t_0$ is the excursion time in the continuum. We also insert a filter function $F(\tau)$ to select the short trajectory: $F(\tau) \approx 1$ for $\tau < 0.65T$ and $F(\tau) \approx 0$ for $\tau > 0.65T$, where $0.65T$ corresponds to the position of the cutoff. The integral in Eq. (3) is then evaluated numerically on a finite grid followed by a numerical Fourier transform for the dipole emission.

Seeding cell. We performed calculations which combine the solution of the time-dependent Schrödinger equation in a single-active electron approximation and propagation in a partially ionized medium[26,5] using a slowly-varying envelope approximation. Our main goal was to examine the influence of the pressure both for low-order and high-order harmonic generation in conditions mimicking the experiment. We found a maximum for HHG at around 10 mbar, while below-threshold, low-order harmonics which are not reabsorbed in the medium continue to increase up to very high pressures (100 mbar).

The generation of the third harmonic in the seeding cell was simulated using a (3 + 1)-dimensional, unidirectional, nonlinear envelope equation[28]. The complete frequency dependent dispersion relation is considered, enabling to propagate the fundamental and the third harmonic simultaneously. It is numerically integrated using a split-step technique, where the linear contributions, such as dispersion and diffraction are treated in k-transverse frequency space, while the nonlinear part, taking into account the Kerr effect, third-harmonic generation as well as plasma dispersion and plasma defocusing is treated in normal space. The method is described in detail in[28]. The calculated phase variation is mainly due to plasma dispersion effects. There are also small contributions from the geometrical phase acquired along the seeding cell as well pressure-dependent third harmonic phase matching.

1. Popmintchev, T. *et al.* Bright Coherent Ultrahigh Harmonics in the keV X-ray Regime from Mid-Infrared Femtosecond Lasers. *Science* **336**, 1287–1291 (2012).
2. Krausz, F. & Ivanov, M. Attosecond Physics. *Rev. Mod. Phys.* **81**, 163 (2009).
3. Constant, E. *et al.* Optimizing High Harmonic Generation in Absorbing Gases: Model and Experiment. *Phys. Rev. Lett.* **82**, 1668 (1999).
4. Kazamias, S. *et al.* Global Optimization of High Harmonic Generation. *Phys. Rev. Lett.* **90**, 193901 (2003).
5. Gaarde, M. B., Tate, J. L. & Schafer, K. J. Macroscopic aspects of attosecond pulse generation. *J. Phys. B* **41**, 132001 (2008).
6. Willner, A. *et al.* Efficient control of quantum paths via dual-gas high harmonic generation. *New J. Phys.* **13**, 113001 (2011).
7. Corkum, P. B. Plasma perspective on strong field multiphoton ionization. *Phys. Rev. Lett.* **71**, 1994–1997 (1993).
8. Schafer, K. J., Yang, B., DiMauro, L. F. & Kulander, K. C. Above threshold ionization beyond the high harmonic cutoff. *Phys. Rev. Lett.* **70**, 1599 (1993).
9. Wirth, A. *et al.* Synthesized Light Transients. *Science* **334**, 195–200 (2011).
10. Eichmann, H. *et al.* Polarization-dependent high-order two-color mixing. *Phys. Rev. A* **51**, R3414 (1995).
11. Mauritsson, J. *et al.* Attosecond Pulse Trains Generated Using Two Color Laser Fields. *Phys. Rev. Lett.* **97**, 013001 (2006).
12. Kim, I. J. *et al.* Highly Efficient High-Harmonic Generation in an Orthogonally Polarized Two-Color Laser Field. *Phys. Rev. Lett.* **94**, 243901 (2005).
13. Raz, O., Pedatzur, O., Bruner, B. D. & Dudovich, N. Spectral caustics in attosecond science. *Nat. Phot.* **6**, 170 (2012).
14. Watanabe, S., Kondo, K., Nabekawa, Y., Sagisaka, A. & Kobayashi, Y. Two-Color Phase Control in Tunneling Ionization and Harmonic Generation by a Strong Laser Field and Its Third Harmonic. *Phys. Rev. Lett.* **73**, 2692 (1994).
15. Kondo, K., Kobayashi, Y., Sagisaka, A., Nabekawa, Y. & Watanabe, S. Tunneling ionization and harmonic generation in two-color fields. *J. Opt. Soc. Am. B* **13**, 424–429 (1996).
16. Pi, L. W., Shi, T. Y. & Qiao, H. X. Enhancement of Bichromatic High-Order Harmonic Generation by a Strong Laser Field and Its Third Harmonic. *Chin. Phys. Lett.* **23**, 1490 (2006).
17. Ishikawa, K. Photoemission and Ionization of He$^+$ under Simultaneous Irradiation of Fundamental Laser and High-Order Harmonic Pulses. *Phys. Rev. Lett.* **91**, 043002 (2003).
18. Ivanov, I. A. & Kheifets, A. S. Tailoring the waveforms to extend the high-order harmonic generation cutoff. *Phys. Rev. A* **80**, 023809 (2009).
19. Chipperfield, L. E., Robinson, J. S., Tisch, J. W. G. & Marangos, J. P. Ideal waveform to generate the maximum possible electron recollision energy for any given oscillation period. *Phys. Rev. Lett.* **102**, 063003 (2009).
20. Schafer, K. J., Gaarde, M. B., Heinrich, A., Biegert, J. & Keller, U. Strong Field Quantum Path Control Using Attosecond Pulse Trains. *Phys. Rev. Lett.* **92**, 23003 (2004).
21. Gaarde, M. B., Schafer, K. J., Heinrich, A., Biegert, J. & Keller, U. Large enhancement of macroscopic yield in attosecond pulse train-assisted harmonic generation. *Phys. Rev. A* **72**, 013411 (2005).
22. Heinrich, A. *et al.* Enhanced VUV-assisted high harmonic generation. *J. Phys. B* **39**, S275 (2006).
23. Takahashi, E. J., Kanai, T., Ishikawa, K. L., Nabekawa, Y. & Midorikawa, K. Dramatic Enhancement of High-Order Harmonic Generation. *Phys. Rev. Lett.* **99**, 053904 (2007).
24. Lewenstein, M., Salières, P. & L'Huillier, A. Phase of the atomic polarization in high-order harmonic generation. *Phys. Rev. A* **52**, 4747 (1995).

25. Dahlström, J. M., L'Huillier, A. & Mauritsson, J. Quantum mechanical approach to probing the birth of attosecond pulses using a two-colour field. *J. Phys. B* **44**, 095602 (2011).
26. Erny, C. *et al.* Metrology of high-order harmonics for free-electron laser seeding. *New J. Phys.* **13**, 073035 (2011).
27. Heyl, C. M., Güdde, J., L'Huillier, A. & Höfer, U. High-order harmonic generation with μJ laser pulses at high repetition rates. *J. Phys. B* **45**, 074020 (2012).
28. Arnold, C. L. *et al.* Pulse compression with planar hollow waveguides: a pathway towards relativistic intensity with table-top lasers. *N. J. Phys.* **12**, 073015 (2010).
29. Takahashi, E., Nabekawa, Y. & Midorikawa, K. Generation of 10-μJ coherent extreme-ultraviolet light by use of high-order harmonics. *Opt. Lett.* **27**, 1920 (2002).
30. Salières, P., L'Huillier, A. & Lewenstein, M. Coherence control of high-order harmonics. *Phys. Rev. Lett.* **74**, 3776 (1995).

Acknowledgements

We thank Erik Mansten, Jörg Schwenke, and Rafal Rakowski for their early contribution to the project, and Byunghoon Kim for his contribution to the $\omega/3\omega$ measurements. This research was supported by the Marie Curie program ATTOFEL (ITN), the European Research Council (ALMA), the Joint Research Programme ALADIN of Laserlab-Europe II, the Swedish Research Council, the Swedish Foundation for Strategic Research, the Knut and Alice Wallenberg Foundation.

Author contributions

F.B., C.M.H. and P.R. contributed equally to this work. F.B., C.M.H., P.R. and L.R. performed the experiments. D.K. and C.L.A. performed the propagation calculations. C.M.H. and J.M.D. performed the SFA calculations. J.M, P.J., A.L. and all the other authors helped with the interpretation and the writing of the article.

Additional information

Competing financial interests: The authors declare no competing financial interests.

How to cite this article: Brizuela, F. *et al.* Efficient high-order harmonic generation boosted by below-threshold harmonics. *Sci. Rep.* **3**, 1410; DOI:10.1038/srep01410 (2013).

Paper VII

Macroscopic Phase Effects in Noncollinear High-order Harmonic Generation

C. M. Heyl, P. Rudawski, F. Brizuela, J. Mauritsson, A. L'Huillier.
(2014) *Phys. Rev. Lett., in print.*

PHYSICAL REVIEW LETTERS

Macroscopic Effects in Noncollinear High-Order Harmonic Generation

C. M. Heyl, P. Rudawski, F. Brizuela, S. N. Bengtsson, J. Mauritsson, and A. L'Huillier
Department of Physics, Lund University, P.O. Box 118, SE-221 00 Lund, Sweden

(Received 12 September 2013)

We study two-color high-order harmonic generation using an intense driving field and its weak second harmonic, crossed under a small angle in the focus. Employing sum- and difference-frequency generation processes, such a noncollinear scheme can be used to measure and control macroscopic phase matching effects by utilizing a geometrical phase mismatch component, which depends on the noncollinear angle. We further show how spatial phase effects in the generation volume are mapped out into the far field allowing a direct analogy with temporal carrier envelope effects in attosecond pulse generation.

DOI: PACS numbers: 42.65.Ky, 42.65.Re

High-order harmonic generation (HHG) in gases using multicolor optical fields is becoming a common tool in attosecond science. Multicolor HHG has been implemented by mixing the fundamental field with waves at low harmonic [1–3] and at incommensurate [4,5] frequencies. Other schemes employ attosecond pulse trains mixed with the fundamental field [6] as well as synthesized light transients [7] for driving the HHG process. The control and flexibility brought about by using two or more driving fields is used, for example, to improve the efficiency of the generation process [3,8], to monitor the single atom response [9,10], and to implement gating techniques [11]. High-order wave mixing can further be beneficial for achieving phase matching [1,12–15].

Using multiple optical driving fields also allows for noncollinear geometries. This concept, used extensively in low-order frequency conversion processes such as optical parametric amplification, has barely been applied to attosecond science. In an early work, Birulin and co-workers [16] addressed theoretically the general concept of HHG in a noncollinear geometry. By mixing the fundamental and a weak second harmonic at an angle, Bertrand and co-workers [17] demonstrated the spatial separation of multiple extreme ultraviolet (XUV) beams corresponding to different sets of absorbed photon numbers from the two fields. A similar scheme was recently used [18] for reconstructing the spatiotemporal characteristics of the generated attosecond pulses. Other authors [19–21] concentrated on noncollinear sum-frequency generation (SFG) processes driven by two identical laser fields. Such a scheme allows us to separate the harmonics from the fundamental but suffers from phase matching problems.

In this Letter, we theoretically and experimentally examine the influence of noncollinear geometries in HHG, analyzing in detail the macroscopic aspects. We show for the first time, to our knowledge, how a weak noncollinear field can be used as a probe to monitor and control phase matching. We show that difference-frequency generation (DFG), where a photon (or several photons) is emitted in the conversion process, is in general more favorable than SFG [30], which becomes very inefficient with increasing noncollinear angle. This leads to the counterintuitive result that the XUV radiation is dominantly emitted outside the angle sector defined by the two driving fields. Our analysis is illustrated in an experiment where high-order harmonics are generated in argon using a high-energy 800 nm laser and its weak second harmonic, crossed under a noncollinear angle of a few mrad (Fig. 1). We identify two important regimes for noncollinear HHG: (i) the generation at noncollinear angles large enough to allow a direct spatial separation of all photon pathways leading to the same final energy [17] and (ii) the generation at smaller noncollinear angles leading to spatially resolved interferences between adjacent photon pathways. At large angles, our noncollinear generation scheme provides the functionality of an all-optical beam splitter, delivering multiple, angularly separated XUV beams. At small angles, the observed spatial interferences directly reflect the harmonic phase variation across the focal plane.

Noncollinear high-order harmonic generation illustrates beautifully the two fundamentally different but equivalent concepts of light, waves or photons. Both concepts are very useful for understanding the underlying principles and will therefore be used alternately in the discussion throughout this Letter. We begin by explaining the main features of noncollinear HHG resulting from the field distribution in the focal plane, followed by a more quantitative description including propagation effects.

In the photon picture, the combination of two laser fields with central frequencies ω_1 and ω_2 leads to radiation with frequency $\omega_q = m_1\omega_1 + m_2\omega_2$, where m_1 and m_2 are

---

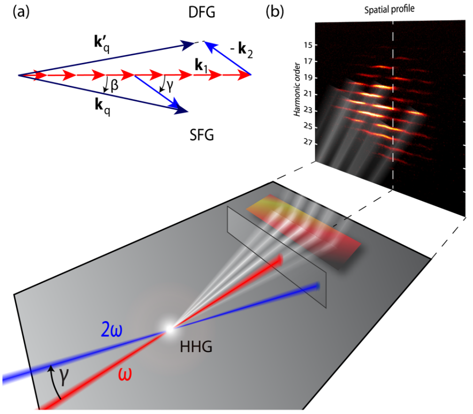

FIG. 1 (color online). (a) Wave vector representation of noncollinear wave mixing. (b) Schematic setup: a red (800 nm) and a blue (400 nm) laser beam are focused in a noncollinear geometry, resulting in the emission of spatially separated high-order harmonic beams. The depicted spectrum is a measured experimental MCPimage recorded at $\gamma \approx 2$ mrad and resampled for a linear energy scale. The noncollinear angle (γ) is exaggerated in this illustration.

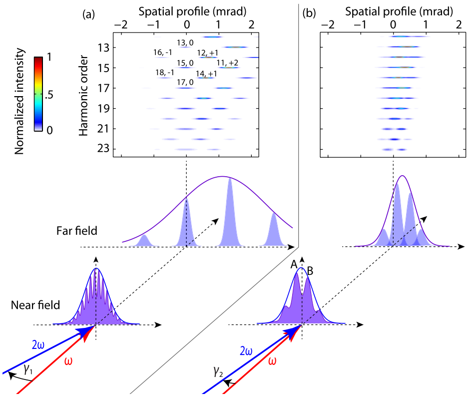

FIG. 2 (color online). Illustration of the interference concept: spatially resolved harmonic spectra as well as near- and far-field intensity distributions for a given harmonic order. (a) $\Delta\beta_q > \Theta_q$ and (b) $\Delta\beta_q < \Theta_q$. The spatial distribution of the high-order harmonic emission in the far field is defined by the interference grating in the focus representing multiple harmonic sources, determining intensity and phase of the emitted harmonics. The displayed far-field spectra were calculated using the strong field approximation, considering $\gamma = 5$ mrad (a) and $\gamma = 1.5$ mrad (b) with $I_{2\omega}/I_{\omega} = 0.05$ and $I_{\omega} = 2 \times 10^{14}$ W/cm^2, where I_{ν} denotes the focus intensity at central frequency ν.

integers. Without loss of generality m_1 can be chosen to be positive and m_2 positive or negative, accounting for sum- and difference-frequency generation processes, respectively. The emission angle β of the generated radiation, measured from the propagation axis of the ω_1 field, can be deduced through k-vector addition and defined by the unit vector of the generated field [31] $\hat{\mathbf{k}}_q = (m_1\mathbf{k}_1 + m_2\mathbf{k}_2)/||m_1\mathbf{k}_1 + m_2\mathbf{k}_2||$ [Fig. 1(a)]. Throughout the Letter we use small angle approximations.

We consider the case of a fundamental beam and its second harmonic, i.e., $\omega_1 = \omega$ and $\omega_2 = 2\omega$. The generated frequencies are $\omega_q = q\omega$ with $q = m_1 + 2m_2$, where the net number of photons absorbed $m = m_1 + m_2$ has to be odd in order to satisfy parity conservation. Denoting by γ the angle between $\mathbf{k}_1$ and $\mathbf{k}_2$, β can be approximated as

$$\beta(q, m_2) \approx \frac{2m_2}{q}\gamma, \qquad m_2 = \begin{cases} \pm 1, 3, \cdots & \text{if } q \text{ is even} \\ \pm 0, 2, \cdots & \text{if } q \text{ is odd} \end{cases}. \tag{1}$$

For sufficiently large γ, the number of ω_2 photons defines a unique emission angle so that all driving photon combinations that lead to the same final energy are spatially separated in the far field. A pattern of harmonic beams can then be detected for each harmonic order, as illustrated in Fig. 2(a). For small noncollinear angles such that $\Delta\beta_q = \beta(q, m_2 + 2) - \beta(q, m_2) < \Theta_q$, where Θ_q is the divergence angle of a single harmonic beam, the harmonic beams with different m_2 orders can partly overlap spatially and interfere [Fig. 2(b)], as discussed in more detail later. The intensities of the two driving fields determine the probability for up-converting photons from one or the other driving field and define therefore the envelope position and width of the pattern in the far field. For the case of a weak ω_2 field, harmonic emission occurs at small angles around $\mathbf{k}_1$ and only low m_2 orders can be expected. For a given harmonic order q, an m_2 order will be separated from the ω beam if $\gamma \geq q/4f_{\#}m_2$, where $f_{\#} = f/D$ is the f number of the ω beam focused with a focal length f and with an initial beam diameter D.

From a wave perspective, the generated far-field pattern can be understood as the interference of multiple harmonic sources. These sources are created by the interference of the two driving fields, as illustrated in Fig. 2. The modulation of amplitude and phase of the $\omega/2\omega$-driving field across the focal plane leads to an amplitude and phase modulation of the dipole oscillating at a given harmonic frequency. Note that the harmonic grating persists over the pulse duration while the intensity modulation at the fundamental frequencies is smeared out in time. All features of the far-field pattern mentioned above can be explained with this concept: the nonlinearity

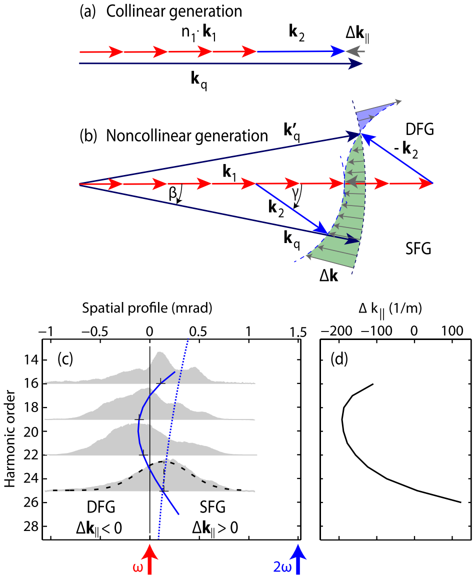

FIG. 3 (color online). (a),(b) Schematic phase matching scheme for noncollinear $\omega/2\omega$ HHG. In conditions where a phase mismatch is present for a collinear generation geometry (here illustrated for a negative $\Delta\mathbf{k}_{||}$ on the optical axis), it is possible to find a corresponding noncollinear geometry at which the total phase mismatch is zero (e.g., considering DFG in the displayed scheme). The shaded areas indicate anegative (green) and positive (blue) $\Delta\mathbf{k}$. (c) Measured harmonic spatial profile averaged over the relative phase between the ω and 2ω fields for $\gamma \approx 1.5$ mrad: the solid blue line indicates the approximate center of the spatial profiles; the dotted blue line marks the calculated center of the harmonic beams in the absence of propagation effects. The two arrows mark the propagation directions of the ω and the 2ω beams. (d) Extracted wave vector mismatch $\Delta\mathbf{k}_{||}$.

of the process determines the harmonic intensity distribution in the focal plane and therefore the width of the envelope over the spatial distribution in the far field. The relative intensity of the two driving fields influences the phase of the source grid, which determines the position of the envelope in the far field.

Phase matching in HHG can be analyzed by adding the relevant wave vectors, as illustrated in Figs. 3(a) and 3(b). The total k-vector mismatch [32] for noncollinear HHG can be expressed as

$$\Delta\mathbf{k} = \Delta\mathbf{k}_{||} + \Delta\mathbf{k}_{<},$$

$$\text{with} \quad \Delta\mathbf{k}_{<} = m_2\gamma^2 \underbrace{\left(\frac{2m_2}{q} - 1\right)}_{<0} \frac{\omega}{c}\hat{\mathbf{k}}_q, \qquad (2)$$

where $\Delta\mathbf{k}_{||}$ is the k-vector mismatch corresponding to the collinear generation geometry [Fig. 3(a)] while $\Delta\mathbf{k}_{<}$ is the geometrical offset added by the noncollinear geometry. Considering a certain m_2, phase matching ($\Delta\mathbf{k} = 0$) can be achieved by choosing the right angle γ. $\Delta\mathbf{k}_{<}$ is positive or negative depending on the sign of m_2, i.e., on whether we consider DFG or SFG [Fig. 3(b)]. $\Delta\mathbf{k}_{||}$ can be written as a sum of four components [22]: the wave vector mismatch due to the geometrical Gouy phase, two components that arise from dispersion in the partially ionized medium, and a contribution due to the intensity-dependent dipole phase. A limiting factor is ionization, which is intrinsically required for HHG but strongly reduces the efficiency due to the negative phase mismatch induced by plasma dispersion. Additionally, the Gouy phase can lead to a significant negative phase mismatch especially in the case of a tight focus or high harmonic orders. In both cases, the resulting negative $\Delta\mathbf{k}_{||}$ can be compensated by a positive $\Delta\mathbf{k}_{<}$. In these conditions high harmonic emission driven by noncollinear DFG can dominate over noncollinear SFG. In the absence of propagation effects and for a weak perturbing 2ω field, the harmonic spatial profile is strongest at $\beta = 0$ ($m_2 = 0$) [17]. If the far field pattern is predominantly emitted outside the angle sector defined by the two driving fields (as in Fig. 1), DFG dominates, indicating that $\Delta\mathbf{k}_{||}$ is negative. If the emission maximum is located inside this angle sector, SFG dominates and $\Delta\mathbf{k}_{||}$ is positive. Not only the sign, but also the magnitude of $\Delta\mathbf{k}_{||}$ can be estimated as shown by the analysis of our experimental results presented below.

We performed experiments using a high-energy 40 fs Ti:sapphire laser system operating at a 10 Hz repetition rate [24]. The second harmonic field, with a pulse energy corresponding to 5% of the fundamental, was generated in one arm of a phase-stable Michelson-like interferometer and loosely focused together with the fundamental field into an argon gas cell ($f_\# \simeq 200$). The interferometer allowed us to spatially displace the two beams so they could be focused with a small angle relative to each other. The generated harmonics were analyzed by an XUV spectrometer with an entrance slit and recorded by a microchannel plate detector. Our experimental conditions are chosen to strongly favor HHG emission from the short trajectory [24]. Due to the small angle, the beams corresponding to different m_2 orders interfere [case (b) in Fig. 2], and the spatial distribution in the far field depends on ϕ, the relative phase between the ω and the 2ω fields. Figure 4(a) shows a single shot harmonic spectrum recorded with $\gamma \approx 1.5$ mrad. Figure 3(c) presents the corresponding spatial intensity distributions for four harmonic orders, averaged over ϕ. The solid blue line in Fig. 3(c) shows that the center of the far field distribution, obtained by fitting Gaussian envelopes to the experimental data, varies with harmonic order. In order to deduce the effect of phase matching from the spatial distribution, the ω-beam

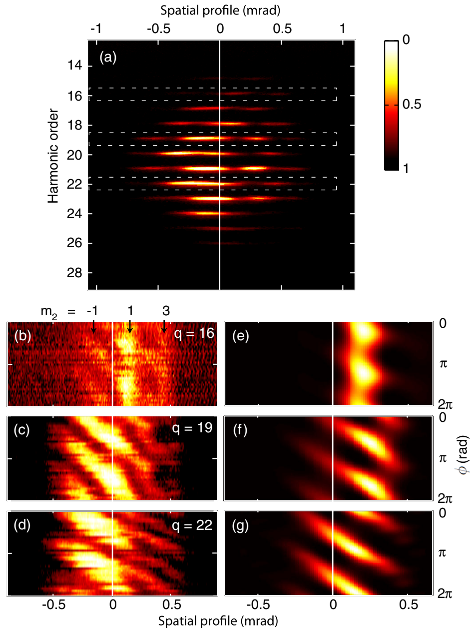

FIG. 4 (color online). (a) Single shot experimental harmonic spectrum generated in the same conditions as shown in Fig. 3(c). The dashed white lines indicate the region displayed spectrally integrated and normalized as a function of ϕ in (b)–(d). Corresponding SFA results are shown in (e)–(g). Note that the center of the spatial distribution is shifted compared to the experimentally measured patterns since propagation effects are not included in the simulations.

direction cannot be used as a reference, since the 2ω-field intensity is not negligible in our experimental conditions. Instead we calculate this reference [dotted blue line in Fig. 3(c)] using numerical simulations based on the strong field approximation (SFA), accounting for the noncollinear overlap of the two driving fields but neglecting propagation effects (see the Supplemental Material [23]). Experimentally, we clearly observe a dominant contribution on the left side from the reference direction, for most harmonic orders, which we relate to a dominant DFG contribution in our experimental conditions. The offset between the experimental beam centers and the SFA results allows us to deduce an approximate value for the effective $\Delta\mathbf{k}_{||}$ as shown in Fig. 3(d) (see the Supplemental Material [23]).

Finally, we examine in more detail noncollinear HHG at small crossing angles and analyze the influence of interference effects on the harmonic spatial profile. Figures 4(b)–4(d) show the far-field profiles for harmonics 16, 19, and 22 as a function of ϕ. The position of the spatial fringes varies periodically with ϕ and this variation becomes more pronounced as the harmonic order increases. This can be understood within the wave model: the harmonics generated at different source locations in the focal plane [e.g., A and B in Fig. 2(b)] interfere in the far field, and the interference pattern depends on their relative phase. The main contribution to this phase difference is due to the single atom response and can be expressed as $\Delta\varphi_s = \alpha_q(I_A - I_B)$, where $\alpha_q I$ denotes the harmonic dipole phase [25] at a corresponding driving field intensity I. When the phase ϕ is varied, the harmonic intensity grating in the focus moves across the focal plane and the difference between I_A and I_B changes. Consequently, the interference fringes in the far-field shift as clearly visible in Figs. 4(c) and 4(d). The slope reveals the dipole phase dependence on the intensity, which is small for low harmonic orders and increases with order, as expected for the short trajectory contribution [26]. Results from our SFA simulations, shown in Figs. 4(e)–4(g), reproduce fairly well the main features of the experimental interference patterns. The differences in width and shape of the spatial profiles (and consequently in the slope of the fringe pattern) can be explained by deviation from Gaussian optics including possible asymmetries of the fundamental beam shape in the focus as well as ionization effects leading to additional spatial broadening.

There is a clear analogy between the presented spatial phase effects and CEP-dependent spectral fringes in HHG. Attosecond pulses are generated by a short fundamental pulse at a few instants in time, e.g., t_a and t_b at the corresponding driving field intensities I_a, I_b. The harmonic spectrum is a consequence of the interference between these pulses. Similarly to the spatial interference effect discussed above, the spectral interference pattern depends on the relative phase $\Delta\varphi_t = \alpha_q(I_a - I_b)$, which changes with CEP [27,28].

In summary, we have theoretically and experimentally investigated noncollinear HHG, focusing on the macroscopic aspects of the generation process. We have shown how a noncollinear second harmonic field can be used to probe phase matching by utilizing a geometrical phase mismatch factor, introduced by the noncollinear geometry. Using difference-frequency generation processes, this factor can be advantageous for phase-matched generation in a partly ionized medium. We further identify different noncollinear angle regimes leading either to well separated harmonic beams or to spatial interference structures in the far-field spectrum. These interferences are the spatial analog of temporal interference structures in attosecond pulse generation with few cycle pulses.

This research was supported by the Marie Curie program ATTOFEL (ITN), the European Research Council (ALMA), the Swedish Research Council, the Swedish Foundation for Strategic Research, and the Knut and Alice Wallenberg Foundation.

[1] H. Eichmann, S. Meyer, K. Riepl, C. Momma, and B. Wellegehausen, Phys. Rev. A **50**, R2834 (1994).

[2] S. Watanabe, K. Kondo, Y. Nabekawa, A. Sagisaka, and Y. Kobayashi, Phys. Rev. Lett. **73**, 2692 (1994).

[3] F. Brizuela, C. M. Heyl, P. Rudawski, D. Kroon, L. Rading, J. M. Dahlström, J. Mauritsson, P. Johnsson, C. L. Arnold, and A. L'Huillier, Sci. Rep. **3**, 1410 (2013).

[4] M. B. Gaarde, P. Antoine, A. Persson, B. Carré, A. L'Huillier, and C.-G. Wahlström, J. Phys. B **29**, L163 (1996).

[5] T. Pfeifer, L. Gallmann, M. J. Abel, P. M. Nagel, D. M. Neumark, and S. R. Leone, Phys. Rev. Lett. **97**, 163901 (2006).

[6] A. Heinrich, M. Lewenstein, and A. Sanpera, J. Phys. B **37**, 2087 (2004).

[7] A. Wirth *et al.*, Science **334**, 195 (2011).

[8] I. J. Kim, C. Kim, H. Kim, G. Lee, Y. Lee, J. Park, D. Cho, and C. Nam, Phys. Rev. Lett. **94**, 243901 (2005).

[9] N. Dudovich, O. Smirnova, J. Levesque, Y. Mairesse, M. Yu. Ivanov, D. M. Villeneuve, and P. B. Corkum, Nat. Phys. **2**, 781 (2006).

[10] D. Shafir, H. Soifer, B. D. Bruner, M. Dagan, Y. Mairesse, S. Patchkovskii, M. Yu. Ivanov, O. Smirnova, and N. Dudovich, Nature (London) **485**, 343 (2012).

[11] J. Mauritsson, P. Johnsson, E. Gustafsson, A. L'Huillier, K. Schafer, and M. Gaarde, Phys. Rev. Lett. **97**, 013001 (2006).

[12] R. Hilbig and R. Wallenstein, Appl. Opt. **21**, 913 (1982).

[13] P. Shkolnikov, A. Kaplan, and A. Lago, Opt. Lett. **18**, 1700 (1993).

[14] S. Meyer, H. Eichmann, T. Menzel, S. Nolte, B. Wellegehausen, B. Chichkov, and C. Momma, Phys. Rev. Lett. **76**, 3336 (1996).

[15] O. Cohen, T. Popmintchev, D. Gaudiosi, M. Murnane, and H. Kapteyn, Phys. Rev. Lett. **98**, 043903 (2007).

[16] A. V. Birulin, V. T. Platonenko, and V. V. Strelkov, J. Exp. Theor. Phys. **83**, 33 (1996).

[17] J. Bertrand, H. J. Wörner, H.-C. Bandulet, É. Bisson, M. Spanner, J.-C. Kieffer, D. M. Villeneuve, and P. B. Corkum, Phys. Rev. Lett. **106**, 023001 (2011).

[18] K. Kim, C. Zhang, A. D. Shiner, S. E. Kirkwood, E. Frumker, G. Gariepy, A. Naumov, D. M. Villeneuve, and P. B. Corkum, Nat. Phys. **9**, 159 (2013).

[19] S. Fomichev *et al.*, Laser Phys. **12**, 383 (2002).

[20] W. Jian and Z. Heping, Opt. Lett. **32**, 3315 (2007).

[21] A. Ozawa, A. Vernaleken, W. Schneider, I. Gotlibovych, Th. Udem, and T. W. Hänsch, Opt. Express **16**, 6233 (2008).

[22] S. Kazamias, D. Douillet, F. Weihe, C. Valentin, A. Rousse, S. Sebban, G. Grillon, F. Augé, D. Hulin, and Ph. Balcou, Phys. Rev. Lett. **90**, 193901-1 (2003).

[23] See Supplemental Material at http://link.aps.org/supplemental/10.1103/PhysRevLett.000.000000 for details.

[24] P. Rudawski *et al.*, Rev. Sci. Instrum. **84**, 073103 (2013).

[25] M. Lewenstein, K. Kulander, K. Schafer, and P. Bucksbaum, Phys. Rev. A **51**, 1495 (1995).

[26] K. Varjü *et al.*, J. Mod. Opt. **52**, 379 (2005).

[27] E. Mansten *et al.*, Phys. Rev. Lett. **102**, 083002 (2009).

[28] G. Sansone *et al.*, Phys. Rev. A **80**, 063837 (2009).

[29] P. Balcou, P. Salières, A. L'Huillier, and M. Lewenstein, Phys. Rev. A **55**, 3204 (1997).

[30] We emphasize that a geometrical phase mismatch introduced by the noncollinear generation geometry leads to enhanced DFG emission, which is different from earlier results that show dominating DFG emission due to dispersion effects in collinear geometries [15].

[31] Strictly speaking, this definition is an approximation, neglecting phase matching effects which can lead to a modified emission direction especially for large noncollinear angles and in the presence of radial field gradient vectors [29] caused e.g., by the intensity dependent dipole phase.

[32] We define the k-vector mismatch as the difference in k vectors between fundamental and harmonic fields, e.g., $q\mathbf{k}_1 - \mathbf{k}_q$.

Supplementary information for "Macroscopic Effects in Noncollinear High-Order Harmonic Generation"

This supplementary information contains:
A. a description of the model used for the numerical simulations
B. a derivation of the method used to extract an effective wave vector mismatch

A. Numerical simulations of the noncollinear HHG process

We performe two-dimensional calculations in order to simulate HHG using a noncollinear geometry. The single atom response was obtained by solving the time dependent Schrödinger Equation within the strong field approximation. The quasi-classical action for the electron motion in the continuum

$$S(\vec{p},t,t_0)=\int_{t_0}^{t}dt'\left(\frac{[\vec{p}-e\vec{A}(t')]^2}{2m}+I_p\right) \tag{1}$$

is calculated for the vector potential $\vec{A}$ of the combined fundamental and second harmonic field. I_p, m and e denote ionization potential, electron mass and charge, respectively. t_0 and t are tunneling and recombination times for an electron with canonical momentum $\vec{p}$. The laser induced dipole [1] was calculated by evaluating the integral:

$$\begin{aligned} x(t)=\mathrm{i}\int_0^\infty \mathrm{d}\tau\left(\frac{\pi}{\epsilon+\mathrm{i}\tau/2}\right)^{3/2} & d_x^*(p_{st}(t,\tau)-A_x(t)) \\ & \times\exp[-\mathrm{iS_{st}(t,\tau)}/\hbar]\mathrm{F}(\tau) \\ & \times d_x(p_{st}(t,\tau)-A_x(t-\tau))E(t-\tau)+c.c., \end{aligned} \tag{2}$$

considering a stationary phase approximation over momentum, with $p_{st}(t,\tau)=[E(t)-E(t-\tau)]/\tau$, where $\tau=t-t_0$ is the excursion time in the continuum. In accordance with our experimental conditions, the short trajectory contribution was selected via a filter function: $F(\tau)\approx 1$ for $\tau<0.65T$ and $F(\tau)\approx 0$ for $\tau>0.65T$, where $0.65T$ corresponds to the position of the cutoff. The integral in Eq. (2) is evaluated numerically on a finite temporal grid for all points along a one dimensional grid in the focal plane. The far-field emission is computed using Fourier methods. We have performed the calculations both in one dimension and in two dimensions and found that the far-field pattern did not change significantly when including the second dimension. Propagation effects are not taken into account.

B. Estimation of the global phase mismatch

As explained in the main letter, the asymmetric distribution of the harmonic beams relative to the reference direction [dotted blue line in Fig. 3(c) of the main letter] can be linked to macroscopic phase matching effects and allows an estimation of $\Delta k_{||}$.

The harmonic signal S_q can be calculated by integrating the dipole response along the propagation axis z over the medium length L, taking into account a global wave vector mismatch $\Delta k=\Delta k_{||}+\Delta k_{<}$ as well as re-absorption of the generated xuv emission in the generation gas, denoted by the absorption coefficient κ_q:

$$S_q\propto\left|\int_0^L d_q\exp\left[i(\Delta k+i\kappa_q)(L-z)\right]dz\right|^2 \tag{3}$$

Approximating the dipole amplitude d_q as well as Δk as constant over the medium length, Eq. 3 reduces to:

$$S_q\propto|d_q|^2e^{-\kappa_q L}\cdot\frac{\cosh(\kappa_q L)-\cos(\Delta kL)}{\Delta k^2+\kappa^2} \tag{4}$$

We now consider $S_q=S_q(m_2)$ for different emission directions, *i.e.* for different m_2 values, defined through Eq. 1 in the main letter. $|d_q|^2$ has to be replaced by a function accounting for a reasonable scaling of the intensity of the harmonic emission corresponding to different m_2-orders. As an approximation and in agreement with our simulations, we replace $|d_q|^2$ in Eq. 4 by a Gaussian function of width Δm_2, centered around m_2^0:

$$S_q(m_2,\Delta k_{||})\propto\exp\left[-4\log(2)\frac{(m_2-m_2^0)^2}{(\Delta m_2)^2}\right]\cdot\frac{e^{-\kappa_q L}\left\{\cosh(\kappa_q L)-\cos\left[(\Delta k_{||}+\Delta k_{<}(m_2))L\right]\right\}}{\left[\Delta k_{||}+\Delta k_{<}(m_2)\right]^2+\kappa^2} \tag{5}$$

$\Delta k_{<}$ is a function of m_2, defined via Eq. 2 in the main letter. m_2^0 has a dominant influence on the distribution $S_q(m_2, \Delta k_{||})$. In our analysis, we use the numerically extracted m_2^0-values shown in Fig. 3 (c) in the main letter. Δm_2 influences $S_q(m_2, \Delta k_{||})$ only weakly and was set to $\Delta m_2 = 7$ in our analysis, reflecting an upper limit of the experimentally measured width. Considering further $L = 2\,\text{cm}$ and a generation pressure of $p = 2$ mbar in order to estimate κ_q, we can fit $S_q(m_2, \Delta k_{||})$ to the experimentally measured distribution by adjusting $\Delta k_{||}$ and thus extract $\Delta k_{||}$.

[1] M. Lewenstein *et al.*, Phys. Rev. A **51**, 1495 (1995).

Paper VIII

Digital in-line holography on amplitude and phase objects prepared with electron beam lithography

J. Schwenke, E. Lorek, R. Rakowski, X. He, A. Kvennefors,
A. Mikkelsen, P. Rudawski, C. M. Heyl, I. Maximov, S. G. Pettersson,
A. Persson, and A. L'Huillier.

Journal of Microscopy **247**, 196201 (2012).

Journal of
Microscopy

Journal of Microscopy, Vol. 247, Pt 2 2012, pp. 196–201
doi: 10.1111/j.1365-2818.2012.03632.x
Received 30 December 2011; accepted 7 May 2012

Digital in-line holography on amplitude and phase objects prepared with electron beam lithography

J. SCHWENKE*,†, E. LOREK*, R. RAKOWSKI*, X. HE*,
A. KVENNEFORS‡, A. MIKKELSEN$, P. RUDAWSKI*,
C. M. HEYL*, I. MAXIMOV‡, S.-G. PETTERSSON*,
A. PERSSON* & A. L'HUILLIER*
**Division of Atomic Physics, Lund University, SE-221 00 Lund, Sweden*
†*MAX-lab, Lund University, SE-221 00 Lund, Sweden*
‡*Division of Solid State Physics/Nanometer Structure Consortium, Lund University, SE-221 00, Lund, Sweden*
$*Synchrotron Radiation Research, Lund University, SE-221 00, Lund, Sweden*

Key words. Electron beam lithography, high-order harmonic generation, holography, spin-coating, thin films.

Summary

We report on the fabrication and characterization of amplitude and phase samples consisting of well defined Au or Al features formed on ultrathin silicon nitride membranes. The samples were manufactured using electron beam lithography, metallization and a lift-off technique, which allow precise lateral control and thickness of the metal features. The fabricated specimens were evaluated by conventional microscopy, atomic force microscopy and with the digital in-line holography set-up at the Lund Laser Centre. The latter uses high-order harmonic generation as a light source, and is capable of recovering both the shape and phase shifting properties of the samples. We report on the details of the sample production and on the imaging tests with the holography set-up.

Introduction

An ultrashort light pulse in the X-ray regime can penetrate and interact with a structurally intact biological sample or macromolecule to yield a high resolution image, before the sample is destroyed by the very same pulse (Neutze *et al.*, 2000; Bergh *et al.*, 2008). The requirements for such an experiment are stringent: The light pulse needs to be of high intensity, because the interaction efficiency is low, and the tolerable pulse duration is just a few femtoseconds, limited by the onset of the Coulomb explosion caused by the intense electromagnetic field of the pulse (Howells *et al.*, 2009). To achieve high spatial resolution, and to image biological samples in their natural state, the photon energy needs to be in the X-ray regime. The absorption of X-rays in matter prohibits the use of glass-based lenses and therefore hinders the application of conventional imaging methods. Despite the difficulties, an experimental implementation is by all means feasible, as has been demonstrated by Chapman *et al.* in 2006, in a groundbreaking experiment at the FLASH Free-Electron Laser (FEL) in Hamburg, Germany (Chapman *et al.*, 2006). In this experiment, a test sample was imaged by diffraction with a coherent soft X-ray pulse of 25 femtoseconds (fs) duration. The method used, coherent diffraction imaging (CDI; Chapman & Nugent, 2010), retrieves the diffraction pattern and requires an iterative algorithm to reconstruct an image of the sample, because of the loss of phase information. Coherent diffractive imaging is also used at the Linac Coherent Light Source FEL at the SLAC National Accelerator Laboratory in the United States (Seibert *et al.*, 2011). Although FELs provide an excellent combination of high degree of coherence, short-pulse duration and high intensity, they are large-scale facilities with limited user access. In recent years, laser-based sources have emerged as an alternative. A very promising light source for these kinds of experiments is high-order harmonic generation (McPherson *et al.*, 1987; Ferray *et al.*, 1988), a process which generates coherent light pulses of ultrashort duration in a medium, i.e. inert gas (Krausz & Ivanov, 2009). The short time duration can be used for time-resolved, single-shot measurements such as CDI, and indeed it was shown that the achievable flux is sufficient for this application (Ravasio *et al.*, 2009). Furthermore, the good coherence of the pulse allows for alternative imaging methods that do not require

Correspondence to: Anne L'Huillier, Division of Atomic Physics, Lund University, P.O. Box 118, SE-221 00 Lund, Sweden. Tel: +46-46-222-7661; fax: +46-46-222-4250; e-mail: Anne.LHuillier@fysik.lth.se

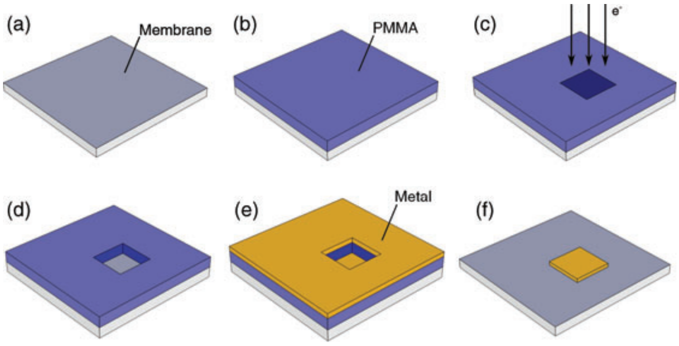

Fig. 1. Schematic of sample fabrication using electron beam lithography (EBL) and lift-off: (a) the membrane is prepared for resist deposition, (b) spin-coating of silicon nitride membrane by PMMA resist, (c) EBL exposure of the resist, (d) removal of the exposed resist in development, (e) thermal evaporation of a thin metal layer and (f) lift-off in acetone to form metal feature.

iterative algorithms to reconstruct an image. In digital in-line holography, the phase information is present in the recorded hologram, and a more direct way of retrieving the object image is available (Gabor, 1948). The method retrieves both the amplitude and phase properties of the sample, and can be used to image a large variety of free-standing objects. Digital in-line holography using high-order harmonic generation has been demonstrated by several groups, including our own (Bartels *et al.*, 2002; Morlens *et al.*, 2006; Genoud *et al.*, 2007). In this paper, we report on the production of test samples for this kind of experiment, in which we used electron beam lithography (EBL) to pattern various materials on ultrathin silicon nitride membranes. Samples on membranes as thin as 20 nm were successfully produced. The method is relevant for all applications that require high transmission in the extreme ultraviolet (XUV) range (30–100 eV). This paper is structured as follows: The next section will describe the sample production in detail as well as the characterization with conventional microscopy. In digital holography section, the holographic imaging set-up is described. The result section shows the experimental results from the produced samples. A summary is given in summary and conclusions section.

Sample fabrication

The patterning of the membrane was performed in the clean room of Lund Nano Lab at the Division of Solid State Physics, Lund University. Before exposure of the membrane in EBL, the sample was spin-coated with a thin layer of polymethyl methacrylate (PMMA). The PMMA layer works as a positive electron beam sensitive resist, i.e. after irradiation by high-energy electrons and development, the resist is locally removed resulting in a well-defined pattern. Subsequent evaporation of a thin metal layer onto the membrane and dissolution of unexposed resist in acetone (lift-off technique) leads to formation of the metal features with precisely controlled shape and thickness (Broers *et al.*, 1996; Vieu *et al.*, 2000). This approach allows fabrication of metal features with lateral size as small as 15 nm, but in the present work we limit the lateral size to 2 μm.

In our experiments we used a commercially available EBL system Raith 150 (Raith GmbH, Germany), thermal evaporation tools for deposition of the metal layers as well as Zeiss AxioVision (Carl Zeiss Microimaging GmbH, Göttingen, Germany) optical microscopes for sample inspection. The 20 nm thick, 500 × 500 μm^2 large silicon nitride (Si_3N_4) membrane, supported by a solid Si frame up to 3 × 3 mm^2 in size, was bought ready-made from SPI Supplies (Structure Probe, Inc., West Chester, PA, U.S.A.). The sample with the membrane was glued onto a stainless steel support structure using melted indium. For spin coating, the rectangular support structure was temporarily attached to a 2" silicon wafer. The samples were spin-coated with a thin layer of PMMA resist, 950KD, dissolved in anisole. After deposition of the resist and its soft baking, the resist layer was exposed to the electron beam in the EBL machine using acceleration voltage 20 kV and a dosage of 340 $\mu C\ cm^{-2}$ for the amplitude object, and 810 $\mu C\ cm^{-2}$ for the phase object. The exposed PMMA was developed in a mixture of methyl-isobutylketone and iso-propanol (MIBK:IPA), rinsed in IPA and nitrogen blow dried. In the following steps, a thin layer of Au or Al was evaporated and carefully lifted-off to make metal features on the silicon nitride membrane. The sample fabrication steps are shown in Figure 1. Microscope images of the samples used in this work are shown in Figure 2. The first example, Figure 2(a), shows a membrane covered with a 20 nm thick layer of gold. The formed pattern consists of squares of varying size, 16, 8, 4 and 2 μm side lengths. Figure 2(b) shows the second sample, where the membrane is covered with aluminium in various shapes. This sample is designed to introduce a phase shift to the

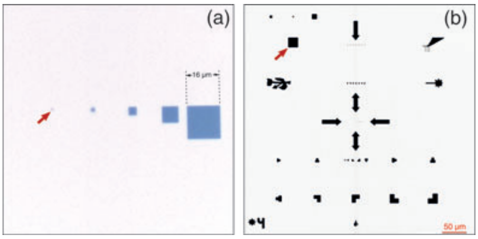

Fig. 2. Sample images taken with an optical microscope. The images were edited to increase the contrast. (a) Layer of Au shaped as squares of varying size. The smallest square with a side length of 2 μm is marked with a red arrow. (b) Layer of Al in various shapes. The red arrow marks the shape used for the phase property measurement. The black arrows are part of the Al layer.

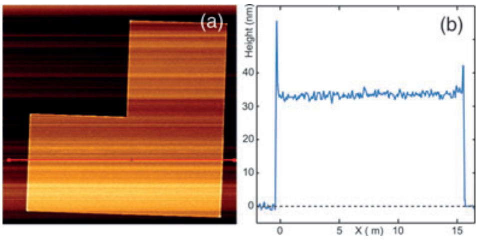

Fig. 3. Details of the phase sample analysed with an atomic force microscope (AFM). (a) Shows a magnified view of one of the produced shapes and (b) shows the height trace along the red line in (a).

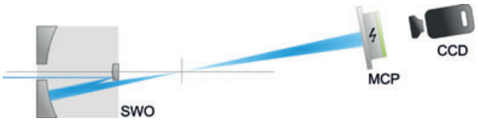

Fig. 4. Schematic of the imaging set-up. The XUV pulses from the HHG source are refocused with a Schwarzschild objective (SWO). The focal point is the source for the holography set-up. The hologram is detected with a combination of a microchannel plate (MCP) and a charge-coupled device (CCD) detector.

transmitted XUV pulse. The produced samples were examined with an optical microscope and an electron microscope. The Al sample was also examined with an atomic force microscope (AFM), to measure the thickness of the layer. The layer was determined to be 34 nm thick (Fig. 3). This method has been demonstrated on Si_3N_4 films before, yet on thicker membranes (Fischbein & Drndic, 2006).

Digital holography

The produced samples were imaged with the digital in-line holography set-up at the Lund Laser Centre, which uses XUV pulses produced in a high-order-harmonic generation (HHG) set-up. The HHG process takes place when an intense laser pulse is focused into a gas medium. The interaction of the laser pulse with the gas atoms results in the emission of overtones of the fundamental frequency. The laser system used in this experiment operates at a wavelength of 800 nm, and Ar is used as a target medium. The generated spectrum reaches into the extreme ultraviolet regime, up to the 29th harmonic at 27.6 nm. More details on the HHG set-up can be found in He *et al.* (He *et al.*, 2009). The XUV pulse is refocused tightly, to get a divergent pulse for the in-line holography scheme (Fig. 4, see Schwenke *et al.*, 2008 for more details). The samples are imaged in transmission, which means that the beam must transmit through the membrane to interact with the sample layer. This requires a sufficient transmittance of the membrane for the XUV. During the experiment, a transmittance of about 46% at 38 nm wavelength was measured. The photon flux from the source of about 3×10^{10} photons per pulse per harmonic (He *et al.*, 2009) allow for single-shot imaging, as has been demonstrated previously (Schwenke *et al.*, 2008). The quality of the holograms is, however, improved by acquiring an image during a few seconds, about 30 shots at a 10 Hz repetition rate.

The fringes of the hologram reveal both the spatial composition of the diffracted light as well as the phase shift relative to the reference part of the beam. A reconstruction of the field in the sample plane can be achieved by applying a numerical algorithm to the recorded hologram. A detailed description of the algorithm can be found in Genoud *et al.* (Genoud *et al.*, 2007). Of particular interest in this work is the correction for the twin-image blurring, which arises from the ambiguity of the interference fringes in the hologram. We apply an iterative algorithm suggested by Latychevskaia and Fink (Latychevskaia & Fink, 2007), which successively recovers the phase information lost in the recording process. This improves the contrast of the reconstructed object image, and can potentially yield the true values of the complex object properties. The spatial resolution of the reconstructed images is limited, because information can only be obtained in the overlap region between the reference wave and the object wave, which is restricted by the divergence of the source. In this set-up, the limit for the spatial resolution is calculated to be about 1.2 μm.

Results

The sample production method allows for a wide range of different designs and materials to be used. For this work, various sample structures made of single layers of Au (20 nm thickness) or Al (21.7 nm; and also Cr, 26.7 nm) were produced. A double-layer sample of Au (15.1 nm) and Ni (6 nm) was produced as well. Here Ni served as an adhesive to the silicon nitride membrane. We found that once a proper handling protocol was in place, the lithographic processcould reliably be applied on membranes as thin as 20 nm. Variations

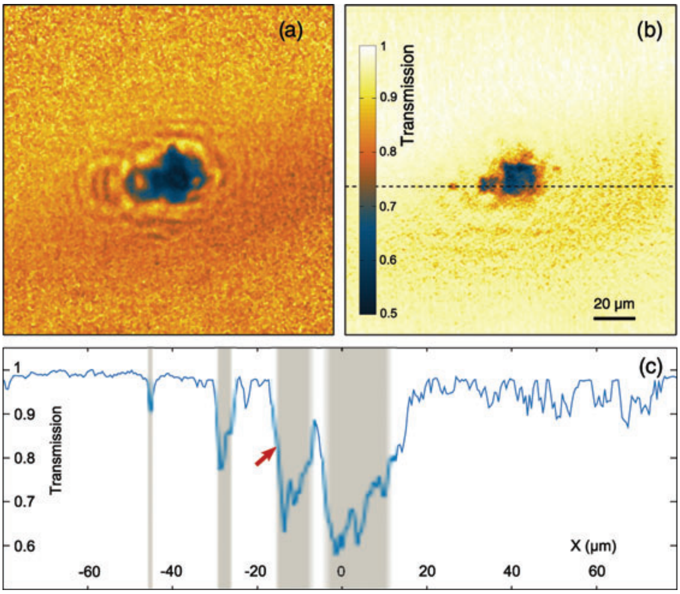

Fig. 5. Experimental hologram and reconstruction of a detail of the sample seen in Figure 2(a). (a) The recorded hologram. (b) The reconstructed transmission. (c) The data along the line in (b). The shaded areas show the position of the squares in (b). The edge marked with the arrow was used for determining the spatial resolution.

of the quality of the produced structures were not observed, yet a systematic study was not performed.

The sample shown in Figure 2(a) was used to determine the spatial resolution of the holography set-up. Figure 5 shows the results from the holography imaging. The first image, Figure 5(a) shows the recorded hologram, although Figure 5(b) shows the reconstructed transmission function. Figure 5(c) shows the data along the line in Figure 5(b). The spatial resolution was determined to be 1.5 μm, measured at the edge indicated with the arrow. Here the resolution was defined as the lateral distance covered by 60% of the full height of the edge. The given number represents the highest achieved spatial resolution. A comparison of the measured edge with other edges shows, that not all edges are resolved equally well. The resolution varies throughout the image, mainly because of artefacts in the recorded holograms, but also because of a reduced signal-to-noise ratio at the edge of the beam. Note that the 2 μm sized square is visible in Figure 5(c).

Figure 6 shows the reconstructed object images for the phase sample. The large square seen in Figure 2(b) was imaged. Although Figure 6(a) shows the recorded hologram, Figure 6(b) shows the reconstructed phase shift and Figure 6(c) shows the data along the line in Figure 6(b). The calculated transmittance is 90%, and the estimated phase shift through the aluminum is 0.51 rad, for 38 nm radiation. The measured transmittance is 87%, and the measured phase shift is 0.57 rad, calculated as the mean values of the complex modulus and phase angle in the area covered by the object in the reconstructed image. The measured transmission and phase shift agree well with the expected values. Figure 6(c) shows the data along the line in Figure 6(b) before applying the iterative algorithm (blue dashed line) and after 300 iterations (orange line). Further iterations do not improve the contrast, but increase the noise in the image and add artefacts. After applying the iterative algorithm, the contrast is significantly enhanced, and the phase shift is similar to the expected value. However, both the two-dimensional image and the line-out show a large amount of noise. The success of the iterative phase retrieval, and the quantitative reconstruction of the object properties, relies strongly on the stability of the source.

Summary and conclusions

We have demonstrated a method to produce arbitrary shapes and layer compositions on ultrathin silicon nitride membranes. The produced objects were used to demonstrate digital in-line holography with a HHG source. The reconstructed images match closely the sample specification.

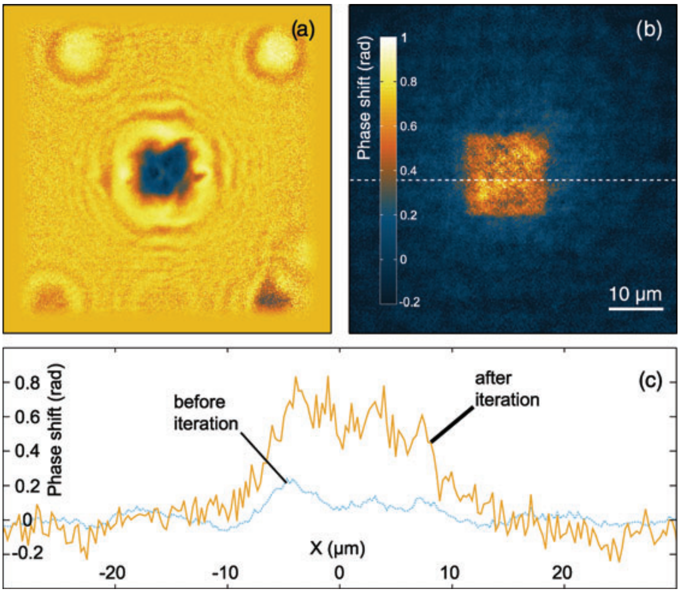

Fig. 6. Experimental hologram and reconstruction of a detail of the sample seen in Figure 2(b). (a) The recorded hologram. (b) The reconstructed phase shift. (c) The data along the line in (b). The two lines show the reconstructed phase shift before (blue dashed) and after (orange) application of the iterative algorithm.

The spatial resolution is limited because of the numerical aperture of the XUV focusing optics. The iterative process increases the image quality by enhancing the contrast and removing contributions from the twin image. The remaining image distortions can be removed by better optics which less aberrations, and by improving the pointing stability of the laser and the mechanical stability of the experimental set-up.

Acknowledgements

This research was supported by the European Research Council (Advanced grant ALMA), the Marie Curie Early Stage Training Site (MAXLAS), the Marie Curie Initial Training Network ATTOFEL, the joint research activity ALADIN of Laserlab-Europe, the Knut and Alice Wallenberg Foundation and the Swedish Research Council. Partial support from the Nanometer Structure Consortium at Lund University (nmC@LU) is greatly appreciated. We would also like to thank Ulf Håkansson for helping with the AFM.

References

Bartels, R.A., Paul, A., Green, H. *et al.* (2002) Generation of spatially coherent light at extreme ultraviolet wavelengths. *Science* **297**, 376–378.

Bergh, M., Huldt, G.S., Tmneanu, N., Maia, F.R.N.C. & Hajdu, J. (2008) Feasibility of imaging living cells at subnanometer resolutions by ultrafast X-ray diffraction. *Q. Rev. Biophys.* **41**, 181–204.

Broers, A., Hoole, A. & Ryan, J. (1996) Electron beam lithography—resolution limits. *Microelectron. Eng.* **32**, 131–142.

Chapman, H.N. & Nugent, K.A. (2010) Coherent lensless X-ray imaging. *Nat. Photon.* **4**, 833–839.

Chapman, H.N., Barty, A., Bogan, M.J. *et al.* (2006) Femtosecond diffractive imaging with a soft-X-ray free-electron laser. *Nat. Phys.* **2**, 839–843.

Ferray, M., Huillier, A.L., Li, X.F., Lompre, L.A., Mainfray, G. & Manus, C. (1988) Multiple-harmonic conversion of 1064 nm radiation in rare gases. *J. Phys. B-At. Mol. Opt.* **21**, L31–L35.

Fischbein, M.D. & Drndic, M. (2006) Nanogaps by direct lithography for high-resolution imaging and electronic characterization of nanostructures. *Appl. Physc. Lett.* **88**, 063116-1-063116-3.

Gabor, D. (1948) A new microscopic principle. *Nature* **161**, 777–778.

Genoud, G., Guilbaud, O., Mengotti, E., Pettersson, S.-G., Georgiadiou, E., Pourtal, E., Wahlström, C.-G. & L'Huillier, A. (2007) XUV digital in-line holography using high-order harmonics. *App. Phys. B-Lasers O.* **90**, 533–538.

He, X., Miranda, M., Schwenke, J. *et al.* (2009) Spatial and spectral properties of the high-order harmonic emission in argon for seeding applications. *Phys. Rev. A* **79**, 063829-1-063829-7.

Howells, M.R., Beetz, T., Chapman, H.N. *et al.* (2009) An assessment of the resolution limitation due to radiation-damage in X-ray diffraction microscopy. *J. Electron Spectrosc.* **170**, 4–12.

Krausz, F. & Ivanov, M. (2009) Attosecond physics. *Rev. Modern Phys.* **81**, 163–234.

Latychevskaia, T. & Fink, H.-W. (2007) Solution to the twin image problem in holography. *Phys. Rev. Lett.* **98**, 233901-1-233901-4.

McPherson, A., Gibson, G., Jara, H., Johann, U., Luk, T.S., McIntyre, I.A., Boyer, K. & Rhodes, C.K. (1987) Studies of multiphoton production of vacuum-ultraviolet radiation in the rare gases. *J. Opt. Soc. Am. B* **4**, 595–601.

Morlens, A.-S., Gautier, J., Rey, G. *et al.* (2006) Submicrometer digital in-line holographic microscopy at 32 nm with high-order harmonics. *Opt. Lett.* **31**, 3095–3097.

Neutze, R., Wouts, R., van der Spoel, D., Weckert, E. & Hajdu, J. (2000) Potential for biomolecular imaging with femtosecond X-ray pulses. *Nature* **406**, 752–757.

Ravasio, A., Gauthier, D., Maia, F.R.N.C. *et al.* (2009) Single-shot diffractive imaging with a table-top femtosecond soft X-ray laser-harmonics source. *Phys. Rev. Lett.* **103**, 028104-1-028104-5.

Schwenke, J., Mai, A., Miranda, M. *et al.* (2008) Single-shot holography using high-order harmonics. *J. Mod. Optic.* **55**, 2723–2730.

Seibert, M.M., Ekeberg, T., Maia, F.R.N.C. *et al.* (2011) Single mimivirus particles intercepted and imaged with an X-ray laser. *Nature* **470**, 78–81.

Vieu, C., Carcenac1, F., Pépin, A. *et al.* (2000) Electron beam lithography: resolution limits and applications. *Appl. Surf. Sci.* **164**, 111–117.

Paper IX

Imaging localized surface plasmons by femtosecond to attosecond time-resolved Photoelectron Emission Microscopy - "ATTO-PEEM"

S.H. Chew, K. Pearce, Ch. Späth, A. Guggenmos, J. Schmidt, F. Süssmann, M. Kling, and U. Kleineberg, E. Mårsell, C.L. Arnold, E. Lorek, P. Rudawski, C. Guo, M. Miranda, F. Ardana, J. Mauritsson, A. L'Huillier, A. Mikkelsen.

(2014) *Manuscript in preparation, chapter of a book "Attosecond Nanophysics", editors Peter Hommelhoff and Matthias Kling, Wiley-VCH Verlag GmbH and Co. KGaA.*

Imaging localized surface plasmons by femtosecond to attosecond time-resolved Photoelectron Emission Microscopy - "ATTO-PEEM"

S.H. Chew[1], K. Pearce[2], Ch. Späth[1], A. Guggenmos[1], J. Schmidt[1], F. Süssmann[2], M. Kling[1,2] and U. Kleineberg[1,2]
[1] Ludwig Maximilians University Munich, Faculty of Physics, D-85748 Garching, Germany
[2] Max Planck Institute of Quantum Optics, D-85748 Garching, Germany

E. Mårsell[1], C.L. Arnold[1], E. Lorek[1], P. Rudawski[1], C. Guo[1], M. Miranda[1], F. Ardana[2], J. Mauritsson[1], A. L'Huillier[1], A. Mikkelsen[1]
[1] Department of Physics, Lund University, Sweden
[2] Paul Scherrer Institut, Switzerland

1. Introduction

The direct detection of the spatiotemporal dynamics of nanolocalized optical nearfields on nanostructured metal surfaces, e.g. imaging of localized surface plasmons on rough or nanostructured metal films or the imaging of propagating surface plasmon polaritons at a vacuum-metal or metal-dielectric interface, e.g. in metallic waveguides, is a pre-requisite to further control and optimize surface-plasmon based ultrafast nanooptics for future device development and applications [Raether88, Maier06].

While the free electrons in metals collectively respond to the excitation from a light pulse, which is resonant to the surface plasmon frequency of the system, and squeeze and amplify the field intensity of the incoming plane light field into a sub-wavelength spatial volume, the typically broad frequency bandwidth of surface plasmon resonances supports an ultrafast response of these fields with rapid field changes on sub-femtosecond time scales.

The sub-wavelength nanoscaled localization of optical fields in the vicinity of metal nanostructures and the ultrafast temporal evolution of such fields on a 0.1-100 fs time scale require the invention and development of new experimental methodologies, which combine nanometer (sub optical) spatial resolution, sub-femtosecond temporal resolution and optionally further nanospectroscopic information.

Resolving the *spatial* distribution of such fields requires a microscopic technique with sub-optical spatial resolution, e.g. in the 10 nm – 100 nm range.

Scanning near field optical microscopy techniques have been successfully applied with spatial resolutions of about ~100 nm, however the combination with ultrashort light pulses is still very difficult. Photoemission electron microscopy is a technique capable of spatially resolving the spatial emission distribution of photoelectrons with an ultimate resolution of ~ 10 nm. Furthermore, the photoemission process turns out to be very sensitive to localized surface fields (like surface plasmons) especially for nonlinear multiphoton excitation schemes. It is for those reasons that PEEM has matured to a very powerful technique for imaging and analyzing localized surface plasmons

Detecting the *temporal* evolution of surface plasmon fields requires femtosecond to attosecond temporal resolution, which is usually enabled by interferometric two-pulse pump-probe experiments using ultrahort resonant optical laser pulses (fsec) for excitation and visible fs to XUV attosecond (High Harmonic Generation) pulses for probing.

A schematic picture for the excitation of localized surface plasmons on a metallic nanoparticle is displayed in Figure 1.

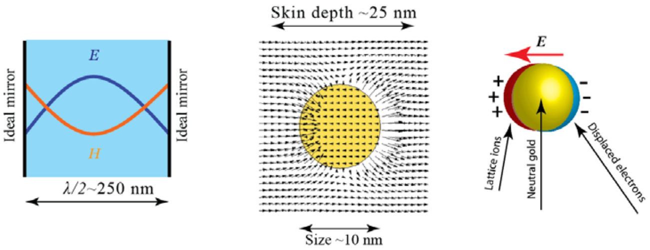

Figure 1 Concentration of optical field energy (λ ~ 500 nm) in the plasmonic nearfield of a metal nanoparticle (typ. 10 nm dia.) induced by collective electron oscillation (picture courtesy of M. Stockman).

Photoelectron Emission Microscopy (PEEM) combined with ultrafast laser-based excitation sources has matured over the last 10 years into a very powerful experimental tool to study the collective electron dynamics and field dynamics from surfaces via a photoemission process with a spatial resolution limit ranging down to ~ 10 nm. Furthermore, state of the art PEEM microscopes are nowadays equipped with electron energy filtering for nanospectroscopic investigation of the emitted photoelectrons.

The following sub-chapters describe the current status (as of the end year 2013) of research and development on ultrafast PEEM experiments over the last 10 years, with a special emphasis on converging to the ultimate goal of ultrafast microscopy with ultimate specifications on the spectral and temporal resolution.

2. Time-resolved multi-photon PEEM with femtosecond time resolution

Rough metal surfaces irradiated by Ti:Sa femtosecond laser pulses in the NIR (e.g. 800 nm) or visible (e.g. SHG at 400 nm) regime show strong emission of photoelectrons even though the incident photon energy (typ. 1.55 eV or 3.1 eV) does not exceed the metal work function (e.g. typ. ~4.5 eV for Ag or Au). This multi-photon (2 photon, 3 photon) excitation process can be strongly enhanced by the resonant excitation of localized surface plasmons, if the incident wavelength hits the surface plasmon resonance frequency of the metallic sample (surface plasmon assisted multiphoton photoemission).

2.1 Observation of surface plasmon enhanced “hot spot” photoemission in fs-PEEM

While first experiments on nonlinear multi-photon photoemission with fs laser pulses have been performed in the 1990s by photoelectron spectroscopy without any spatial resolution, the investigation of the strongly localized emission characteristics of photoelectrons from localized surface plasmons voids or potrusions of rough metal films or even from lithographically formed metal nanostructures (see Fig. 1) was only possible by first experiments using Photoelectron Emission Microscopes coupled to short pulse laser sources.

First fs-PEEM experiments published in 2003 by the group of Schönhense (University of Mainz) on lead nano-cluster films and rough silver films revealed strongly localized photoemission intensities in so-called “hot-spots” with sub-optical spatial dimensions, and with a pronounced intensity dependence on the lateral orientation of the incoming linear light polarization.

Shortly after the discovery of this “hot-spot” photoemission from plasmonic metal surfaces, the nature of the photoemission process has been investigated by time-of-flight

PEEM microspectroscopy by measuring the lateral intensity distribution as well as the kinetic energy distribution of the emitted photoelectrons in a ToF-PEEM.

The results (from the same group) obtained on a polycrystalline copper surface show distinct differences in the kinetic electron energy spectra revealed from hot-spot and non-hot-spot surface areas, pointing to change of the local work function.

2.2 Interferometric time-resolved fs-PEEM

A first experiment combining nanoscopic spatial with femtosecond temporal resolution was successfully performed and published by the group of Hrvoje Petek at the University of Pittsburgh in 2005.

They combined interferometric time-resolved two-photon photoemission (ITR-2PPE) excited by two identical 400nm/10fsec replica laser pulses with a spatially resolving detection of the emitted photoelectrons by PEEM. The sample under investigation was a silver grating structure, whose line edge roughness gave rise to pronounced hot spot emission. By analyzing the hot spot intensities of different local areas as a function of the pump-probe time delay the researchers could observe the localized surface plasmon field evolution as a function of time via the instantaneous photoemission intensity. While all hot-spot intensities initially oscillated in phase with the exciting 10 fs laser pulse, they converge towards their plasmonic eigenfrequencies for later times up to their T_2 dephasing time (see Figure 2).

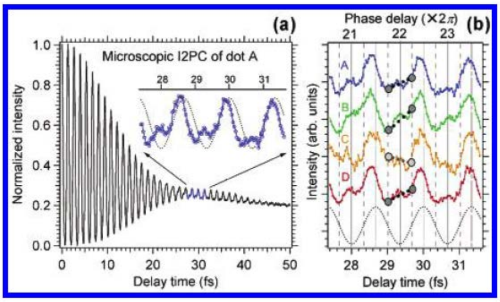

Figure 2 Interferometric two-photon correlation measurement of the photoelectron emission intensity from one distinct Ag hotspot A as a function of the relative time delay (a). A detailed comparison of the temporal variation of the photoemission signal as a function of time delay for 4 different hotspots A-D show different behavior.

3. The “Atto-PEEM”

In a theoretical paper published by M. Stockman et. al. in 2007 [Stockman07], the development of a new type of ultrafast photoelectron microscope was proposed, which for the first time could potentially see and spatially as well as temporally resolve the ultrafast nearfield oscillations of localized surface plasmons on their genuine nanometer spatial and attosecond temporal time scales.

In 2009 PEEM imaging using attoseond pulse trains was then demonstrated experimentally by Mikkelsen et al [Mikkelsen09], and it was realized for single attosecond pulses by Chew et. al. [Chew12] in 2012. While these and further experiments showed the immense potential of the technique [Mikkelsen09, Chew12, Marsell13], it was also clear from these studies that an important limiting factor to fully realize the great potential of Atto-PEEM is the repetition rate of the high harmonic generation (HHG) light sources. At the end of this chapter the use of a new generation of laser technology enabling attosecond light pulses with repetition rates in the hundreds of kHz range is demonstrated to yield exactly the improvements needed to take this technology to a qualitative new level.

In section 3.1 we discuss the theoretical proposal of attosecond PEEM plasmonic that was a precursor to this whole experimental endeavor. This is followed by two sections elaborating on the two different approaches towards Atto-PEEM that have been developing until now. In section 3.2 the experimental developments and conceptual ideas, of the group of Kleineberg at LMU Munich, to realize this concept using a ToF-PEEM and a single attosecond HHG source. In section 3.3 we discuss the development and conceptual ideas of the Mikkelsen & L'Huillier groups at Lund University, using HHG attosecond pulse trains, synchrotron sources (for comparison) and recently a ≥200kHz HHG source. Our hope is that this will be a helpful guide for future atto-PEEM imaging experiments and developments.

3.1 Theoretical description of the attosecond nanoplasmonic field microscope

The theoretical proposal to study plasmonic effects to the attosecond level was based on a few-cycle femtosecond laser pump pulse resonantly exciting surface plasmons (very similar like in nonlinear multiphoton PEEM experiments), while the temporal evolution of the plasmonic field from the enforced excitation converging towards the plasmonic eigenmodes within the plasmonic dephasing time is being probed by linear photoemission process induced by a single extreme ultraviolet attosecond pulse (see Fig. 3).

The high XUV photon energy (typ. ~ 90 eV) gives rise to the emission of fast photoelectrons from the valence band close to the Fermi edge (in contrast to usually slow photoelectrons emitted via multiphoton excitation), which are quickly penetrating through the plasmonic surface nearfield and take up momentum from that field.

Depending on the relative time delay between the femtosecond NIR excitation pump pulse and the attosecond XUV probe pulse, the measured energy change of the emitted photoelectron bears a fingerprint of the instantaneous plasmonic surface nearfield at the time of the photoelectron release. Their energy change is proportional to the local electrical field potential at the time of electron release and is independent of the electron emission angle, which makes high-resolution PEEM collection with a large numerical aperture possible.

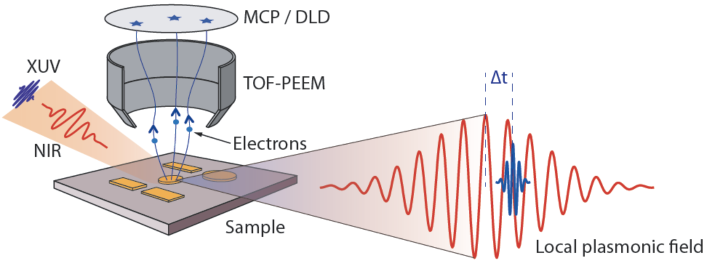

Figure 3 Scheme of the attosecond plasmonic nearfield microscope comprising of a few-cycle resonant optical pump pulse exciting a local plasmonic nearfield oscillation followed by an attosecond XUV pulse for linear emission of fast photoelectrons within a fraction of the nearfield oscillation period.

The concentration of the incident light field in the vicinity of metallic nanostructures (when illuminated close to the plasmonic resonance) gives rise to a localized enhancement of the electromagnetic field on the nanoscale, which is dubbed "hot-spot". In photoelectron emission these plasmonic hot-spots act as local surface points of enhanced electron emission, because the transition probability of a dipole-allowed electronic transition scales with the square of the electrical field.

The temporal response of such a plasmonic hot-spot field upon resonant excitation by a very short few-cycle laser pulse is displayed in Fig. 4. The chosen parameters (pulse duration 5.5 fs, wavelength 800 nm, intensity 10GW/cm^2) of the simulated few-cycle laser pulse (a) are very similar to typical few-cycle laser pulses, which nowadays can be experimentally achieved by state-of-the-art femtosecond laser sources.

The simulated hot-spot field response is displayed in panel b. The magnitude of the hot-spot field has been normalized to the maximum amplitude of the exciting laser field, which has been set to “1”. The initial time response of the plasmonic field closely resembles the field oscillations of the driving laser field, due to the large spectral bandwidth of surface plasmon resonances supporting sub-femtosecond field oscillations.

At longer time delays > 20 fs a complex interference beating of several plasmonic eigenmodes occurs, which is characteristic for each nanoscaled hot-spot.

It is the idea of nanoplasmonic field microscopy to trace the field beating of plasmonic eigenmodes by XUV photoelectrons liberated from a single attosecond XUV pulse (pulse duration indicated by the arrow in panel (b)).

Furthermore, at this particular nanosystem the simulated hot-spot field is enhanced by a factor of approximately 30 compared to the incident laser field.

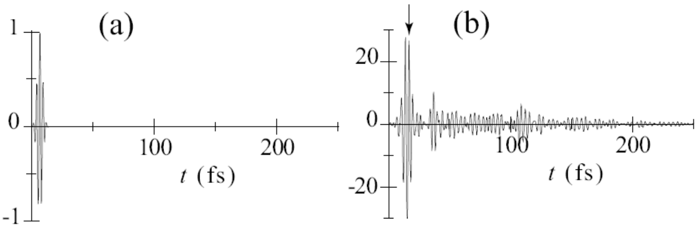

Figure 4 Simulated few-cycle (5 fs, 800 nm) excitation pulse (a) and simulated nanoplasmonic field response in a plasmonic “hot spot” (b).

3.2 High-Harmonic PEEM with single attosecond XUV pulses

A first realization of a PEEM experiment with excitation by single attosecond XUV pulses from High Harmonic Generation has been reported by the Garching group in 2012.

A High Harmonic spectrum has been generated from 5fs/0.6mJ/1kHz driver laser pulses from a carrier envelope phase stabilized Ti:Sa amplifier focused into a Ne gas target.

The HHG spectrum together with the transmitted NIR driver laser pulse is further propagating in a high-vacuum beamline towards the ToF-PEEM. The NIR beam is being blocked by a 150 nm Zr filter, which has a transmissive window for the HHG XUV spectrum above 60 eV. The HHG spectrum can be then optionally analyzed by a transmission grating XUV spectrograph.

The HHG spectrum at the spectral cutoff is further being monochromatized and refocused onto the PEEM sample at an angle of incidence of ~ 65 deg by means of a near-normal incidence Mo/Si multilayer mirror (Fig. 5).

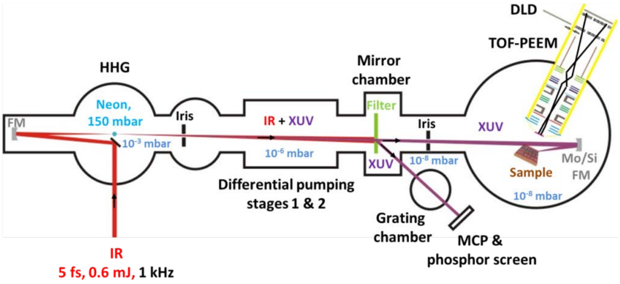

Figure 5 Experimental setup of an HHG-PEEM experiment using a 1 kHz repetition rate HHG source filtered for single isolated attosecond pulses at around 93 eV.

The measured HHG spectrum behind the Zr filter is displayed in Fig. 6, together with the XUV reflectivity curve of the Mo/Si multilayer mirror. The multilayer mirror is reflecting a spectrum of 5.4 eV FWHM spectral bandwidth centered around 93 eV close to the cutoff of the HHG spectrum (~97 eV). The resultant spectral bandwidth of the HHG spectrum corresponds to an XUV pulse duration of ~ 400 attoseconds.

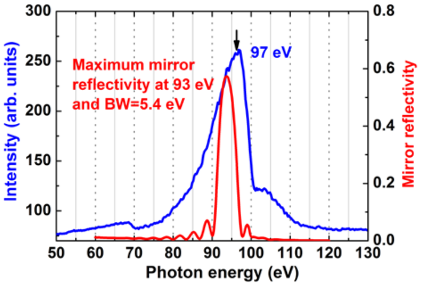

Figure 6 Measurement of the HHG spectrum after 150 nm Zr metal filter plus reflectivity curve of the Mo/Si multilayer focusing mirror. The bandwidth of the mirror (5.4 eV FWHM) corresponds to attosecond pulses of approx. 400 as duration.

A comparison of the PEEM imaging performance with conventional CW UV irradiation from a mercury discharge lamp at 4.9 eV photon energy and the attosecond pulsed HHG irradiation described above has been performed on a microstructured gold chessboard sample, consisting of alternating 1 micron Au squares on a SiO_2 surface (Fig. 7).

The PEEM images exhibit two different contrast mechanisms: While the UV-PEEM image contrast is dominated by work function differences at the surface, with Au appearing bright due to its work function (4.7 eV) being lower than the UV excitation energy (4.9 eV), while SiO2 appears dark due to its higher work function exceeding 4.9 eV, the XUV PEEM image is dominated by the different yield of inelastically scattered electrons which dominated the XUV photoelectron spectrum. This contrast (in case of Au and SiO2) is much lower than the work function contrast of both materials, thus giving rise to a lower contrast PEEM image. Furthermore, the achieved spatial resolution also differs due to physical reasons. While the energy distribution of photoelectrons emitted at the work function threshold is very narrow, resulting in monochromatic photoelectron emission and reduced chromatic aberrations in the PEEM imaging process, the energy distribution of the XUV excited secondary electrons is much broader, giving rise to significant chromatic aberration in the PEEM image.

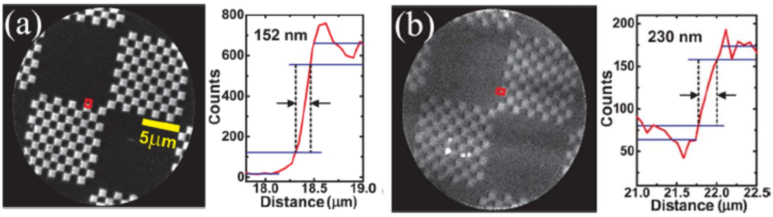

Figure 7 Comparison of a UV PEEM image (c.w., 4.9 eV) and an HHG PEEM inage (400 as, 93 eV) of a Au/Si microstructured chessboard sample.

Accordingly, a resolution of about 150 nm has been deduced from the UV PEEM image along a 16%/84% line edge criterion, while the spatial resolution has been degraded to about 230 nm for comparable PEEM settings in the case of the HHG XUV irradiation. Please note, that achieving this resolution is only possible, if space charge effects are reduced by attenuating the HHG intensity (see text below).

This attenuation extends the required image acquisition time to a few hours, making time resolved experiments merely impossible at 1 kHz repetition rate. This finding underlines the demand for further improving the HHG pulse rate into the multi kHz or even low MHz repetition regime.

A detailed analysis of the influence of space charge due to the short HHG excitation pulses on the PEEM image performance as well as the resulting photoelectron spectra was possible by applying Time-of-Flight spectroscopic measurements at different illumination intensities (Fig. 8).

The HHG intensity has been over 3 orders of magnitude by changing the Ne gas pressure in the gas target. Optimum intensity is achieved at around 100 mbar partial pressure, however no image contrast and resolution could be achieved under these illumination conditions. In short pulse photoemission, the tolerable number of photoelectrons per pulse may not exceed one electron, because multiple electrons emitted quasi simultaneously suffer from coulomb repulsion either at the sample, or more severely, at the conjugated image plane inside the PEEM column, where the electron beam trajectory crosses. The approximate XUV photon intensity of 10E6 photons per shot results (with a photon-electron conversion of ~ 0.001 at 93 eV) in about 1000 emitted photoelectrons per pulse way exceeding the tolerable number of 1 photoelectron per shot. While attenuating the XUV pulse intensity by gradually decreasing the Ne gas pressure, the image contrast as well as the image resolution improves, finally being optimized for a Ne gas pressure of about 50 mbar. This gas pressure corresponds to an attenuation of the XUV HHG spectrum by a factor of approximately 1000, bringing the number of emitted photoelectrons per pulse into the desired range. However, one has to notice, that the achieved parameters are a tradeoff between reasonable photon flux (image acquisition time) and space charge suppression, but even under these conditions at 1 kHz repetition rate space charge is not totally avoided.

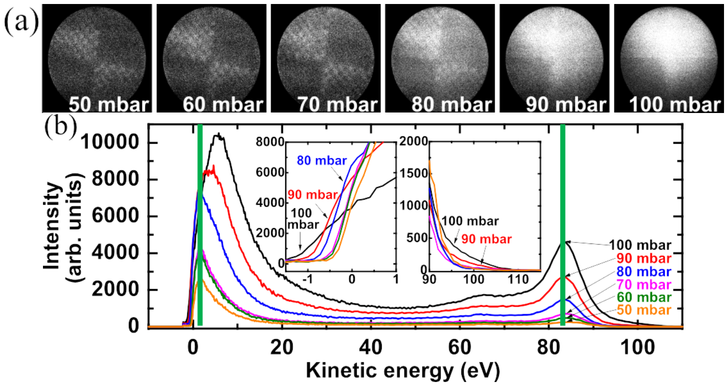

Figure 8 Space charge investigation of the HHG-PEEM images as a function of incoming HHG inensity. The optimum HHG intensity achieved at ~ 100 mbar Ne gas pressure has to be attenuated by approx. a factor of 1000 to achieve distortion free images. The electron ToF spectra show distinct shifts of the secondary electron energy while the valence band electrons remain unchanged (see text).

A deeper insight into the effect of space charge is delivered by analyzing the kinetic photoelectron spectra at different HHG intensities (Fig. 8b). The ToF electron spectra range from the inelestically scattered secondary electrons at low kinetic energies (between 0 and ~ 20 eV) up to the high energy valence band electrons at the Fermi edge around 87 eV.

While the secondary electrons (which are the majority of electrons and contribute most to the XUV PEEM image formation with no energy filtering applied) show a strong energy shift and broadening with increasing HHG intensity, the valence band electron spectra remain merely unchanged. This is a very important result, because it underlines the feasibility of the ATTO-PEEM concept, which is based upon the image acquisition and analysis by the fast valence band electrons, which carry information about the instantaneous electrical field potential of the localized surface plasmon fields. However, it also shows that kinetic electron energy image filtering of the valence band electrons is a prerequisite for ATTO-PEEM.

Besides filtering PEEM images for kinetic electron energies, electron time of flight analysis bears the potential for microspectroscopy in HHG-PEEM, which was previously only possible by applying Synchrotron Radiation illumination. This is illustrated by selected microarea spectra from a lithographic sample of Au ellipsoids fabricated onto a native oxide covered Si wafer by electron beam lithography.

The UV PEEM image (a) as well as the HHG PEEM image (b) displays the array of Au ellipsoids, with three distinct different intensity areas visible in the HHG PEEM image: the dark background intensity from the Si wafer surface, a moderately brighter intensity from the Au ellipsoids, and very bright intensities observed at localized areas at the rim of the Au frame as well as some distinct hotspots from the Au ellipsoids. When defining these three different regions of interest (ROI), as displayed colored areas of Fig. 9b, we could acquire three different ToF spectra representing these ROI.

The Au spectra show a distinct secondary electron intensity at low kinetic energies and (less intense) emission from primary photoelectrons from the 5d valence band of Au at high kinetic energies (upper panel of 11c). The corresponding emission from the SiO_2 surface shows less intense emission from secondary electrons (also due to the larger work function of SiO_2), and the contrast in secondary electron emission between Au and SiO_2 is mainly determining the observed image contrast in non-filtered PEEM imaging. At high kinetic energies, the emission from the sp valence band in Si(O_2) is observed. Note, that the emission intensities between Au and SiO_2 valence band electrons are very similar, which could prevent achieving valence band filtered PEEM image contrast for this combination. Furthermore, some indication of the emission from O-2s core level states is observed. Interestingly, the emission spectra from the most intense PEEM image areas show a distinct and very intense emission of very low energy electrons which could point to the emission of surface plasmon assisted hotspot electrons excited by leaking NIR laser radiation through the Zr metal filter.

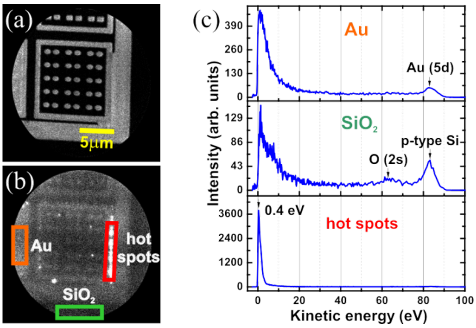

Figure 9 Microspectroscopic analysis of a nanostructure Au/SiO_2 sample using ToF energy analysis. The occurrence of hotspot photoemission from the rim of the Au frame stems from residual NIR radiation leaking through pores of the Zr film.

3.3 PEEM with high-order harmonics: Attosecond pulse trains and 1 to 200 kHz repetition rate light sources.

In this section, we discuss the quality of high-order harmonics generated in a gas as an XUV light source for PEEM (HHG-PEEM), as developed at Lund University. Our considerations have the underlying premise of using the high-order harmonic generation (HHG) light source for achieving attosecond time resolution in the Atto-PEEM. This goal requires solving fundamental and technological challenges, which we have gradually been addressing since publishing the first PEEM images using attosecond XUV pulse trains in 2009 [Mikkelsen2009]. From a fundamental point-of-view, restricting the pulse duration of the excitation light to a few hundred attoseconds or less inevitably leads to very broad energy distribution, with FWHMs between 10 and 20 eV, thus affecting spectral resolution and imaging contrast. From a technical point-of-view, the high temporal resolution required for Atto-PEEM implies high optical and mechanical stability, which is difficult to maintain over the long time needed for acquiring an image.

One of the major concerns for Atto-PEEM is the low repetition rate (<10 kHz) of the laser sources used for HHG. Space charge problems associated with the release of too many photoelectrons per event severely limits the useable harmonic pulse peak intensities (if no image degradation is to occur). On the other hand, it is necessary to detect many photoelectrons in total in order to get a good image. Combining this requirement with the necessity to limit the acquisition time for stability reasons and to take images at different pump/probe delays for temporal resolution is one of the main difficulties of Atto-PEEM. The development of high harmonic sources in the hundreds of kHz to low MHz range is a crucial next step to make Atto-PEEM and HHG-PEEM useful techniques for applications in surface physics.

We now describe the experimental developments necessary for PEEM imaging with high-order harmonics and discuss possible imaging modes. We also compare HHG-PEEM with PEEM using other light sources such as the MAX II synchrotron [Zakharov12]. We end with an experimental demonstration of how achieving high resolution in both time and space will be possible especially with the advent of attosecond light sources going into the low MHz repetition rate range.

3.3.1 Experimental setup and requirements

The experiments described in this section were carried out with two femtosecond laser systems at Lund University, based on different ultrafast laser technologies, Chirped Pulse Amplification (CPA) and Optical Parametric Chirped Pulse Amplification (OPCPA). In both cases the seed pulse is temporally stretched in order to avoid parasitic nonlinear effects in the amplification process, but the energy transfer from pump to signal radiation is realized in fundamentally different ways. The CPA laser is based on Titanium:Sapphire (Ti:Saph) as active laser material. It delivers pulses of 35 fs full width half maximum duration and 3 mJ pulse energy at a repetition rate of 1 kHz. The OPCPA laser system delivers much shorter pulses (<7 fs) at much higher repetition rate (200 kHz – 2 MHz), but at the expense of pulse energy, which is around 10 µJ. Both laser systems will be described in detail in the following and in subsequent sections we will generally term the 1 kHz system as the “kHz laser system”, while we will use the term “MHz laser” for the OPCPA based laser although it will often be operated in the few hundreds of kHz regime.

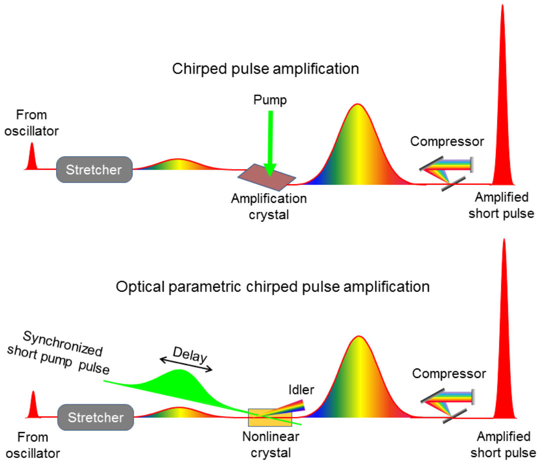

Figure 10 Comparison between chirped pulse amplification (CPA) and optical parametric chirped pulse amplification (OPCPA).

The development of ultrashort laser technology has recently reached a turning point where traditional CPA and OPCPA coexist and compete. The differences between normal chirped pulse amplification and optical parametric chirped pulse amplification are illustrated in Figure 10. After the first demonstration in 1985 [Strickland85], CPA became the method of choice for obtaining the shortest and most energetic laser pulses for applications in science and industry, such as refractive surgery of the human eye, skin cancer detection, cutting, drilling and micro- and nano-structuring. In 2001 CPA laser technology allowed for the first time the generation and characterization of single attosecond pulses and attosecond pulse trains [Hentschel01, Paul01]. The attosecond community has a large share in continuously driving the development of CPA laser technology towards shorter pulses, higher pulse energy, and faster repetition rate. However, reaching down to pulse durations below ~20 fs still remains a challenge because of gain-bandwidth narrowing. Furthermore, the heat load deposited in the laser crystal, resulting in effects like thermal lensing, is a current limitation for Ti:Saph-based high-average power CPA lasers.

OPCPA was first demonstrated in 1992 [Dubietis92], but it took until recently for the technology to mature and become suitable for applications in attosecond science. In OPCPA the energy transfer from pump to signal wavelength relies on parametric amplification. A pump pulse, which has approximately the same duration like the stretched signal pulse, is nonlinearly mixed in an optical crystal, resulting in amplification of the signal pulse and emission of an idler pulse. Since only virtual energy levels are populated in parametric amplification, no energy is being stored in the nonlinear crystal; thus heat dissipation and thermal effects are usually negligible and OPCPA scales very favourably towards high repetition rate and high average power. In optimum phase-matching conditions, *i.e.* under energy ($\omega_P = \omega_S + \omega_I$) and momentum ($\vec{k}_P = \vec{k}_S + \vec{k}_I$) conservation, the energy transfer from pump to signal pulse can be highly efficient with up to 30% in a single pass. Here ω and k are the frequencies and wave vectors, respectively of the pump (P), signal (S), and idler (I) beams. Noncollinear pump-signal arrangements provide phase-matching bandwidths for direct amplification of few-cycle pulses (one optical cycle at 800 nm wavelength is 2.7 fs long), considerably below 10 fs duration. While optical parametric amplification can often be realized in very compact dimensions, elaborate pump laser technology and precise synchronisation of pump and signal pulses in the amplification crystals is required. Indeed, the pump sources are often sophisticated CPA lasers, since short pump pulses in the picosecond range are required for efficient OPCPA pumping.

Today OPCPA schemes are particularly interesting for very short pulse duration (<10 fs) and high repetition rate (MHz) [Krebs13, Matyschok13], as well as for carrier wavelengths in the IR and MIR spectral regions, where no conventional broadband laser media exist [Biegert12].

The 1 kHz-repetition rate CPA laser system used for atto-PEEM experiments in Lund has a Ti:Saph ultrafast oscillator (Femtolasers Rainbow) as front-end, followed by a grating stretcher, a regenerative amplifier, a multi-pass power amplifier, and a grating compressor. The Ti:Saph crystal in the last amplifier is cryogenically cooled to -90° C in order to minimize thermal lensing. A programmable acousto-optic filter (Fastlite, DAZZLER), placed between the stretcher and the regenerative amplifier, is used to shape the seed spectrum to minimize gain bandwidth narrowing in the amplifiers and to correct residual spectral phase. Pulse energy of 3 mJ and pulse duration of 35 fs are obtained behind the compressor.

For the attoPEEM experiments the laser pulses are sent into an actively stabilized Mach Zehnder interferometer [Kroon14], as illustrated in Figure 11. In one arm of the interferometer, attosecond XUV pulse trains are produced via high-order harmonic generation by focusing the laser in a pulsed Ar gas cell. The XUV is subsequently separated from the pump IR light by transmitting through a 200 nm thick Al filter. A probe beam propagates in the second arm of the interferometer. The probe radiation is recombined with the XUV on a holey mirror, where the attosecond pulses propagate through the hole and the IR is reflected from the boundary. A piezo delay stage in the probe arm of the interferometer allows for precise sub-cycle temporal delay between the attosecond pulses and the IR laser pulses. After the recombination mirror the XUV and IR pulses propagate collinearly and are focused by a toroidal mirror into the sensitive region of a magnetic bottle time of flight electron spectrometer (MBES). By cross-correlating IR probe pulses with the XUV attosecond pulse train in a detection gas the average pulse duration of the pulses in the attosecond pulse train can be characterized by the RABBITT technique (reconstruction of attosecond bursts by interference of two-photon transitions) [Paul01] (Figure 12).

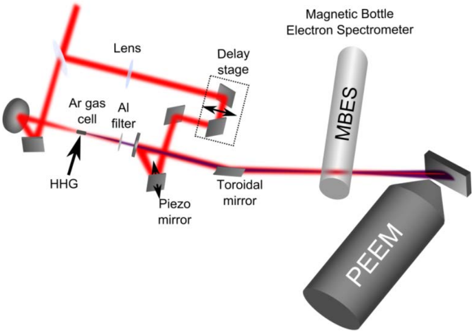

Figure 11 Sketch of the experimental setup developed for atto-PEEM measurements, consisting of an attosecond pump-probe interferometer, followed by a Magnetic Bottle Electron spectrometer (MBES) for attosecond pulse characterization and the PEEM.

The PEEM is placed behind the MBES and the sample to be illuminated is located approximately 70 cm behind the focus of the XUV. Due to strong space charge effects in the PEEM imaging path, as will be discussed later in this section, the XUV intensity was not an issue in these experiments.

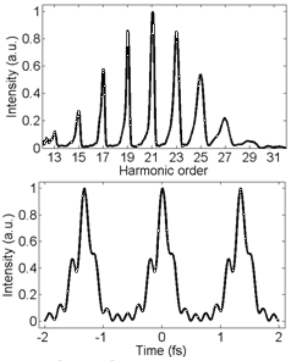

Figure 12 (top) Typical harmonic photo-electron spectrum measured in the magnetic bottle time of flight spectrometer; (bottom) Attosecond pulse train obtained from a RABBITT measurement.

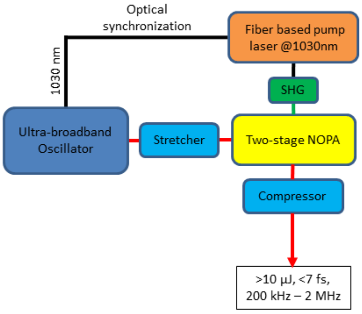

Figure 13: Sketch of the few-cycle, high repetition rate OPCPA laser source used in HHG-PEEM imaging in Lund.

The OPCPA laser source, used for HHG-PEEM imaging experiments at high repetition rate, was co-developed with an industrial partner (VENTEON Femtosecond Laser Technologies). The frontend is a few-cycle Ti:Saph oscillator (VENTEON Pulse-one) with pulse duration below 6 fs. Unlike in CPA, where gain bandwidth narrowing increases the pulse duration significantly, most of the oscillator bandwidth can be preserved in the optical parametric amplification process, resulting in output pulse duration below 7 fs [Matyschok13]. A sketch of our OPCPA laser source is presented in Figure 13. The pump laser is a Ytterbium-doped fiber CPA chain with two rod-type large-mode area fibres as last amplification stages, emitting pulses of ~1.5 ps pulse duration at an average power of ~40 W. The output of the fibre laser is converted to green by second harmonic generation in order to pump the parametric amplification stages. The fibre laser chain is optically seeded with part of the oscillator spectrum around 1030 nm in order minimize the timing jitter between pump and seed pulses in the optical parametric amplification stages. Parametric amplification is realized in a non-collinear geometry, where the pump and signal pulses are overlapped with an angle of ~2.5° in two subsequent BBO (Beta Barium Borate) crystals, where each crystal is pumped by one of the two rod-type final amplification stages of the fibre laser. The signal pulses are stretched by a pair of wedges to duration of several hundred femtoseconds before parametric amplification. Compression is realized with commercial chirped mirrors (Venteon). An output power of ~2 W is achieved after compression, which at the current repetition rate of 200 kHz leads to a pulse energy of 10 µJ. The repetition rate can be increased to up to 2 MHz on the expense of pulse energy, while the average power remains approximately constant. The carrier envelope phase (CEP), i.e. the offset between the peak of the pulse envelope and the peak of the electric field, can be stabilized for hours with two feedback loops. CEP stability is a very important requisite for the generation of single attosecond pulses [Hentschel01].

We currently develop a high-repetition rate HHG-based XUV source to facilitate atto-PEEM experiments. The output of the OPCPA laser system is focused with a short focal length (f=50 mm) achromatic lens into a high pressure Ar gas jet located in vacuum. In order to obtain the shortest pulse duration in the interaction region, the positive dispersion of the lens is pre-compensated with an additional chirped mirror pair behind the laser output. The generated harmonic spectrum is filtered with a 200 nm thick Aluminum filter. The XUV spectrum is detected with a spectrograph based on a concave grazing incidence grating and a multi-channel plate (MCP) followed by a phosphor screen. A typical XUV spectrum is shown in Figure 14. We are routinely able to generate harmonics in the 40-50 eV energy region.

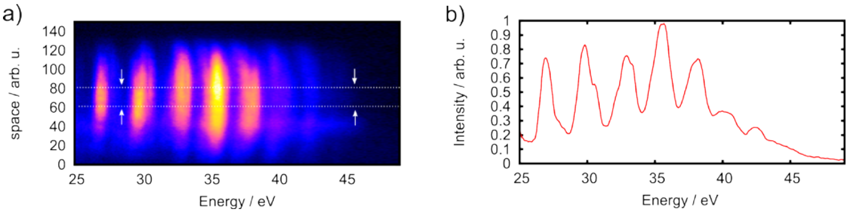

Figure 14 High order harmonic spectrum: a) spectral and space information and b) integrated spectrum.

Some considerations are also needed regarding the PEEM and the in-vacuum guiding of the beam from the laser to the PEEM setup. At a synchrotron facility, the beam onset is obviously fixed by the position of the ring and has to be in-vacuum manipulated and re-focused at the PEEM using X-ray mirrors. A typical concept is that a well-focused X-ray spot is created at some (reasonable) position in the experimental hall and then the PEEM instrument itself is aligned carefully at this position with mm precision, minimizing the X-ray spot size. This can be a long process taking several weeks. Exactly the same conditions are in practice needed for HHG sources. Conditioning these systems for the optimal and extremely stable operation conditions necessary for Atto-PEEM needs long periods of optimization upon which the laser output position will be fixed as any movement of the laser system or HHG gas chamber will demand plenty of realignments. Also a HHG laser beamline typically has to be used for several different purposes. As a result, the concept is to create the optimum focus of the XUV radiation in a specific spot in the laser laboratory and then position the PEEM at this spot. As in the synchrotron case some flexibility can be awarded using re-focusing X-ray mirrors. One important difference between the synchrotron environment and the laser environment is physical space (which is a somewhat overlooked commodity). When designing the experimental setup at a synchrotron ample floor space typically exists for placing the systems. As a result, the Elmitec PEEM/LEEM system at the MAX-II ring can be placed on a 3x2x1m concrete block by itself for vibrational stability. This type of freedom is rarely available in a laser laboratory. For this reason, the electrostatic PEEM as for example our Focus PEEM is more suitable for a laser environment. This instrument is a roughly 1.5m long (depending on attached energy filtering units) and 0.6m long cylinder. In addition it has the sample stage integrated directly with the PEEM column, making it less sensitive to vibrations and is no need for a special sample manipulator. Below we will go through the two experimental setups used in the laser laboratories for these systems, but it is worth noting that in extreme cases we have placed the PEEM on a laser table directly connected to the laser system in use. This worked fine and the resolution limit of this instrument (20-50nm) could be reached.

Having access to PEEM at both a synchrotron and a HHG source is highly advantageous for comparison of image contrasts of the same nanostructure with different types of radiation. Thus since we will be describing results from both systems we should describe the two instruments. First we will briefly discuss the synchrotron based instrumentation, followed by a more in-depth discussion of the PEEM setup for HHG.

X-ray PEEM experiments were performed at beamline I311 [Nyholm01] at the Swedish national synchrotron laboratory - MAX IV laboratory. The beamline is equipped with a modified SX-700 monochromator providing light for two stations. The first experimental station is built around a large hemispherical electron analyzer for photoelectron and X-ray absorption spectroscopy. The Spectroscopic PhotoEmission and Low Energy Electron Microscope (SPELEEM) (Elmitec LEEMIII) is installed downstream from the first experimental station. The present set-up allows three basic operation modes using X-rays: 1) energy filtering imaging, 2) energy filtered micro-diffraction and 3) micro-XPS or dispersive plane imaging. The first harmonic of the undulator is used for the excitation, normal incident to the sample surface plane. This is in fact somewhat unconventional and is only possible due to the 60 degree angle of the PEEM (and LEEM) columns with respect to the sample (the light goes through the beam separator of the microscope). This is in contrast to the PEEM used for HHG (discussed below) in which the light must come in at an angle of 65 degrees to the surface normal of the sample, which in this instrument coincides with the optical axis of the PEEM column. The electrons in the Elmitec instrument are extracted with a set voltage of 20 kV on the sample. The energy filtering function is realized by utilizing a hemispherical analyzer in the electron optical path. The transition between different operation modes is accomplished by changing the excitation of two lenses (intermediate and projective), two apertures (selected area and contrast aperture) and the energy slit in the dispersive plane of the analyzer [Schmidt98].

The PEEM used in the HHG experiments is a commercial Focus PEEM supplied by Omicron [Omicron1]. Photoelectrons are extracted from the sample stage with voltages that can be varied from 100V up to 15 kV and focused using an electrostatic focusing system. Contrast apertures ranging from 30 µm to 1500 µm in diameter could be inserted into the back focal plane of the objective lens to achieve improved resolution - at the expense of severe reduction in the electron intensity measured at the MultiChannel Plate (MCP) in connection with a fluorescent (YAG) screen used for displaying the electron intensities.

In the very first test setup employed for HHG PEEM measurements [Mikkelsen09] we used a scaled down Ultra High Vacuum system relying on only one turbo-pump for vacuum, with no special damping. At this point the PEEM had no energy filtering capabilities. Nevertheless resolution down to ~100 nm could be achieved with a standard Hg-Lamp light source. For this first setup, the PEEM vacuum chamber was directly connected to the HHG vacuum chamber with no additional diagnostics in-between. This positioned the PEEM exactly in the geometric focus of the HH beam. Alignment of the PEEM could be done via XY-stages. The IR laser beam can be used as a guide in the alignment procedure. The IR beam co-propagates with the XUV beam, and is usually cut by an Al filter. Final alignment and initial characterization of the XUV beam was done using the PEEM in low magnification. This setup has several shortcomings, both in terms of mechanical vibrations, lack of energy filtering, and perhaps most importantly, no easy way to diagnose the HHG signal. The last point is absolutely crucial in order to determine exactly the energy and time structure of the XUV laser pulses by HHG in more long term experiments going beyond the initial demonstration. Still, this first generation experiments clearly demonstrated that the biggest problem in these types of experiments is space charge effects coming from the photo excited electrons passing from the sample through the PEEM imaging optics (we discuss this in detail below). For a continuous source this is not a problem, but as the photoelectrons in the 1kHz HHG system are released in extremely short bursts essentially “using” only ~10^{-11} of each second for electron emission we end up with a dense electron cloud at each pulse which will smear out any resolution in energy or space (as seen below). To reduce this effect below the detection limit we had to attenuate the 1 kHz laser system by a factor of ~300, which led us to conclude that for such a system it can be of value to place the PEEM significantly out of the focus point of the XUV.

In the next experiments, the XUV and IR pulses were focused into the sensitive region of our magnetic bottle electron spectrometer (MBES) in order to observe the spectrum of the HH and to measure the time structure of the attosecond pulse trains. The PEEM was placed at 70 cm from the focus. The spatial resolution that could be achieved with XUV attosecond pulse trains and Hg lamp in this setup were on the order of 200 nm and 50 nm, respectively. In order to get high enough IR intensities (for pump-probe experiments), we moved the IR laser focus closer to the target by adding a lens in the IR arm of the interferometer. While the angle of illumination was fixed at 65° to the normal (due to the extractor column/sample geometry) the polarization of the beams could be controlled. In this version of atto-PEEM we also made necessary improvements to the vacuum systems setup. An ion-pump was added to the PEEM UHV chamber for vibration free pumping. Since pressures in the HHG chamber can be rather high it would normally not be possible to run an ion-pump in the adjacent chamber exclusively. However, the MBES chamber which had been added in between the PEEM and the HHG chamber also had the function of acting as a differential pumping chamber for the PEEM. Thus a pressure in the PEEM below the 10^{-7} mbar range could be maintained even with high pressures in the HHG chamber. It should be noted that the turbo pumps in the HHG and MBES were magnetically suspended and the PEEM and the MBES was coupled via a stretchable bellow which could further reduce vibrational issues. All in all, with this setup the optimal resolution of the PEEM (20-50nm) could be achieved using the Hg-lamp.

In the third PEEM setup used with the MHz system a couple of features were again modified. Firstly since the number of photons per pulse was strongly reduced, we now needed to use a higher part of the XUV peak intensity. The radiation was focused to a spot of the same size as the maximum relevant PEEM Field of View (FoV) with a re-focusing mirror. We had the option to insert an XUV reflection grating to disperse and divert the beam onto a channel plate system for diagnostics for the XUV radiation. The PEEM was placed on a specially designed laser worktable which allows for static damping and placement of optical components at the PEEM optical access windows. Further, as MHz atto-PEEM increases the average intensity by orders of magnitudes, it became interesting to upgrade the PEEM with an energy filter. We chose the high-pass, retardation grid imaging energy filter (IEF) as it works independently of the laser system and is the simplest in terms of adding extra electron optics components.

Crucial for successful Atto-PEEM experiments is also the correct choice of samples. For our purposes we need both lithographic samples for establishing lateral image quality and tailored samples (both via synthesis and lithography) for studying for example plasmonic responses. Because of the very broadband nature of attosecond XUV pulses, obtaining a good contrast with this type of radiation (without strong energy filtering) is a challenge. One standard sample used throughout our experiments was a lithographic sample consisting of a Si substrate with a 65 nm thick, patterned Au film. Nine arrays of holes were made in a 150 µm × 150 µm region of the Au film. The region was divided into nine 50 µm × 50 µm squares using 1 µm wide lines. In the center part of each square, there is an array of holes with a coverage area of 20 µm × 20 µm. The diameter of the holes was 100 nm in all the nine arrays and the separation between holes was designed to be different in different arrays and was systematically changed from 240 nm to 400 nm. The hole diameter and the separation between holes in each hole array were indicated by text numbers made lithographically with 200 nm wide text lines (Figure 15a). Other structures imaged in our experiments, were size-selected 50 nm Au aerosol nanoparticles, deposited on a conducting Si substrates with a density of 1 per µm^2, as well as 35 nm diameter III-V nanowires also deposited on a conducting Si substrate. Growth and deposition of these structures are described elsewhere [Hjort12]. We also investigated Ag nanowires and nanoparticles, which have been used in a number of previous plasmonic studies [Wei11]. We deposited the Ag nanostructures from colloidal solutions onto different substrates. We used nanowires, near-spherical nanoparticles, nanorice and nanocubes all dispersed in ethanol solution [Sun02, Liang09, Wei10]. A drop of the solution was placed onto a substrate which was blow-dried after 30 seconds. The sample was then cleaned in acetone in an ultrasonic bath for 5 min. We tested a variety of substrates in this case (All highly conducting): 50 nm thick Au film on Si, 50 nm Cr film on Si and 150 nm ITO film on borosilicate glass. Specific structures investigated in the PEEM could be relocated and studied in SEM. We also recorded XPS spectra at beamline I311 at the MAX-II synchrotron of the different samples, to monitor overall surface chemical composition and energy distribution of photoemitted electrons over a wide energy range.

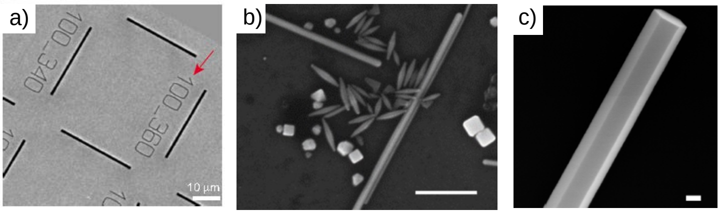

Figure 15 Samples used for the studies a) SEM image of part of a lithographic pattern inscribed in Au. In total, 9 square arrays of holes were fabricated in a square region of 150 µm ×150 µm of the Au film. Red arrow indicates text with 200nm wide lines. An array of holes with 100nm in diameter is found in the center (not visible in this magnification of the SEM image). b) Ag nanowires, nanoparticles and nanorice, scalebar is 1 micrometer. c) Thick InAs semiconductor nanowire (Scale bar is 200 nm). These nanowires can be made in all diameters from a few nanometers up to hundreds of nanometers.

With the 1 kHz laser repetition rate, the quality of PEEM imaging and temporally-resolved measurements was severely compromised by space charge blurring effects. To obtain a sharp image, we had to turn down the gas pressure in the HHG cell. We estimate that the necessary reduction in the signal was more than a factor of 300 compared to the highest achievable values. At higher intensities the images gradually became blurred until only a broad (>200 µm) footprint of HHG beam was observed. The space charge effects can be understood in this way: although the average electron density on the scale of seconds (like the exposure time of the PEEM) is moderate, the short duration of the XUV pulses leads to high peak photoelectron intensities (more than 10^{10} times the average photocurrent). This leads to Coulomb repulsion which manifests itself in three ways: temporal, lateral, and energy broadening, resulting in significant blurring of the images. Theoretical and experimental work on short electron pulses and photoemission have shown similar space charge problems, in good quantitative agreement with our results [Collin05]. Our results are also comparable to those obtained using the femtosecond XUV pulses from the free-electron laser FLASH [Pietszch08]. As the electron distribution in our experiments already has an energy FWHM of ~15 eV, the energy broadening will not cause much additional smearing of the image. Thus we expect that the pure geometrical broadening is the most important effect in distorting the images. It was found in two-photon or three-photon photoemission microscopy experiments using a laser system operating at 1 kHz repetition rate (as ours), that the intensity had to be reduced to levels where imaging was only possible by measurements over 15 min [Buckanie09]. In this case the space charge problems were believed to occur at the crossover point near the entrance to the hemispherical energy analyzer incorporated in the design, when the electrons are decelerated to 1 keV. This energy analyzer is not installed in our PEEM and as we can achieve imaging at much shorter exposure times (indicating less space charge problems) it seems quite conceivable that a simpler PEEM design (as in our case) can also reduce the degree of space charge problems observed.

To illustrate the space charge problems, we imaged Au particles illuminated by an IR field and displaying resonant enhancement either by being separated by a distance matched to the laser wave length, or overlapping in configurations resulting in a resonance. Combining now a HHG and IR beam, it can be observed that the IR and XUV beams influence each other, leading to a defocusing of the image. We have investigated this influence as a function of delay between the IR and the XUV beam when the XUV pulse is before and after the IR, we find that the effect disappears by separating the pulses by some picoseconds. This means that the electric fields from the charges created by the two pulses influence each other. Such effects should be most important at the point where the charges are closest to each other and therefore most concentrated. Charge density is generally highest in the focal points of the PEEM or at the surface when the electrons are first photo emitted – i.e. in the back focal plane of the objective lens or in the area near the sample. The distance between the two electron pulses will be smallest in the region between the extractor and the sample where they are accelerated. In a simple model, the central position of an electron pulse in this region will vary as $z(t)=eV_0/(2md)*t^2$, where z is distance between the pulse and the sample, d is the distance between the extractor and the sample, m is the electron mass, V_0 is the extractor voltage (V_0 =14 kV) and e is the electron charge. From this formula, we calculate that the total time spent in the extractor region is 60 ps. Assuming that the two pulses generated are separated by 5 ps, we calculate that after the second pulse is released the distance between the two pulses is between 15 and 80 µm during the first 10 ps – less than the estimated diameter of the pulses of ~250 µm. The separation between the centers of the pulses after they leave the accelerating field can be calculated to ~350 µm. This is also the distance between the two pulses in the back focal plane. Thus we estimate that the interaction between two pulses, when separated in time, is strongest near the sample. In a simple model considering the first stage of the PEEM and the sample described as a cathode/anode lens, the observed effect can be understood as a result of the field from the photoelectrons released by the XUV pulse effectively spreading out the photoelectrons from the IR pulse as indicated in Fig 16 - thus acting as an additional electrostatic element in the system. As is also observed, this effect would exist no matter which pulse comes first as the photoelectron bunches would affect each other while moving through the lens system. Finally, if the charge created by one pulse acts as a simple electrostatic lens on the other pulse moving the focal point, one can under some conditions refocus the spots in the images by changing the focus of the PEEM. Indeed we find that by changing the focus of the PEEM we can refocus the bright spots of electrons emitted due to the IR beam. Finally, we have observed that this space charge effect can also be removed be reducing the intensity of the IR beam, while still observing multi-photon electron emission.

For the MHz laser system some simple calculations can be done to avoid space charge effects. Using the double MCP of the PEEM instrument, it is possible to detect single electron events at very low image intensities, which is a way to correlate the image intensity and the number of detected electrons. With this method, we estimate that we detect on the order of 0.1 electrons per pulse in a 20 µm field of view when working with PEEM using the 200 kHz HHG source at typical conditions. With a contrast aperture of 70 µm, we further estimate the average transmission of the instrument for the secondary electron peak to be on the order of 5%, meaning that the number of electrons per pulse created at the sample in the FoV is roughly 1-10. At these low photocurrents we do not detect any significant space charge effects. The size of the beam on the sample does not play a major role here. Our studies show that electrons originating from different light pulses do not interact to create space charge effects if the pulses are separated by more than 10 ps, as discussed above. With an acceleration voltage of 10 kV and a sample-extractor distance of 1.8 mm, this corresponds to electrons from the two pulses never being closer than 20 µm to each other. This in turn tells us that a large spot size does not lead to significant parasitic space charge effects from photoelectrons generated outside the FoV, as long as the spot size is on the order of 20 µm or larger.

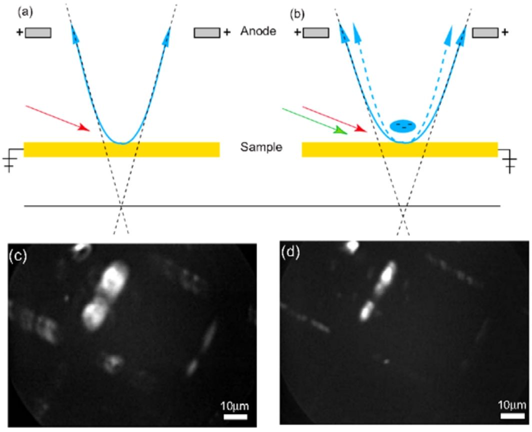

Figure 16. Simplified illustration of the mechanism behind the interaction of the electrons created by the IR and the XUV pulses respectively. The first stage of the PEEM lens system consists of the sample as cathode and the first lens of the PEEM as anode. a) If only one electron excitation source (red arrow) is used, the electron paths (indicated by blue lines) will pass into the microscope being bend by the first lens, thus effectively creating a focus point behind the sample. The focus point of the PEEM behind the sample is indicated by the crossing of the broken black lines. b) If two consecutive excitation pulses follow rapidly after each other (red & green arrows), the electric field from the charges excited from the first pulse will act to bend the trajectories of the electrons excited by the second pulse. This also effectively moves the focus point. c) PEEM image (12 kV) of the lithographic structure using the 1.55 eV IR laser beam and the XUV beam with no time delay between the two beams. d) PEEM image (12 kV) of the same structure and area as in c) using the 1.55 eV IR laser beam and the XUV beam with a time delay of 10 ps between the two beams.

3.3.2 XUV Imaging

One important aspect of PEEM in combination with HHG (and synchrotron) light sources is the wide variety of imaging modes possible, depending on both the configuration of the light sources and the PEEM.

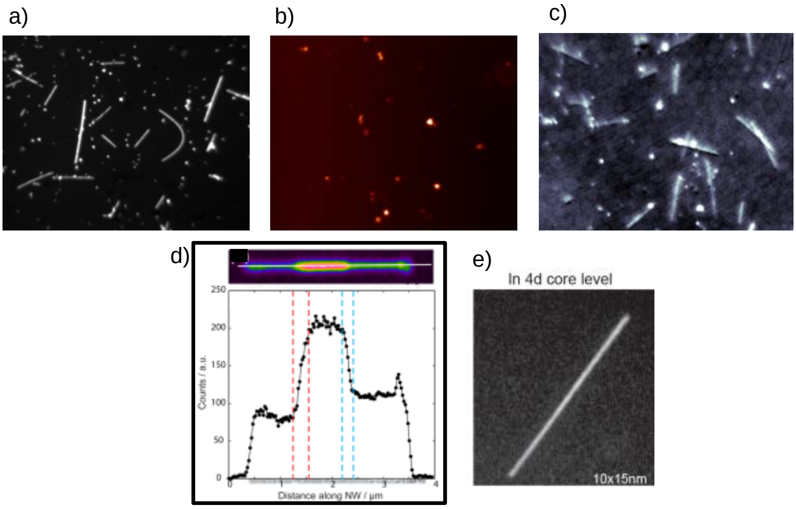

Figure 17 a) Hg-PEEM image of Ag nanowires, b) 3PPE image of Ag nanowires (same area as Hg lamp image), c) XUV PEEM image of nanowires, d) Secondary Electron image of an atomic hydrogen cleaned InP n-i-n-NW (hν=133 eV) recorded at the MAX II synchrotron (top). Intensity profile along the wire is seen as well (bottom). The dotted red and blue lines mark the two space charge regions (SCRs): The first (red) SCR is 300 nm wide and the second one (blue) 200 nm. The Au seed particle can be found at the far right in the image. e) PEEM image recorded using directly emitted In 4d photoelectrons (hν = 70 eV, kinetic energy = 47.6 eV) at the MAX II synchrotron.

The fundamental imaging mode of the PEEM is achieved by using an Hg-lamp UV source which images just around the work function threshold of the metal (4-5eV). With such a source the main contrast comes from topography and work function differences. As the photon energy is just above the work function threshold, this also means that the released photoelectrons have very low initial energies (<1-2 eV), which does give a reasonably narrow energy distribution with little necessity for energy filtering. Thus the technical limits of resolution for a PEEM in a given setup can quickly be tested in this mode, and it is also an excellent mode for observing all nanoscale objects placed on the surface, and even small chemical differences. On the negative side, since several contrast mechanisms are involved interpretation of the contrast can be challenging. Still, Hg lamp imaging is an indispensable mode to have available during HHG PEEM experiments as it gives an immediate report on any changes to the surface and aids in optimizing the lenses in the PEEM for optimum resolution.

Another important imaging mode is multi-photon photoemission using a laser pulse with an energy below the work function threshold. Since HHG is the result of intense IR pulses interacting with a gas medium, intense ultrashort IR pulses are always available as an excitation source and will often also be the pump pulse in an atto-PEEM pump-probe experiment. While a single IR photon does not have enough energy to release a photoelectron, multiphoton processes, in which the electron is excited through several short-lived states in the gap between the Fermi level and the vacuum level, may also lead to photoemission. The probability of such processes will scale with I^n, where n is the number of photons involved in the multiphoton process and I is the intensity of the laser field. As is seen in Fig 17, multiphoton photoemission can be observed using only a small percentage of the IR intensity available in HHG laser systems. If the intensity the IR is further increased the sample will instead be structurally damaged. Interestingly, we have imaged multiphoton emission up to at least n=8 with no apparent damage to the sample [ref 8photon PEEM]. The contrast observed in multiphoton photoemission is a very sensitive map of the field intensity across the surface as it scales with I^n (for the fundamental ~800nm IR used for HHG, this corresponds to n=3). As a result, this imaging mode allows us to observe any resonance structure (such as a plasmonic structure) giving rise to locally enhanced fields on the surface. We can immediately visualize where we expect the strongest interaction between the IR beam and nanostructures to takes place on the surface – which is especially relevant for nanoplasmonic studies. For pump-probe studies in which the IR is the pump pulse (exciting a surface plasmon) and the XUV is the probe pulse, one must limit the multiphoton photoemission as it is the electrons emitted by the XUV photons that we are interested in. Our measurements indicate though that this is not a significant problem – we have very appreciable IR field strength on the surface and still have a clearly discernible signal from the XUV beam.

A third imaging mode is monochromatized X-ray radiation (between 30-1000 eV at MAX II), which gives a very clearly resolved energy structure of the photoelectrons. As an illustration we show in Fig 17 imaging of 80nm thick Au seeded InP nanowires with an undoped segment sandwiched between highly sulfur doped n-type segments [Hjort11]. The nanowires can be characterized both using directly emitted photoelectrons from specific core levels and secondary electrons (SEs) from inelastic scattering inside the sample.. From imaging the In4d core level electrons we immediately get information specific to the parts of the wires containing In (in this case it shows the very homogeneous distribution of In along the nanowire). As can be expected- the primaries give clear and easily interpretable information, but the intensity is lower than for SEs. Dopant induced contrast in SEs was observed very clearly, and did not change with different kinetic energies, nor with different photon energies used for excitation. SE dopant imaging favors a contrast scale with p-type as the brightest, and the SE intensity gradually decreasing as n-doping is increased. This can be explained by a locally varying vacuum level potential outside the sample surface where electrons emitted from the n-part need a higher energy in order to reach the detector, which will thus lead to a lower SE yield. The difference in the secondary electron emission can be used to extract a rough estimate of the change in carrier concentration between the different segments. One can for example find that the top segment has a higher SE yield corresponding to a significantly lower charge carrier concentration.

We now turn back to imaging using XUV radiation from HHG (attosecond pulse trains). Due to signal intensity and photon energy PEEM-imaging used all of the emitted electrons and thus primarily secondary electrons. The preceding example and many other works clearly show that SEs can give much information about structural [Locatelli08], chemical [Hjort11], and magnetic properties [Stöhr93] with nanoscale resolution. SEs are thus in principle an excellent source of information, however as with the electron emitted via the Hg lamp, since several different phenomena play a role in determining the SE intensity, interpreting and predicting how a given sample will display in SEs can be tricky. We have thus experimentally investigated the contrast that can be achieved detecting all electrons emitted by broadband attosecond pulse trains of duration of ~20 fs. We investigated Ag nanowires and nanoparticles on different substrates: ITO, Cr, and Au. The Ag nanostructures are among the most studied in plasmonics and thus present a good basis for exploratory attosecond studies. We also tested semiconductor substrates such as Si or InAs, but the lower conductivity of these substrates led to severe problems with charging of the samples. The contrast obtained with SE PEEM imaging depends on a number of different aspects, such as topography, work function, and ionization cross-section. The ITO, Cr, and Au substrates give very different contrast. On the

ITO substrate, most nanowires appear black (i.e., they show a photoemission yield significantly lower than that from the substrate). There is also no clear orientation dependence. This suggests an electronic structure contrast mechanism that is sensitive to the surface of the wire, with the vast majority of structures emitting significantly less than the substrate. On the Cr substrate, the wires show almost no contrast. Some wires appear slightly brighter than the substrate and some slightly darker. A strong dependence on the direction of the nanowire can also be seen, with nanowires lying in the plane of incidence (horizontally) being completely invisible. The contrast, in this case, is topological and mainly due to a shadowing effect of the nanowire. The nanowires have diameters of 150-200 nm, which is well above the wavelength of the XUV radiation (~40 nm). The increased brightness on the side facing the illumination can be explained by a mirror effect, where light reflected off the surface before the nanowire yields a higher XUV intensity at the side facing the illumination. The shadowing effect explains the dark side of the nanowires, and also why nanowires oriented parallel to the incoming radiation are not seen in the images (since the small shadow at the short end of the nanowire cannot be resolved in the images). Finally - on the Au substrate, the Ag nanowires appear significantly brighter than the substrate, giving a clear contrast. One can also see that vertical nanowires have one brighter and one darker side, while horizontal wires show a more homogeneous bright intensity distribution. The bright contrast is due to electronic structure differences, while the dark part is a topological shadowing effect. From profiles across wires, we found that the nanowires were up to 30% brighter than the Au substrate, while the contrast on the Cr substrate was below 10%, both for the bright side and the dark side of the wire. On the ITO substrate, the wires were ~15% darker than the substrate. These contrast differences come from the SEs, since they constitute more than 90% of the total electron yield. This shows that, even with a broadband light source and no energy filtering, good imaging conditions using SEs can be obtained for samples that are relevant for plasmonic studies. Differences in SE emission can be explained by differences in absolute work function and in excitation probabilities of either primary or secondary electrons. For example, Au has a higher work function than Ag (5.1eV for Au and 4.1-4.7 for Ag) which explains the contrast differences in this case.

The ultimate resolution in PEEM at photon energies much above the work function threshold can be estimated from the use of synchrotron sources which have narrow energy bandwidths and high average intensity. Under favorable conditions the highest achievable resolution is around ~20 nm. The resolution is limited by the wide secondary electron energy distribution and the relatively large field of view. Using highly monochromatized electron sources for excitation in the same microscope (so called low-energy electron microscopy (LEEM)), a resolution of 5-10 nm can be achieved. A dramatic breakthrough in the field of electron microscopy is the advent and practical realization of aberration correction optics capable of significantly improving the spatial resolution in LEEM down to <2 nm. Along with much better spatial resolution for an aberration-corrected microscope, the electron transmission is also significantly (ten-fold) increased which is very important for the flux hungry PEEM experiments. The first aberration corrected PEEM/LEEM systems are now coming into operation and are living up to their promises. It should be noted though that the amount of electron optics in the microscope is almost doubled, making the instrumentation much more complex to handle. With the additional lenses, space charge issues at new points in the microscope could also be a concern.

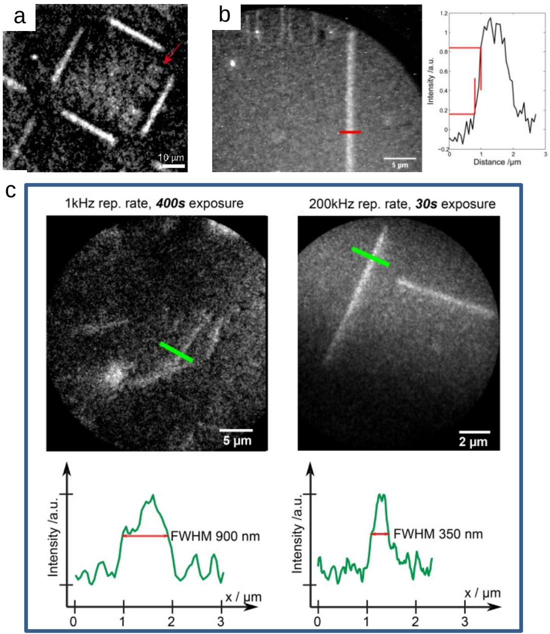

Figure 18 a) 1st 1 kHz image of lithographic structures, b) images at optimal conditions with kHz laser of the lithographic structure, with estimates of resolution c) 1st images taken with 200kHz rep rate (right) of 200 nm wide Ag nanowires compared to 1 kHz rep rate images (left) of the same type of Ag wires. Notice the nice resolution and the decrease in exposure time of more than a factor of 10.

Figure 18a illustrates the spatial resolution achieved in our first HHG-PEEM imaging experiments. By comparing several features from the imaged lithographic structures we estimate that the spatial resolution to be between 200 to 300 nm [Mikkelsen09]. In later studies we tried to push the resolution down as much as possible, by limiting mechanical vibrations, carefully adjusting the electron optics, using smaller contrast apertures, and going to longer exposure times with the use of a cooled, slow-scan CCD camera. With these improvements, the fundamental limit in resolution of the PEEM (20-50 nm) could be reached when using the Hg lamp as light source, while with HHG-PEEM led to a resolution of about 200 nm. Our resolution limit with the XUV pulses with an energy bandwidth of 20-40 eV was measured using a lithographically defined structure with clear edges and a 16%-84% measure criterion as explained in Fig 18b.

To check if chromatic aberration was the reason for our spatial resolution limit, we made a test at the Elmitec PEEM at the MAX-II synchrotron radiation source. Using 34 eV photons we imaged semiconductor nanowires, with diameters of 35 nm and length of several microns, spread randomly across a Si substrate. Removing any energy filter (resulting in a bandwidth comparable to the HHG, i.e. larger than 10eV), the nanowires could not be observed and only large features wider than 100 nm were seen. Inserting an electron energy filter with a width of 0.7 eV, the wires could easily be imaged. This suggests that a normal spatial resolution of <50 nm or below could be achieved with the HHG-PEEM setup provided an energy filter is introduced in the PEEM. What prevents us from using this feature was the low average flux at 1 kHz repetition rate. In order to form images in any reasonable periods of time we had to use large apertures and no energy filtering. In contrast to spectroscopy experiments where data collection over days is possible, this is in practice difficult in imaging experiments, obtaining and keeping a good focus in the image, and thus in practice realizing high resolution, demands acquisition times which are compatible with the present stability of PEEM setups, using laser based sources.

These issues are the origin of our efforts towards high repetition rate using OPCPA laser technology – Fig 18 compares measurements of Ag nanowires imaged with HHG-PEEM operating at 1 and 200 kHz respectively. In addition to the order of magnitude improvement in exposure time a clear improvement in image quality of a factor of 2-3 is observed. This is because smaller apertures can be inserted in the image taken at 200 kHz thus reducing both the spherical and chromatic aberrations. Future studies will be necessary to confirm that we can reach the ultimate resolution limit for our PEEM setup using high repetition rate HHG sources. The sources also open up new imaging opportunities allowing us to select energy windows, as presented below.

We now proceed with a more in-depth analysis of HHG imaging for attosecond experiments. XUV or X-ray photons interacting with a solid give rise to many excitation processes. Electrons can be emitted from the sample by direct photoemission (corresponding to core level or conduction band photoemission), and by photoexcitation followed by subsequent electron–electron interaction (such as Auger or secondary electron emission). Some of these processes are pictured in Figure 19, where the mechanisms are schematically drawn in an energy diagram on the left side and correlated with their respective spectral signatures in the typical spectrum shown to the right.

For photon energies in the XUV range, the SE contribution to the spectrum typically contains 90-95% of all the emitted electrons. The width of the SE peak is on the order of a few eV, but can vary significantly [Yang07]. All of these photoelectrons can be used for PEEM imaging, as has been widely explored using synchrotron radiation. Using energy-filtered PEEM in combination with X-ray sources with high average flux, both core-level electron levels and the valence band region can be used for imaging. However, if the secondary electrons are instead selected, the image contrast is qualitatively different arising from several features of the surfaces, as discussed in section 2a. Still, the number of electrons originating from the substrate should be minimized, since these only add to the noise levels and contribute to space charge effects in the PEEM, while the electrons from the nanostructures themselves constitute the interesting signal. This means that the materials system should be chosen to create a clear contrast with the features of interest appearing bright in the image, which in some circumstances can be done by an appropriate choice of substrate [Mårsell13], as discussed in 2a. The contrast can also be modified by surface manipulation such as adsorption of molecules or alkali metals [Aeschlimann07].

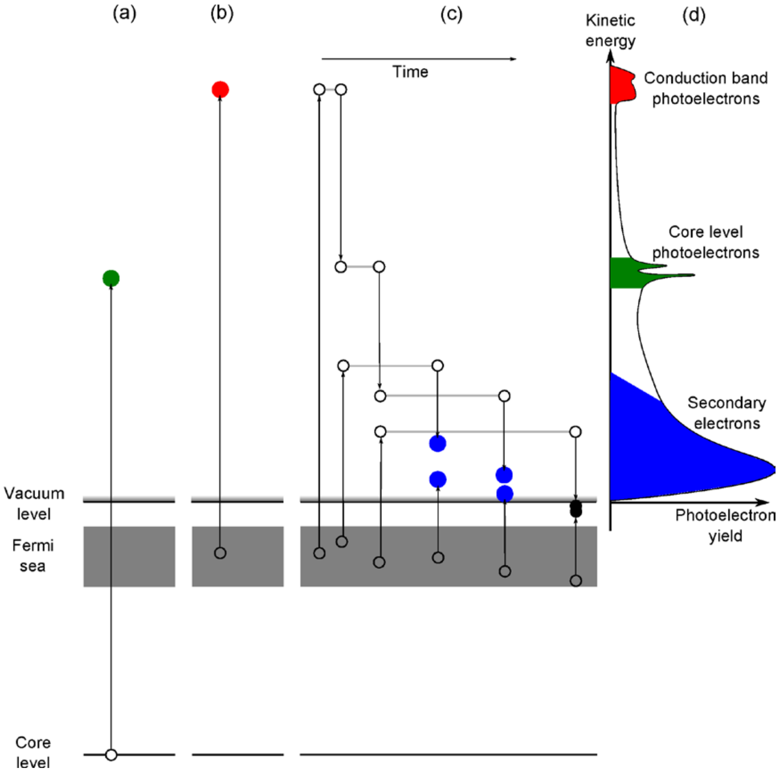

Figure 19 Schematic illustration of some different mechanisms for photoelectron emission. (a) Direct excitation of a core level electron to the vacuum. (b) Direct excitation of a conduction band electron to the vacuum. (c) Excitation of a conduction band electron to a higher-lying state, followed by a secondary electron cascade where the excited electron distribution is thermalized via electron–electron interactions. (d) Schematic photoelectron spectrum, showing the typical spectral signatures of the different processes. The secondary electron peak is typically much higher than shown in the figure, but it has been scaled down for clarity. Note also that this is a schematic of a spectrum recorded with a monochromatic soft X-ray source.

From a practical point of view, imaging SEs is easier than imaging primary electrons because of the lower energy of the electrons to be imaged. Because of the generally low average intensity used in HHG-PEEM alignment and focusing of the instrument constitutes a significant practical challenge. For the SEs, this challenge is of minor importance since the electron energies are similar to those used for threshold PEEM using an Hg discharge lamp. For primary electrons on the other hand, finding the optimum settings of the microscope can be quite a challenge, since typical image acquisition times are on the order of five minutes to more than one hour [Mårsell13, Chew12]. Thus all successful imaging in HHG_PEEM using 1 kHz sources has been done with SEs. These exposure times can also be expected to be longer for primaries than for secondaries, since the latter constitute the vast majority of the emitted electrons.

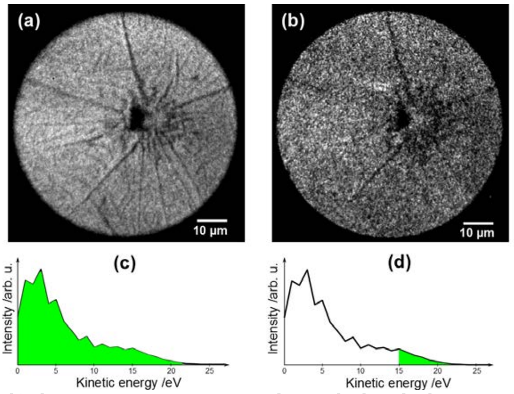

Figure 20 (a-b) shows PEEM images acquired using high-order harmonics from the MHz laser system in Lund (set at 200kHz rep rate). There, a nanostructured Au/Si surface is imaged using the primary electrons (with kinetic energy above 15 eV) and the entire photoelectron distribution, dominated by secondary electrons. This type of energy selective imaging is one of the new features made available by the MHz HHG setup that allows significantly higher average photocurrents to be used for the experiments.

In order to realize pump–probe PEEM imaging on the attosecond time scale, several conditions need to be met. First of all, as mentioned earlier, a stable interferometer needs to be built (see Fig. 12) to produce (optical) pump and (XUV) probe pulses. Secondly, an ultrafast process must be initiated by the optical pulse and a measurable signal that still carries information about the dynamics on an attosecond time scale needs to be generated by the attosecond pulse. This signal has to be strong enough to be detected with the PEEM, i.e. a satisfactory signal-to-noise ratio needs to be reached. While the time scale for direct photoemission from a solid has been shown to be ultrafast [Cavalieri07], less is known about the SE cascade. However, the high electron density in metals leads to a large probability for electron–electron scattering, and thus to a short mean free path (on the order of 5 Å). For excitation using photons in the 30 eV range, a typical excited electron only undergoes 2-3 scattering events before being thermalized to a state below the vacuum level, and thus unable to escape from the material. This can be further investigated using a semiclassical Monte Carlo model, as we have previously shown [Mårsell13]. Simulations based on the model developed by Wolff in the 1950s [Wolff54], and recently used for application in attosecond spectroscopy from surfaces [Baggesen09], show that more than 80% of the secondary electrons escape from the surface within one femtosecond after excitation with an attosecond pulse with a central energy of 30 eV and FWHM of 15 eV, thus showing that also the secondary electrons contain information about sub-femtosecond surface dynamics.

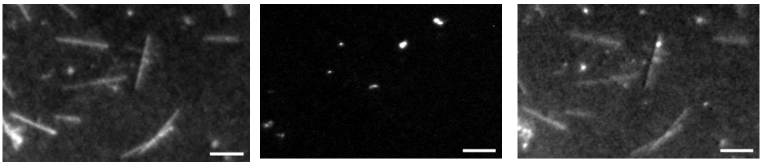

Figure 21 XUV image (left), IR image (middle) and XUV+IR image (right) of the same area. Scalebars are 10µm. The XUV and IR signals can have similar intensities.

Attosecond pump-probe PEEM requires the detection of an oscillating signal on top of a constant background. In order to determine the relationship between the oscillation strength and the statistics needed to be gathered to detect the signal, some estimates can be made about the signal-to-noise ratio. Measuring the pixel values from a featureless area of the substrate in PEEM images recorded with different exposure times, we can define a noise level as a function of exposure time as the ratio between the standard deviation and the mean of the pixel values in the area. For experiments using the 1 kHz laser, this ratio reaches 0.035 at an exposure time of about 500 s. This noise level corresponds to a sinusoidal oscillation with 10% peak-to-peak variations compared to the background, and thus gives an estimate of what exposure times are needed to pick up an oscillating signal of certain strength, assuming that the oscillating signal occurs in a single pixel. If several neighboring pixels oscillate in phase, the oscillation will be easier to identify. Using the new MHz laser setup, we have shown that we can reduce the exposure times by at least an order of magnitude, while at the same time improving the spatial resolution, allowing us to observe more easily local variations in the signal. We therefore believe that it is now possible to detect a 10% peak-to-peak oscillation in the electron yield using exposure times of 30 seconds.

By removing the metallic filter in the beam path and shutting down the gas for HHG in the pump-probe PEEM setup, it is possible to perform IR-IR interferometric measurements on the sample. Such measurements can, besides probing the stability of the interferometer, give information on several points. First of all, they can be used to map out the localized surface plasmon resonances on the sample, and even measure their dephasing times as long as the pulses are short enough. Furthermore, the measurement is a direct way of calibrating a Mach-Zehnder type interferometer since it can map out the absolute zero delay with high precision. Figure 22 shows part of such an interferometric autocorrelation recorded with the kHz laser system (35 fs pulses) and a sample consisting of Ag nanowires on a Au substrate.

The multiphoton photoemission used in these IR-IR pump-probe studies can also be a limiting factor in attosecond pump-probe experiments. The IR pump pulse must be intense enough to create a measurable variation in the signal depending on the delay, whether this signal is in the total primary or secondary electron yield or in the yield in a specific energy region of the photoelectron spectrum. If the IR pulse, however, is strong enough to induce multiphoton photoemission, this will disturb the desired signal from the XUV pulse. At moderate intensities, this disturbance is just an added constant signal that can contribute to extra noise, but at higher intensities the multiphoton photoemission can give rise to space charge effects and thus deteriorate the image quality. The effect will be smaller the higher the kinetic energy of the electrons, since the electrons emitted by multiphoton photoemission will have rather low kinetic energies and therefore only interact with high-energy photoelectrons just at the surface.

The new generation of laser systems capable of producing high-order harmonics at repetition rates of hundreds of kHz or even higher is a key component for atto-PEEM experiments. We have shown that the high-repetition rate system can give large improvements in resolution while also reducing exposure times by more than an order of magnitude. It can also be used for energy selective imaging, either for band-pass filtering to reduce chromatic aberrations, or for imaging of primary photoelectrons. In general, transmission lowering elements such as apertures and filters can be inserted into the PEEM without increasing the exposure times to unreasonable levels.

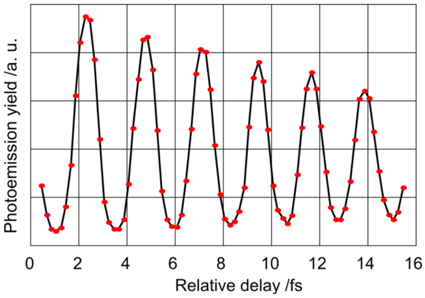

Figure 22 The sum of the photoemission yield from 5 hot spots in a series of PEEM images recorded with different delays between two femtosecond IR pulses. Adapted from [Mårsell13].

Conceptually the most straightforward IR/XUV experiment involves a single femtosecond IR pump pulse followed by a single attosecond XUV probe pulse. By varying the time delay between the IR and the attosecond pulse, the time-evolution of a single surface plasmon excitation can be investigated on the attosecond scale. Another interesting possibility is to use a single femtosecond IR pump pulse and a synchronized attosecond pulse train [Mårsell13]. In this type of experiment the time evolution that can be probed is reduced to a half-cycle (for APTs with two pulses per cycle) or to a cycle i.e. 2,7 fs (for APTs with one pulse pr cycle [Mauritsson06]), but the signal increases due to repetition of the process several times for each laser pulse. Such experiments could be advantageous for observation of plasmons on a surface. While we have shown that imaging using attosecond light pulses are feasible even with 1kHz HHG light sources, new developments in terms of MHz rep-rate atto-laser systems and tailoring of experimental setups and samples will open up for the true potential of atto-PEEM.

References

[Raether88] H. Raether, Springer: Berlin (1988).
[Maier06] S. A. Maier, Springer Science(2007).
[Stockman07] M. I. Stockman, M. F. Kling, U. Kleineberg, F. Krausz, *Nature Photonics* **1**, 539-544 (2007).
[Mikkelsen09] A. Mikkelsen, J. Schwenke , T. Fordell, L. Gang, K. Klünder, E. Hilner, N. Anttu, A.A Zakharov, E. Lundgren, J. Mauritsson, J. N. Andersen, H. Q. Xu, A. L'Huillier, Review of Scientific Instruments, **80** (2009) 123703.
[Chew12] S. H. Chew et al., Appl. Phys. Lett. **100,** 051904 (2012).
[Zakharov12] A. A. Zakharov, A. Mikkelsen, J. N. Andersen, J. of Elec. Spectro. and Related Phenomena **185** (2012) 417.
[Strickland85] D. Strickland and G. Mourou, Opt. Commun., **56** (3):219, (1985).
[Hentschel01] M. Hentschel et al, Nature, 414:509 (2001).
[Paul01] P. M. Paul et al, Science, **292**:1689-1692 (2001).
[Dubietis92] A. Dubietis, G. Jonusauskas, and A. Piskarskas, Opt. Commun. **88** (4,5,6):437, (1992).
[Krebs13] M. Krebs et al., Nature Phot., **7**:555 (2013).
[Matyschok13] J. Matyschok et al., Opt. Express, **21** (24):29656 (2013).
[Biegert12] J. Biegert, P.K. Bates, and O. Chalus, IEEE J. Sel. Top. Quantum Electr., **18** (1):531 (2012).

[Kroon14] D. Kroon et al., manuscript in revision.

[Nyholm01] R. Nyholm, J.N.Andersen, U.Johansson, B.N.Jensen, and I.Lindau Nuclear Instruments and Methods in Physics Research A467-468, **520** (2001).

[Schmidt98] Th. Schmidt, S. Heun, J.Slezak, J.Diaz, K.C.Prince, G.Lilienkamp and E.Bauer, Surface Review and Letters, v.**5**, no.6, pp.1287-1296, 1998.

[Omicron1] See www.omicron.de for details of the Focus IS-PEEM instrument manufactured by Omicron Nanotechnology GmbH.

[Hjort12] M. Hjort, J. Wallentin, R. Timm, A. A. Zakharov, U. Hakanson, J. N. Andersen, E. Lundgren, L. Samuelson, M. T Borgstrom, and A. Mikkelsen, ACS Nano **6**, (2012) 9679.

[Sun02] Sun, Y. G. & Xia, Y. N. *Adv. Mater.* **14,** 833-837 (2002).

[Liang09] Liang, H. Y., Yang, H. X., Wang, W. Z., Li, J. Q. & Xu, H. X. *J. Am. Chem. Soc.* **131,** 6068-6069 (2009).

[Wei10] Wei, H., Reyes-Coronado, A., Nordlander, P., Aizpurua, J. & Xu, H. X. *ACS Nano* **4,** 2649 (2010).

[Wei11] Wei, H. *et al. Nano Lett.* **11,** 471-475 (2011).

[Collin05] S.Collin, M. Merano, M. Gatri, S. Sonderegger, P. Renucci, J.-D. Ganière, and B.Deveaud J.Appl.Phys. **98**, 094910 (2005); W. Knauer, J. Vac. Sci. Technol. **16**, 1676 (1979); B.W. Reed, J. Appl. Phys. **100**, 034916 (2006); S.Passlack, S. Mathias, O. Andreyev, D. Mittnacht, M. Aeschlimann and M.Bauer J.Appl.Phys. **100**, 024912 (2006); S.Hellmann, K. Rossnagel, M. Marczynski-Buhlow, and L. Kipp, Phys.Rev.**B79**, 035402 (2009).

[Pietzsh08] A.Pietzsch, A. Föhlisch, M. Beye, M. Deppe, F. Hennies, M. Nagasono, E.Suljoti, W. Wurth, C. Gahl, K. Döbrich, and A. Melnikov New J.Phys.**10**, 033004 (2008).

[Buckanie09] N.M. Buckanie, J. Göhre, P. Zhou, D. von der Linde, M. Horn-von Hoegen and F.-J.Meyer zu Heringdorf J.Phys.:Condens.Matter **21**, 314003 (2009).

[Aeschlimann07] M. Aeschlimann et al., Nature **446,** 301-304 (2007).

[Baggesen09] J. C. Baggesen and L. B. Madsen, Phys. Rev. A **80,** 030901 (2009).

[Cavalieri07] A. L. Cavalieri et al., Nature **449,** 1029-1032 (2007).

[Hjort11] M. Hjort et al., Appl. Phys. Lett. **99,** 233113 (2011).

[Locatelli08] A. Locatelli and E. Bauer, J. Phys.: Condens. Matter **20,** 093002 (2008).

[Mårsell13] E. Mårsell et al., Ann. Phys. (Berlin) **525,** 162-170 (2013).

[Stöhr93] J. Stöhr et al., Science **259,** 658 (1993).

[Wolff54] P. A.Wolff, Phys. Rev. **95,** 56–66 (1954).

[Yang07] W. L. Yang et al., Science **316,** 1460-1462 (2007).

[Mauritsson06] J. Mauritsson et al, PRL **97**, 013001 (2006).